STUDIES OF ATMOSPHERIC WATER VAPOR BY MEANS

OF PASSIVE MICROWAVE TECHNIQUES

by

NORMAN EUGENE GAUT

B.A., University of California at Los Angeles

1959

S.M., Massachusetts Institute of Technology

1964

SUBMITTED IN PARTIAL FULFILLMENT OF THE

REQUIREMENTS FOR THE DEGREE OF

DOCTOR OF PHILOSOPHY

at the

MASSACHUSETTS INSTITUTE OF TECHNOLOGY

September, 1967

Signature of Author_____
                Department of Meteorology, July 17, 1967

Certified by_____
                                        Thesis Supervisor

Accepted by_____
        Chairman, Departmental Committee on Graduate Students

STUDIES OF ATMOSPHERIC WATER VAPOR BY MEANS

OF PASSIVE MICROWAVE TECHNIQUES

by

NORMAN EUGENE GAUT

Submitted to the Department of Meteorology on July 17, 1967 in partial

fulfillment of the requirements for the degree of Doctor of Philosophy.

ABSTRACT

The theory of water vapor rotational spectral lines is reviewed for the special conditions found in the atmosphere of the earth. Operational equations for the absorption coefficient of water vapor near the two lowest frequency rotational lines (22.237 GHz and 183.310 GHz) are given. The equations are used to compute spectra for several diverse climatic regions which approximate observations of total zenith opacity, zenith emission, and emission seen from space for an antenna pointing at the nadir. A study of the origin, frequency characteristics, and stability of water vapor weighting functions for the lower frequency line is presented.

Thirty two days of zenith opacity observations at five frequencies from 19 to 32 GHz are outlined and compared to spectra computed from radiosonde data taken during or near the times of the observations. It is shown that the correlation between the observed and computed spectra is dependent upon prevailing weather conditions. The observations are investigated for evidence of an enhancement in the spectra near resonance due to stratospheric water vapor. No such evidence is found which is shown to be a reasonable result on the basis of computed spectra for fourteen possible stratospheric water vapor distributions.

A method for determining integrated water vapor using zenith opacity observations is derived and evaluated. Errors of less than $\pm$ 5 percent are shown to be reasonable for good spectral data. Examples using simulated observations at two and three frequencies are given. A method of estimating the total oxygen opacity from measurements of surface temperature and pressure is derived in order that the total water vapor opacity may be extracted from observations of total opacity.

Finally, an optimum linear estimation scheme for the vertical distribution of water vapor is derived and evaluated for opacity spectral data. On the basis of limited statistics, it is shown to yield good

estimates even when noisy spectral data is inverted. Its estimate of
integrated water vapor for noiseless data is shown to be consistently
within a few percent of the true value. Inversions of real data
appear satisfactory but are difficult to evaluate.

Thesis Supervisor: Alan H. Barrett

Title: Professor of Physics

ACKNOWLEDGMENTS

This thesis is an extension and development of ideas and procedures which mostly originated with Professors Alan Barrett and David Staelin. I appreciate both the generosity of their inputs and their unwavering encouragement of my work.

Numerous other people provided help to me which collectively made this thesis possible. Some of those people are: Roger Neal, who put in many hours with and without me taking solar drift scans; Professor James Austin, who removed many administrative obstacles from my path; Eric Jensen, a master manipulator of the PDP-1; Marie-Louise Gabbe, the typist for the thesis; and Isabelle Kole, who drafted many of the diagrams.

Substantial help for the radiosonde flights was furnished by the Air Force through Air Force Cambridge Research Laboratories, and the Meteorology Department at M.I.T.

The final thank you must go to my wife who has been patient and helpful in every respect.

TABLE OF CONTENTS

LIST OF TABLES

LIST OF FIGURES

Chapter 1

INTRODUCTION

Important advances in numerical weather prediction have occurred over the last one and a half decades. They have paralleled the introduction and rapid improvement of electronic computing machines. Indeed, the advancement of the former is inextricably related to the advancement of the latter.

The pace of improvement for electronic computers has not slackened. It is reasonable to expect that microelectronics and other innovations will increase the capacity, speed, and versatility of future machines. Numerical weather prediction, however, appears to be on a plateau of achievement which will be substantially unaltered by the new opportunities provided by computer technology. It has become apparent that the limiting factor for predicting future weather events, somewhere near two to three days in advance at the present time, is not the speed or capacity for processing data, but the data itself. (See Lorenz[1] for a possible theoretical upper time limit to forecasting the state of the atmosphere.)

Perhaps 500 upper air reporting stations are in somewhat regular service today over the entire earth. The surface of the planet totals about 500 million square kilometers. If the radiosonde network were spread evenly over the globe, each station would represent approximately 1,000,000 square kilometers, or a square approximately 1000 kilometers

on a side. The ideal is considered to be closer to perhaps 300-400
kilometer separation between stations. To achieve this, the network
would need to expand at least by a factor of from six to eight.

Further aggravating the situation beyond the simple argument
of numbers given above is that reporting upper air stations are invar-
iably concentrated in well populated land regions; so much so that
perhaps only ten percent of the earth's atmosphere is under adequate
surveillance. Most oceanic regions fall within the ninety percent
which is poorly known.

Simple economic reasoning rules out further expansion of the
present radiosonde network to fill the data gaps. Novel and unconven-
tional methods will be required. Toward this end, a number of proposals
and experiments have been initiated to test new approaches to the data
problem. Of great interest and promise is the program involving the
GHOST balloons (Global Horizontal Sounding Technique). Free floating,
constant density balloons will carry small frangible sensors and trans-
mitters to measure and report the ambient conditions of the atmosphere
in which they are embedded. Strategically located ground stations or
perhaps interrogating satellites will receive and relay the data to
weather centers where numerical prediction schemes will utilize the data
immediately. Certain problems remain to be answered, however, before
GHOST becomes operational.

A more unconventional approach to the data problem involves
remote sensing of the atmosphere's properties from artificial satellites

of the earth. It has long been realized that satellites offer unique opportunities for world wide surveillance of the atmosphere. The simplicity of their orbits, their world-wide coverage, the number of observations per day, all combine to provide an ideal observational platform.

Already weather satellites using television and infrared sensors have widened our knowledge of world wide cloud formations, cloud top heights, and through the use of infrared spectrometers have begun to probe the vertical profiles of temperature and water vapor above the clouds. The information so gathered, however, does not provide the necessary data concerning the lower troposphere which is necessary for numerical weather prediction. The cloud top limit effectively shields the majority of the lower atmosphere from infrared sensors.

In order to circumvent this limitation, attention has been drawn to microwaves, that region extending arbitrarily from millimeter to meter wavelengths. Several important advantages exist for passively probing the atmosphere in this part of the electromagnetic spectrum rather than in the infrared: (1) clouds are not opaque at these frequencies allowing the cloud itself and the region below the cloud to be studied; and (2) instrumentation exists whose bandwidth is much smaller than the widths of spectral lines arising from several of the most important atmospheric gases. This latter fact allows detailed analysis of line shape which in turn facilitates the inference of the atmospheric conditions in which the lines arise.

From considerations and experiments already performed, it is clear that remote passive microwave sensors can never hope to recover the detailed structure of the atmosphere which is possible by probes passing directly through the medium; nor can they hope to compete in providing a three dimensional view of the wind patterns. However, the fidelity for producing the gross features of the temperature and water vapor profiles along with the total water vapor abundance and some information about water content of clouds may prove to be sufficient to add a great deal of useful information to the data now routinely input to the numerical weather forecasting schemes. The potential for passive microwave atmospheric measurements appeared great enough, in fact, even several years ago, to have inspired the initiation of the study presented hereafter.

The following investigation has as its purpose to present a theoretical, numerical, and where possible, observational investigation of the potential meteorological uses of measurements made near the two lowest frequency spectral lines of water vapor.

The observations which were taken were of total atmospheric extinction of sunlight at various frequencies near 22 GHz. Extinction measurements were made because their interpretation was the simplest of the various measurements which can be made and which are correlated to atmospheric water vapor.

The observations were possible because a multichannel radiometer was already in existence at M.I.T. for the specific purpose

of measuring the water vapor spectral line near 22 GHz. It had been
originally built by D.H. Staelin for planetary radio astronomical
studies, with the strong secondary intent of using it for terrestrial
water vapor investigations.

The actual measurements of atmospheric absorption were taken
during the summer of 1965 and the winter of 1966. In all, thirty-seven
days were monitored for water vapor absorption, of which thirty-two
were used in the study. Atmospheric condition on all thirty-two days
were also monitored by at least single radiosonde flights and on several
days by multiple flights. In most instances the launches occurred during
the period in which absorption measurements were being taken.

The organization of the thesis is logically based on the subject
matter. The theory of water vapor absorption in Chapter 2 is followed
in Chapter 3 by the theory peculiar to atmospheric radiation measurements.
The experimental procedures and results from the observations are outlined
in Chapter 4. Chapters 5, 6, and 7 comprise the part of the thesis con-
cerned with the application of the experimental results to the deduction
of the abundance and distribution of water vapor in the troposphere and
stratosphere. And in Chapter 8, thoughts and ideas for future work are
outlined. An appendix closes the thesis which includes tables and data
of interest to the subject matter but is either too bulky or not directly
applicable to the particular details of any given chapter.

Chapter 2

THE THEORETICAL ABSORPTION OF MICROWAVE RADIATION BY WATER VAPOR

The purpose of Chapter 2 is to: (1) provide sufficient background to understand the nature of atmospheric absorption arising from pure rotational spectral lines of water vapor; and (2), to provide expressions of sufficient detail to compute absorption due to the two lowest frequency lines, one of which occurs at 22.2 GHz and the other at 183.3 GHz.

2.1 Origin of Pure Rotational Spectral Lines of Water Vapor

2.1.1 The Rotational Energy Levels of the Water Vapor Molecule.

If one draws arbitrarily oriented axes through the center of mass of a molecule and calculates the moment of inertia about each (where the moment of inertia is defined by $I = \Sigma m_i r_i^2$, r_i being the perpendicular distance of m_i from the axis), one finds that if the moments are represented by vectors whose lengths are proportional to the magnitude of the moment and whose directions point along the axis of reference, then an ellipsoid is formed, called the ellipsoid of inertia. (For a more complete discussion of the present subject see 2 and 3). An ellipsoid may always be described most simply through the use of what are called the perpendicular principal axes. The moments along these axes are called the principal moments of inertia. If an axis of symmetry exists for the molecule, this is always a principal axis. The equation describing the ellipsoid of inertia is

$$\frac{x^2}{I_x^2} + \frac{y^2}{I_y^2} + \frac{z^2}{I_z^2} = 1 \qquad\qquad (2.1\text{-}1)$$

provided I_x, I_y, and I_z are the moments of inertia along the three principal axes.

For a diatomic molecule, the ellipsoid of inertia is a flat disk whose plane is perpendicular to the internuclear axis. This is clear when one considers that the moment of inertia about the line connecting the nuclei (an axis of symmetry) must be very small compared to the equal moments about the two perpendicular principal axes.

If two principal axes are of equal magnitude, then an ellipsoid of revolution is formed. A molecule featuring such an ellipsoid is called a symmetric rotor or symmetric top molecule. If the two equal principal moments are of larger magnitude than the third, then the molecule is called an oblate symmetric top; if the two equal moments are of smaller magnitude than the third, then the molecule is known as a prolate symmetric top.

The water vapor molecule consists of one oxygen atom and two hydrogen atoms associated in the configuration shown in Figure 2-1. It falls into neither of the two classes above; all three principal moments of inertia are unequal. Such a molecule is called an asymmetric rotor or asymmetric top molecule.

For any degree of symmetry, the energy associated with the rotation of a molecule is given by

THE WATER VAPOR MOLECULE

$$= 1.87 \times 10 \quad \text{e.s.u.}$$

Moments of Inertia

$I_a = 1.01 \times 10^{-40} \text{g cm}^2$

$I_b = 1.93 \times 10^{-40}$

$I_c = 2.81 \times 10^{-40}$
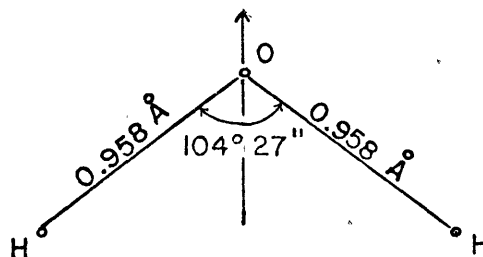
Rotational Constants

$A = 8.332 \times 10^2$ GHz

$B = 4.347 \times 10^2$

$C = 2.985 \times 10^2$

Figure 2-1. Geometrical configuration and physical constants of the water vapor molecule.

$$W \;=\; \frac{P_x^2}{2I_x} \;+\; \frac{P_y^2}{2I_y} \;+\; \frac{P_z^2}{2I_z}$$

$$\;=\; \frac{4\pi^2 A}{h} P_x^2 \;+\; \frac{4\pi^2 B}{h} P_y^2 \;+\; \frac{4\pi^2 C}{h} P_z^2 \qquad (2.1\text{-}2)$$

in which the rotational constants A, B, and C in decreasing order of
size are related inversely to the moments of inertia about the principal
axes x, y and z, and P_x, P_y, and P_z are the values of the angular momen-
tum along each axis.

The degree of asymmetry may be expressed in a number of ways but
one convenient index is Ray's parameter given in terms of the rotation
constants as

$$k \;=\; \frac{2B - A - C}{A - C} \qquad (2.1\text{-}3)$$

For a prolate symmetric top molecule in which B = C, k = -1. For an
oblate symmetric top molecule in which A = B, k = +1.

The square of the total angular momentum $\left(P_{TOTAL}^2 = P_x^2 + P_y^2 + P_z^2 \right)$ of
a rotating molecule is quantized with magnitude equal to $J(J+1)\dfrac{h^2}{4\pi}$,
where J is an integer. The component of the total angular momentum
projected on some axis fixed in space is also quantized with magnitude
$M \dfrac{h}{2\pi}$, where M is an integer restricted to values running from
-J to +J, taking on, therefore, 2J + 1 values for any given J. In sym-
metric tops, this axis can be the symmetry axis, a choice which leads
to a reasonably simple expression for the rotational energy of the
molecule in terms of the rotational constants, J, and K(= M), neglecting
second order effects. However, in an asymmetric top this axis does not

coincide with any axis fixed in the molecule and therefore lacks any easily expressible relationship with the energy of the molecule.

A convenient expression for the energy of an asymmetric top is given by

$$\frac{W}{h} = \frac{1}{2}(A+C)J(J+1) + \frac{1}{2}(A-C)E_\tau \qquad (2.1-4)$$

in which E_τ is a complicated function which depends upon the parameter τ, an integer which describes the order of energy levels of a molecule with given J. τ therefore runs from $-J$ to J and is the asymmetric equivalent to the physically interpretable quantum number K for symmetric tops.

As a further and more explicit designation of the energy state of an asymmetric top, the K values for the limiting prolate and oblate symmetric tops may be used, i.e., the energy associated with τ for an asymmetry given by k smoothly changes its magnitude with changing k from a level designated by some J and K_{-1} associated with a prolate symmetric top (k = -1) to another value associated with an oblate symmetric top (k = +1) designated by the same J but by some value, in this case, of the quantum number K_{+1}. If the limiting quantum numbers K_{+1} and K_{-1} are known, τ may always be found from the relationship

$$\tau = K_{-1} - K_{+1} \qquad (2.1-5)$$

The value of E_τ in (2.1-5) is only a function of the asymmetry parameter and has been computed and tabulated (see Townes and Schawlow[2],

Appendix IV). Figure 2-2 shows the relationship between energy levels of prolate, oblate and the connecting asymmetric cases for several J states.

2.1.2 Transitions Between Pure Rotational Energy Levels.

The discussion in 2.1.1 tacitly assumed that the molecular energy was derived only from rotation and not from vibration or excited electronic states. The levels so derived are called, consequently, pure rotational energy states. Transitions occur between some of the rotational energy states giving rise to absorption of electromagnetic energy if the final state is a higher energy level than the initial state, and to emission if the final state is a lower energy level. Two so-called selection rules define allowed transitions between energy levels. They are briefly outlined below for the case of water vapor:

(1.) The water molecule has a permanent dipole moment which is arranged along the symmetry axis, which in turn is associated with the intermediate principal moment of inertia (I_b). The first selection rule applies generally to transitions involving dipoles. It is found from a quantum mechanical evaluation of the intensity of a transition between two energy states of a rotating dipole. The transition intensity is zero unless the change in the quantum number J obeys the rule

$$\Delta J = 0, \pm 1 \tag{2.1-6}$$

Spectral lines arising from transitions where $\Delta J = -1$ are classified as belonging to the P branch of the spectra. $\Delta J = 0$ and $\Delta J = +1$
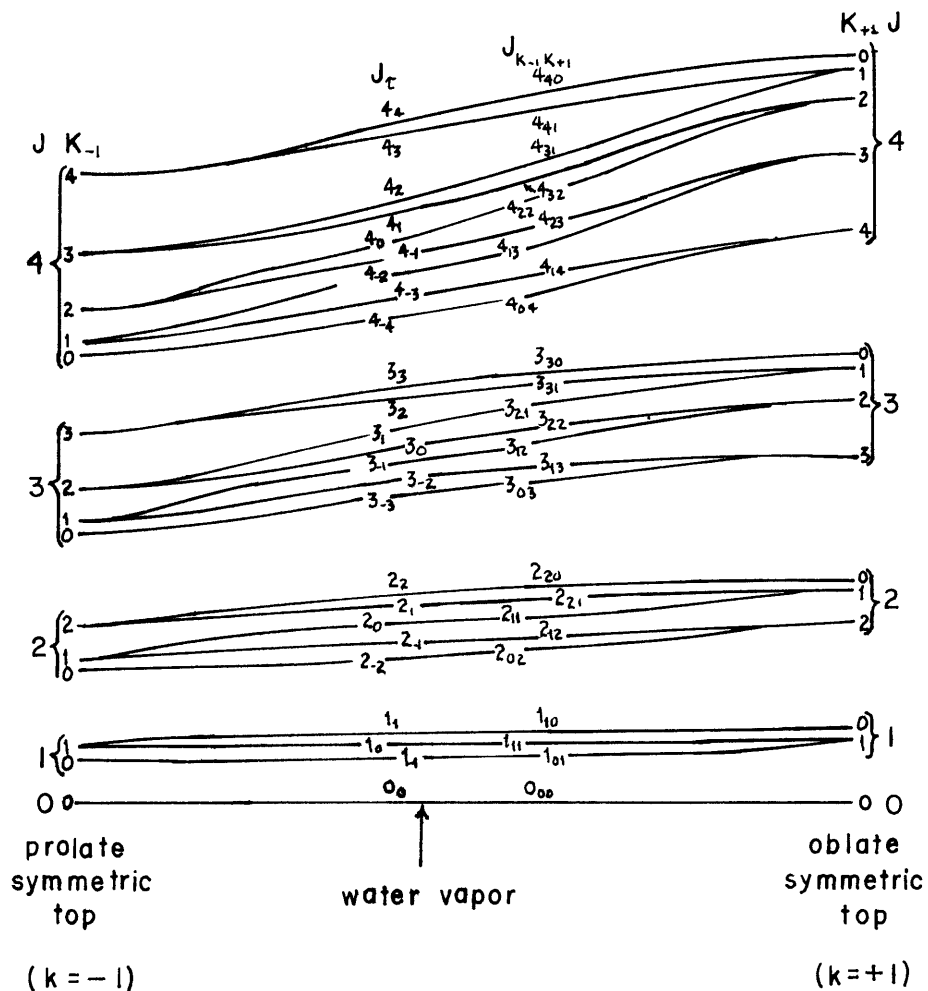
Figure 2-2. The energy levels of the asymmetric rotors related to the two limiting cases, the prolate and oblate symmetric tops. (After Townes and Schawlow.)

transitions give rise to the Q and R branches of the spectra, respectively.

(2.) The second selection rule is a result of symmetry considerations of the molecule. Any 180° rotation of a molecule about a principal axis of inertia leaves the ellipsoid of inertia unchanged. The wave function associated with the energy state, however, may or may not change sign with respect to such a rotation (neglecting degenerate cases). If it does not change sign, the particular state which it describes is called a symmetric one; if it does change sign, it is known as an antisymmetric state with respect to the given rotation.

For the case of symmetric top molecules, both prolate and oblate, it is found that the symmetry of a state with respect to the relevant rotations depends solely on the quantum number K. If K_{-1} (prolate) is even, the state is symmetric with respect to rotations about the axis of least moment of inertia (I_a). If K_{-1} is odd, it is found that the state is antisymmetric to such rotations. Similarly, for oblate symmetric rotors, it is found that with respect to rotations about the axis of largest moment of inertia (I_c) the wave functions are symmetric or antisymmetric as to whether K_{+1} (oblate case) is even or odd.

For the asymmetric molecule, the symmetry of the wave functions with respect to rotations about a principal axis are unchanged from the limiting prolate case and limiting oblate case; i.e., the symmetry for an asymmetric wave function with respect to a rotation about the axis of least moment of inertia is the same as the symmetry for the

limiting prolate symmetric top; it depends upon the quantum number K_{-1}. The same is true for rotations about the axis of maximum moment of inertia and the limiting oblate symmetric top; symmetry depends upon K_{+1}.

For rotations about the intermediate principal axis, it is necessary to nullify the effect of rotation about each of the other two axes, i.e., if the molecule rotates 180° about all three axes, it returns to its original orientation and parity and therefore whatever parity remains after a rotation about axes a and c must be nullified or left unchanged by a rotation about the b axis. If rotation about a is antisymmetric and rotation about c is symmetric, then rotation about b is antisymmetric to restore the original parity.

The symmetry properties are applicable to the calculation of the strength of a given transition. The intensity of a transition is proportional to the square of what is called the dipole matrix element. This matrix element for the x component of the dipole moment of the molecule is given by

$$\mu_{xij} = \int \psi_i \, \mu_x \, \psi_j^* \, d\tau \qquad (2.1\text{-}7)$$

in which ψ_i is the wave function for the initial stationary energy state defined by J, K_{-1}, and K_{+1}; μ_x is the component of the permanent electric dipole moment of the molecule along the x axis; ψ_j^* is the complex conjugate of the wave function associated with the final stationary energy state, defined by J', K'_{-1}, and K'_{+1}; and τ in this

case is the integration variable taken over all the possible spatial configurations of the molecule. The total matrix element for a transition is related to its components as follows:

$$\mu_{ij}^2 = \mu_{x_{ij}}^2 + \mu_{y_{ij}}^2 + \mu_{z_{ij}}^2 \quad . \qquad (2.1-8)$$

If the electric dipole is aligned along the intermediate axis of inertia (b axis) as it is in the water molecule, 180° rotations about the axis of smallest moment of inertia (a axis), or about the axis of largest moment of inertia (c axis) cause the dipole to reverse its direction. μ_{ij} however, cannot change sign for such a symmetrical interchange, and therefore the product $\psi_i \psi_j^*$ must change sign when the orientation of μ reverses. Recalling the symmetry discussion above, if rotation occurs about axis a, the wave function is symmetric or antisymmetric when K_{-1} is even or odd respectively. Therefore, to retain the sign of μ_{ij} in the case of such a rotation, either $K_{-1,i}$ or $K_{-1,j}$ must be even while the other is odd. This is condition one. Further, if rotation occurs about axis c, then either $K_{+1,i}$ or $K_{+1,j}$ must be even while the other is odd for the same reasoning. This is condition two. Both of these conditions are met by the transitions which are specified for all the various initial conditions listed in Table 2-I below. These restrictions constitute the second selection rule.

TABLE 2-I. Allowed transitions for Asymmetric Tops with Dipole Moment Parallel to Principal Axis of Intermediate Moment of Inertia. e stands for an even state (K even) and o for an odd state (K odd).

Initial Conditions			Acceptable Final Conditions	
K_{-1}	K_{+1}		K_{-1}	K_{+1}
e	e	$\longrightarrow$	o	o
o	o	$\longrightarrow$	e	e
e	o	$\longrightarrow$	o	e
o	e	$\longrightarrow$	e	o

The only spectral lines which exist then are those which arise from transitions which simultaneously obey both the selection rules for J (Equation (2.1-6)) and K_{+1} and K_{-1} (Table 2-I). Their center frequency is given closely for low pressures by the Bohr relationship

$$\nu_{ij} = \left\lceil \frac{w_j - w_i}{h} \right\rceil \qquad (2.1-9)$$

If one searches the possible transitions between rotational energy levels sufficiently close to give ν_{ij} a value in the micro-wave region, many possibilities arise. However, when the selection rules are applied, most combinations are eliminated. Two, however, which are not eliminated give rise to the lines of principal interest in this study. They are the transitions below:

Initial State			Final State			Branch	Frequency
J	K_{-1}	K_{+1}	J	K_{-1}	K_{+1}		
5	2	3	6	1	6	R	22.237 GHz
2	0	2	3	1	3	R	181.310 GHz

For convenience, the transitions are written as $5_{2,3} \rightarrow 6_{1,6}$ and $2_{0,2} \rightarrow 3_{1,3}$ or in the J, τ notation $5_{-1} \rightarrow 6_{-5}$ and $2_{-2} \rightarrow 3_{+2}$. (For a list of the rotational transitions of water vapor resulting in the 53 lowest resonant frequencies, together with their strengths, initial and final term values, line widths, and statistical weights, see Appendix A-I).

2.2 The Microwave Absorption Coefficient for Water Vapor.

The general expression for the absorption coefficient due to the transition of molecules between the energy states i and j is given by (adapted from Equation 1 of van Vleck[4])

$$\gamma_{ij} = \frac{8\pi^3 \nu}{3\hbar c} |F(\nu_{ij}, \nu)| \left\{ N_i |\mu_{ij}|^2 - N_j |\mu_{ji}|^2 \right\} \quad (2.2-1)$$

in which γ_{ij} is the absorption coefficient for the transition i → j; ν is the frequency of the incident radiation; N_i and N_j are the number densities of molecules in the lower and higher energy states respectively; $|\mu_{ij}|^2$ is the square of the dipole matrix element associated with the transition i → j; and $F(\nu_{ij}, \nu)$ is what may be called the "structure" factor or "line shape" factor for the transition. c and h are the speed of light and Planck's constant, respectively.

Equation (2.2-1) explicitly brings out that γ_{ij} is the result of the difference between the energy absorbed by all molecular transitions from the state of lower energy to that of higher energy, and the energy which returns to the radiation field from molecules making the reverse transition. If the population of state i is greater than the population of state j, γ_{ij} is positive and represents absorption; if the opposite is true, then γ_{ij} is negative and represents amplification.

2.2.1 The Partition Function.

The number of molecules in a given state, say the i th, may be found from Boltzmann theory for a gas in thermal equilibrium. For the case of water vapor N_i may be written as

$$N_i = N P_i \qquad (2.2-2)$$

where N is the total number of absorbing particles per cc and P_i is a number between 0 and 1 which gives the fraction of N in the state i.

For the case of water vapor P_i is given by (see Herzberg[3], Chapter V).

$$P_i = P_{v_i} P_{R_i} \qquad (2.2-3)$$

in which P_{v_i} represents the fraction of all molecules which are in the vibrational energy state of interest, and P_{R_i} the fraction in the rotational energy state of interest. Equation (2.2-3) assumes that all molecules remain in the electronic ground state. P_{v_i} may be expanded as (Townes and Schawlow[2], Chapter 4).

$$P_{v_i} = \exp\left(-W_{v_i}/kT\right) \prod_n \left[1 - \exp\left(-hc\,\omega_n/kT\right)\right]^{d_n} \qquad (2.2\text{-}4)$$

where k is Boltzmann's constant, T the temperature of the gas, h is Planck's constant, W_{v_i} is the energy of the stationary vibrational energy state of interest, ω_n the wave number equivalent to the normal vibration frequencies of the molecule, and d_n is the degeneracy of the nth normal molecular vibration. For the water vapor spectral lines of interest $W_{v_i} = 0$ so that P_{v_i} depends upon the extended product of (2.2-4). The smallest normal vibrational wave number of water vapor is associated with ω_2 and is approximately 1600 cm^{-1}. For the maximum atmospheric temperature expected the quantity $\exp(-hc\omega_2/kT)$ is only 0.00083. The exponentials associated with ω_1 and ω_3 are even smaller; P_{v_i} is, therefore, approximately 1 and P_i is taken to be equal to P_{R_i}.

The fraction of molecules in a given rotational state may be expressed as (see Townes and Schawlow[2] Equation (4-25), and the discussion of nuclear spin beginning on page 102, or the discussion of G on page 427 in van Vleck[5])

$$P_{R_i} = \frac{g_{\tau_i}\left(2J_i + 1\right) e^{-E(J_i,\tau_i)/kT}}{\sum_J \sum_\tau g_\tau \left(2J + 1\right) e^{-E(J,\tau)/kT}} \qquad (2.2\text{-}5)$$

In Equation (2.2-5), the numerator is the Boltzmann factor for the stationary energy state i in the transition i → j of Equation (2.2-1). The rotational energy associated with the state is given in the J, τ

notation. The statistical importance of each J, τ energy state is modified in two ways: (1) by the non-dependence of the energy on the space orientation of J ($2J + 1$ degeneracy); and (2), by the ratio of the number of possible symmetric to possible antisymmetric nuclear spin states. The statistical weight due to nuclear spin, designated g, is for the asymmetric rotor a function of τ only. For water vapor its value is 1 when a transition occurs between levels where K_{-1}, K_{+1} change from even-even to odd-odd, (or vice versa), i.e., when τ is even, and 3 when a transition occurs between even-odd and odd-even levels (τ odd).

The double sum in the denominator of (2.2-5) is called the rotational partition function G and is only a function of temperature since the rotational energy states are fixed. An approximation to the sum with its temperature dependence is given in van Vleck[5] as

$$G = 170 \left(\frac{T}{293} \right)^{3/2} \qquad (2.2\text{-}6)$$

A reevaluation of the constant using values for $E_{J,\tau}$ which included all τ values for J = 1 through 11 and several τ values for J = 12, 13, and 14[8] shows a more precise estimate for the constant to be 172.4. The difference is about one percent. A comparison of the true value of G with the power law approximation of Equation (2.2-6) is presented in Figure 2-3. A final form for P_{R_i} with the reevaluation of G considered may be written as

$$P_{R_i} = \frac{g_{\tau_i} (2J+1) e^{-\varepsilon(J_i, \tau_i)/kT}}{0.0344 \, T^{3/2}} \qquad (2.2\text{-}7)$$
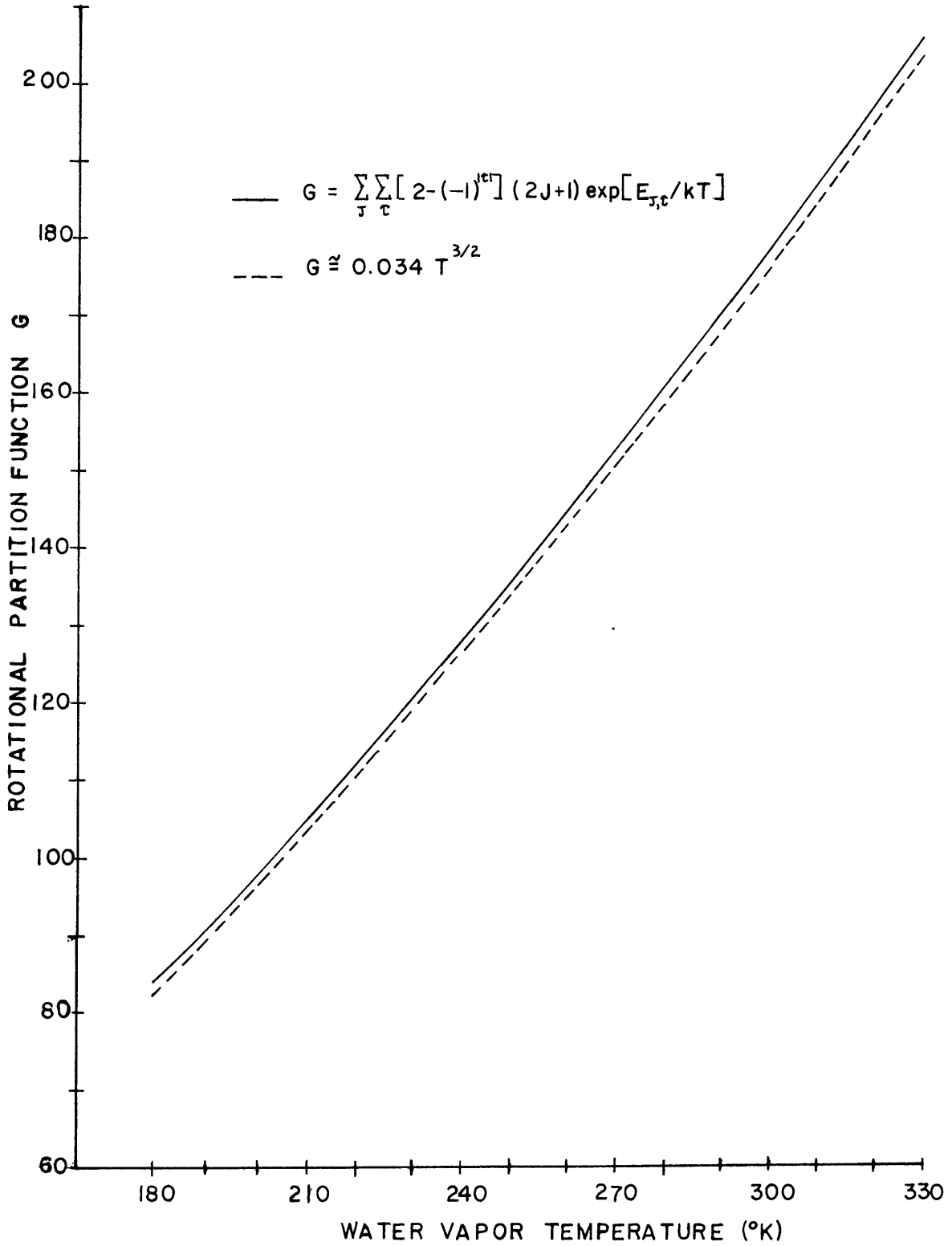
Figure 2-3. The rotational partition function G and the approximation to it by van Vleck [5] .

The statistical weights due to nuclear spin and the space quantization factor (2J + 1) cause P_R to deviate substantially from a straight Boltzmann distribution for a system in thermal equilibrium. Figure 2-4 presents the relative distribution of molecules as a function of their energy together with a straight Boltzmann curve.

2.2.2 The Line Strength Parameter.

Explicitly, the value of μ_{ij} used in Equation (2.2-1) is given by the solution to Equations (2.1-6) and (2.1-7). They refer to a particular transition from quantum numbers J (total angular momentum), τ (order of the energy level within a given J state), and M the space quantization of J to another state J', τ' , M' . In the absence of a magnetic field, the energy is independent of M and μ_{ij} applies to the 2J + 1 degenerate states of the lower energy state.

For the opposite transition J', τ' , M' $\rightarrow$ J, τ , M another matrix element applies, namely, μ_{ji} related to μ_{ij} as follows:

$$\left(2J+1\right)\left|\mu_{ij}\right|^2 = \left(2J'+1\right)\left|\mu_{ji}\right|^2 \quad . \tag{2.2-8}$$

Associated with the matrix elements μ_{ij} and μ_{ji} but more general is the so-called "transition strength" defined as

$$\sum \left|\Phi_{ij}\right|^2 = \frac{\left|\mu_{ij}\right|^2 (2J+1)}{\mu^2} \tag{2.2-9}$$

where μ is the permanent dipole moment of the molecule, J is the rotational quantum number of the initial energy state, and $\sum\left|\Phi_{ij}\right|^2$ is
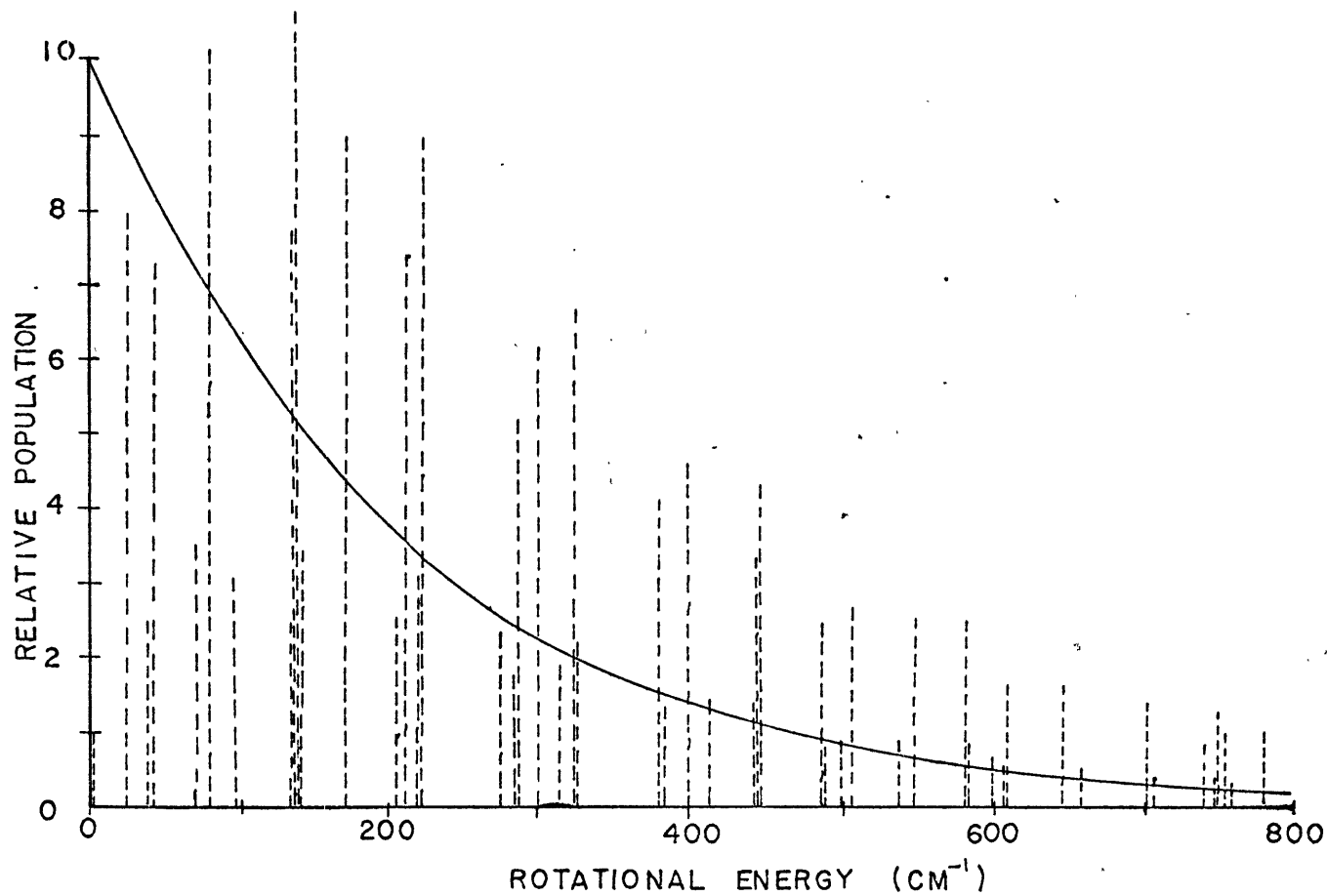
Figure 2-4. The relative distribution of water vapor molecules over the first 52

energy states at 293° K compared to a straight Maxwell-Boltzmann distribution.

defined as the squares of the elements of the direction cosine matrices

summed over the Zeeman components and three directions of space for the

transition i → j. King et al.[7] have tabulated the $\sum |\Phi_{ij}|^2$ for

the particular asymmetry of water vapor (k = -0.436426) for most of the

important transitions through J = 6. General tables of $\sum |\Phi_{ij}|^2$ have

been computed for various values of k for J as great as 35 in Wacker et

al.[9] These latter tables can be used for roughly estimating $\sum |\Phi_{ij}|^2$

for transitions involving J higher than 6. This was done for several of

the lines listed in Table A-1 in the Appendix. Those so interpolated

are indicated. The utility of tabulating the $\sum |\Phi_{ij}|^2$ rather than

$|\mu_{ij}|^2$ is apparent when its invariance with the order of i, j is

considered.

Incorporating Equations (2.2-7) and (2.2-9) in (2.2-1) the absorp-

tion coefficient of a microwave absorption line of water vapor may be

written as

$$\gamma_{ij} = \frac{8\pi^3 N \nu}{3 \hbar c} \frac{\mu^2 g_{ij} \sum |\Phi_{ij}|^2}{0.0344 \, T^{3/2}} \left\{ e^{-E_i/kT} - e^{-E_j/kT} \right\} \qquad (2.2-10)$$

where i and j are particular energy states designated by some J, τ and

J', τ' .

Equation (2.2-10) brings out very clearly that the absorption

intensity depends upon the difference in the Boltzmann factors. Since

the difference between energy levels which produce microwave spectra

must be small, the term in brackets is the difference between terms

which are almost equal. To remove this compensation, the following
approximation is commonly made when thermal equilibrium obtains:

$$e^{-\varepsilon_i/kT} - e^{-\varepsilon_j/kT} = e^{-\varepsilon_i/kT}\left\{1 - e^{-h\nu_{ij}/kT}\right\}$$

$$\cong e^{-\varepsilon_i/kT}\,\frac{h\,\nu_{ij}}{kT} \qquad\qquad (2.2\text{-}11)$$

(It should be emphasized that the temperature T which occurs in Equation (2.2-11) is associated with the distribution of molecules over the possible energy states. It is an excitation temperature and is conceptually unrelated to the kinetic temperature of the gas. Only when the kinetic and rotational energy states are in thermal equilibrium do the two become identical numerically).

The approximation made in (2.2-11) is valid when $\nu_{ij} \ll \frac{kT_{MIN}}{h}$. The lowest expected atmospheric temperature is near 180° K leading to a value for $\frac{kT_{MIN}}{h}$ equal to approximately 3600 GHz. The line of highest resonant frequency which we will consider in detail is centered near 183 GHz, below $\frac{kT_{MIN}}{h}$ by a factor of twenty, validating the approximation. Equation (2.2-11) will be retained for lines whose center frequencies are as great as 1500 GHz, primarily because only their effect on frequencies below 200 GHz is desired and great accuracy is not required.

Equation (2.2-10) may be rewritten incorporating (2.2-11) as

$$Y_{ij} = \frac{8\pi^3 \nu N}{3 c k T} \frac{\mu^2 g_{ij} \sum |\Phi_{ij}|^2}{0.0344 \, T^{3/2}} \nu_{ij} \, e^{-E_i/kT} \left| f(\nu_{ij}, \nu) \right| \qquad (2.2\text{-}12)$$

where now i refers to the initial energy state and N to the total number density of absorbing particles.

2.2.3 The Line Shape Factor

A number of mechanisms can cause absorption to occur at frequencies removed from the theoretical resonance of a molecular energy transition. Broadening mechanisms include the natural line width, Doppler effects, collisions between molecules, saturation effects, and collisions with the container of the gas [2]. By far the most important mechanism over most of the atmospheric range of temperatures and pressures is collisional broadening, although in the region above 60-70 km Doppler broadening must also be considered. The particular form of the shape factor, $f(\nu_{ij}, \nu)$ in which we are interested is dominated by the effect of collisions.

Derivations of theoretical line shapes for collision broadened lines have been done by Lorentz[24], van Vleck and Weisskopf[10], Anderson[15], Ben Reuven[16], Zhevakin and Naumov[17], and Gordon[13] among others. The original work was done by Lorentz who was concerned mainly with spectral lines in the visible region of the electromagnetic spectrum. The important assumptions upon which it was founded were: (1) rotating molecules could be treated as classical oscillators of natural frequency ω_o driven by the external field to oscillate at ω ; and (2) collisions between

rotating molecules leave the phases of the oscillators randomly distributed. The resulting line shape factor was then shown to be of the form

$$f(\nu_{ij}, \nu) = \frac{1}{\pi}\left[\frac{\Delta\nu}{(\nu_{ij}-\nu)^2 + \Delta\nu^2} - \frac{\Delta\nu}{(\nu_{ij}+\nu)^2 + \Delta\nu^2}\right] \qquad (2.2\text{-}13)$$

For spectral work in the visible where both $\frac{\Delta\nu}{\nu} << 1$ and $\frac{|\nu_{ij}-\nu|}{\nu} << 1$ the formula was shown experimentally to be quite accurate.

A criticism of (2.2-13) was based on the fact that if ν_{ij} were taken to equal zero, it would be expected that the resulting shape should reduce to the expression derived by Debye[18] for non-resonant absorption in a polar gas. It did not. Van Vleck and Weisskopf removed this difficulty by changing assumption (2) in the Lorentz derivation as follows: Instead of random phases after collision for the interacting molecules, they assumed that the phases would be constrained by the external field to a Boltzmann distribution for thermal equilibrium. Application of the new assumption led to a modification of (2.2-13) as follows

$$f(\nu_{ij}, \nu) = \frac{\nu}{\pi\nu_{ij}}\left[\frac{\Delta\nu}{(\nu_{ij}-\nu)^2 + \Delta\nu^2} - \frac{\Delta\nu}{(\nu_{ij}+\nu)^2 + \Delta\nu^2}\right] \qquad (2.2\text{-}14)$$

which, when applied to absorption, reduces to the Debye expression for polar gases in the limit $\nu_{ij} \longrightarrow 0$. The Boltzmann distribution

after collision requires that the period of the oscillation of the external field is long enough to present the colliding molecules with essentially a static field over the time of collision.

For many microwave applications, Equation (2.2-14) has been shown to qualitatively describe the shape of spectral lines. However, from further experimental work, a number of shortcomings have come to light.[11,12,17,21,25] They include:

(1) If the shape is quantitatively accurate in the region of resonance, often the wings of the spectral lines are not accurately represented.

(2) As higher pressures are encountered the resonant frequency shifts toward lower frequencies, a result not obtainable from Equation (2.2-14).

(3) The line width per unit pressure is not constant over all pressures so that the use of (2.2-14) is applicable only in the pressure region in which binary collisions occur.

Anderson[15], in his study of collisional broadening, provided for a shift of the resonant frequency, and Ben-Reuven[16] drawing from the work of Baranger[79], Kolb and Griem[80], and Fano[81], has, with considerable success reproduced the shift and shape of the ammonia inversion spectra at high pressures and in the wings at lower pressures. His line shape factor may be written as

$$F(\nu_{ij}, \nu) = \frac{1}{\pi} \frac{\nu}{\nu_{ij}} \left\{ \frac{2(\Delta\nu - \zeta)\nu^2 + 2(\Delta\nu + \zeta)[\nu_{ij} + \delta + \Delta\nu^2 - \zeta^2]}{[\nu^2 - (\nu_{ij} + \delta)^2 - \Delta\nu^2 + \zeta^2]^2 + 4\nu^2\Delta\nu^2} \right\} \quad (2.2\text{-}15)$$

in which γ is essentially a parameter which describes the variation

of the line width with pressure, and δ is a parameter which allows

for the shift of the resonance peak toward zero frequency. The theory

is built upon the "impact" approximation introduced by Baranger in

which it is assumed that the average time interval between strong

collisions is long compared to the duration of such a collision. The

parameter arises from the consideration of inelastic collisions which

cause transitions responsible for a given spectral line. When it may

be considered negligible, (2.2-15) reduces to (2.2-14) with the reten-

tion of the possibility through δ of a shift in the resonance frequency.

Gordon[13] has generalized the approach which Baranger originated

to produce a line shape which has considerably improved the pressure

dependence of the absorption spectrum for oxygen. Two important aspects

of Gordon's approach have been: (1) to differentiate between strong

(Hund's case a) and weak (Hund's case b) coupling between the electronic

spin and the rotation of the molecule; and (2) to theoretically treat

the interference which occurs between overlapping resonance lines. It

is a result of the latter consideration that strongly overlapping lines

are not a sum of individual Lorentz terms.

Unfortunately, for the specific case of water vapor, the more

sophisticated line shapes have not been applied, although considerable

evidence has accumulated to the effect that the simple van Vleck-Weisskopf

line shape is inadequate in several ways. The evidence begins with the

measurements of water vapor absorption by Becker and Autler[21] near 1 cm

and the attempt to match them utilizing the van Vleck Weisskopf line shape. Figure 2-5 is presented to show the comparison between the data collected by Becker and Autler for conditions of 10 g/m^3 of water vapor mixed with air at one atmosphere pressure and a temperature of 318° K utilizing (2.2-12) and a direct application of Equation (2.2-14). The theoretical curve to compare is labeled van Vleck-Weisskopf (uncorrected). It is clear from Becker and Autler that the contribution to the theoretical absorption from the resonance term at 1.35 cm would not be far wrong if the contribution from the wings of all higher lines were greater by a factor of 4 to 6. The curve labeled van Vleck-Weisskopf (corrected) in Figure 2-5 results from the application of Equations (2.2-12) and (2.2-14) again, but this time the contribution to the absorption by all resonances excepting only the 1.35 cm line have been increased so that near resonance there is a subjective best fit between the experimental and the theoretical values.

A new problem arises however. If we are to accept the stated accuracy of the experimental points (nowhere greater than 10 percent, probably less than 5 percent near resonance) then even though the theoretical curve is adequate over most of the resonant peak, it now shows values which are too great in the high frequency wing even for the quoted errors. This would appear to be a problem of the line shape also. However, before the latter discrepancy can be adequately treated, it is imperative that a re-examination of the experimental line shape in the vicinity of the 1.35 cm resonance be conducted.
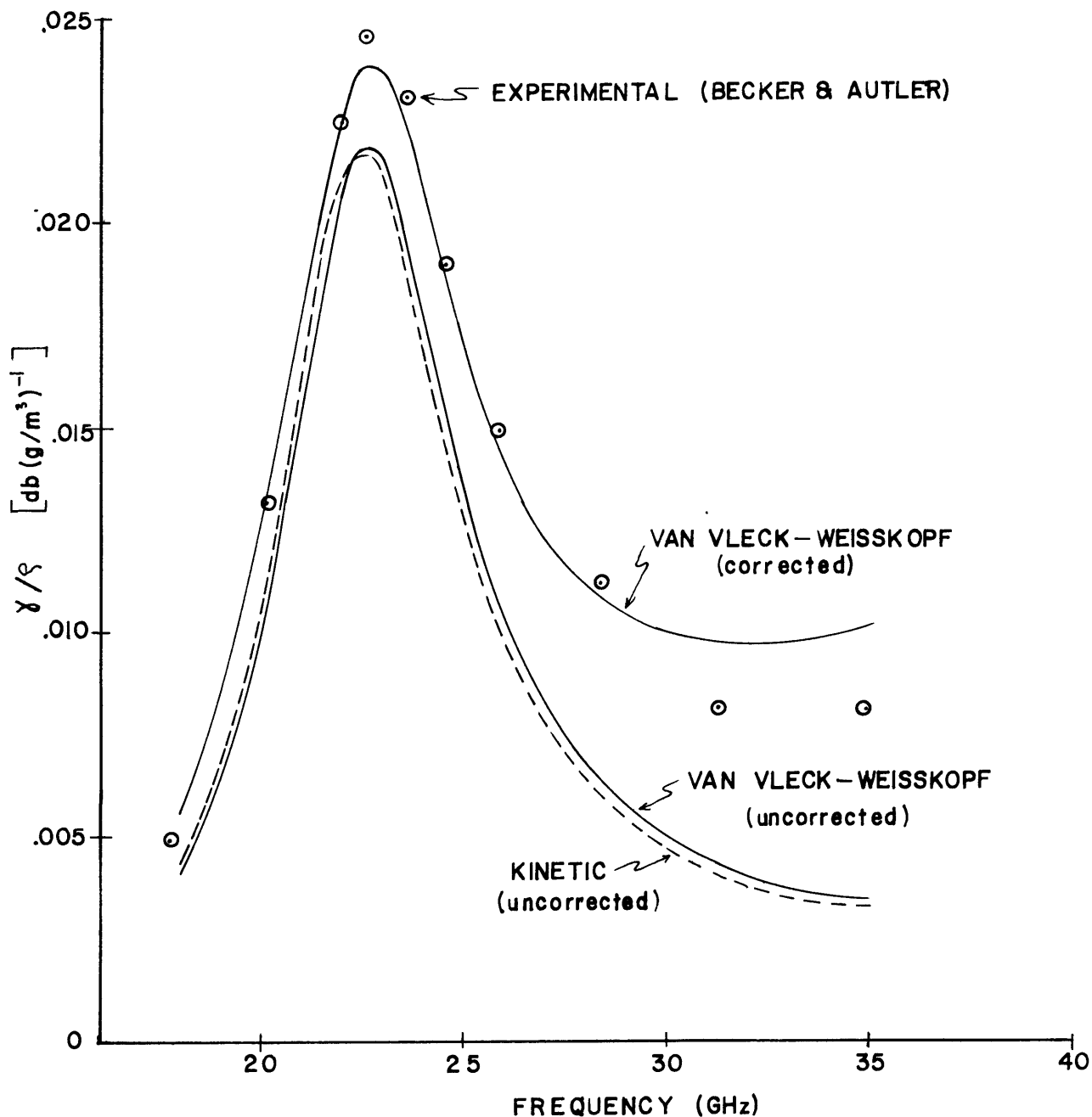
Figure 2-5. Three theoretical representations of the 22 GHz res-
onance of water vapor compared to experimental data: (1) van Vleck
with the non-resonant term multiplied by a factor of six; (2) van
Vleck with with no correction to the non-resonant term; and (3) the
Kinetic line shape with the van Vleck uncorrected non-resonant term.

If one turns to the water vapor spectral line centered near 183.3 GHz, a similar situation to the 1.35 cm case is found. Frenkel and Woods[25] have made measurements with a Fabray-Perot type resonant transmission cavity to determine the line shape. Their conclusions are that near resonance, a Lorentzian line shape also consistent with the theory of van Vleck and Weisskopf is justified, but that in the wings the theoretical residual effects of other lines is too low by at least a factor of 4 to 5.

An empirical relationship was derived to approximate the experimental results which they obtained. In the region between 100 and 300 GHz, the absorption coefficient and line shape as they determined it for a mixture of water vapor and nitrogen can be expressed as

$$\gamma_{1.64}/\rho = C_1 \left(\frac{\nu}{\nu_{1.64}} \right) \frac{\nu \left(\Delta \nu_{wv}^o + \Delta \nu_N^o \right)}{\left(\nu - \nu_{1.64} \right)^2 + \left(\Delta \nu_{wv}^o + \Delta \nu_N^o \right)}$$

$$+ C_2 \left(\frac{\nu}{\nu_{0.92}} \right) \frac{\nu \left(\Delta \nu_{wv}^o + \Delta \nu_N^o \right)}{\left(\nu - \nu_{0.92} \right)^2 + \left(\Delta \nu_{wv}^o + \Delta \nu_N^o \right)^2}$$

$$+ C_3 \frac{\nu^2 \left(\Delta \nu_{wv}^w + \Delta \nu_N^w \right)}{\nu_w^3} \tag{2.2-16}$$

in which C_1 , C_2 , C_3 are computed from the theoretical line strengths given by Benedict and Kaplan[19], $\nu_{1.64}'$ and $\nu_{0.92}'$ are the resonant frequencies for the 183 GHz and 324 GHz lines respectively, ν_w is taken as 183.3 GHz and ν is the frequency of the radiation being absorbed. The first two terms are resonance terms, and the last is an approximation to the contributions from the wings of all other

lines excepting only the two explicitly represented. The four para-
meters $\Delta\gamma_{wv}^{o}$, $\Delta\gamma_{N}^{o}$, $\Delta\gamma_{wv}^{w}$, and $\Delta\gamma_{N}^{w}$ are the contributions
to the line width from self-broadening and from nitrogen, respectively,
near resonance (designated by the superscript o), and in the wings of
the line (designated by the superscript w). Each of the contributions
can be written as

$$\Delta\gamma_{n}^{m} = k_{n}^{m} P_{n} \qquad (2.2\text{-}17)$$

where m designates the part of the resonance line being represented
(center or wings), n stands for the gas involved which broadens the
water vapor line, k_{n}^{m} refers to the line width per unit pressure
appropriate to the region m and broadener n , and P_{n} is the partial
pressure of the broadening gas designated by n.

Equations (2.2-16) and (2.2-17) imply: (1) that the line widths
are directly proportional to pressure, at least over the pressures of
interest; (2) that the contributions of the various gases to the total
line width combine linearly; (3), that the line width parameters for
the resonance at 0.92 mm (324 GHz) which is represented by the second
term in (2.2-14) is approximately the same as that one found for the
1.64 mm (183.3 GHz) line represented by the first term; and (4), that
the two resonance lines combine linearly, i.e., no interference between
the lines occur.

There is ample justification for the first implication. The
work at low pressures (see Townes and Merritt[23] and Rusk[26]) and at

high pressures (see Becker and Autler[21] and Frenkel and Woods[25]) tend

to confirm that the line width of the two lowest frequency water vapor

lines are linear in pressure over the pressure range of interest in the

atmosphere, i.e., from a few tenths of a mm of Hg to approximately one

atmosphere. (see also Hemmi[27] for further confirmation for the 183.3

GHz line). The second implication is probably not exactly true, but

for small ratios between the partial pressure of water vapor and the

partial pressure of the broadening gas it is not an important source

of error. From the work of Benedict and Kaplan[19] the ratio of the

theoretical line widths between the 183.3 GHz line and the 325 GHz line

is 1.25 which means that some bias away from the true value of $\Delta \nu_N$

for the 183 GHz line should occur when computed from Equation (2.2-13).

And from the work of Gordon[13], the fourth implication must be considered

of doubtful validity, although the error introduced by this implicit

assumption is unknown.

Nevertheless, for the k_N^o which represents the region at

and near resonance, for nitrogen as the broadening gas, Frenkel and

Woods arrive at a value between 4.1 and 4.7 Mc/mm Hg compared to a

value of 3.76 Mc/mm Hg found by Rusk in an experiment done at low

pressure. For the half width contribution near resonance due to self

broadening, Frenkel and Woods measured a value for k_{wv}^o between

22 and 24 Mc/mm Hg which compares to the value which Rusk found of

19.1 Mc/mm Hg.

In order to retain the Lorentzian resonance terms, in the wings

of the line it was necessary to hypothesize an increase in the line width as the frequency observed moved away from resonance. The effective line width contribution from self broadening resulted in a value for k_{wv}^{w} of approximately 200 Mc/mm Hg, an increase above the resonance term by a factor of nine to ten. The increase in line width from near resonance to the wings for nitrogen was a factor of 4 to 5 with the result that k_{N}^{w} was approximately equal to 19 Mc/mm Hg. The effect of increasing the k's for the third term of Equation (2.2-16) is qualitatively similar to increasing the whole non-resonant contribution as was done for the corrected curve in Figure 2-4 for the 22.2 GHz line.

The 183.3 GHz line is shown in Figure 2-6 represented by the Frenkel and Woods empirical equation (2.2-16), a single resonance van Vleck-Weisskopf expression using theoretical line parameters (Equations (2.2-12) and (2.2-14)) ,and a van Vleck-Weisskopf expression where the next 53 lines are explicitly taken into account.

Further evidence of the inadequacy of the uncorrected van Vleck-Weisskopf line shape is found in the experiments done by workers at the University of Texas. It is difficult to evaluate much of the work presented in these reports because of the unknown conditions which the atmosphere presents during many of the measurements. However, in a series of papers and reports (see for example Hemmi[27], Straiton and Tolbert[28], Tolbert, Krause and Straiton[29], and Tolbert, Straiton and Simons[30]), the general conclusion has been that the theoretical
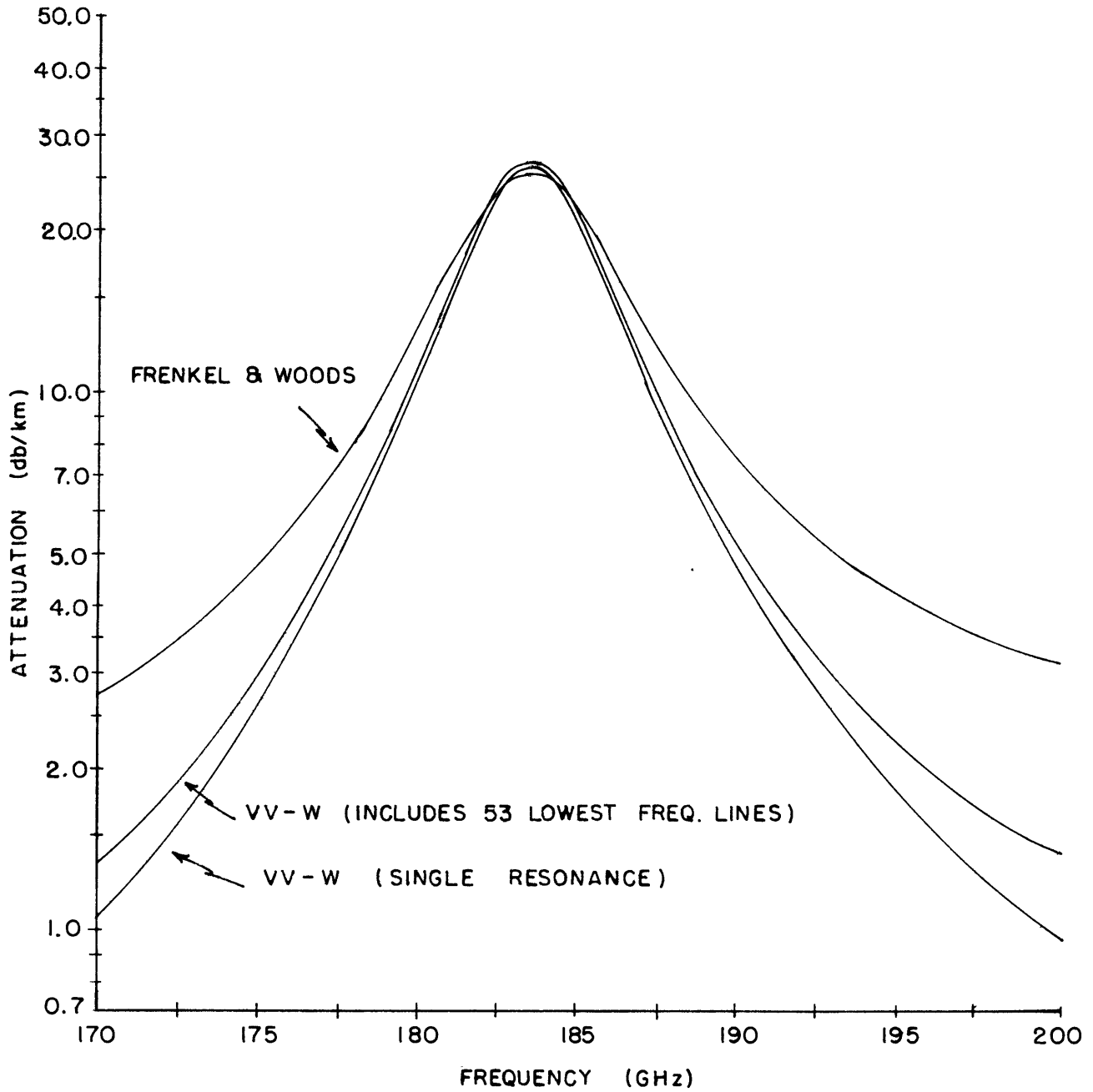
Figure 2-6. Comparison of absorption near the 183 GHz water vapor rotational line as predicted by: van Vleck-Weisskopf single resonance expression; van Vleck-Weisskopf expression considering the first 53 water vapor rotational resonances; and the Frenkel and Woods empirical formula. Conditions in the gas are: nitrogen, 1000 mb; water vapor, 7.23 g/m^3 (7.50 mm Hg), temperature; 300°K.

absorption from the uncorrected application of the van Vleck-Weisskopf

equations is low for the wings of the water vapor lines in the milli-

meter region by a factor of approximately 4, and for the attenuation

in the wings of the oxygen lines by a factor of around 2.

In the last few years, workers in the USSR have derived a new

line shape, based on the solution of the kinetic equation. Zhevakin

and Naumov[17] have arrived at a line shape factor given by

$$F(\nu_{ij}, \nu) = \frac{1}{\pi} \nu \nu_{ij} \left\{ \frac{4 \Delta \nu}{(\nu_{ij}^2 - \nu^2) + 4\nu^2 (\Delta \nu)^2} \right\} \qquad (2.2\text{-}18)$$

in which parameters have similar meaning to those in Equation (2.2-14).

The application of (2.2-18) to the region near 1.35 cm is shown in

Figure 2-4. The non-resonant part of the curve is taken to be the same

as for the uncorrected van Vleck-Weisskopf curve. The resonant shape

is close enough to the van Vleck shape so as to make a decision impos-

sible as to the better fit of either to the Becker and Autler data.

Indeed, near resonance, most line shapes are indistinguishable. From

the discussion in Zhevakin and Naumov, it is apparent that the line

shape does provide for somewhat higher absorption between resonances

in the millimeter range, but still does not completely close the gap

between experiment and theory.

2.2.4 The Line Width Parameter.

Of all the quantities in Equations (2.2-12) and (2.2-14) which

depend upon molecular parameters and processes, the line width

has been the most difficult to theoretically compute. There are
several mechanisms which can broaden a microwave spectral line but
only two of consequence for conditions found in the lowest 100 km of
the earth's atmosphere. They are broadening due to the collisions
between molecules, and in the regions above 60 km, Doppler broadening
must be considered.

The latter effect is due to the translational motion of the
molecule parallel to the direction of propagation of the radiation.
A frequency shift of $\pm \nu \left(\frac{V}{V_p} \right)$ occurs, when ν is the fre-
quency of the radiation, V the velocity component of the molecule
parallel to the direction of propagation and V_p is the phase velocity
of the radiation, nearly equal in most cases of interest to the velocity
of light. When translated to a change in intensity, it is found[2] that
the half width of a Doppler broadened spectral line is given by

$$\Delta \nu_b = 3.581 \times 10^{-7} \left(\frac{T}{M} \right)^{1/2} \nu \ sec^{-1} \qquad (2.2\text{-}19)$$

where T is the gas temperature in $^{\circ}K$, M the molecular weight, ν the
frequency in sec^{-1} and it is assumed the distribution of molecular
velocities is that resulting from thermal equilibrium of the gas.
The units of $\Delta \nu_b$ are the same as ν .

Perhaps the most successful theory to date for collisional
broadening of spectral lines which is also based on the physical
processes which are thought to occur between colliding molecules
has been given by Anderson[15]. The exact treatment of the problem

requires detailed knowledge of the interacting forces and processes
which occur during collisions not all of which are well known or
understood. And even then, computations to take all of what is known
into account can become prohibitively complex. Nevertheless, the
estimations of line width from Anderson's theory when compared with
what accurate measurements which do exist show reasonable agreement
(see Anderson).

Two important assumptions are made: (1) molecules are considered
to follow classical trajectories; and (2), collisions are adiabatic,
i.e., no energy is lost or gained by the molecule during the collision.

The width of any spectral line when binary collisions are the
dominant interaction are expected to be and actually show a direct
dependence upon the number of particles colliding. $\Delta\nu$ is therefore
proportional to the pressure over a wide range of values; for water
vapor, from a few millimeters of mercury to more than one atmosphere.

The temperature dependence of $\Delta\nu$ is much more difficult to
theoretically predict. Normally, for temperatures of meteorological
interest, it is assumed that $\Delta\nu$ follows a power law of T of the
form

$$\Delta\nu \propto T^{-n} \tag{2.2-20}$$

where n for atmospheric gases is in the range from -0.2 to +1.2.
However, actual theoretical prediction of line widths and their vari-
ation with temperature cast doubt upon the exactness of (2.2-20)

(see below). Nevertheless, because (2.2-20) approximates the behavior of $\Delta \nu'$ with temperature and a more precise dependence is not available, the power law temperature dependence is generally retained.

The width of spectral lines at constant temperature and pressure are found to depend upon the rotational states of the molecule before and after transition, and upon the perturbing potential of the transition causing molecule. For perturbing gases with large numbers of possible states the evaluation of $\Delta \nu'$ requires that each state be considered. The computations can therefore be very lengthy for each spectral line.

In the case of water vapor, Benedict and Kaplan using Anderson's theory have evaluated the theoretical line widths expected from collisions between water vapor and nitrogen[19], water vapor and oxygen[20] and water vapor and water vapor[20]. Results from the nitrogen computations at $300^\circ K$ and one atmosphere total pressure show that widths vary between a maximum of 0.12449 cm^{-1} $(3.735$ GHz$)^*$ to a minimum of 0.03584 cm^{-1} $(1.075$ GHz$)^*_.$ The former occurs for the transition between the states 1_1 (J_i) and 1_{-1} ; the latter between the states 14_{-1} and 13_{-1} . In general, line widths decrease for increasing J; for a given J are a maximum for intermediate τ ; and even τ levels produce wider lines than close by odd τ levels. All of the results in Benedict and Kaplan[19] are based upon several poorly known parameters which were

---

*corrected

adjusted so that they yielded results which duplicated the measurements by Becker and Autler of the line width of the $5_{-1} \longrightarrow 6_{-5}$ transition of water vapor. However, it should be noted that the measurements in Becker and Autler were done for broadening by air and not by nitrogen. (The values for the line widths in 19 for pure nitrogen broadening were later adjusted upwards by 12 percent (see 20 page 266) because of a misinterpretation of the strength of the nitrogen quadrupole moment used in the calculations reported. The authors now suggest the values in 19 be interpreted as representing line widths for broadening in dry air since in 20 they show the effect of oxygen on water vapor broadening is not as effective as nitrogen).

Also reported in Benedict and Kaplan[20] are the results of self broadening of water vapor. As might be expected, the theoretical effectiveness of water vapor to perturb itself is much greater than that of a foreign molecule, being on the average 5.5 times more effective than nitrogen. It becomes therefore necessary to take into account the abundance of water vapor on the line width at a given temperature and pressure.

If we draw together all of the above information, the result is Equation (2.2-21) below for the dependence of $\Delta \nu$ on the variables of state and the abundance of ρ_{H_2O} .

$$\Delta \nu = S \frac{P}{1013.25} \left(\frac{T}{300} \right)^{-n} \left(1 + \alpha \frac{e}{P} \right) \qquad (2.2\text{-}21)$$

In (2.2-21) S is the breadth of the line at one atmosphere pressure,

a temperature of $300^{\circ}K$ and an infinitesimal amount of water vapor;

n is the theoretically or experimentally determined exponent of Equa-

tion (2.2-20) different for each line; T is the atmospheric tempera-

ture; P is the total atmospheric pressure; e is the partial pressure

of water vapor; and α is a factor, again varying from line to line,

which is a measure of the increased effectiveness of H_2O to broaden

itself over the foreign gas broadeners determining S. α will be

discussed in more detail in Section 2.3. The term $\frac{e}{P-e} \approx \frac{e}{P}$ is the

ratio of water molecules to dry air molecules.

Of the relationships expressed in Equation (2.2-21), the pres-

sure dependence is probably most accurate. S is reliable when measured

for definite transitions under definite conditions; computed values of

S are thought to be accurate to within perhaps 10 percent. The temper-

ature dependence no doubt is the least accurate part of the expression

not only because there is strong indications that the power law is not

universally valid, but also because the choice of the best n becomes

very difficult in a mixture such as moist air. Exactly how good the

representation of $\Delta\nu$ by (2.2-18) for water vapor broadened by air

over the entire range of meteorological temperatures is not known.

2.3 The Absorption Coefficient for the Water Vapor Rotational

Resonances Centered Near 22.2 GHz and 183.3 GHz.

In preceding sections, we have discussed the general properties

of rotational resonances of water vapor and the absorption they cause.

This section is devoted to obtaining operationally usable expressions

for the absorption coefficients of the two lowest frequency resonances.

2.3.1 The 22.2 GHz Spectral Line.

It has long been customary to think of the absorption coefficient

in terms of linear combinations of separate spectral lines. Contribu-

tions to the absorption near resonance have consequently been written

as

$$\gamma = \gamma_{RES} + \gamma_{NON} \tag{2.3-1}$$

where γ_{RES} and γ_{NON} are separate and unrelated, and refer respect-

ively to the contribution of the line being studied and to the contri-

bution from all other lines.

In light of the work by Gordon[13] this is not satisfactory for

strongly overlapping lines. However the 22.2 GHz line is almost an

order of magnitude in frequency below the next water vapor line (183

GHz) and therefore even from Gordon's work, it appears that (2.3-1) is

valid.

We therefore write,

$$\gamma_{1.35} = \left(\gamma_{RES}\right)_{1.35} + \left(\gamma_{NON}\right)_{1.35} \tag{2.3-2}$$

Consider the resonant term first. From Equations (2.2-12) and

(2.2-14), $\left(\gamma_{RES}\right)_{1.35}$ may be written in complete form as

$$\left(\gamma_{RES}\right)_{1.35} = \frac{8\pi^2 \nu^2 N}{3c\,kT} \frac{\mu_{H_2O}^2\, g_o\, \Sigma\, |\phi_{L35}|^2}{0.0344\, T^{3/2}} e^{-E_{S_{-1}}/kT} \times$$

$$\left[\frac{\Delta\nu}{(\nu_{1.35} - \nu)^2 + \Delta\nu^2} + \frac{\Delta\nu}{(\nu_{1.35} + \nu)^2 + \Delta\nu^2}\right] \tag{2.3-3}$$

where $\Delta\nu_{1.35}$ is given by Equation (2.2-21) as

$$\Delta\nu_{1.35} = S_{1.35}\frac{P}{1013.25}\left(\frac{T}{300}\right)^{-n_{1.35}}\left(1 + \alpha_{1.35}\frac{P_{H_2O}T}{P}\right)$$

(2.3-4)

$\left(\gamma_{RES}\right)_{1.35}$ is given in nepers/cm when ν is in GHz, N is in

particles/cc, the speed of light c is in cm/sec, Boltzmann's constant

k is equal to 1.3804×10^{-16} ergs/$^{\circ}$K, the kinetic temperature T is in

degrees Kelvin, total atmospheric pressure is given in millibars, water

vapor density is in g/m^3, and the molecular parameters are used as they

appear in Table 2-II below.

TABLE 2-II. The values and sources for the parameters
of Equations (2.3-3) and (2.3-4) for

Parameter	Value	Theoretical or Measured	Source
μ_{H_2O}	1.87×10^{-18} e.s.u	M	22
g_0	3	odd	
$\sum\lvert\phi_{1.35}\rvert^2$	0.0549	T	7
$\dfrac{E\,(5,1)}{C}$	446.39 cm^{-1}	M	8
$\dfrac{E\,(6,-5)}{C}$	447.17 cm^{-1}	M	8
$\nu_{1.35}$	22,237.$\pm$ 5 MHz	M	23
$S_{1.35}$	2.70 GHz/Atm.	M	21
$n_{1.35}$	0.626	T	19
$\alpha_{1.35}$	1.46×10^{-2} mb (g/m^3)$^{-1}$ ($^{\circ}$K)$^{-1}$	M	21

Only the last parameter needs further explanation. The value

of the line width in the Becker and Autler experiment when extrapolated

to a water vapor density (or partial pressure) of zero was found to be

0.087 cm^{-1}, while for ρ_{H_2O} = 50 g/m^3, $\Delta\nu$ was found to be 0.107

cm^{-1}. Evidently, the effective collision cross-section for H_2O - H_2O

encounters is larger than for H_2O - air encounters. The increase of

$\Delta\nu$ over the interval from 0 to 50 g/m^3 of H_2O shows in the experi-

ment as a linear increase with ρ_{H_2O} . The water vapor increase

manifests itself on the molecular level as a substitution of water

vapor molecules for air molecules, each of which is more effective in

broadening the line than a dry air molecule. Therefore, since $S_{1.35}$

refers to the effectiveness of air molecules to broaden the spectral

line, consideration of the number of molecules which are actually

water vapor must be taken into account. This may be done by giving

a weight of one to the fraction of dry air molecules and some other

weight to the fraction of water volecules. A correction factor to

the straight dry air broadened line would be of the form

$$\left[(P_{TOTAL} - e) + \eta_{1.35}\, e\right] / P_{TOTAL}$$, where $\left(P_{TOTAL} - e\right)/P_{TOTAL}$

represents the dry air fraction of molecules (since number of mole-

cules is proportional to partial pressure, and equal partial pressures

of two gases at the same temperature have equal numbers of molecules),

and e would be the partial pressure of water vapor. $\eta_{1.35}$ in this

expression would be the factor of increased effectiveness of water

vapor-water vapor broadening over water vapor-dry air broadening.

The correction factor may be rewritten as $\left(1 + \alpha'_{1.35}\, \dfrac{e}{P_{TOTAL}}\right)$ where $\alpha'_{1.35}$ will be related to $\eta_{1.35}$ as $\alpha'_{1.35} = \eta_{1.35} - 1$. For convenience the partial pressure of water vapor may be expressed as

$$e = \frac{\rho_{H_2O}\, R^*\, T}{M_{H_2O}}$$

in which ρ_{H_2O} is the water vapor density, R^* the universal gas constant, T is the absolute temperature and M_{H_2O} is the molecular weight of water vapor. Then the correction factor must be written as

$$\left(1 + \alpha_{1.35}\, \frac{\rho_{H_2O}\, T}{P_{TOT}}\right)$$ the form used in Equation (2.3-4). To find $\alpha_{1.35}$ from the Becker and Autler experiment it is only necessary to evaluate

$$\frac{\left(\Delta\nu_{1.35}\right)_{P=0}}{\left(\Delta\nu_{1.35}\right)_{P=50}} = \frac{1}{1 + \alpha_{1.35}\, \dfrac{\rho_{50}\, T}{P}} = \frac{1}{1 + \dfrac{\alpha_{1.35}\cdot 318}{1013}} \qquad (2.3\text{-}5)$$

which leads to

$$\alpha_{1.35} = 1.46 \times 10^{-2}\ \text{mb}\ (g/m^3)^{-1}\ (^\circ K)^{-1}$$

the value quoted in Table 2-II. Each water molecule which displaces an equivalent air molecule is found to be approximately 4.2 times more effective in broadening the water vapor line at 1.35 cm (i.e., $\eta_{1.35} \cong 4.2$).

For convenience of usage, equations (2.3-3) and (2.3-4) are reduced to their simplest forms in the following two equations with more familiar inputs replacing less familiar ones and all constants evaluated:

$$\left(\gamma_{RES}\right)_{1.35} = 1570 \frac{\rho_{H_2O}\, \nu^2\, e^{-642/T}}{T^{5/2}} \left\{ \frac{\Delta\nu'_{1.35}}{(\nu'_{1.35}-\nu)^2 + \Delta\nu'^2} + \right. \qquad (2.3\text{-}6)$$

$$\left. \frac{\Delta\nu'_{1.35}}{(\nu'_{1.35}+\nu)^2 + \Delta\nu'^2} \right\} \quad db/km$$

$$\Delta\nu'_{1.35} = 2.62 \left(\frac{P}{1013.25}\right)\left(\frac{T}{300}\right)^{-0.626}\left\{1 + 0.015\,\frac{\rho_{H_2O}\,T}{P}\right\} GHz \qquad (2.3\text{-}7)$$

The primed frequencies are in GHz; ρ_{H_2O} remains in g/m³, temperature T in °K, and total pressure P in millibars.

The detailed expression for the non-resonant part of Equation (2.3-2) is much less satisfactory than (2.3-6) and even (2.3-7). Van Vleck[5] offers the approximation to this contribution as

$$\left(\gamma_{NON}\right)_{1.35} = \frac{8\pi^2\, \nu^2\, N}{3\,c\,kT}\, \mu_{H_2O}^2\, \sum_{ij}\, g_{\tau_i}\, \sum |\Phi_{ij}|^2\, e^{-E_i/kT}\, \frac{2\,\Delta\nu}{\nu_{ij}^2} \qquad (2.3\text{-}8)$$

where the indices i,j range over all the spectral lines above the 22.2 GHz resonance, and each parameter is appropriately chosen for a given resonance i,j. The approximation of $F(\nu_{ij}, \nu)$ as $\frac{2\Delta\nu}{\nu_{ij}^2}$ should be valid when $\nu_{ij} \gg \nu$ and $\nu_{ij} \gg \Delta\nu$ both of which are true for resonances other than the 22.2 GHz line. An approximation of the sum over rotational states was given by van Vleck[6] at 293°K as

$$\left(\gamma_{NON}\right)_{1.35} = \frac{0.012\,\rho_{H_2O}\,\frac{\Delta\nu}{c}}{\lambda^2} \quad db/km \qquad (2.3\text{-}9)$$

which transposes into our notation as

$$\left(\gamma_{NON}\right)_{1.35} = 2.21 \times 10^{-3} \frac{\rho_{H_2O} \, \nu'^2 \Delta\nu'}{T^{3/2}} \quad db/km \qquad (2.3\text{-}10)$$

The temperature dependence has been given in van Vleck[6].

The expression (2.3-8) has already been shown to be too small by a factor of 4 to 6 (see Figure 2-5); therefore, for work done throughout the remainder of the paper Equation (2.3-10) will be increased by a factor of 5. The final form of the non-resonant term for the 1.35 cm line is

$$\left(\gamma_{NON}\right)_{1.35} = 1.11 \times 10^{-2} \frac{\rho_{H_2O} \, \nu'^2 \Delta\nu'}{T^{3/2}} \quad db/km \qquad (2.3\text{-}11)$$

Equations (2.3-6), (2.3-7) and (2.3-11) are equivalent to those used by Barrett and Chung[31].

2.3.2 The 183 GHz Spectral Line

The nearest line to the 1.35 cm line occurs at 1.64 mm (183 GHz) removed by a factor of eight in frequency. Towards even higher frequencies, one finds that in the interval between the 1.64 mm line and eight times its resonant frequency 53 other water vapor resonances occur.

Even though equation (2.3-1) may be approximately applied to the 1.64 mm line, it will be impossible to treat $\left(\gamma_{NON}\right)_{0.164}$ as we did in (2.3-7). Lines nearby will have to be taken explicitly

into account or some new approximation will be needed, especially
since nearby lines probably constructively interfere with the absorption of the 183 GHz line. However, before resolving this problem, it is appropriate first to formulate   .

There appears to be no reason why the line shape near resonance will be better fitted by any other than the van Vleck-Weisskopf formulation. Therefore, it will be retained. The equation for the resonance at 183 GHz may be written, analogously to Equation (2.3-3), as

$$\left(\gamma_{RES} \right)_{0.164} = \frac{8\pi^2 \nu^2 N}{3c\,kT} \frac{\mu_{H_2O}^2 \, g_e \sum |\Phi_{0.164}|^2}{} \, e^{-E_{2-2}/kT} \times$$

$$\left\{ \frac{\Delta\nu_{0.164}}{(\nu_{0.164} - \nu)^2 + \Delta\nu^2} + \frac{\Delta\nu_{0.164}}{(\nu_{0.164} + \nu)^2 + \Delta\nu^2} \right\} \quad (2.3\text{-}12)$$

where $\Delta\nu$ for this case is given by

$$\Delta\nu_{0.164} = S_{0.164} \left(\frac{P}{1013.25} \right) \left(\frac{T}{300} \right)^{-n_{0.164}} \left\{ 1 + \alpha_{0.164} \frac{\rho_{H_2O} T}{P} \right\} \quad (2.3\text{-}13)$$

(If P, T, and ρ_{H_2O} are in millibars, degrees Kelvin and grams per cubic meter, respectively, and $S_{0.164}$ is in GHz/atm then $\Delta\nu_{0.164}$ is given in GHz in Equation (2.3-13).

The choice of values for the molecular parameters in the case of air broadening is more difficult for the 183 GHz resonance, however, than for the 22 GHz line. Table 2-III draws together all the informa-

tion on the 183 GHz line for the various broadeners that make up air and presents the derived (and in one case measured) parameters for an air-water vapor mixture. There are many conflicting measurements and values in the table and the final choices must be based on judicious but unavoidably subjective reasoning.

We start by choosing the theoretical line strengths as computed by King, Hainer and Cross[7]. No substantial uncertainties have been presented to throw doubt on these results. This choice, together with the other well known molecular parameters of (2.3-12) (i.e., $\mu_{n_{2}}^{2}$, g_e, E_{2-2}, k, c, $\nu_{0.164}$) leaves the main uncertainties with $S_{0.164}$, $\eta_{0.164}$, and $\alpha_{0.164}$ all connected with the line width parameter.

The most precise measurements for the line width appear to have been done by Rusk[26], for nitrogen, oxygen, and self broadening. The derived value of $\Delta\nu$ for air from that work, equal to 3.52 Mc/mm Hg is the choice we will make for $S_{0.164}$.

The most difficult parameter to choose a value for is $\eta_{0.164}$. Benedict and Kaplan[19] computed the value for $\eta_{0.164}$ for nitrogen broadening as 0.649. Hemmi[27] m asured a value of $\eta_{0.164}$ in nitrogen with about 1% water vapor present as 0.579 and computed the nitrogen value alone from those measurements as 0.736. This latter value agrees quite well with the Benedict and Kaplan estimate. Values of the temperature exponent for oxygen, however, were not reported in Benedict and Kaplan[20], and in Hemmi they showed no resemblance to a power law of T.

MOLECULES	TEMP. °K	$(\gamma/\rho_w)_{res} \frac{db}{km}\left(\frac{g}{m^3}\right)^{-1}(atm.)^{-1}$	$\Delta\nu/P$ MHz/mm Hg	% H_2O	n	SOURCE
$H_2O - N_2$	300 °K	(3.81) K.H.C	3.76	0		(26)
	300	(3.38) K.H.C.	4.24	0	0.649	(19) (20)
	300	(3.21)	4.4	0		(25)
	300		3.54	0	0.736	(27)
	301.5	3.00				(27)
$H_2O - O_2$	300		2.72	0		(26)
	302.5	4.30	2.62	0		(27)
$H_2O - H_2O$	300		19.06	100	1.2	(26)
	300		19.0	100		(25)
	300		(19.5) .	100	0.90	(20)
$H_2O - Air$	300	(4.04) K.H.C	(3.52)	0		(27)
	300	(3.76) K.H.C	(3.79)	0	-0.649	(19) (20)
	302	(3.28)	(3.27)	0		(27)

TABLE 2-III. Various parameters associated with the 183 GHz water vapor rotational line as reported from various sources. Parentheses indicated derived values. No parentheses indicate a measured value. K.H.C refers to King, Hainer, Cross[7] line strength.

Rusk, in the supplement to 26 , did measure a value for

for the case of water vapor self broadening as 1.2.

A highly convincing choice for $n_{o.164}$ for air from all these

reports is not possible. However, since it appears that both oxygen

and water vapor have values of n greater than that for nitrogen alone,

it would appear that a value for $n_{o.164}$ near 0.70 would be a defen-

sible estimate. In any case, that will be the value we choose. For

a rough idea of the error involved in this exponent, it can be remembered

that if the value of $\Delta \nu$ is measured with perfect accuracy at $300^{\circ}K$

and the power law is used to extrapolate to say $250^{\circ}K$, a discrepancy

of 3.5% occurs between values computed using $n_{o.164}$ = 0.6 and

$n_{o.164}$ = 0.8.

The value of $\alpha_{o.164}$ may be obtained using the following rea-

soning: the effective collision cross section for two gases may be

written as

$$\sigma_e = \sigma_1 R_1 + \sigma_2 (1 - R_1) \qquad (2.3\text{-}14)$$

in which σ_e is the effective cross section, σ_1 is the collision

cross section for gas one, R is its fraction of the total molecules,

and σ_2 is the collision cross section for gas two. The cross section

for collisions is directly proportional to the line width for a given

gas. Therefore, we can write

$$\Delta \nu_e = \Delta \nu_{H_2O\text{-}H_2O} R_{H_2O} + \Delta \nu_{H_2O\text{-}AIR} (1 - R_{H_2O}) \qquad (2.3\text{-}15)$$

From the data of Rusk,

$$\frac{\Delta \nu_{H_2O-H_2O}}{\Delta \nu_{H_2O-AIR}} \doteq \frac{19.06}{3.52} \doteq 5.4$$

where $\Delta \nu_{H_2O-AIR}$ is the line width with negligible water vapor in the

mixture. For 50 g/m^3 of water vapor in one atmosphere total pressure of

air, a temperature of 318°K, R_{H_2O} = 0.0724. Therefore

$$\frac{(\Delta \nu_c)_{\rho=50}}{(\Delta \nu_c)_{\rho=0}} = \frac{\Delta \nu_{H_2O-H_2O} R_{H_2O} + \Delta \nu_{H_2O-AIR}(1-R_{H_2O})}{\Delta \nu_{H_2O-AIR}} \quad (2.3-16)$$

Substituting this into Equation (2.3-5) gives us a value for

$$\alpha_{0.164} = 2.03 \times 10^{-2} \text{ mb (g/m}^3)^{-1} (^{\circ}K)^{-1}.$$

Table 2-IV below collects the values for the molecular parameters

of the 1.64 mm line which we will use in Equations (2.3-12) and (2.3-13).

TABLE 2-IV. The values and Sources for molecular
parameters needed to compute

Parameter	Value	Theoretical or Measured	Source		
μ_{H_2O}	1.87x10^{-18} e.s.u	M		22	
g_e	1	τ even			
$\Sigma \|\Phi_{0.164}\|^2$	0.1015	T		7	
$E(2_{+2})/c$	136.15 cm^{-1}	M		8	
$E(3_{-2})/c$	142.30 cm^{-1}	M		8	
$\nu_{0.164}$	183,310.12 ± 0.10 Mc/s	M		26	
$S_{0.164}$	2.68 GHz/Atm.	M		26	
$n_{0.164}$	0.70		19	26	27
$\alpha_{0.164}$	2.03x10^{-2} mb (g/m^3)$^{-1}$ ($^{\circ}$K)$^{-1}$	T		26	

It should be noted that by using 2.68 GHz/Atm. for the line width per unit pressure and the King, Hainer and Cross line strength, the value of $(\gamma_{Res})/P_{0.14\ H_2O}$ at 1 atmosphere pressure and $300^{\circ}K$ is 19% higher than the same parameter estimated by Hemmi from his measurements on nitrogen and oxygen. This is true despite the estimation in Hemmi that $\Delta\nu/P$ for air is 2.48 GHz/Atm. If Hemmi's measurements are correct, it would mean that the true line strength is actually 25% smaller than that computed by King, et al.

Only Frenkel and Woods[25] have attacked the nonresonant absorption dilemma and achieved results which can be considered as reliable. However, the measurements were done with nitrogen and water vapor only, so that there is no direct analogy with air broadening. Nevertheless, so sparse is quantitative data in the region around 183 GHz, we will rely heavily on the results and procedures in Frenkel and Woods.

As was pointed out in Section (2.2-3), the nonresonant absorption in and around the 183 GHz line was handled by Frenkel and Woods by using the resonant expression for the nearest higher line of consequence (324 GHz)* and an empirically determined function proportional

*There are actually two lines very near to 324 GHz. One, however, has a term value for the lower state equal to 1283 cm^{-1}. The Boltzmann population factor is consequently proportional to $\exp\left[-1283\ c/kT\right]$, a value which, at $300^{\circ}K$, is more than 450 times smaller than the Boltzmann factor for the 183 GHz line. This line ($9_{-3} \to 10_{-7}$) will be disregarded in favor of the line arising from the $4_{0} \to 5_{-4}$ transition. Its lower term value is 326.5 cm which, at $300^{\circ}K$, causes the population, when in thermal equilibrium, to be less than that of the lower energy state for the 183 GHz line by a factor of 4 to 5. It will be the line we refer to as the 324 GHz line or 0.093 cm resonance.

to γ^2 for the contributions of all remaining lines. We will do the same. However, to be consistent with $\left(\gamma_{RES}\right)_{0.164}$, the 324 GHz line parameters will be those determined from theory and applied to an equation of the form used for $\left(\gamma_{RES}\right)_{1.35}$ and $\left(\gamma_{RES}\right)_{0.164}$ [Equations (2.3-3) and (2.3-12)] . The equation for the contribution of the remaining lines will be slightly modified from the Frenkel and Woods expression. $\left(\gamma_{NON}\right)_{0.164}$ will therefore be given by

$$\left(\gamma_{NON}\right)_{0.164} = \frac{8\pi^2 \, \nu^2 \, N}{3 c \, k T} \; \frac{\mu_{H_2O}^2 \; g_e \; \sum_i \left| \phi_{0.093} \right|^2}{0.0344 \; T^{3/2}} \; e^{-E_{4_0}/kT}$$

$$\times \left\{ \frac{\Delta\nu_{0.093}}{\left(\nu_{0.093} - \nu\right)^2 + \Delta\nu_{0.093}^2} + \frac{\Delta\nu_{0.093}}{\left(\nu_{0.093} + \nu\right)^2 + \Delta\nu_{0.093}^2} \right\}$$

$$+ \; C_3 \; \frac{\nu^2}{\nu_{0.164}^3} \; \left(\Delta\nu_{WV}^W + \Delta\nu_N^W\right) \left(\frac{300}{T}\right)^{3/2} \; \frac{db}{km} \qquad (2.3-17)$$

where

$$\Delta\nu_{0.093} = S_{0.093} \left(\frac{P}{1013.25}\right) \left(\frac{T}{300}\right)^{-n_{0.093}} \left(1 + \alpha_{0.093} \, \frac{\rho_{H_2O} T}{P}\right) \; GHz \qquad (2.3-18)$$

$$\Delta\nu_{WV}^W = 1.04 \; k_{WV}^W \; \rho_{H_2O} \left(\frac{T}{300}\right)^{-n_{0.093}} \left(1 + \alpha_{0.093} \, \frac{\rho_{H_2O} T}{P}\right) \; GHz \qquad (2.3-19)$$

$$\Delta\nu_N^W = 0.66 \; k_N^W \; P \left(\frac{T}{300}\right)^{0.62} \; GHz \qquad (2.3-20)$$

and the units of total atmospheric pressure P are millibars, the units of T are degrees Kelvin, the units of ρ_{H_2O} are grams per cubic meter, c and k are in cgs units and all molecular parameters are as

shown in Table 2-V. $\Delta\nu_N^{'W}$ is corrected for oxygen by reducing the effective line width by a factor 1/2.11 for the fraction of oxygen molecules (see 20 , p. 466).

The temperature dependencies of $\Delta\nu_{WV}^{'W}$ and $\Delta\nu_N^{'W}$ have been established as follows: $\Delta\nu_{WV}^{'W}$ is proportional to the partial pressure of water vapor which, in turn, is proportional to $\rho_{H_2O}\cdot T$. However, in 20 (see page 465), Benedict and Kaplan have established that the line intensity weighted average for the temperature exponent is -0.9, i.e., the temperature dependence of the rotational band is proportional to $T^{-0.9}$; therefore the $T^{0.1}$ dependence of $\Delta\nu_{WV}^{'W}$.

For the nitrogen derived line width, $\Delta\nu_N^{'W}$, the $T^{-0.62}$ temperature dependence is that derived for the line intensity weighted average for all the nitrogen broadened water vapor line widths computed in 19 (see page 395).

Table 2-V below presents the values for the molecular para-meters of Equations (2.3-17) through (2.3-20) necessary to compute $\left(\gamma_{NON}\right)_{0.164}$.

TABLE 2-V . Molecular parameters necessary to
compute   .

Parameter	Value	Theoretical or Measured	Source
μ_{H_2O}	1.87×10^{-18} e.s.u	M	22
g_e	1	τ odd	
$\sum \lvert \Phi_{0.093} \rvert^2$	0.0891	T	7
$E(4_0)/c$	315.70 cm^{-1}	M	8
$E(5_{-4})/c$	326.50 cm^{-1}	M	8
$\nu_{0.093}$	323.758 GHz	T	8
$S_{0.093}$	2.79 GHz/Atm.	T	19
$n_{0.093}$	0.619	T	19
$\alpha_{0.093}$	2.10×10^{-2} mb $(9/m^3)^{-1}({}^\circ K)^{-1}$	T	18
C_3	2.55	M	25
k_{wv}^w	0.200 GHz/mm Hg	M	25
k_N^w	0.019 GHz/mm Hg	M	25

When the constants of Equation (2.3-12) and (2.3-17) are
evaluated and more familiar parameters are substituted, the final
operational equations for the 183 GHz line are (2.3-13), (2.3-18),
(2.3-19), (2.3-20) and Equation (2.3-21) below:

$$\gamma_{0.164} = 978 \frac{\rho_{H_2O} \, \nu'^2}{T^{5/2}} \, e^{-197.3/T} \left\{ \frac{\Delta \nu_{0.164}}{(\nu'_{0.164} - \nu')^2 + \Delta \nu_{0.164}^2} + \frac{\Delta \nu_{0.164}}{(\nu'_{0.164} + \nu')^2 + \Delta \nu_{0.164}^2} \right\}$$

$$+ \, 849 \frac{\rho \, \nu'^2}{T^{5/2}} \, e^{454/T} \left\{ \frac{\Delta \nu_{0.093}}{(\nu'_{0.093} - \nu')^2 + \Delta \nu_{0.093}^2} + \frac{\Delta \nu_{0.093}}{(\nu'_{0.093} + \nu')^2 + \Delta \nu_{0.093}^2} \right\}$$

$$+ \, C_3 \frac{\nu'^2}{\nu_{0.164}^3} \left(\Delta \nu_{WV}^W + \Delta \nu_N^W \right) \left(\frac{300}{T} \right)^{3/2} \quad db/km \qquad (2.3\text{-}21)$$

The temperature dependence of the last terms of (2.3-21) is that
expected in the wings of water vapor spectral lines (see footnote on
p. 661 of van Vleck[6]).

Further simplification of (2.3-21) may be accomplished without
substantial loss of accuracy, if one confines his observations to a
frequency region near to the 183 GHz resonance. The major contribution
to $\left(\gamma_{NON} \right)_{0.164}$ within 50 GHz of 183 GHz is overwhelmingly due to
the third term of Equation (2.3-11), the contributions of lines other
than the 324 GHz and 183 GHz line. The ratio of the two last terms
over this region is approximately 200 : 1. Only as one approaches 300
GHz does the second term begin to contribute a substantially greater
percentage to the absorption. Below 183 GHz, the only contribution at
all is the 22 GHz line, which does not make its contribution felt until
well below 100 GHz.

The final operational equation for spectral work at and near the 183 GHz resonance is Equation (2.3-22) below:

$$\gamma_{0.164} \cong 978 \frac{\rho_{H_2O} \, \nu'^2}{T^{5/2}} \, e^{-197.3/T} \left[\frac{\Delta\nu'_{0.164}}{(\nu'_{0.164} - \nu')^2 + \Delta\nu'^2_{0.164}} + \frac{\Delta\nu'_{0.164}}{(\nu'_{0.164} + \nu')^2 + \Delta\nu'^2_{0.164}} \right]$$

$$+ \; 2.55 \; \frac{\nu'^2}{\nu'^3_{0.164}} \left(\Delta\nu^w_{wr} + \Delta\nu^w_{N} \right) \left(\frac{300}{T} \right)^{3/2} \quad db/km \quad (2.3-22)$$

The definitions for the parameters of Equation (2.3-21) apply equally to (2.3-22).

Figure 2-7 illustrates water vapor broadened by air in the frequency interval from 170 to 200 GHz using Equation (2.3-22).

Although water vapor absorption will dominate over oxygen in the regions near 22 GHz and 183 GHz, nevertheless, it must be taken into account for the measurements and numerical experiments near the lower frequency line. (It is entirely negligible near 183 GHz). The computational equations for oxygen absorption are therefore presented in Appendix A-II.
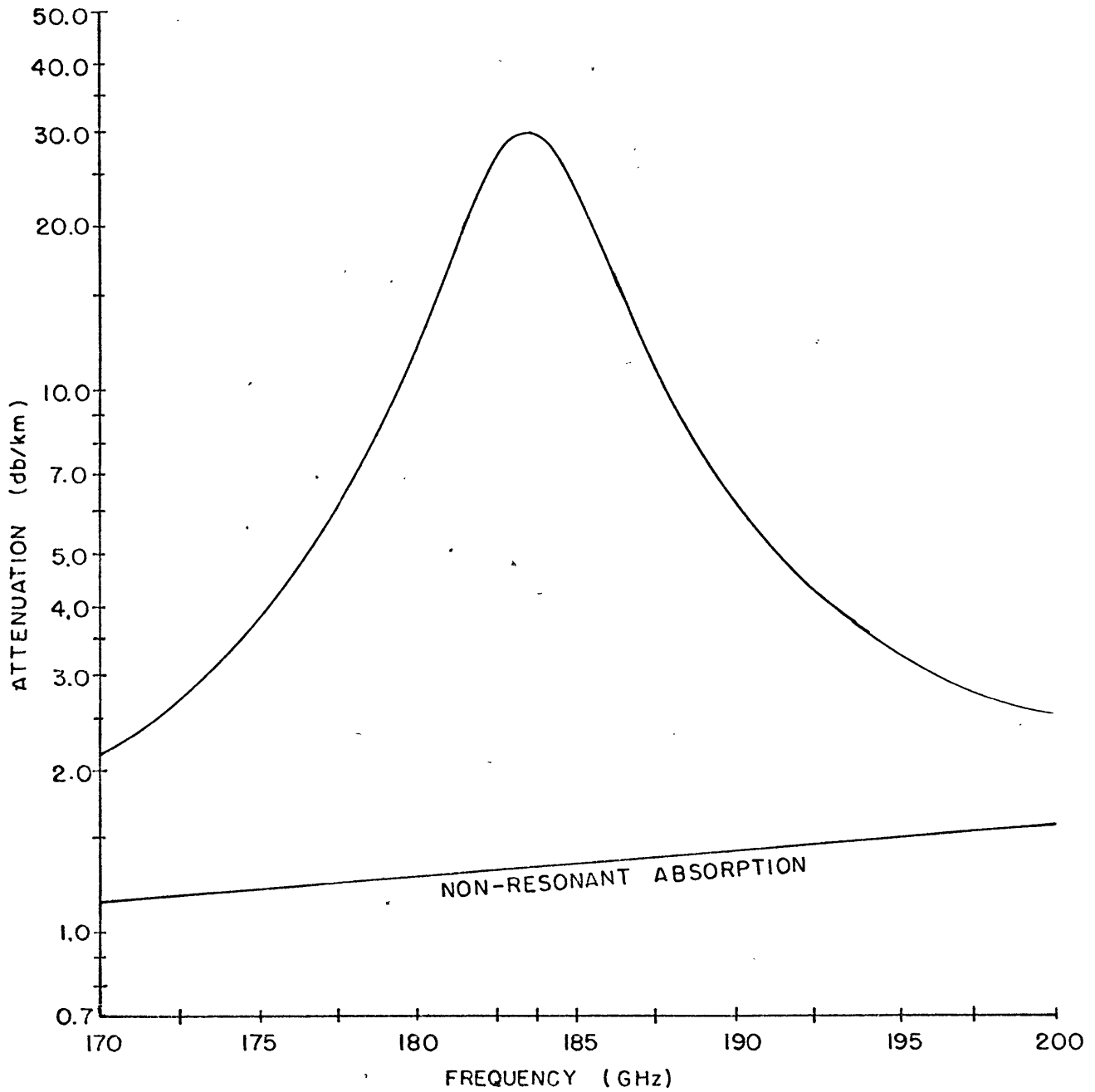
Figure 2-7. The 183 GHz rotational resonance of water vapor as repre-
sented by Equation (2.3-22). Conditions in the gas are: 1000 mb of
dry air; 7.23 g/m^3 of water vapor (7.5 mm Hg); and temperature of 300 $^{\circ}$K.

Chapter 3

RADIATIVE TRANSFER IN THE EARTH'S ATMOSPHERE

In this chapter the equation of radiative transfer for the at-
mosphere of the earth is reviewed for the special conditions of an
absorbing, non-scattering atmosphere in local thermodynamic equilibrium.
In addition, the question of existence of local thermodynamic equilib-
rium in the earth's atmosphere is discussed; weighting functions for
radiation attenuated or emitted by water vapor in the atmosphere around
the two resonant frequencies of interest are derived for several geo-
metries and illustrated by numerical examples; and finally, the quasi-
stationary character of the weighting functions over various climato-
logical conditions is investigated.

3.1 Fundamental Definitions and the Equation of Radiative Transfer

The strength of a flow of radiation may be defined by reference
to Figure 3-1. The distance R must be large with respect to the differ-
entials of area $d\sigma$ and $d\sigma'$ so that no matter where the points P and P'
are placed on their respective surfaces, the solid angles $d\omega$ and $d\omega'$
subtended by the opposite incremental areas remain substantially un-
changed. The solid angles are defined as

$$d\omega' = \frac{d\sigma' \cos\theta'}{R^2}$$

(3.1-1)

and

$$d\omega = \frac{d\sigma \cos\theta}{R^2}$$

(3.1-2)
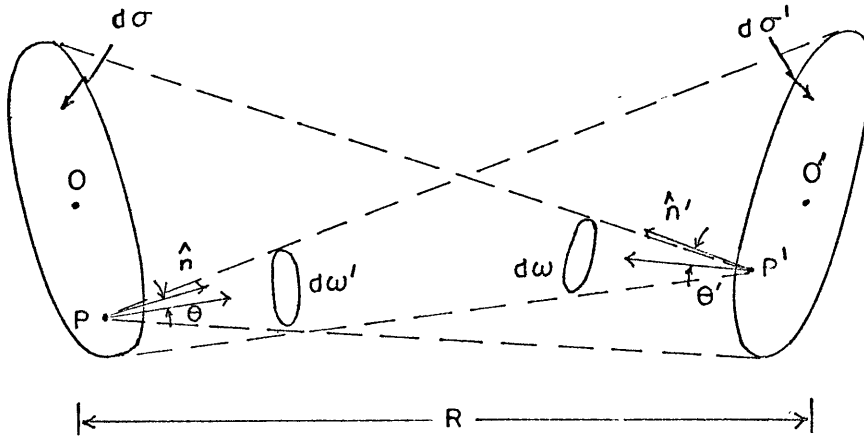
Figure 3-1. The geometry used to define the intensity of a flow of electromagnetic energy.
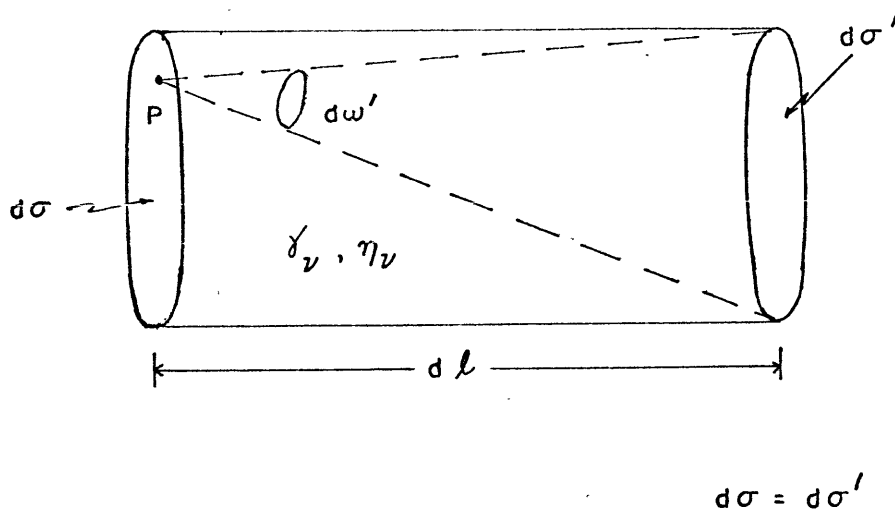
Figure 3-2. The geometry used to formulate the equation of radiative transfer in an absorbing medium.

in which θ and θ' are the angles between the normals n and n' to the differential surfaces at P and P' respectively and the lines PO' and P'O respectively.

In a small interval of frequency between ν and $\nu + d\nu$ an amount of energy $dE_\nu \, d\nu$ will flow through $d\sigma$ and on through $d\sigma'$ in a given time dt. From any point on $d\sigma$ its direction will be confined to a core of solid angle $d\omega'$. The amount of energy passing through $d\sigma$ toward $d\sigma'$ in time dt will therefore depend upon $d\sigma$, $d\omega'$, $d\nu$, and θ . The dependency can be written as

$$dE_\nu \, d\nu = I_\nu \, d\sigma \, \cos\theta \, d\omega' \, dt$$

$$= I_\nu \, d\sigma \, \cos\theta \, \frac{d\sigma' \cos\theta'}{R^2} \, dt \qquad (3.1\text{-}3)$$

where the constant of proportionality I_ν is called the specific intensity and is a measure of the average strength of the radiation flow over the frequency band $d\nu$ and time dt . The energy passing through $d\sigma'$ which has already passed through $d\sigma$ in the frequency interval ν to $\nu + d\nu$, call it $dE'_\nu \, d\nu$, will depend upon the solid angle $d\omega$, the area $d\sigma'$, the angle θ' , such that

$$dE'_\nu \, d\nu = I'_\nu \, d\sigma' \, \cos\theta' \, d\omega \, dt$$

$$= I'_\nu \, d\sigma' \, \cos\theta' \, \frac{d\sigma \cos\theta}{R^2} \, dt \qquad (3.1\text{-}4)$$

If no emission or absorption occurs between $d\sigma$ and $d\sigma'$, then

$$dE_\nu \, d\nu = dE'_\nu \, d\nu \qquad (3.1\text{-}5)$$

and therefore

$$I_\nu = I_\nu'$$

(3.1-6)

(More subtle considerations concerning the definition and application of the intensity are found in Planck[38].)

If in the intervening distance between $d\sigma$ and $d\sigma'$ absorption or emission does occur, in general Equation (3.1-6) does not hold. For an atmosphere whose index of refraction deviates negligibly from unity, the effects of the absorption or emission can best be assessed from a geometrically simplified version of Figure 3-1. In Figure 3-2 a right circular cylinder is shown. Energy passes through $d\sigma$ toward $d\sigma'$ in the solid angle $d\omega'$ (again dl must be considerably larger than the linear dimensions of $d\sigma'$ to insure that $d\omega'$ does not vary substantially as P moves over $d\sigma$). The quantity of energy in time dt is given by

$$dE_1 \, d\nu = I_1 \, d\nu \, d\sigma \, d\omega' \, dt$$

(3.1-7)

where it is understood that dE_1 and I_1 are specific energy and specific intensity respectively and that the two surfaces are perpendicular to the axis of the elemental cylinder. The amount of energy absorbed is given by

$$dE_2 \, d\nu = \gamma_\nu \, dE_1 \, d\nu \, dl$$

(3.1-8)

in which γ_ν is the absorption coefficient and is generally a function of frequency along with dE_2 and dE_1 . The amount of energy emitted in the cylinder is given by

$$dE_3 \, d\nu = \eta_\nu \, dV \, d\omega' \, dt \, d\nu$$

(3.1-9)

which defines the volume emissivity η_ν as the energy which is

emitted into the solid angle $d\omega'$ in time dt per unit frequency interval

from the elemental volume $dV = d\ell \, d\sigma$. Finally, we can write

from the principle of energy conservation that the energy dE_4 which

passes through $d\sigma'$ in solid angle $d\omega'$, frequency interval ν to

$\nu + d\nu$, and time dt, is the energy which originally passed through

$d\sigma$, minus the energy absorbed, plus the energy emitted

$$dE_4 \, d\nu = dE_1 \, d\nu - dE_2 \, d\nu + dE_3 \, d\nu \qquad (3.1-10)$$

Using (3.1-7), (3.1-8) and (3.1-9) and the spectral intensity notation

for dE_4 , one obtains

$$I_4 \, d\nu \, d\omega' \, d\sigma' \, dt = I_1 \, d\nu \, d\sigma \, d\omega' \, dt$$

$$- \gamma_\nu \, d\ell \, I_1 \, d\nu \, d\sigma \, d\omega' \, dt + \eta_\nu \, d\ell \, d\sigma' \, d\omega' \, dt \, d\nu \qquad (3.1-11)$$

or

$$I_4 - I_1 = -\gamma_\nu \, d\ell \, I_1 + \eta_\nu \, d\ell \qquad (3.1-12)$$

Equation (3.1-12) may be put in differential form since the decrease

of intensity is over a vanishingly small distance.

$$\frac{dI_\nu}{d\ell} = -\gamma_\nu \, I_\nu + \eta_\nu \qquad (3.1-13)$$

in which I_ν with no numerical subscript represents the specific in-

tensity at the point of interest in the medium. Equation (3.1-13) is

the fundamental equation of radiative transfer for an atmosphere whose

index of refraction is unity. For a more complete derivation without

the assumption of the unchanging index of refraction see Woolley and

Stibbs[42].

Equation (3.1-13) is usually written in a form utilizing the concept of optical depth, sometimes called optical thickness, or opacity and is defined by

$$\tau_\nu = \int_0^{\tau_\nu} d\tau_\nu = \int_0^1 -\gamma_\nu \, d\ell = +\int_\ell^0 \gamma_\nu \, d\ell \qquad (3.1\text{-}14)$$

where dl is positive in the direction of energy flow (dσ to dσ') and $d\tau_\nu$ is positive in the opposite direction (dσ' to dσ). Equation (3.1-13) transforms to

$$\frac{d I_\nu}{d \tau_\nu} - I_\nu = -\frac{\eta_\nu}{\gamma_\nu} \qquad (3.1\text{-}15)$$

which readily integrates to

$$\left(I_\nu \, e^{-\tau_\nu} \right)_0^{\tau_{max}} = -\int_0^{\tau_{max}} \frac{\eta_\nu}{\gamma_\nu} \, e^{-\tau_\nu} \, d\tau_\nu \qquad (3.1\text{-}16)$$

in which

$$\tau_{max} = \int_0^{\ell_{max}} -\gamma_\nu \, d\ell$$

To apply (3.1-16) to the atmosphere of the earth, consider the geometry of the horizontally stratified, plane parallel atmosphere depicted in Figure 3-3. An antenna on the ground with main beam half power points ϕ_m degrees apart views an extraterrestrial source through the atmosphere at an angle away from the zenith of θ degrees. The extraterrestrial source fills the main beam. Because of horizontal stratification and the planar geometry, it is most convenient to
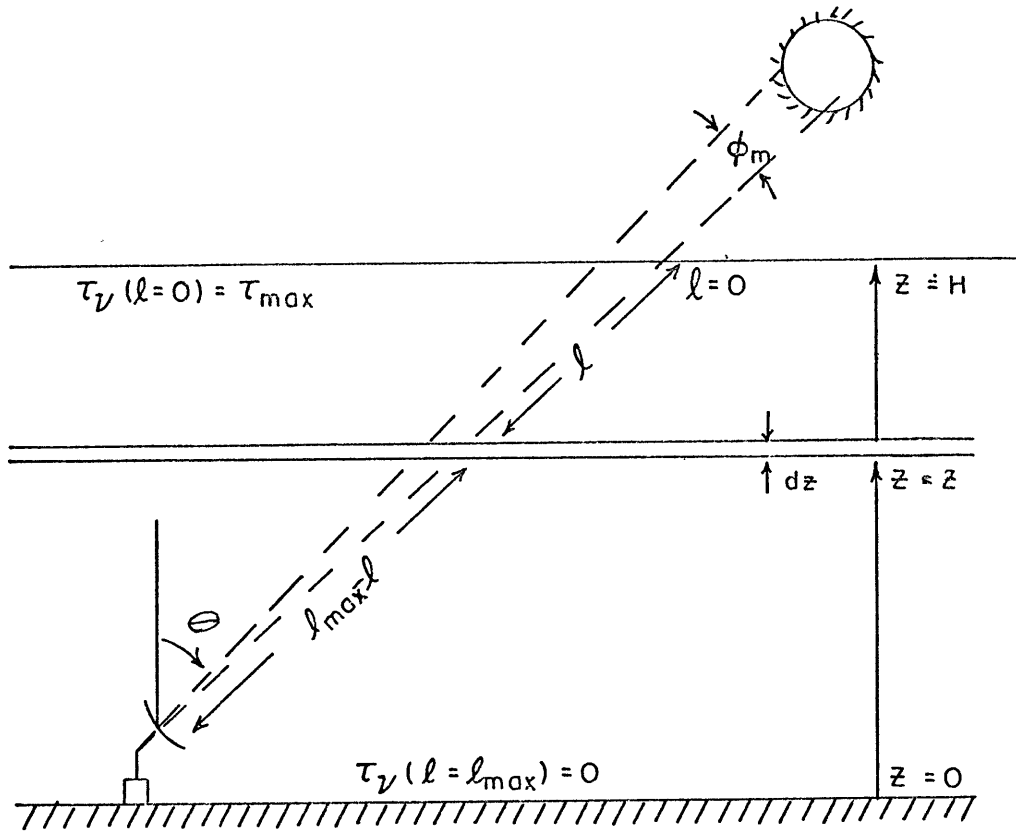
Figure 3-3. The geometry for microwave observations in a planar, horizontally stratified atmosphere.

redefine τ_ν in terms of z and θ as

$$\tau_\nu (z, \theta) = \int_{l=l_{max}}^{l} \gamma_\nu \, dl = \int_0^z \gamma_\nu \sec \theta \, dz \qquad (3.1\text{-}17)$$

More simply, for zenith angles other than zero, the opacity from z = 0 to z = z is given by $\tau_\nu (z, 0) \sec \theta$. Equation (3.1-16) may now be rewritten for the geometry of Figure 3-3 and the definition from Equation (3.1-17) as

$$I_\nu (0) = I_\nu (\infty) e^{-\tau_{max} \sec \theta} + \int_0^{H} \frac{\eta_\nu}{\gamma_\nu} e^{-\tau_\nu (z, 0) \sec \theta} \gamma_\nu \sec \theta \, dz \qquad (3.1\text{-}18)$$

where now

$$\tau_{max} = \int_0^{H} \gamma_\nu \, dz \qquad (3.1\text{-}19)$$

The intensity reaching the antenna at z = 0 is $I_\nu (0)$. It is composed of two components, the first of which is the intensity at z = H, a level above all significant attenuating gases, diminished by its passage through the atmosphere $\left(e^{-\tau_{max} \sec \theta} \right)$. The second component originates in the atmosphere and is represented by the integral on the r.h.s. of (3.1-18). The atmospheric contribution to $I_\nu (0)$ represents the radiation from thin slabs of atmosphere of effective thickness dz sec θ . The strength of the radiation received at the antenna from any slab is equal to the volume emissivity of that slab times the effective volume of a unit cylinder along the propagation

path diminished by the absorption of all the intervening layers. The absorption factor is represented by $e^{-\tau_\nu(z,0)\sec\theta}$ where $\tau_\nu(z,0) = \int_0^z \gamma_\nu \, dz$.

Rather than simply cancelling the $\gamma_\nu's$ which appear in the integral of (3.1-18) and deal with the volume emissivity it is more convenient to define a new quantity

$$J_\nu = \frac{\eta_\nu}{\gamma_\nu} \qquad (3.1\text{-}20)$$

called the source function and investigate its properties.

We have, from the beginning, stated that the condition for which we would derive the equation of radiative transfer would be for local thermodynamic equilibrium. That is, the conditions which would prevail within an enclosure of constant temperature. Far enough from the walls of the enclosure the energy emitted in any direction, at any frequency, for any polarization by a bit of matter must be just balanced by the energy flowing in the opposite direction for the same frequency and polarization; otherwise the piece of material would gain or lose energy and change its temperature, contrary to our original hypothesis. When these conditions prevail, the emitted and absorbed energy for the infinitesimal cylinder of Figure 3-2 must be equal. Therefore, from Equations (3.1-7), (3.1-8) and (3.1-9)

$$\gamma_\nu \, I_1 \, d\nu \, d\sigma \, d\omega' \, dt \, d\ell = \eta_\nu \, d\sigma \, d\ell \, d\omega' \, dt \, d\nu \qquad (3.1\text{-}21)$$

or

$$I_1 = \frac{\eta_\nu}{\gamma_\nu} \qquad (3.1\text{-}22)$$

This relationship is known as Kirchhoff's Law and was first enunciated

in 1882. It follows, therefore, from Equations (3.1-20) and (3.1-22)

for thermodynamic equilibrium within the atmosphere that

$$J_\nu = I_1 \qquad (3.1-23)$$

and Equation (3.1-18) may be rewritten as

$$I_\nu(o) = I_\nu(H) e^{-\tau_{max} \sec \Theta} + \int_0^H I_\nu \gamma_\nu e^{-\tau_\nu \sec \Theta} \sec \Theta \, dz \qquad (3.1-24)$$

This is the fundamental equation of transfer for radiation in a planar,

horizontally stratified atmosphere in thermodynamic equilibrium.

For microwave radiation it is possible to rewrite Equation

(3.1-24) in somewhat simpler terms. The intensity as used is defined

by Planck's radiation law for an enclosed body in thermodynamic equi-

librium as

$$I_\nu = \frac{2h\nu^3}{c^2} \frac{1}{e^{h\nu/kT} - 1} \qquad (3.1-25)$$

wherein h is Planck's constant, ν is the frequency, c the speed of

light, k is Boltzmann's constant, and T is the temperature. When

$h\nu \ll kT$ as is the case for microwave radiation the Rayleigh-

Jeans approximation can be made with negligible error, i.e.,

$$I_\nu \approx \frac{2kT\nu^2}{c^2} \qquad (3.1-26)$$

From (3.1-26), the term brightness temperature may be defined

as

$$T_B = \frac{I_\nu c^2}{2k T} \qquad (3.1-27)$$

It corresponds to the temperature which a thermally enclosed body at
constant temperature throughout would have which radiated energy of
intensity I_ν in the frequency region ν to $\nu + d\nu$. It should
be clear that T_B is a general term and will be a function of the fre-
quency except when the gas is in thermodynamic equilibrium.

The equation of transfer applicable to a non-scattering atmo-
sphere in thermodynamic equilibrium can be written in final form as

$$T_B(0) = T_B(H) e^{-\tau_{max} \sec \theta} + \int_0^H T_{RT} \gamma_\nu e^{-\tau_\nu \sec \theta} \sec \theta \, d\tau \qquad (3.1\text{-}28)$$

3.2 Thermodynamic Equilibrium in the Atmosphere

In the light of Equation (3.1-24) it is necessary to evaluate
the assumption that the atmosphere is in thermodynamic equilibrium, and
for that matter what thermodynamic equilibrium means in terms of rota-
tional spectra.

Thermodynamic equilibrium, in general, refers to a state for an
assemblage of particles in which the total energy of the assemblage is
distributed over the particles in the most probable statistical manner,
i.e., a state which is identified by the maximum value of the entropy
possible for the conditions of the gas (see Planck[38]). When thermodynamic
equilibrium exists the distribution of energy is given by Boltzmann's
equation

$$\frac{N_i}{N} = \frac{g_i \, e^{-E_i/kT}}{\sum_i g_i \, e^{-E_i/kT}} \qquad (3.2\text{-}1)$$

in which N_i is the number of particles of energy E_i , N is the total

number of particles, g_i is the statistical weight of the energy level

E_i , k is Boltzmann's constant, and T is a temperature. For discrete

energy levels which exist for rotation, vibration and electronic excita-

tion, the summation is appropriate in the denominator. In the limit of

a continuous energy distribution as for energy of translation, the sum-

mation should be replaced by an integral. The denominator of the r.h.s.

is called the partition function for the energy mode it describes. A

similar expression was evaluated in Chapter 2 for the distribution of

energy over rotational states in an assemblage of water molecules.

For molecules, several semi-independent domains of energy exist:

kinetic energy of translation, rotational energy, vibrational energy,

and electronic excitation energy. The last three energy modes are

quantized and can interact with the radiation field. Energy can be

redistributed between the modes when collisions occur. It is possible

for the various energy modes to separately approach thermodynamic equi-

librium. Goody[39] has analyzed the conditions in the atmosphere which

allow the translational, vibrational, and rotational energy distributions

to maintain thermodynamic equilibrium against naturally occurring per-

turbations.

The distribution of energy over the translational motions of the

molecule is most easily maintained in a state of thermodynamic equilib-

rium. Every collision acts to readjust the velocity distribution towards

one which can be described by a single temperature, the kinetic temperature

of the gas, defined by the Boltzmann equation (3.1-23). Therefore a kinetic temperature is meaningful up to that height in the atmosphere where collisions are no longer likely. That is up to the region where molecules can escape to space without much probability of colliding with another molecule. This level is at the upper levels of the ionosphere hundreds of kilometers above the region where water vapor can exist.

The vibrational energy is maintained in thermodynamic equilibrium by collisions. Spontaneous emission is the mechanism by which the excited vibrational levels return to the ground state and disrupt the collisionally imposed equilibrium. The natural lifetime of the second vibrational mode of water vapor (the vibrational mode of lowest energy) is reported by Goody to be roughly 0.12 seconds. The relaxation time needed to distribute energy between vibrational modes to establish thermodynamic equilibrium is inversely proportional to the rate of collisions, a quantity directly proportional to the total pressure. Therefore the collisional relaxation time goes as $1/P$ where P is the total atmospheric pressure. Goody estimates that the natural lifetime and collisional relaxation time for the vibrational energy of water vapor are roughly equal near pressures of 0.034 mb, a height in the Standard Atmosphere of about 74 kilometers.

The most important energy domain to investigate for thermodynamic equilibrium for this paper is of course the rotational energy domain. Upon it depends the validity of the equation for absorption

which we have developed in Chapter 2. Natural lifetimes for rotational

energy levels of water vapor are of the order of 0.1 to perhaps 10 se-

conds, values which may be computed from the dipole matrix elements.

The relaxation time for collisional redistribution of energy is again

proportional to 1/P and at standard temperature and pressure has a value

approximately equal to 10^{-10} seconds. This estimate is based upon

Anderson's theory[15] in which the relaxation time is shown to be related

to the line width. From these estimates Goody concludes that rotational

energy levels should be distributed according to Boltzmann's law at

least down to pressures of 10^{-6} mb, a height in the Standard Atmosphere

of approximately 150 km. From other considerations, notably the fact

that photodissociation of water vapor molecules probably becomes impor-

tant at less than one half this altitude, it is reasonable to expect

that wherever water vapor occurs it will be in rotational thermodynamic

equilibrium.

The rotational temperature and kinetic temperature defined by

separate statements of Equation (3.1-23) will, under all natural condi-

tions, be the same since the energy of the system will be equally

available to translational as well as rotational degrees of freedom at

the pressures and temperatures found in the atmospheric regions where

water vapor absorption will be important.

Finally, a remark should be made about electronic transitions

for water vapor. At the ground, the ratio of the lifetime for colli-

sion induced transitions to the lifetime of spontaneous transitions is

very large; thermodynamic equilibrium cannot exist. However, the energy required to cause electrons to transition to excited states is so great that this is a rare and unimportant process in any equation of transfer for the atmosphere at any frequency below the visible.

3.3 Microwave Measurements and Atmospheric Water Vapor Weighting Functions near the 22.2 GHz Resonance

A number of measurements at microwave frequencies can be made which contain information about the water vapor in the beam of the receiving antenna. In effect, the various measurements are made to simplify Equation (3.1-28) or to take advantage of some special geometry, such as that afforded by a satellite. Each of the measurements have peculiarities which enhance or make more difficult their interpretation in terms of the atmospheric conditions which produce the radiation being measured. It is the goal of this section to point out the advantages and difficulties.

3.3.1 Total Zenith Opacity near 22.2 GHz

One of the microwave properties of the atmosphere is its total (zenith) opacity τ_{max} . A practical technique which can be used to obtain τ_{max} is given in detail in Chapter 4. For the moment, allow that it can be done. It is defined as

$$\tau_{max} = \hat{\tau}_\nu \left(H, 0 \right) = \int_0^H \gamma_\nu \, dz \qquad (3.3-1)$$

where γ_ν is the total absorption from all constituents of the gas

at the frequency ν . In the atmosphere of the earth, on clear days, only oxygen and water vapor contribute non-negligible absorption to $\hat{\tau}_{max}$ over the microwave range. Therefore, since $\gamma_\nu = \gamma_{H_2O} + \gamma_{O_2}$ then τ_{max} can be written as

$$\tau_{max} = \left(\tau_{max}\right)_{H_2O} + \left(\tau_{max}\right)_{O_2} = \int_0^H \gamma_{H_2O}\, dz + \int_0^H \gamma_{O_2}\, dz \quad (3.2-2)$$

If the two contributions to τ_{max} can be separated, then the zenith opacity of atmospheric water vapor may be studied as a function of frequency. γ_{H_2O} and γ_{O_2} are those absorption coefficients derived in Chapter 2 and presented in Appendix A-II. γ_{H_2O} for the 1.35 cm line, as will be recalled, is composed of $\left(\gamma_{RES}\right)_{1.35}$ and $\left(\gamma_{NON}\right)_{1.35}$ and can be written as

$$\gamma_{H_2O} = \left(\gamma_{RES}\right)_{1.35} + \left(\gamma_{NON}\right)_{1.35} = 1.57 \left\{ \frac{\rho\, \nu'^2 e^{-642/T}}{T^{5/2}} \right\}$$

$$\times \left\{ \frac{\Delta\nu'}{(\nu' - \nu_0')^2 + \Delta\nu'^2} + \frac{\Delta\nu'}{(\nu' + \nu_0')^2 + \Delta\nu'^2} \right\}$$

$$+ 1.11 \times 10^{-5} \left\{ \frac{\rho\, \nu'^2\, \Delta\nu'}{T^{3/2}} \right\} \frac{db}{m}$$

$$= \rho\, g\left(\nu, P, T, \rho\right) \qquad (3.3-3)$$

where the dependence of g on ρ is quite small. It is clear that the same water vapor density will show different values for absorption

at different levels in the atmosphere. If we know the structure of the atmosphere, then we can compute a weighting function for water vapor contributions to $\left(\mathcal{T}_{max}\right)_{H_2O}$. By definition, therefore

$$W_{\mathcal{T}}' (\nu, z) = \frac{\gamma_{H_2O} (\nu, z)}{\rho (z)} \qquad (3.3\text{-}4)$$

so that

$$\left[\mathcal{T}_{max} (\nu)\right]_{H_2O} \cong \int_0^H W_{\mathcal{T}} (\nu, z) \, \rho (z) \, dz \qquad (3.3\text{-}5)$$

The dependence of the weighting function $W_{\mathcal{T}} (\nu, z)$ on P, T, and ρ is shown implicitly through z.

The formulation of a weighting function is important because it shows at what height in a particular atmosphere the attenuation for a given amount of water vapor is greatest, i.e., where it is most "sensitive" to water vapor. This sensitivity is a function of frequency.

For the 22.2 GHz water vapor line, Figure 3-4 presents three weighting functions as computed from Equation (3.3-4) and normalized to unity in each case. They represent typical shapes for weighting functions which one can expect for spectral measurements around this particular resonance. The wings of the line (represented by the 19.00 GHz curve) show an exponential like decrease with altitude. At resonance (22.237 GHz), the weighting function increases roughly exponentially with height. For frequencies near resonance, there is a maximum sensitivity at some intermediate altitude.
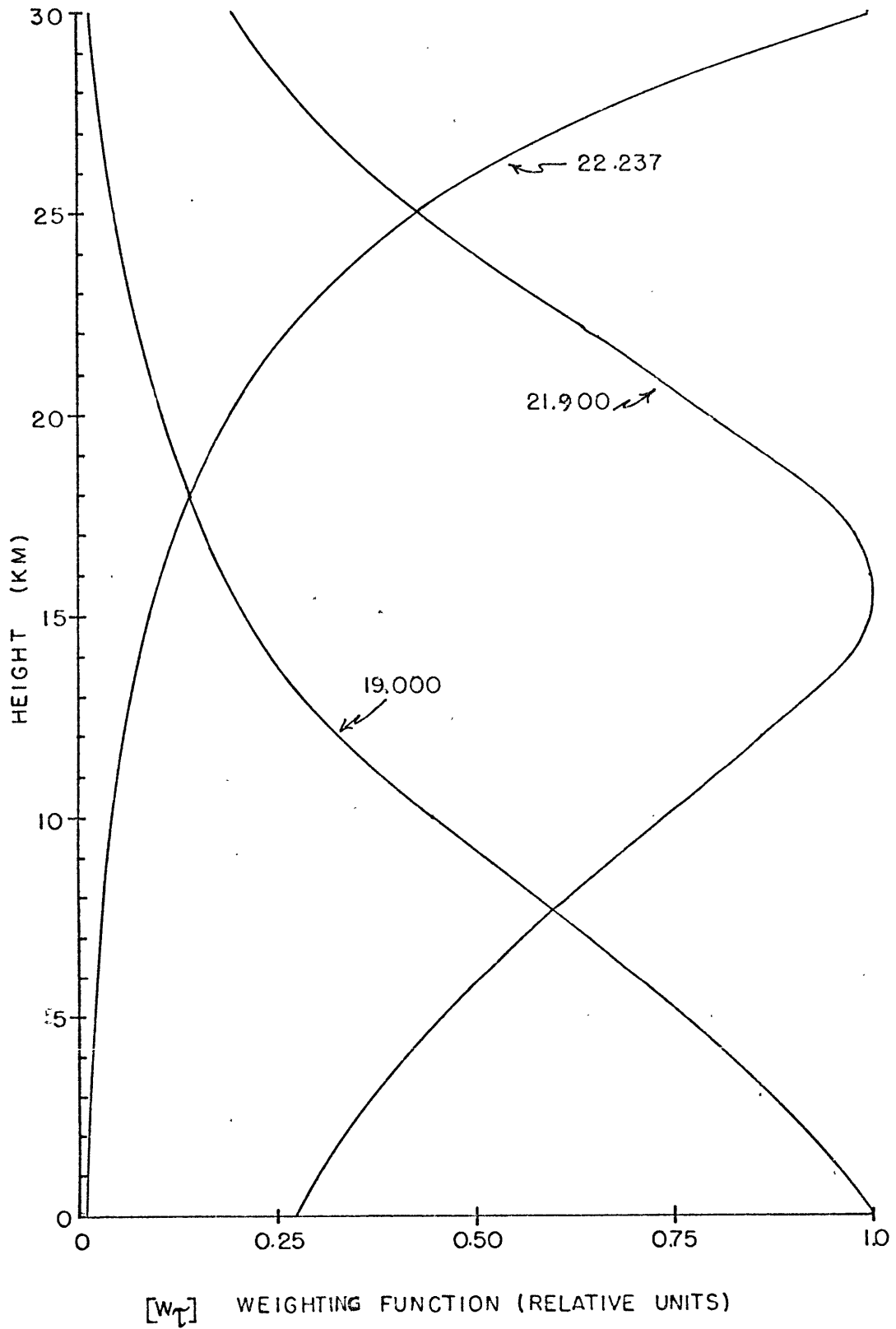
Figure 3-4.   Normalized zenith opacity weighting functions for
atmospheric water vapor.

The height of the maximum decreases for frequencies further from resonance. The frequency dependence of this maximum height is shown in Figure 3-5. No maxima appear for frequencies below about 19.75 GHz nor above 24.70 GHz. The rate of change of the height at which the maximum sensitivity occurs, with respect to frequency, approaches infinity at resonance. Therefore, to accurately know where maxima occur at high levels in the atmosphere one must have a precise knowledge of the frequency. The width at half strength of those weighting functions with maxima at intermediate levels is approximately 18 km.

The characteristic shapes of the three representative weighting functions arise from the effect of decreasing pressure in the line width parameter and the effective role of this parameter near and far from resonance. If one examines the line shape factor of Equation (2.3-6) one finds that at resonance the $(\nu - \nu_0)^2$ term in one of the denominators is zero and the whole factor is closely proportional to $1/\Delta\nu$ and thus $1/P$. Far away from resonance, the $(\nu - \nu_0)^2$ term dominates over the $\Delta\nu^2$ term in the denominator and the line shape factor is more nearly proportional to $\Delta\nu$ and therefore P. In between, the situation is best illustrated by Figure 3-6. In the figure, at three frequencies, sequences of numbers are provided to direct the readers attention to the effects of decreasing pressure, and thus decreasing line width and increasing altitude in the atmosphere. (1) is associated with the highest pressure and widest line width. (2) is an intermediate pressure level and (3) is the lowest pressure and narrowest
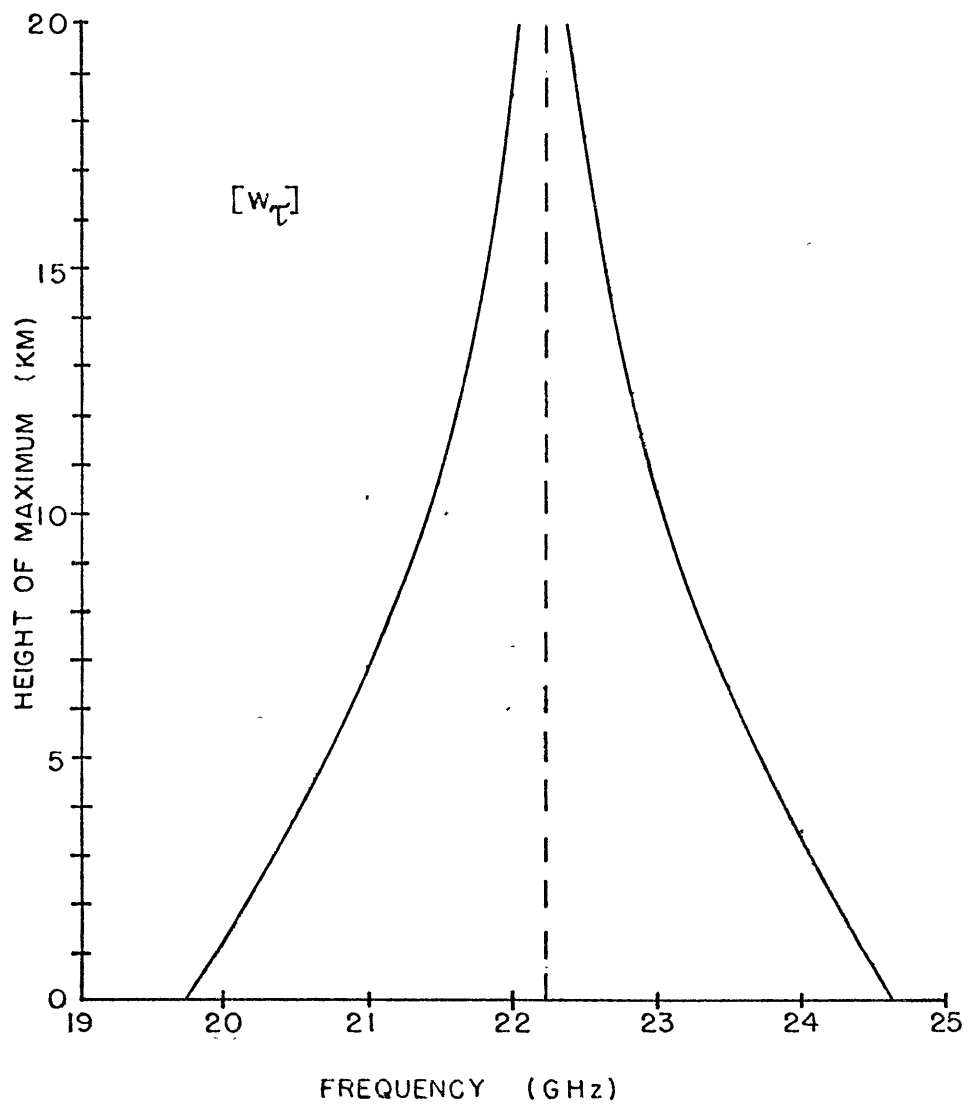
Figure 3-5. The frequency dependence of the height of the
zenith opacity weighting function maxima.
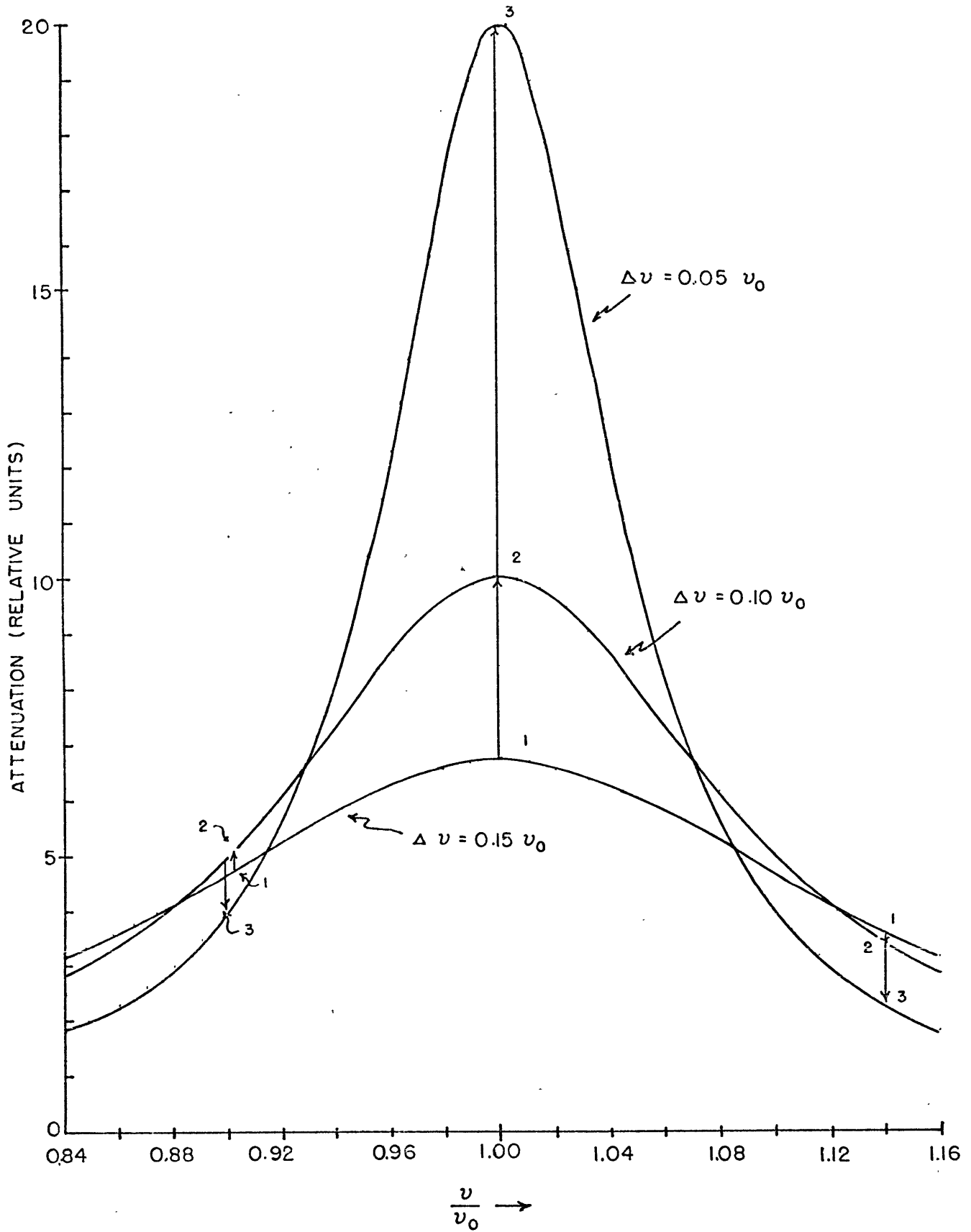
Figure 3-6. The origin of atmospheric water vapor weighting functions.

line width. At resonance (ν/ν_o' = 1.0) and far enough into the wings (ν'/ν_o = 1.14), the attenuation acts monotonically as previously discussed. For intermediate frequencies (represented on Figure 3-6 by ν'/ν_o = 0.90) the attenuation at first increases, then falls monotonically as the line progressively narrows. This causes a maximum attenuation to occur at some pressure, and therefore some height.

Besides the utility of illustrating the sensitivity of a particular atmosphere to water vapor, it would be of considerably greater importance for the interpretation of microwave measurements if weighting functions were constant for various atmospheric conditions. To investigate this point for zenith opacity weighting functions, Figure 3-7 was prepared. Weighting functions at 19.00 GHz were computed for four diverse climatological regions: the tropics (15°N); midlatitudes (40°N); subarctic summer (60°N); and the arctic (75°N). The atmospheres used for the comparisons were the Standard Atmosphere 1962, and the Supplemental Atmospheres thereto, all taken from Valley[41]. (See Chapter 5 for details of these atmospheres).

The largest differences in the weighting functions occur at the surface between those atmospheres south of the arctic and the Arctic atmosphere. The extreme cold of the latter atmosphere plays a dominant role in elevating the surface attenuation. In other than arctic regions, differences of perhaps five percent occur. Within any climatological region, even smaller differences can be expected. At frequencies near to resonance, the differences between the arctic and other atmospheres
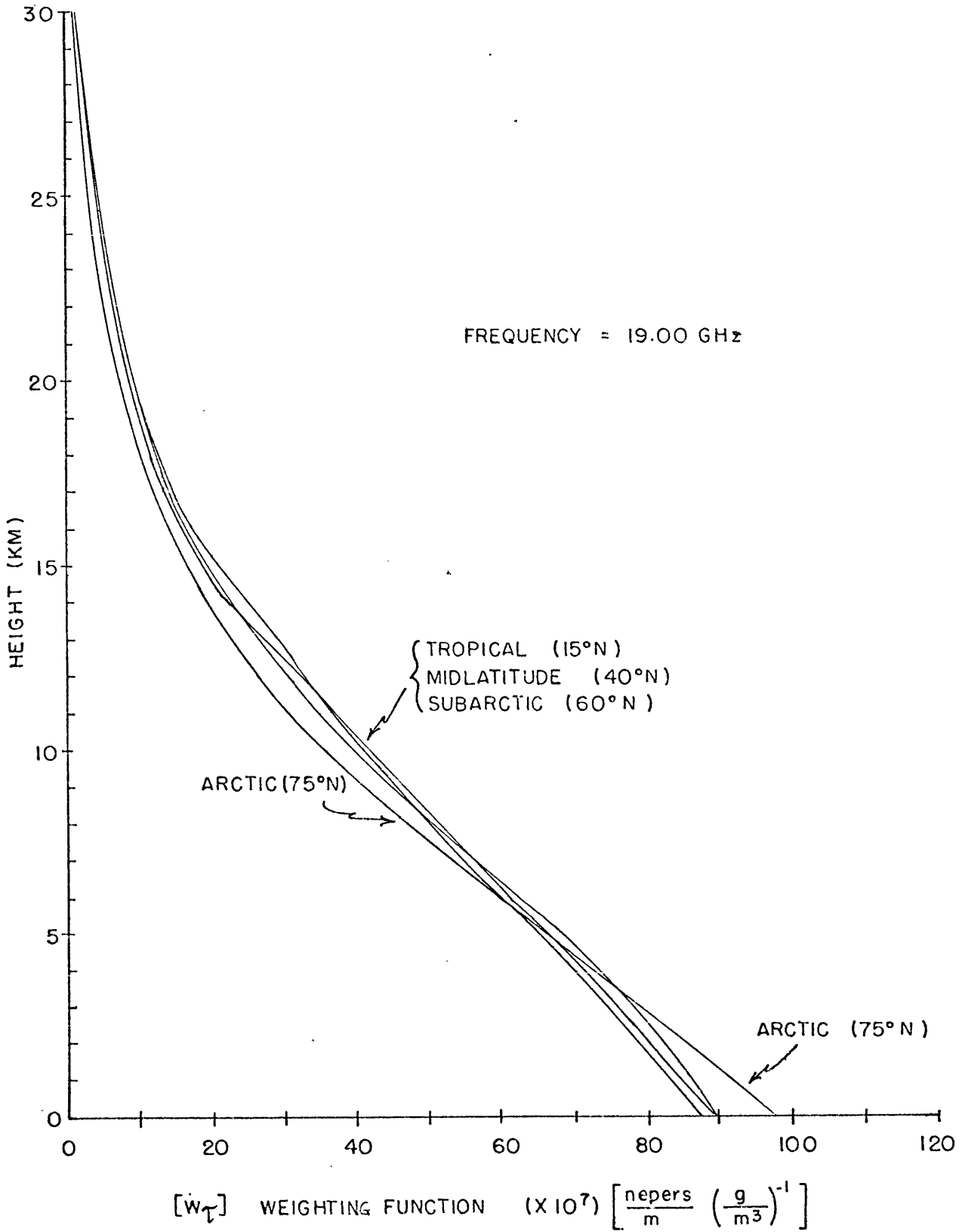
Figure 3-7. The stability of the 19 GHz zenith opacity weighting function for differing climatic regions.

at the surface mostly disappear as may be seen in Figure 3-8; farther

from resonance, the differences at the surface increase. The midlati-

tude curve in Figure 3-8 has not been plotted because at all altitudes

it falls within the other curves. For the summertime at least, and

from the surface to perhaps 10 km, the zenith opacity weighting functions

vary very little over perhaps 80% of the earth's surface.

As a final investigation of the gross features which one might

expect for microwave measurements of total zenith opacity, Figure 3-9

is presented. The tropical, midlatitude, and arctic opacities as a

function of frequency are plotted. These curves represent water vapor

only; oxygen attenuation is not included. This gives some feeling for

the range of amplitude which world-wide water vapor opacity measurements

might show. The variation of the line amplitude shown in Figure 3-9 can

also be obtained on a seasonal basis in midlatitude continental regions

as will be seen in Chapter 4.

3.3.2 Surface Observations of Atmospheric Brightness
Temperature near 22 GHz

Another microwave spectral observation of the atmosphere which

one might wish to make is the emission as a function of frequency.

Since the emission from space is small and approximately steady, unless

one's antenna is viewing the sun or moon, or some strong radio source

with a very narrow beam, the first term on the r.h.s. of Equation (3.1-28)

can be neglected. One has left
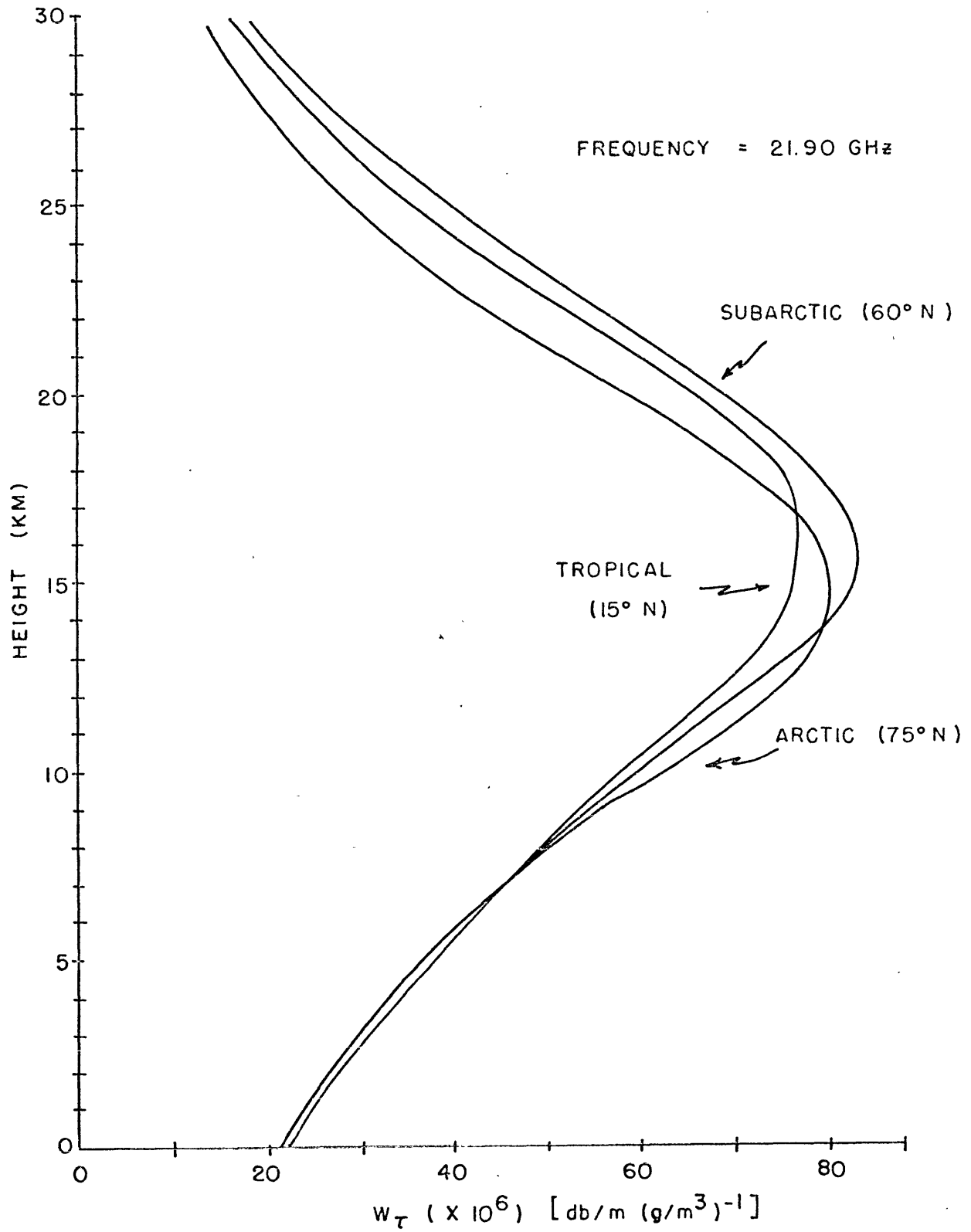
Figure 3-8. The stability of the 21.9 GHz zenith opacity weighting function for differing climatic regions.
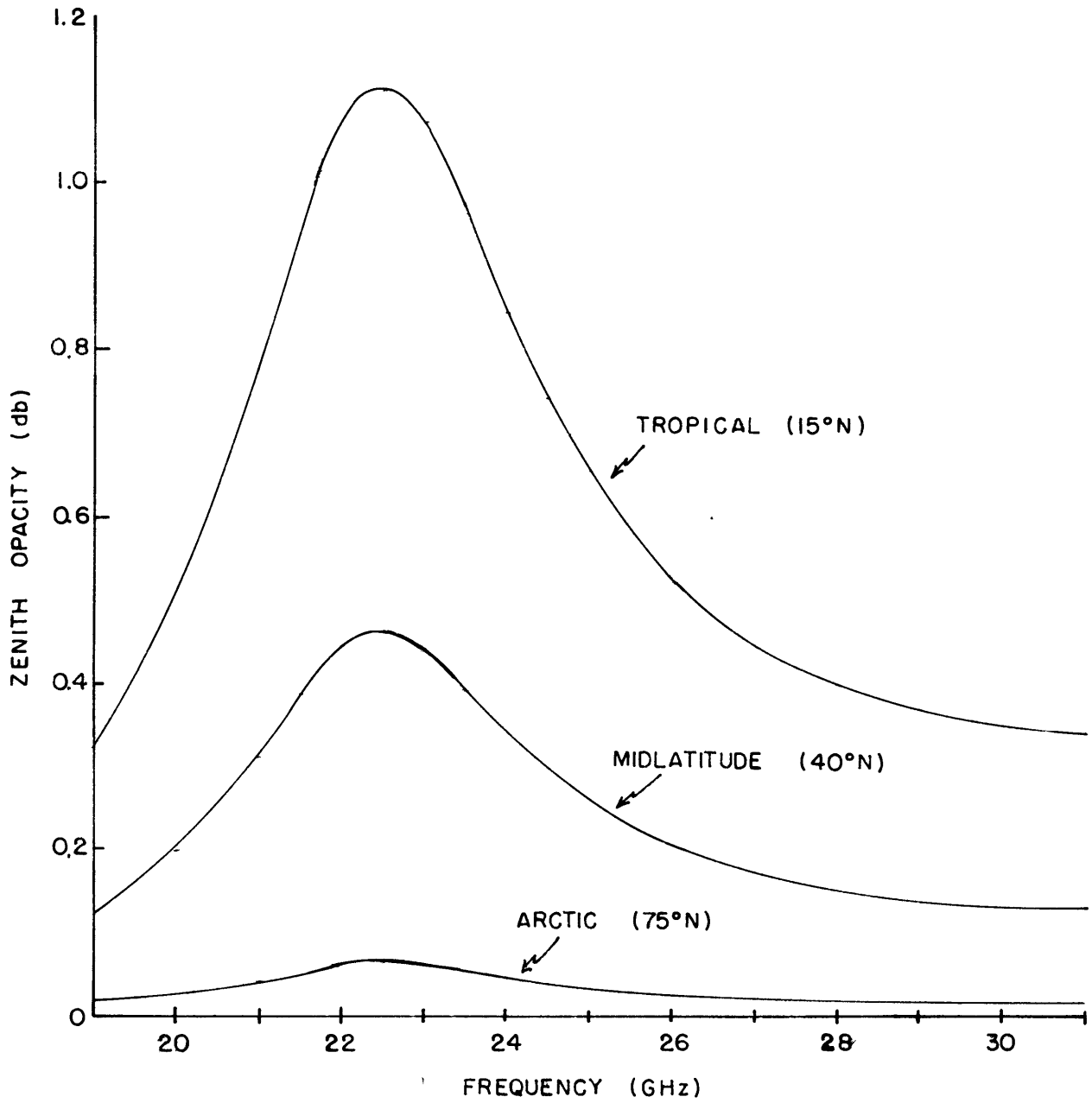
Figure 3-9. Absorption spectra computed for mean conditions in several
climatic regions.

$$T_B (\nu) = \int_0^H T_{AT} \, \gamma_\nu \, e^{-\tau_\nu (z, 0) \sec \theta} \sec \theta \, dz \qquad (3.3\text{-}6)$$

The water vapor weighting functions which would be appropriate for such a measurement can be defined as

$$[W_\tau]_{up} = \frac{T_{AT}(z) \, \gamma_{H_2O}(z) \, e^{-\tau_\nu (z, 0) \sec \theta} \sec \theta}{\rho (z)} \qquad (3.3\text{-}7)$$

so that

$$T_B (\nu) = \int_0^H [W_\tau]_{up} \, \rho (z) \, dz + \int_0^H T_{AT} \gamma_{0_2} \, e^{-\tau_\nu (z, 0) \sec \theta} \sec \theta \, dz$$

Equation (3.3-7) is a considerably more complicated function than the weighting function for $[\tau_{max}]_{H_2O}$ alone. Atmospheric pressure appears in the expression for $\gamma_\nu (= \gamma_{H_2O} + \gamma_{0_2})$ and cumulatively in $\tau_\nu (z, 0)$. Atmospheric temperature appears in both of these terms in addition to its explicit appearance. In addition, both γ_ν and $\tau_\nu (z, 0)$ are dependent upon the water vapor distribution. However, despite the complexity and nonlinearity of (3.3-7) it remains a useful concept as may be judged from Figure 3-10.

Weighting functions for the same three frequencies which were analyzed for the zenith opacity weighting functions are presented in Figure 3-10. Their shapes are very similar to the opacity shapes. It is apparent that the attenuation factor still dominates the functions;
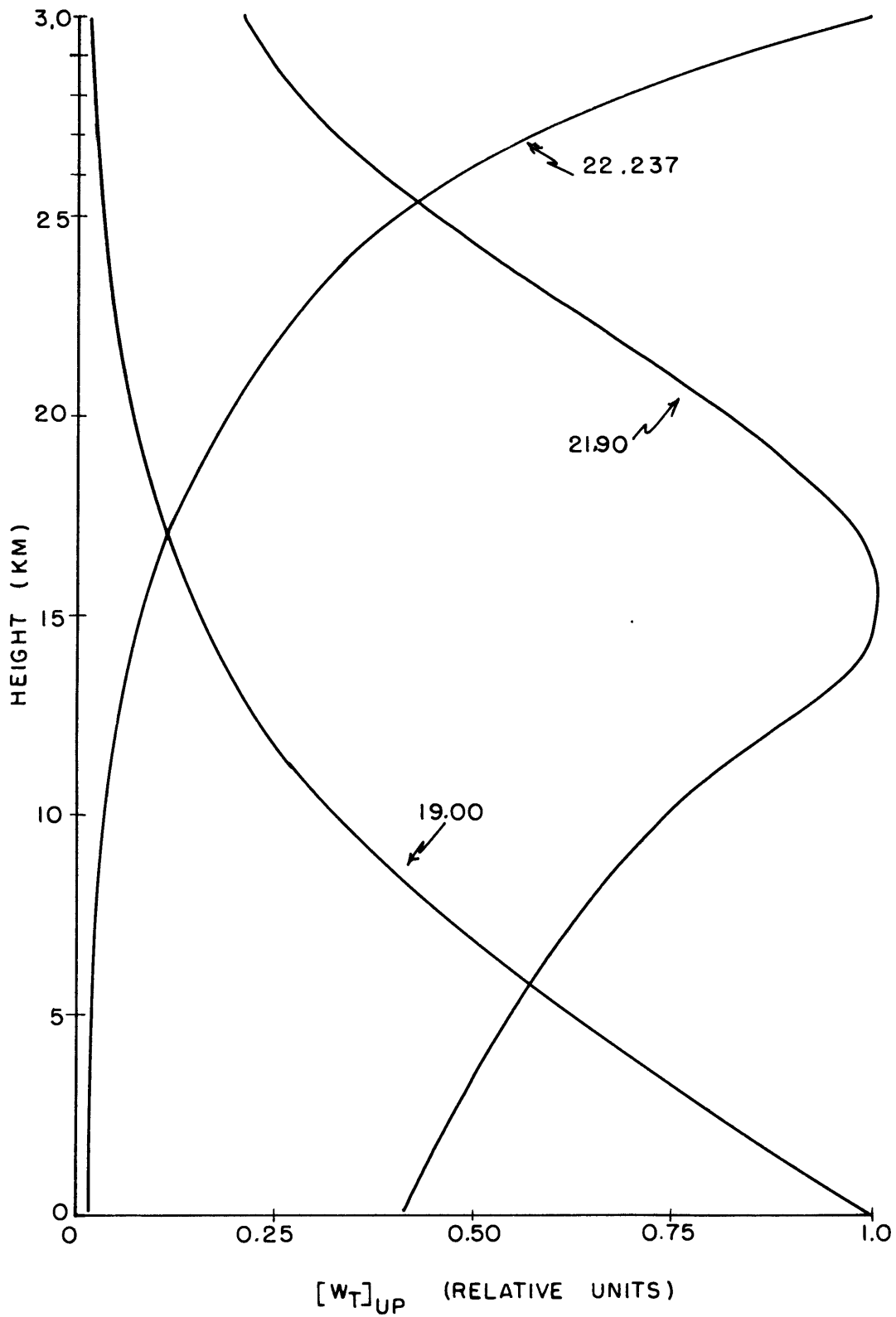
Figure 3-10. Normalized zenith emission weighting functions for
atmospheric water vapor.

the percentage temperature changes are so small and the exponential

factor is so unimportant that between them they only introduce the

changes in shape seen between Figure 3-4 and Figure 3-10. The reason

the amplitude of the function between the surface value and the maxi-

mum is less than for the opacity is a result of the temperature

decrease between these two levels.

The height at which a maximum occurs for a given frequency is

plotted in Figure 3-11. The curves are considerably narrower than

the opacity maxima curves, again an alteration due to changes intro-

duced mostly by the temperature profile.

The variation of the weighting functions over world-wide climates

may be seen in Figures 3-12 and 3-13. The midlatitude curve is not

plotted in Figure 3-12 because it fell very close to the tropical and

subarctic plots everywhere. The stability of the function at 19.0 GHz,

at least away from the arctic, is greater than the analogous opacity

weighting function.

The variation with climate of the 21.9 GHz upward looking bright-

ness temperature weighting function is considerably greater everywhere

than its opacity counterpart. The climatic temperature variations show

up strongly near the surface. Especially noticeable is the decrease of

the tropical weighting function near the surface due to the prevailing

temperature and moisture inversion. But the great divergence of tropo-

pause heights and temperatures causes the largest discrepancies between

the weighting functions to appear in the vicinity of the sensitivity
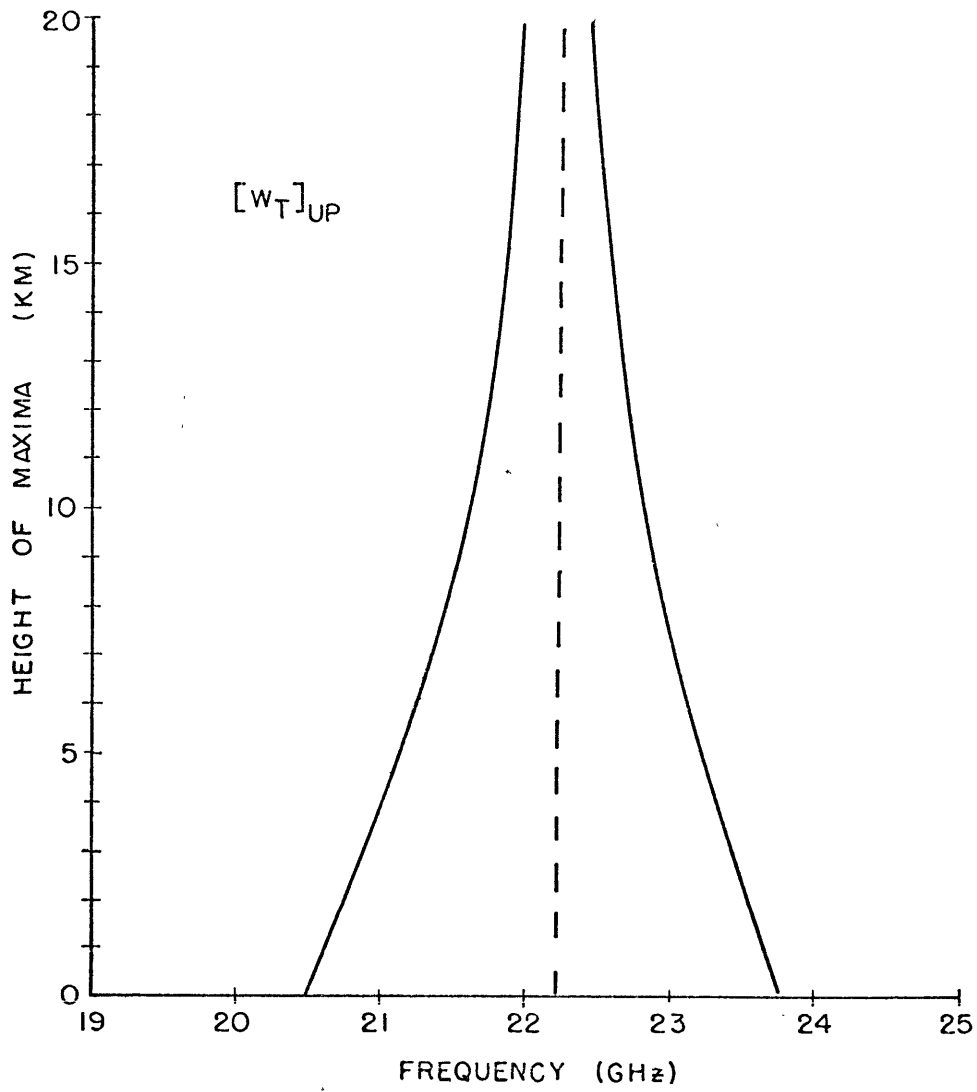
Figure 3-11. The frequency dependence of the height at which
maxima occur for zenith emission weighting functions.
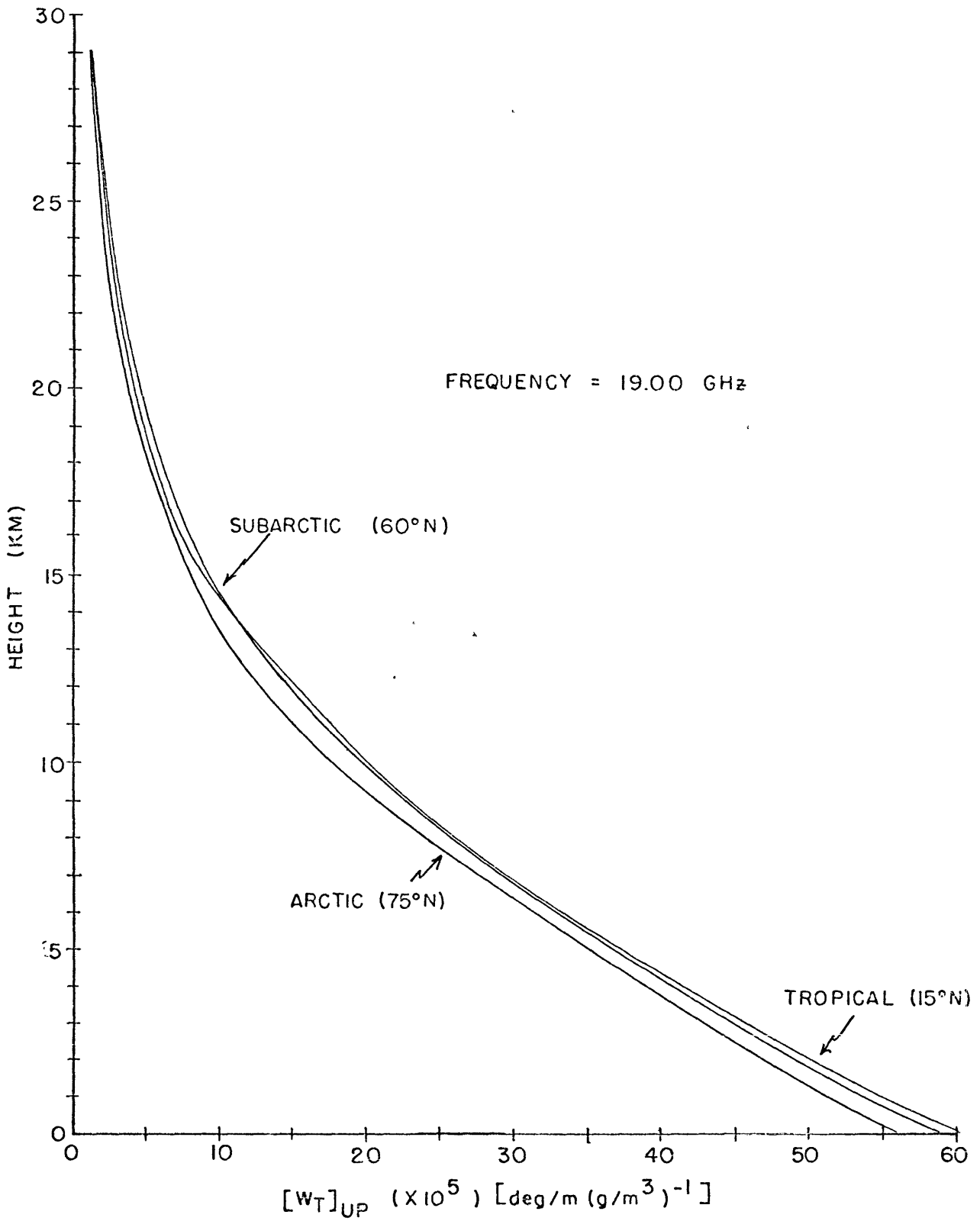
Figure 3-12. Climatic variations in the 19 GHz zenith emission weighting function.
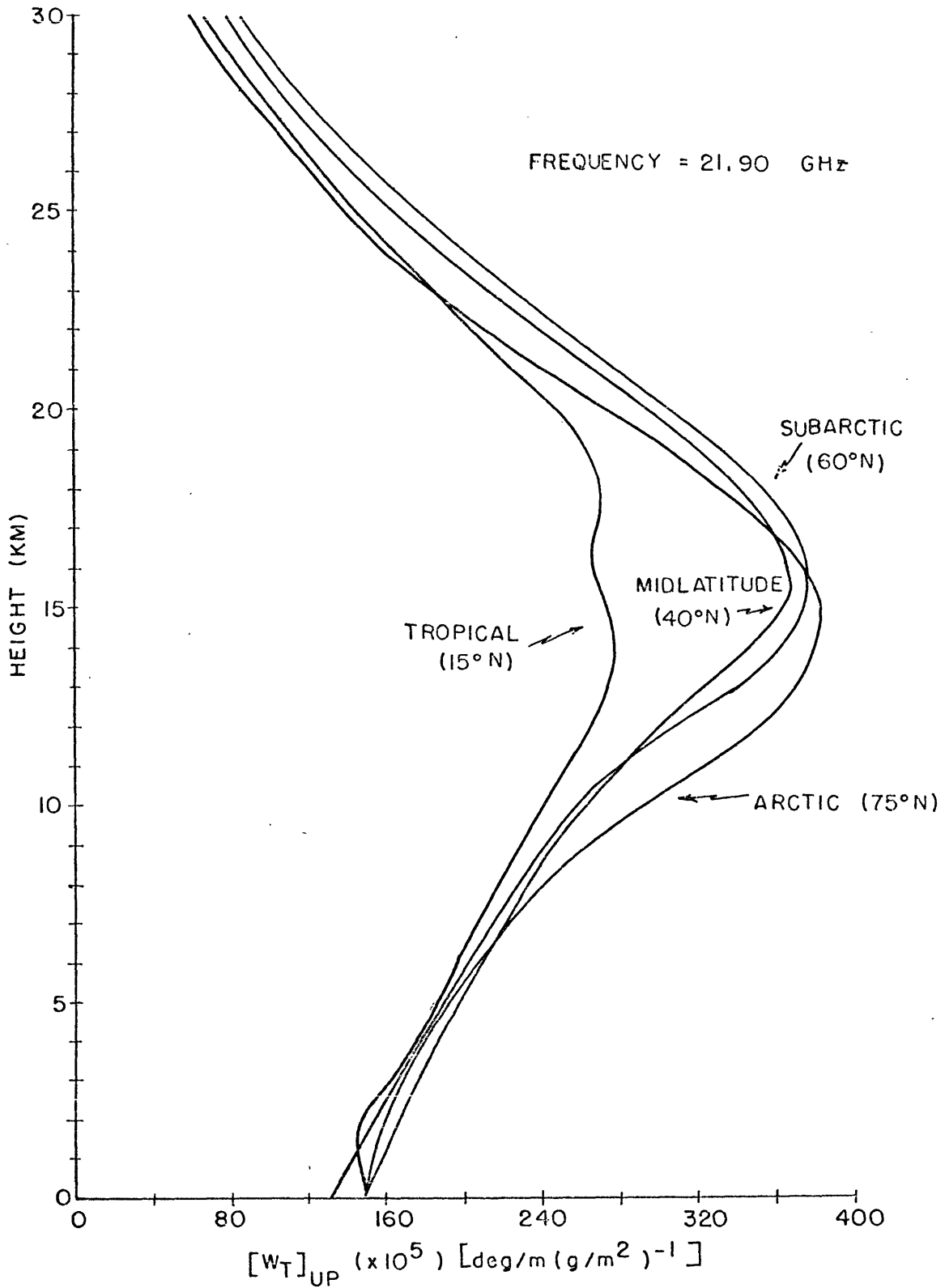
Figure 3-13.   Climatic variations in the 21.9 GHz zenith emission weighting function.
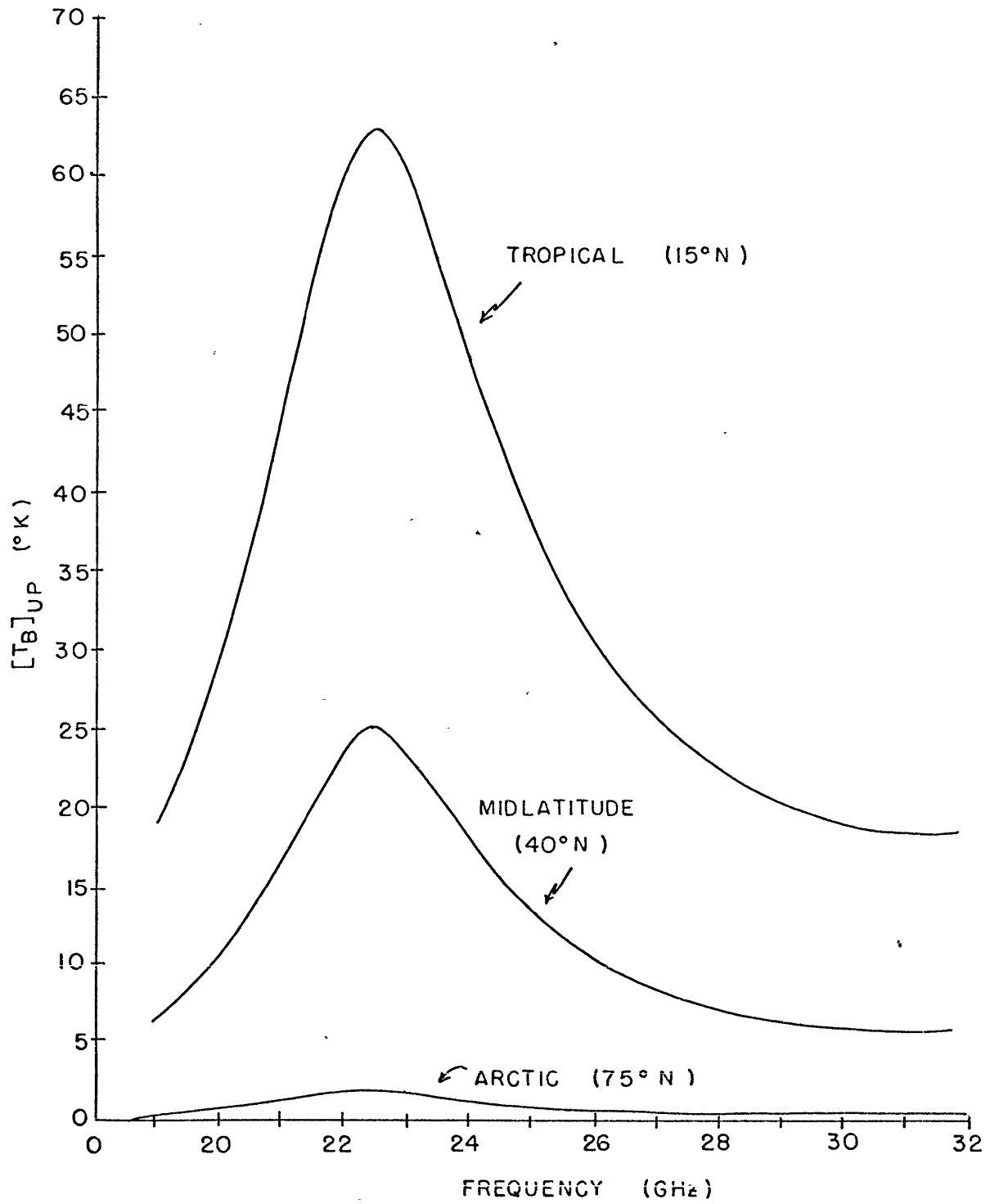
Figure 3-14. Zenith emission spectra for mean conditions in several climatic regions.

maximum. The extreme cold of the tropical tropopause which occurs at roughly 16 km even causes a minor minimum to appear in that climatic regions weighting function.

As a last set of characteristic curves for the brightness temperature spectrum one might measure from the ground, Figure 3-14 is presented. It conveys the amplitude variation one might expect over the world's climates. These curves are means and therefore at each latitude a great deal of variation from the mean curves can be expected.

3.3.3 Observations of the Atmosphere from Space near 22 GHz

If the natural advantages of a satellite borne radiometer are to be exploited, observations from above the atmosphere must be proven to be feasible. For observations from space, one finds that the full equation of radiative transfer must be used. Equation (3.1-28) must be modified to read

$$T_B(H) = T_b(o)\, e^{-\tau_{max}\sec\theta} + \int_0^H T_{AT}\, \gamma_\nu\, e^{-\int_z^H \gamma_\nu \sec\theta\, dz'} \sec\theta\, dz \qquad (3.3\text{-}8)$$

in which the attenuation factor for the atmospheric contribution must be computed from the source level upward to the satellite height H rather than downward as in Equation (3.1-28); and rather than an extra-terrestrial source of radiation attenuated by the full atmosphere, an effective brightness temperature for the earth's surface must be supplied. $T_B(o)$ is not easy to evaluate. It may be expanded, however, as follows:

$$T_B(0) = (1-R) T_g + R \int_0^H T_{RT} \, \gamma_\nu \, e^{-\int_0^z \gamma_\nu \sec\theta \, dz'} \sec\theta \, dz \qquad (3.3-9)$$

where the first term on the r.h.s. of (3.3-9) represents the temperature of the earth T_g diminished by its emissivity equal to (1-R) where R is the power reflection coefficient at the frequency of interest. The second term is the radiation from the atmosphere reflected by the earth's surface.

A weighting function may be derived for satellite observations. Rewrite Equation (3.3-8) using (3.3-9).

$$\begin{aligned}
T_B(H) = &\int_0^H T_{RT} \left(\gamma_{H_2O} + \gamma_{O_2}\right) e^{-\int \gamma_\nu \sec\theta \, dz} \sec\theta \, dz \\
&+ \left\{ R \int_0^H T_{RT} \left(\gamma_{H_2O} + \gamma_{O_2}\right) e^{-\int_0^z \gamma_\nu \sec\theta \, dz'} \sec\theta \, dz \right. \\
&\left. + (1-R) T_g \right\} e^{-\tau_{max} \sec\theta}
\end{aligned} \qquad (3.3-10)$$

Recalling that $\gamma_\nu = \gamma_{H_2O} + \gamma_{O_2}$ separate the oxygen and water vapor terms.

$$T_B(H) = T'_{H_2O} + T'_{O_2} + (1-R) T_g \, e^{-\tau_{max} \sec\theta} \qquad (3.3-11)$$

where

$$\begin{aligned}
T'_{H_2O} = &\int_0^H T_{RT} \, \gamma_{H_2O} \, e^{-\int_z^H \gamma_\nu \sec\theta \, dz'} \sec\theta \, dz \\
&+ R \int_0^H T_{RT} \, \gamma_{H_2O} \, e^{-2\tau_{max} \sec\theta + \int_z^H \gamma_\nu \sec\theta \, dz'} \sec\theta \, dz
\end{aligned} \qquad (3.3-12)$$

and

$$T'_{O_2} = \int_0^H T_{RT}\, \gamma_{O_2}\, e^{-\int_z^H \gamma_\nu \sec\theta\, dz}\, \sec\theta\, dz$$
$$+ R \int_0^H T_{RT}\, \gamma_{O_2}\, e^{-2\tau_{max}\sec\theta + \int_z^H \gamma_\nu \sec\theta\, dz'}\, \sec\theta\, dz \qquad (3.3\text{-}13)$$

Regrouping (3.3-12) and (3.3-13) leads to

$$T'_{H_2O} = \int_0^H T_{RT}\, \gamma_{H_2O} \left[e^{-\int_z^H \gamma_\nu \sec\theta\, dz} + R\, e^{-2\tau_{max}\sec\theta + \int_z^H \gamma_\nu \sec\theta\, dz'} \right] \sec\theta\, dz \qquad (3.3\text{-}14)$$

and

$$T'_{O_2} = \int_0^H T_{RT}\, \gamma_{O_2} \left[e^{-\int_z^H \gamma_\nu \sec\theta\, dz} + R\, e^{-(\tau_{max}\sec\theta - \int_z^H \gamma_\nu \sec\theta\, dz')} \right] \sec\theta\, dz \qquad (3.3\text{-}15)$$

The last term from Equation (3.3-10), representing emission from the earth, can be expanded if $\tau_{max}\sec\theta$ is small as

$$(1-R)\, T_g\, e^{-\tau_{max}\sec\theta} = (1-R)\, T_g \left\{ 1 - \tau_{max}\sec\theta + \cdots \right\} \qquad (3.3\text{-}16)$$

For total attenuation of 1.5 db, the error introduced into the bracketed term of (3.3-14) by neglecting the terms higher than first order amount to about 9.4%, i.e., the value of the bracketed term would be low by 9.4%. For total attenuation of 1 db, the error drops to about 3.5%, and for 0.5 db the error is 0.8%. The effect on $T_B(H)$, if one uses the approx-

imation, is to flatten the peak of the brightness temperature curve.

$\hat{\tau}_{max}$ in (3.3-16) may be separated into the water vapor and oxygen components

$$\hat{\tau}_{max} = \left(\hat{\tau}_{max}\right)_{H_2O} + \left(\hat{\tau}_{max}\right)_{O_2} \qquad (3.3\text{-}17)$$

and the new terms resulting may be redistributed with the water vapor and oxygen components of (3.3-11). The oxygen component can be written in final form as

$$T_{O_2} = T'_{O_2} - (1-R)\, T_g \int_0^H \gamma_{O_2} \sec\theta \; dz$$

$$= \int_0^H T_{RT} \left\{ e^{-\int_z^H \gamma_\nu \sec\theta \, dz} + R\, e^{-\left(2\hat{\tau}_{max}\sec\theta - \int_z^H \gamma_\nu \sec\theta dz\right)} \right.$$

$$\left. - (1-R)\, T_g \right\} \gamma_{O_2} \sec\theta \; dz \qquad (3.3\text{-}18)$$

The water vapor component in final form is

$$T_{H_2O} = T'_{H_2O} - (1-R)\, T_g \int_0^H \gamma_{H_2O} \sec\theta \; dz$$

$$= \int_0^H T_{RT} \left\{ e^{-\int_z^H \gamma_\nu \sec\theta \, dz} + R\, e^{-\left(2\hat{\tau}_{max}\sec\theta - \int_z^H \gamma_\nu \sec\theta dz\right)} \right.$$

$$\left. - (1-R)\, T_g \right\} \gamma_{H_2O} \sec\theta \; dz \qquad (3.3\text{-}19)$$

The brightness temperature at the satellite is

$$T_B(H) = T_{H_2O} + T_{O_2} + (1-R)\, T_g + \epsilon\left(\hat{\tau}_{max}\right) \qquad (3.3\text{-}20)$$

where $\epsilon\left(\hat{\tau}_{max}\right)$ is a correction for the approximation made in Equation

(3.3-16). It should be pointed out that T_{H_2O} and T_{O_2} are

not independent of γ_{O_2} and γ_{H_2O}, respectively, since both contain

$\gamma_\gamma = \gamma_{H_2O} + \gamma_{O_2}$ in exponentials.

A weighting function for atmospheric water vapor may now be

easily extracted from Equation (3.3-17). It is

$$\left[W_T\right]_{DOWN} = T_{AT} \left\{ e^{-\int_z^H \gamma_y \sec\theta\, dz} + R\, e^{-\left(\tau_{max}\sec\theta - \int_z^H \gamma_y \sec\theta\, dz\right)} \right.$$

$$\left. -(1-R)\, T_g \right\} \frac{\gamma_{H_2O}}{\rho} \sec\theta \qquad (3.3-21)$$

evaluated at some height z in the atmosphere. The derivation of the

weighting function above is due to Staelin[40]. Equation (3.3-20) can

be written using (3.3-21) as

$$T_B(H) = \int_0^H \left[W_T\right]_{DOWN} \rho(z)\, dz + T_\alpha + (1-R)\, T_g + \epsilon(\tau_{max}) \qquad (3.3-22)$$

More must be said about the quantity R, the power reflection coeffi-

cient of the earth. In general, this is a very complicated function.

For a surface which is smooth within approximately one eighth of a wave-

length, and which is electrically homogeneous, it can be computed from

Fresnel's equations. The results depend upon the complex dielectric

constant for the material, the angle from which the surface is viewed,

and the polarization of the antenna. However, buried in the complex

dielectric constant are more dependencies: frequency, temperature,

for sea water its salinity, and for solid materials the nature of the

surface, i.e., how compacted is the material, what sizes are the grains

making up the surface, etc.

Finally, the real surface of the earth presents no smooth surfaces or large areas composed of electrically homogeneous materials. The closest approximation to the latter is sea water which does change its salinity from one region to another but only slightly. And, even though the sea surface is seldom if ever smooth, the emissivity of sea water offers the most hope at the moment of yielding to an analytical analysis. For more on the microwave properties of sea water, see Appendix A-III.

For want of better information, we have assumed a reflectivity value and computed weighting functions according to Equation (3.3-21). The same four diverse atmospheres used to examine the other weighting functions have been used in Figure 3-15. The value of R for all weighting functions has been taken as 0.6, a reasonable value for sea water near 1 cm. The ground (or water) temperature T_g has been taken in each case as the ground level atmospheric temperature. It must be borne in mind that these weighting functions are quite dependent upon R, T_g, and ϵ near resonance, and therefore those functions depicted in Figure 3-15 should be construed as only illustrative of the most general properties of the downward brightness temperature weighting functions.

The shapes of the weighting functions for the water vapor part only of the emission received at a satellite conform closely to the upward looking weighting functions, as might be expected. The differences, in fact, between the upward and downward brightness temperature weighting functions are not so much as those caused by climatic variations
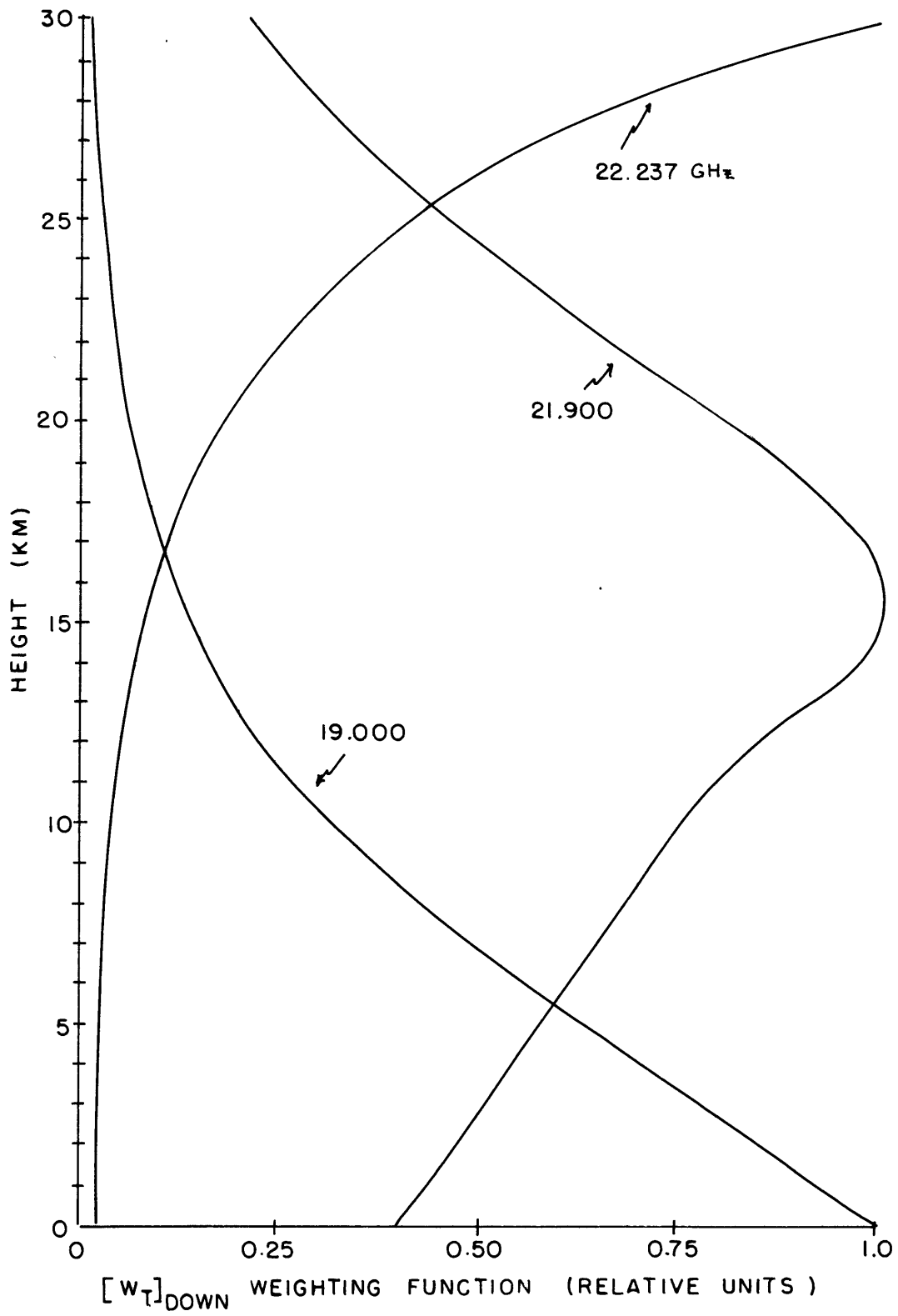
Figure 3-15.   Normalized atmospheric water vapor emission
weighting functions for observations from space.

within either group. The stability of the 19.0 GHz weighting function shown in Figure 3-16 is somewhat greater than its upward looking counterpart. The 21.0 GHz functions plotted for various climates in Figure 3-17 are quite divergent above about 8 km but they have the redeeming feature that below 8 km the midlatitude, subarctic, and arctic curves are closely similar. Only the tropical curve deviates substantially from the others. However, most of the discrepancy is caused by ignoring ϵ since the attenuation for this atmosphere is about 1.1 db at 21.9 GHz.

The height at which the maximum sensitivity occurs at a given frequency is plotted in Figure 3-18. The separation of the curves is slightly greater than the upward looking curves but slightly less than the similar opacity curves.

The amplitude of T_{H_2O} for the Tropical, Midlatitude, and Arctic atmospheres is shown in Figure 3-19. The amplitudes are similar to those computed for ground emission measurements.

Finally, the total brightness temperature which might be seen by a satellite in midlatitudes is depicted in Figure 3-20. The bulk of the radiation originates from the ground emission term of Equation (3.3-20), a small contribution increasing with frequency comes from the oxygen term, and the remaining from the water vapor term. The effect of clouds would tilt the high frequency side of the curve upward an amount depending mostly upon the liquid water content of the clouds in the beam. The curves in Figure 3-19 and Figure 3-20 have been calculated
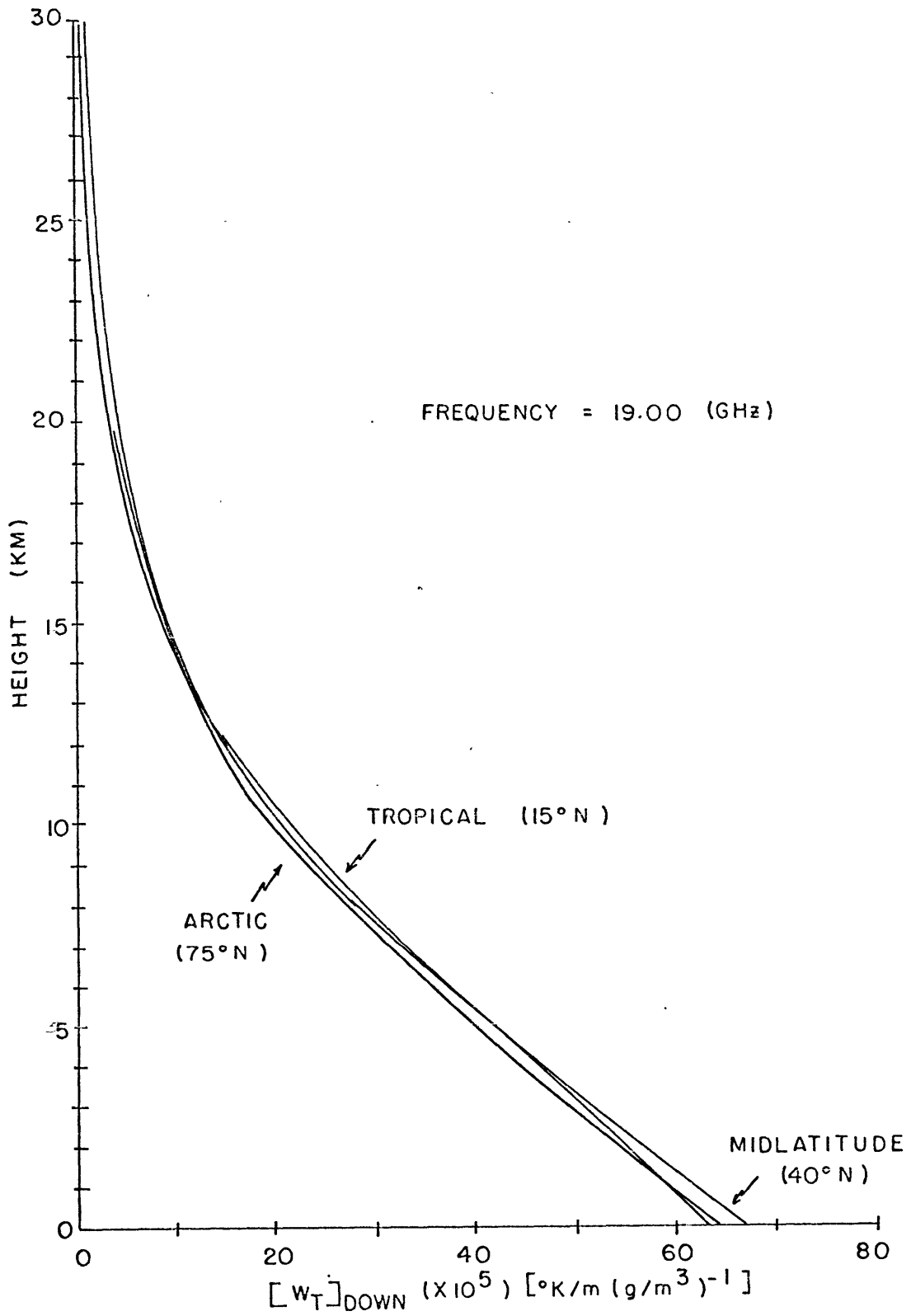
Figure 3-16. Climatic variations in the 19 GHz emission weighting function for observations from space.
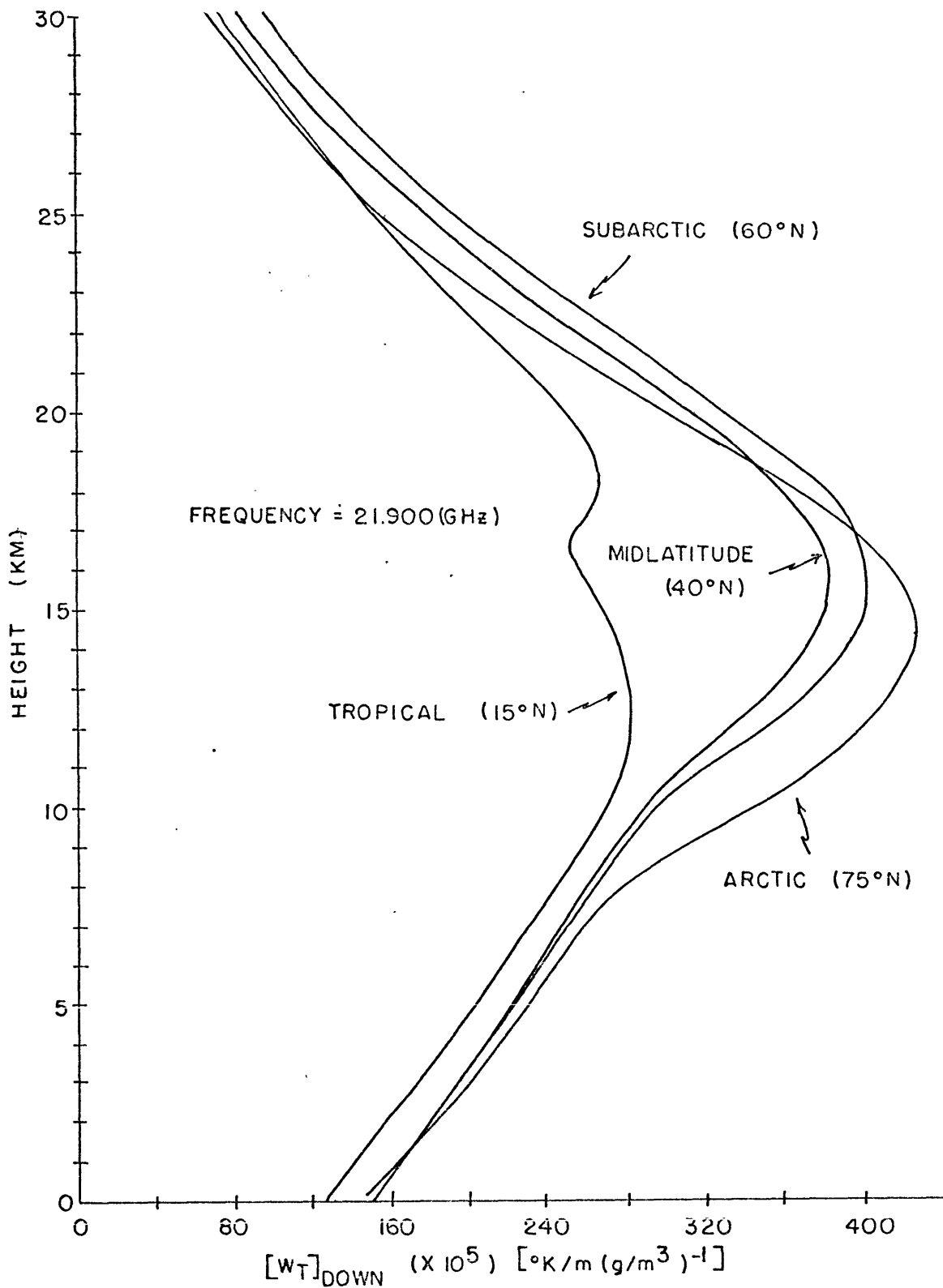
Figure 3-17. Climatic variations in the 21.9 GHz emission weighting function for observations from space.
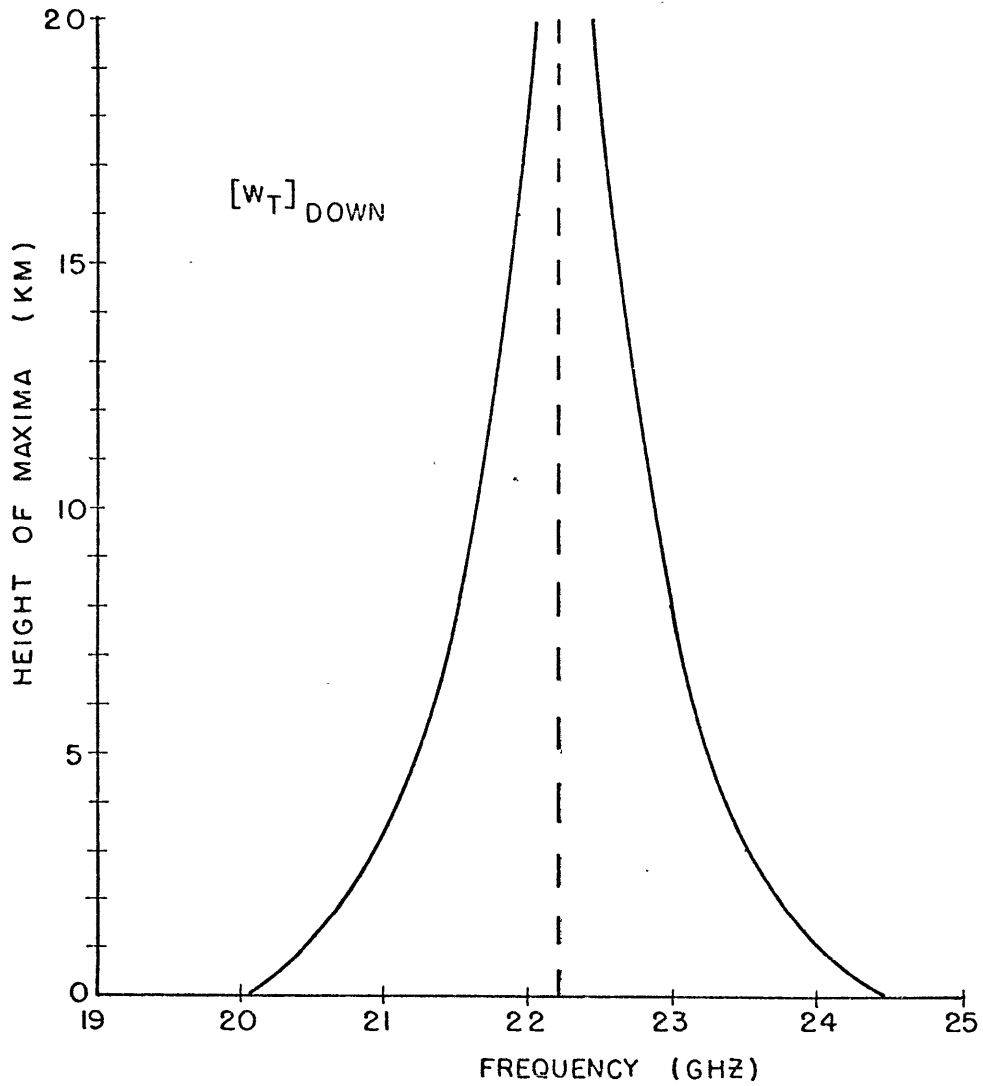
Figure 3-18. The frequency dependence of the height at which
maxima occur for nadir emission weighting functions.
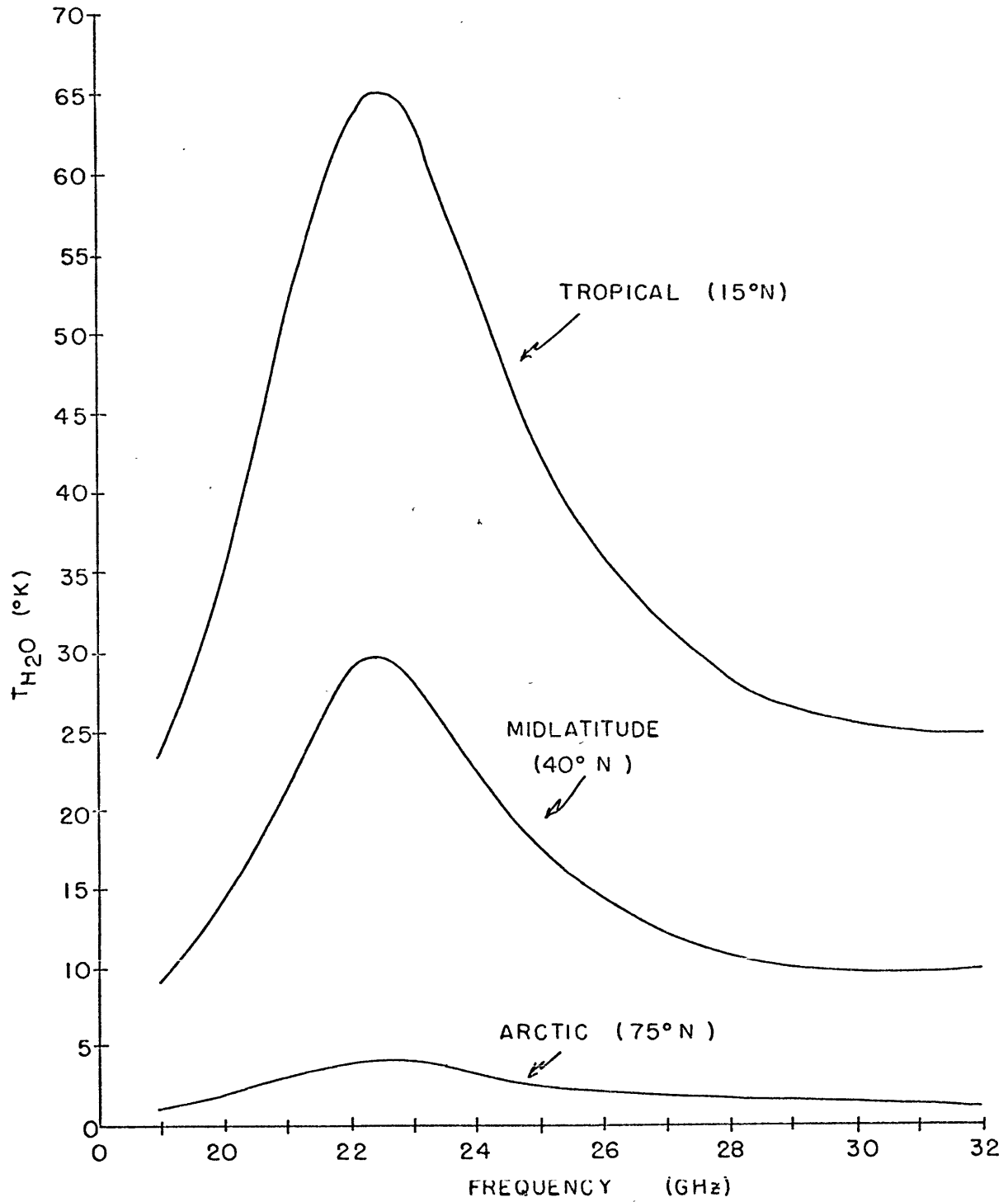
Figure 3-19. Atmospheric emission spectra for observations from space for several climatic regions.
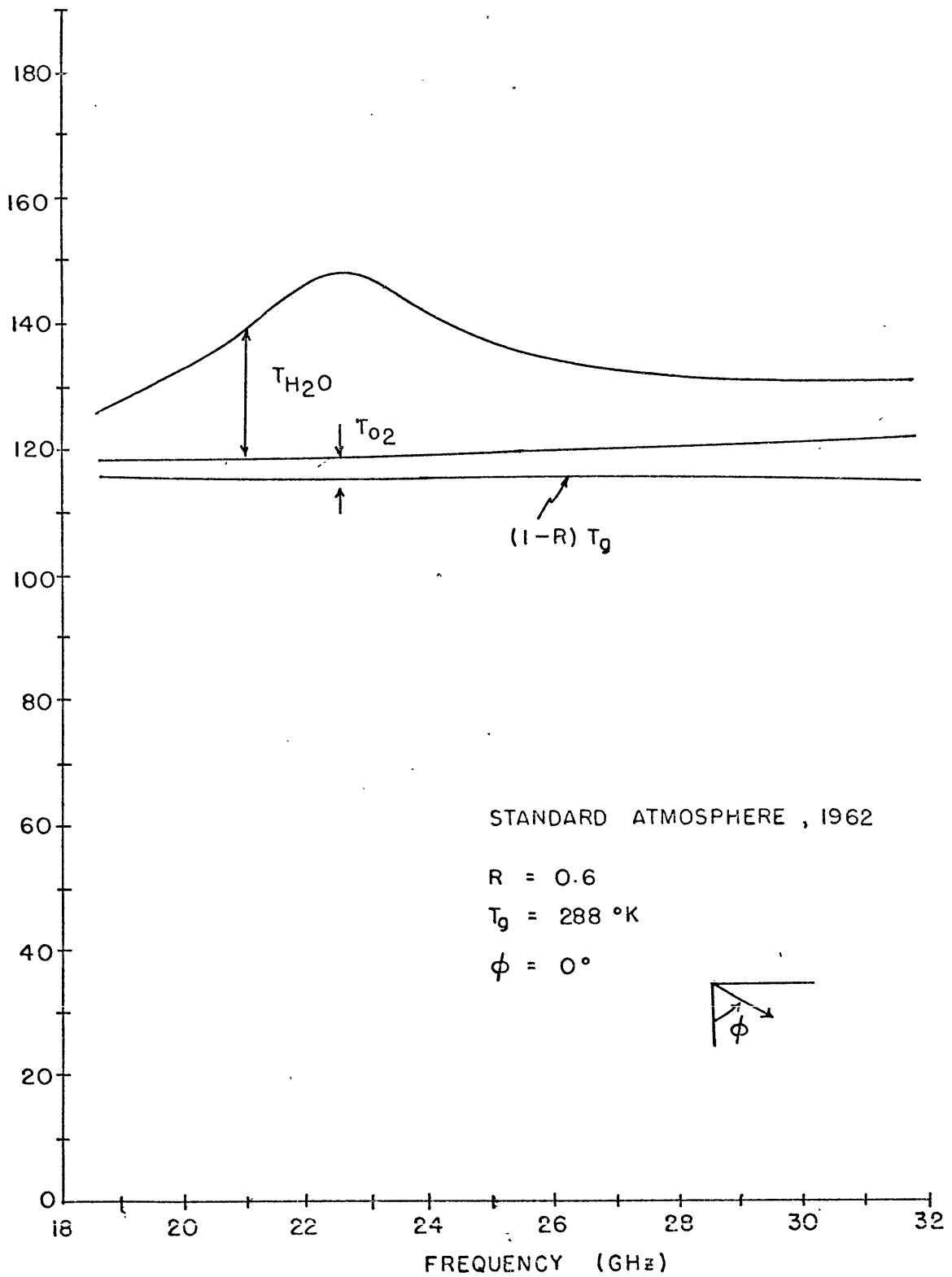
Figure 3-20. The contributions to the total emission seen from space by water vapor, oxygen, and the surface of the earth.

using Equation (3.3-8) and therefore have no approximations in them.

3.4 The 183.3 GHz Resonance Observed from Ground Level from

Balloon and from Space

The water vapor spectral line at 22.2 GHz is a relatively weak line, seldom if ever reaching a total atmospheric attenuation of 1.5 db at resonance. In contrast, the 183.3 GHz resonance is a very strong spectral line. How strong may be deduced from Figure 3-21. In the moist tropical regions, the peak one-way attenuation through the atmosphere reaches over 200 db. In dry arctic regions the peak attenuation falls below 20 db, still, however, optically thick. In midlatitudes, at frequencies as low as 150 GHz, the zenith attenuation falls to about 2 db a value which remains greater than the attenuation expected anywhere over the earth for the 22.2 GHz line.

For surface measurements, such a strong line effectively screens off all radiation originating very far from the receiving antenna. The attenuation factor in the integral on the r.h.s. of Equation (3.1-28) is only small enough to allow radiation to reach the antenna from distances very close to the receiver. The first term of the same equation, of course, is totally lost. For surface measurements, one would expect a uniform temperature over a wide band of frequencies centered on resonance. This is exactly what occurs.

The cumulative percentage of the radiation which makes up the signal measured by a ground based radiometer is plotted in Figure 3-22
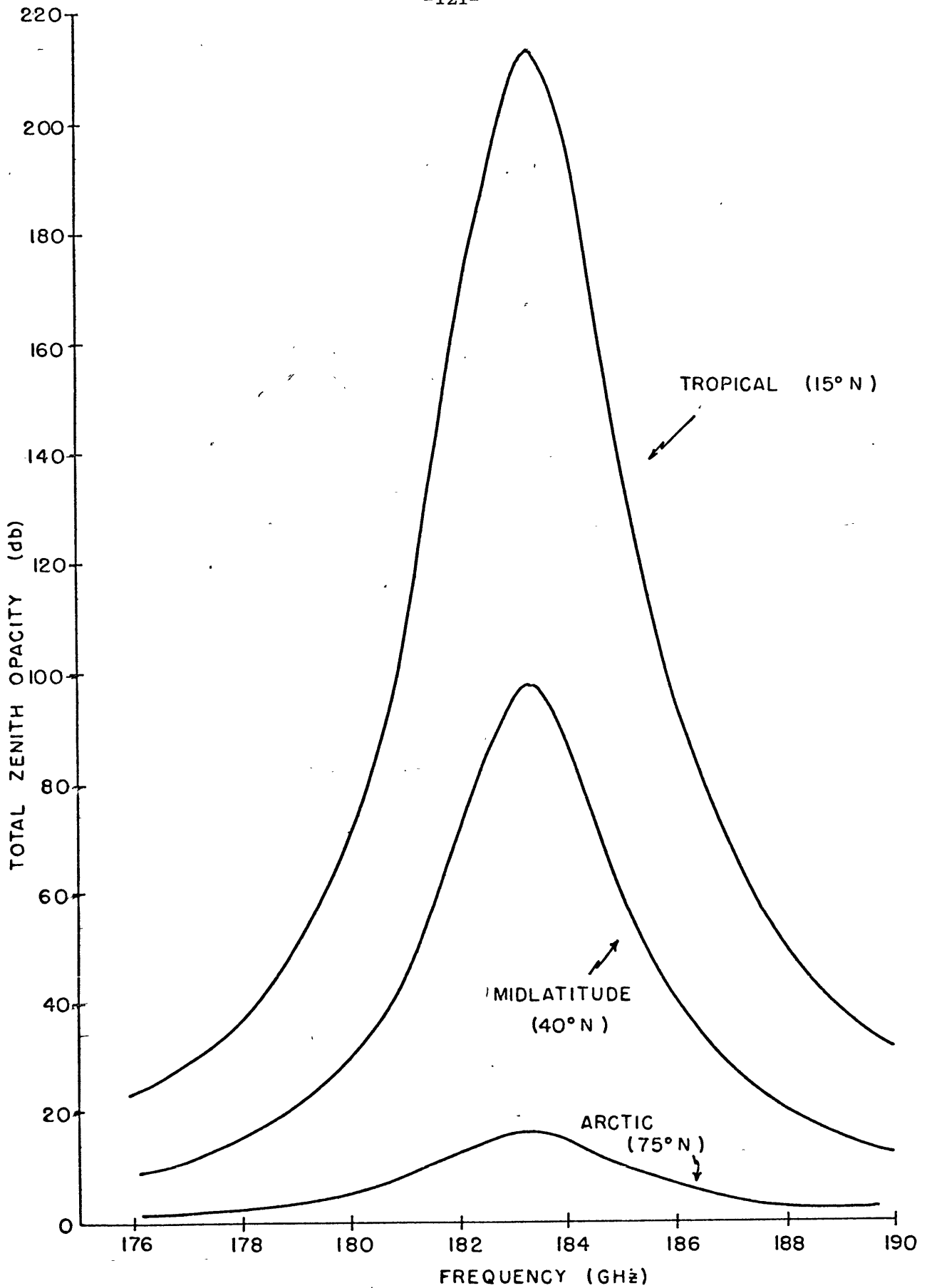
Figure 3-21. The total zenith opacity for a spectral region near
183.3 GHz for several mean climatic conditions.
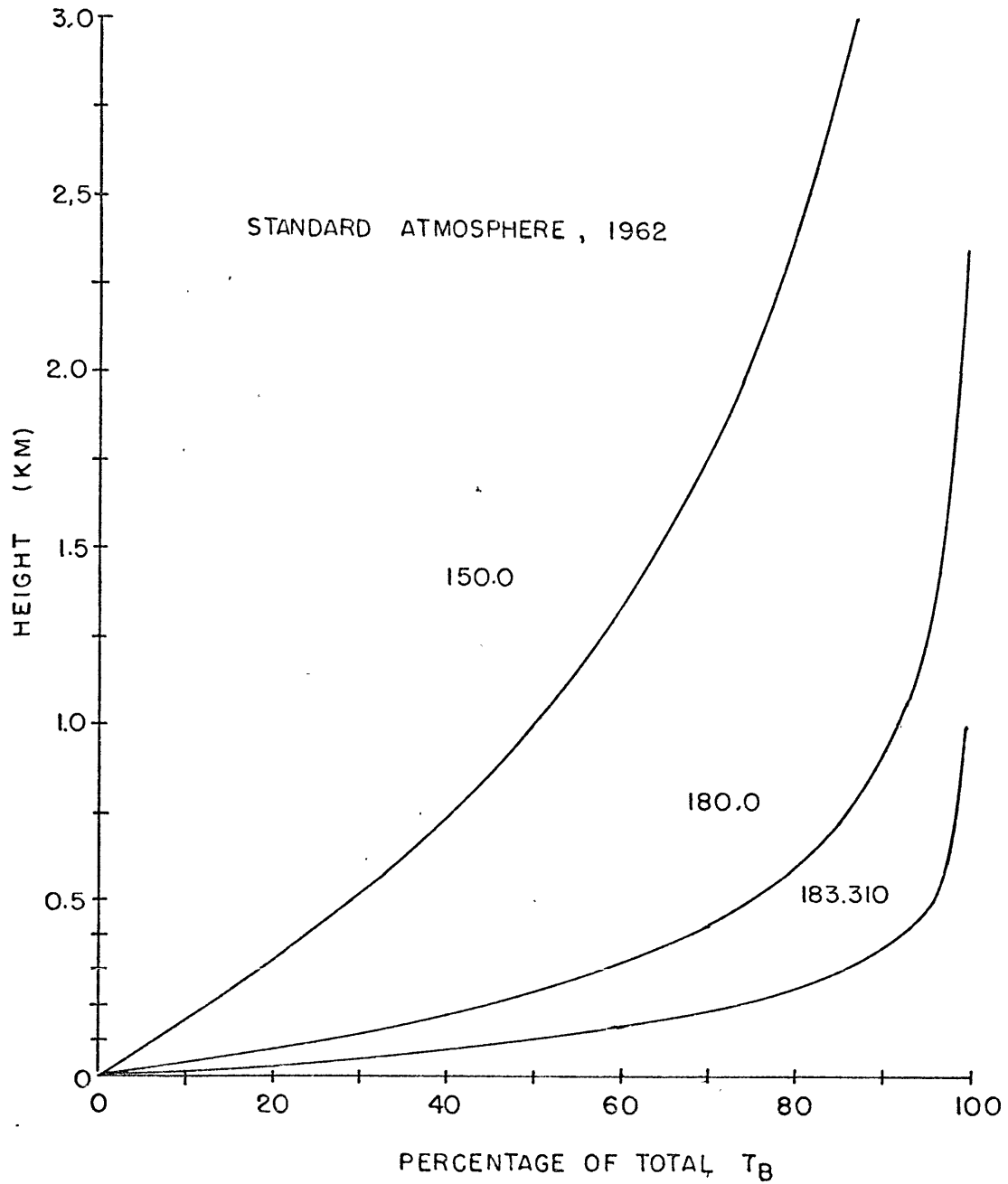
Figure 3-22. The percentage of the total energy received from layers of increasing thickness at several frequencies.

against height for a midlatitude Standard Atmosphere. Three frequencies are depicted: resonance, (183.310 GHz), a frequency where the attenuation is reduced approximately two-thirds (180 GHz), and another frequency far below resonance (150 GHz). The height below which 90% of the radiation originates for each of the frequencies is 480 m, 875 m and 3500 m respectively.

In Figure 3-23, the variation of this cumulative percentage versus height for several climates is depicted for one frequency, in this case resonance. The 90% heights vary from 125 m in the Tropical atmosphere to 3250 m in the Arctic atmosphere.

The curves for satellite observations using the 183 GHz line show that the meteorological information to be gained is confined to the stratosphere. Because Chapter 5 is devoted to the stratosphere, we will defer discussions of relevant curves for 183 GHz observations from space to that chapter.
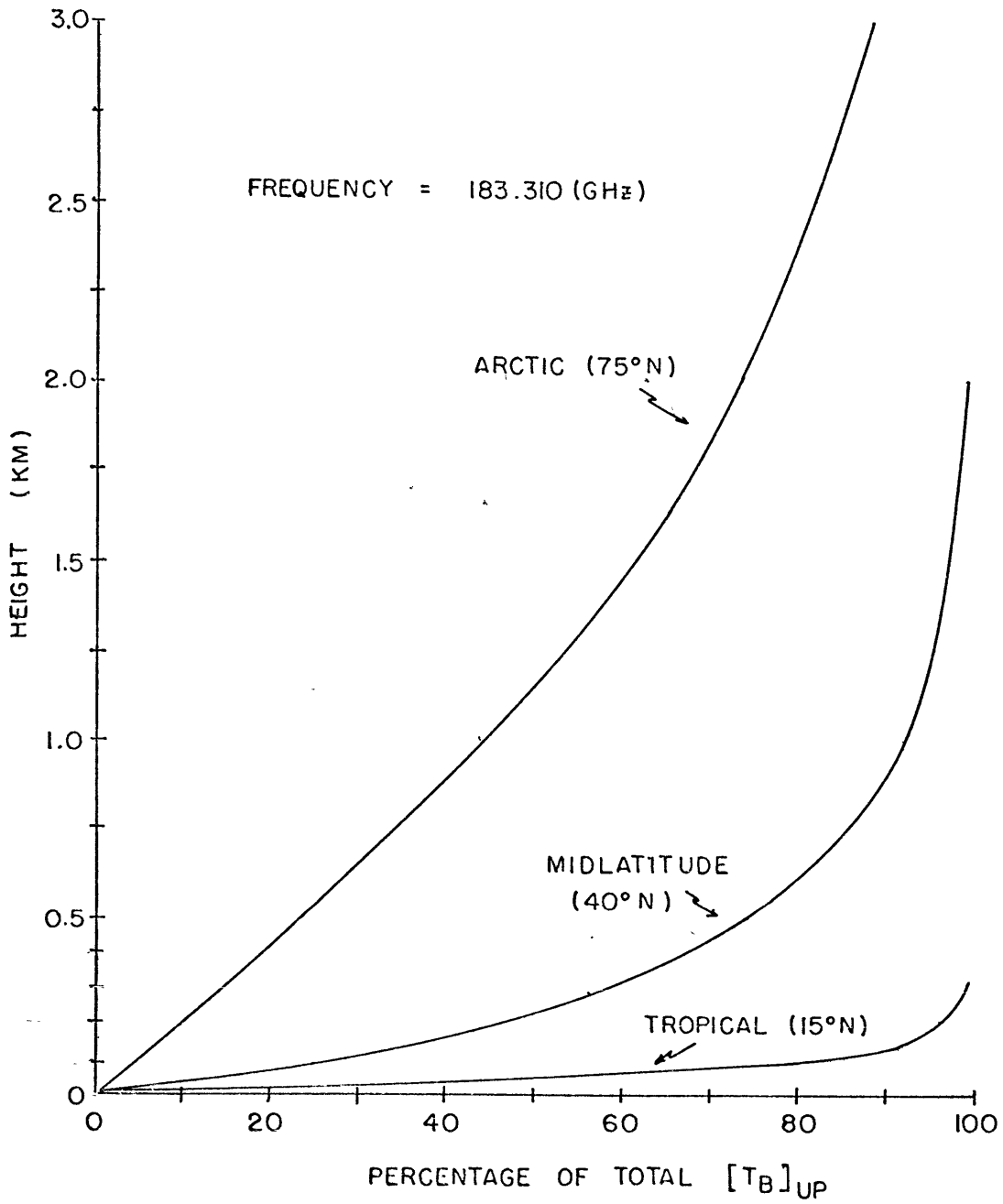
Figure 3-23. The percentage of the total energy received from
layers of increasing thickness at 183.31 GHz
in several mean climates.

Chapter 4

OBSERVED AND COMPUTED ATMOSPHERIC ATTENUATION OF SOLAR RADIATION

During the summer of 1965 and the winter of 1966, an extended
program was conducted to obtain high quality atmospheric opacity
measurements near the 22 GHz rotational resonance of water vapor.
The measurements were taken at the Lincoln Laboratory of the Massachu-
setts Institute of Technology. Radiosondes were launched nearby to
monitor atmospheric conditions during the periods of radiometer obser-
vations. The data which they returned were used as a basis to compute
the expected absorption for that day. These computed absorption spec-
tra were finally compared to the actual observations.

The purpose of Chapter 4 is to systematically review the obser-
vations and computations in the following format: (1) to outline the
experimental procedure and data reduction process which were used to
obtain the atmospheric opacities; (2) to compare the results with the
absorption computed from radiosonde data; and (3), to discuss the prob-
lems inherent in using radiosondes as a standard of comparison for
radiometer measurements, relying on the previously obtained data for
examples.

4.1 Measurement of Atmospheric Attenuation of Solar Radiation

near 1 cm

A microwave radiometer measures energy over a given bandwidth

centered at some frequency in the microwave range of frequencies. The antenna temperature is the quantity actually recorded and is related to the brightness temperature distribution surrounding the antenna as follows:

$$T_A(\theta', \phi') = \frac{1}{4\pi} \int_{4\pi} G(\theta-\theta', \phi-\phi') \, T_B(\theta, \phi) \, d\Omega \qquad (4.1-1)$$

Here, $T_A(\theta', \phi')$ is the temperature which a black body would have which would produce the same average intensity over the spectral interval being monitored, $G(\theta-\theta', \phi-\phi')$ is the power gain function of the antenna whose axis is pointed at an elevation angle of θ' and an azimuth angle of ϕ' measured with respect to an arbitrarily chosen reference system, and $T_B(\theta, \phi)$ is the brightness temperature distribution which the antenna is monitoring. The integral is taken over all solid angles. T_A may be more clearly related to T_B in the following manner: using the power gain function as a weighting factor an average brightness temperature may be computed as

$$\overline{T_B} = \frac{\frac{1}{4\pi} \int_{4\pi} G(\theta-\theta', \phi-\phi') \, T_B(\theta, \phi) \, d\Omega}{\frac{1}{4\pi} \int_{4\pi} G(\theta-\theta', \phi-\phi') \, d\Omega} \qquad (4.1-2)$$

However,

$$\frac{1}{4\pi} \int_{4\pi} G(\theta-\theta', \phi'-\phi') \, d\Omega = \eta_R \qquad (4.1-3)$$

where η_R is the radiation efficiency of the antenna at the wave-

length and for the conditions of the measurements. It therefore follows that

$$T_A = \eta_R \overline{T_B} \qquad (4.1-4)$$

For antennas of highly precise surface contours and large aperture, the power gain function is distributed such that the brightness temperature in a region only a small angular distance around the antenna axis contributes significantly (typically 60%) to $\overline{T_B}$.

The equation governing the brightness temperature at a surface based antenna pointing up into a planar, horizontally stratified atmosphere was shown in Chapter 3 to be

$$T_B (\nu) = T_E \, e^{-\int_0^H \gamma (\nu, z)\sec\theta \, dz} + \int_0^H \gamma(\nu,z) T_{Ar}(z) \, e^{-\int_0^z \gamma(\nu, z)\sec\theta \, dz} \sec\theta \, dz \qquad (4.1-5)$$

in which T_E is the brightness temperature of any source outside the atmosphere, but filling the antenna beam.

The second term of Equation (4.1-5) was effectively eliminated by a carefully chosen observational procedure:

1. Observations of the sun were made. T_E therefore is T_S the brightness temperature of the sun at the frequency of observation.

2. An antenna was used whose main beam was considerably smaller than the angular size of the sun's disk for all observed frequencies.

3. Drift scans were taken of the solar disk by placing the antenna axis ahead of the apparent path of the sun across the sky and

recording the brightness temperature of the sun plus atmosphere,
then after the sun had moved through the beam recording the atmo-
spheric contribution alone.

4. Finally, the atmospheric contribution was subtracted from the com-
bined total of sun plus atmosphere.

This procedure leaves one with

$$T_B(\nu) = T_s \, e^{-\int_o^\infty \gamma(\nu,z) \sec\Theta \, dz} = T_s \, e^{-\tau_{max} \sec\Theta} \qquad (4.1\text{-}6)$$

The contribution of the atmosphere in Equation (4.1-6) is now confined
to the integral exponent of e . However, the direct use of Equation
(4.1-6) is associated with many practical difficulties.

Even though T_s may be constant in time, the exact value may be
imperfectly known. Further, the absolute measurement of T_B introduces
additional difficulties to the experiment: the absolute gain of the
antenna must be known and careful calibrations must be performed.
Since the absolute value of neither T_s nor T_B contains information
about the atmosphere, the necessity to measure them absolutely is
eliminated by manipulating Equation (4.1-6). First restate (4.1-6) as

$$C_1 \, T_B'(\nu) = C_2 \, T_s' \, e^{-\tau_{max} \sec\Theta} \qquad (4.1\text{-}7)$$

where the real brightness temperature being measured is $T_B = C_1 T_B'$
and the actual solar brightness temperature is $T_s = C_2 T_s'$; C_1 and

C_2 are constants. If (4.1-7) is rearranged and the natural logarithm of both sides is taken, one has

$$\ln\left\{\frac{T_B'}{T_s'}\right\} = \ln\frac{C_2}{C_1} - \tau_{max}(\nu)\sec\theta \qquad (4.1\text{-}8)$$

Finally, by making several drift scans at different values of sec θ , one may compute τ_{max} from the following finite difference equation:

$$\tau_{max}(\nu) = -\frac{\Delta\ln\left\{\frac{T_B'(\nu)}{T_s'}\right\}}{\Delta(\sec\theta)} \qquad (4.1\text{-}9)$$

It is clear from Equation (4.1-9) that in order to measure $\tau_{max}(\nu)$ it is only necessary to measure quantities which are proportional to T_B and T_s or to their ratio as a function of zenith angle. This simplifies the experimental procedure and divorces the results from any absolutely calibrated measurements. The method was first used by Dicke, Beringer, Kyhl and Vane[32] in 1946.

4.1.1 The Experimental Equipment

The actual equipment which was used to measure the T_B' of Equation (4.1-11) consisted of a five channel radiometer whose block diagram is shown in Figure 4-1.[83] The signal from the antenna was fed into a five section filter where the frequencies of interest were tapped off and sent to five identical Dicke microwave radiometers[32]. Provisions were made at the front end of the filters for a source of noise which could be used for tuning the radiometers. Each filter led
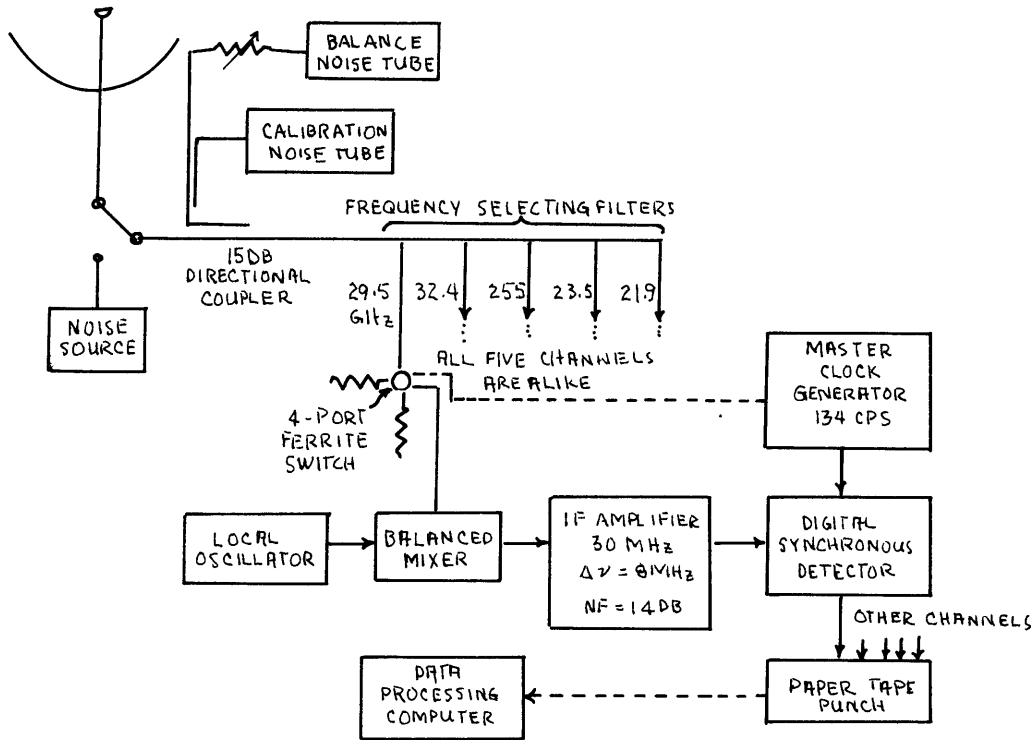
Figure 4-1. Block diagram of the five-channel radiometer
used in the observations.

to a ferrite switch driven by a 134 cycle square wave generator. The output part from the switch alternately observed a matched load at ambient temperature and the signal from the filter section. From the ferrite switch, the alternating signal was fed into a balanced crystal mixer into which a reflex klystron signal was also introduced. The output from the ferrite switch was next amplified by an intermediate frequency amplifier whose 8 MHz passband was centered at 30 MHz. Because of the mixing, the output from the IF amplifier consister of two 8 MHz bands originally centered 30 MHz above and below the local oscillator frequency.

From the IF amplifier, the signal was introduced to the synchronous detector driven in phase with the ferrite switch. The synchronous detector measured, in effect, the difference between the signal from the filter section and the matched load of the ferrite switch. This synchronous detection feature is the heart of the Dicke radiometer and allows slow gain fluctuations in the amplifiers preceding the synchronous detector to be greatly reduced in importance to the measurements.

From the synchronous detector, the information was encoded digitally and punched on paper tape for later analysis.

The antenna used for the solar observations was a 28 foot spun cast model designed for radiometer and radar measurements at millimeter wavelengths. It was mounted atop the Lincoln Laboratory in Lexington, Massachusetts. Remote controlled servos controlled the antenna pointing at accuracies far above the needs of the solar extinction observa-

tions. A picture of the antenna and mount is presented in Figure 4-2.

4.1.2 The Experimental Procedure.

The daily routine for taking observations was the following:

1. Several hours before measurements were to be taken the radiometers and all supporting equipment were turned on and allowed to warm up.

2. Perhaps an hour before observations were to begin the radiometer was configured to look at the front end noise source instead of the antenna and each radiometer was tuned to give the best possible noise figures. (Noice figures ranged from a low of 8.0 to a high of 15.0 with the mean for the summer observations near 12.0 and for the winter observations near 10.0).

3. The radiometer front end was reconnected to the antenna and while the sun was tracked, the gain of the final amplifiers for each radiometer was adjusted for optimum signal strength with respect to the digital analyser. The radiometer was then considered ready for observations.

4. Observations consisted of repeated 10 minute cycles. The antenna was pointed at a position in the sky where the sun would be at some convenient time. Two and one half minutes before the center of the sun reached the aimed for position, the radiometer was set to recording. Approximately every 2 seconds the output from the synchronous detector connected to each radiometer was sampled and together with a
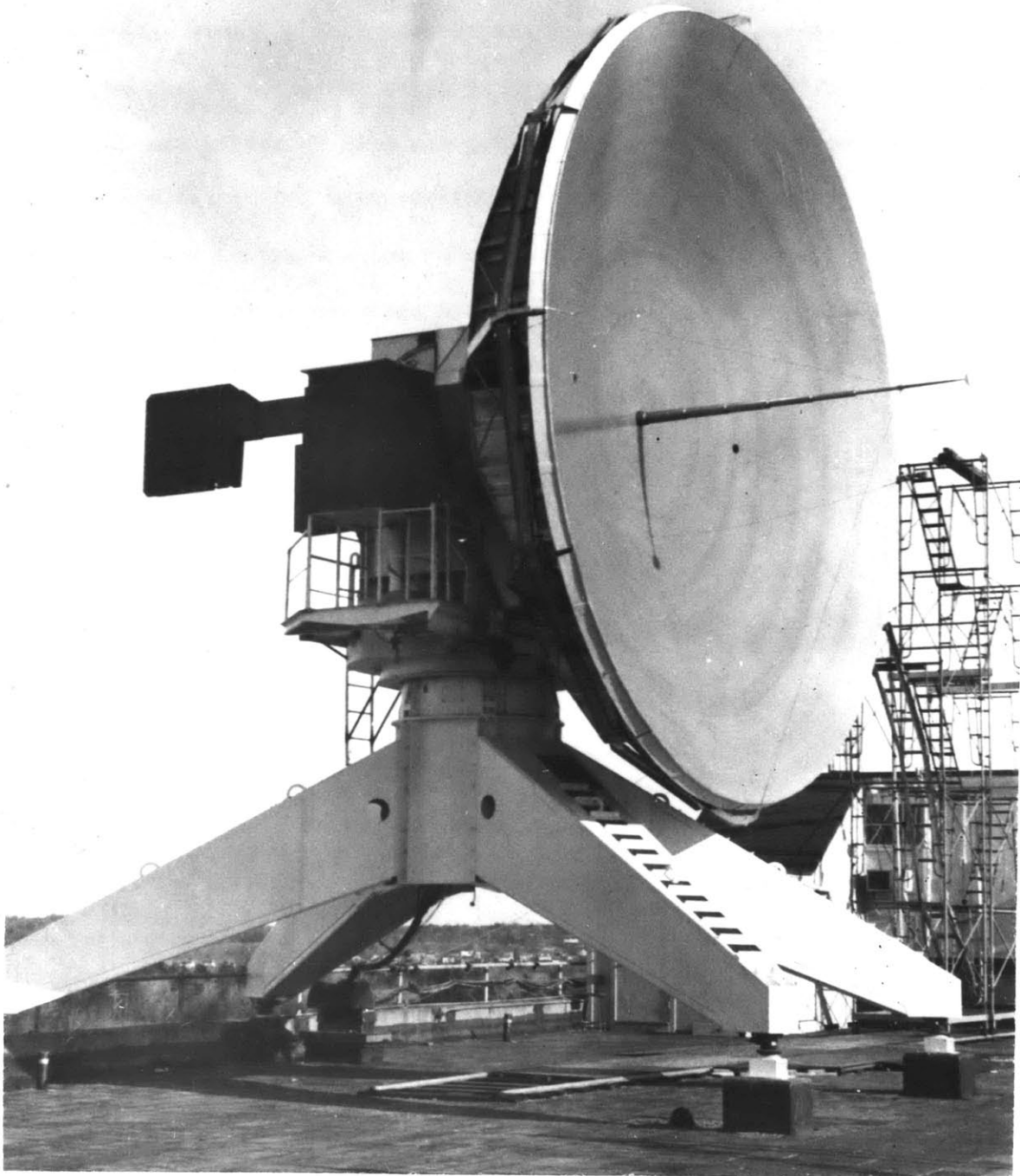
Figure 4-2. The 28-foot **spu**n cast antenna mounted on top of the Lincoln Laboratory in Bedford, Mass.

code number indicating the source of the radiation was punched as output on paper tape. For five total minutes the sun was allowed to drift across the antenna position. By the end of five minutes, the sun was far enough from the main beam of the antenna that a baseline measurement of atmospheric radiation could be taken. This was done for one minute. A final one minute of data was punched with the calibration noise tube on. This introduced an unvarying amount of energy into the radiometers and was used to measure the relative gain in each channel. The 3 minutes remaining in the observation cycle were taken up by repositioning the antenna for a new scan which began exactly 10 minutes after the first. In short, the cycle was:

sunscan	–	5 minutes
baseline (atmosphere)	–	1 minute
calibration	–	1 minute
reposition	–	3 minutes

repeat.

5. Antenna elevation and azimuth angles for each scan along with all pertinent information concerning the operation of the radiometer were recorded.

6. While the sunscans were being taken, observations were made visually on the general weather conditions, and the conditions which the antenna saw (via a bore sighted TV camera). Both were entered in the data log book. Further, the hourly weather observations taken at

Hanscom Field, a U.S. Air Force base approximately one and one half miles away, were also recorded.

A typical summer day's date consisted of about 20 scans. The maximum number of scans for any day was 36. In winter, the average number was closer to 10 scans per experiment.

4.1.3 The Reduction of the Data

Considerable attention was given to the reduction of the data in order to extract from it the most accurate values of atmospheric attenuation that one could obtain by the equipment and the technique described above.

Because the system which was used for the solar observations was also being used and had been used for extensive radio astronomical observations, a great deal of data reduction experience had already been gained. The punched paper tape format had been devised so that it would be accepted without alteration by a small MIT computer (PDP-1). Programs (primarily a special assembler named FAITH from which data handling programs could be easily written) existed at the end of the summer of 1965 which would do the following:

1. Read into the machine one complete 10 minute sunscan cycle.

2. Display each 2 second average data point as a point on a CRT scope so that one could examine the amplitude of the antenna temperature from one channel as a smooth function of time for a complete sunscan.

3. Allow doubtful data to be removed by erasing points on the

CRT display with a light pen connected to the computer.

4. Process the cleaned up data automatically for means of the amplitudes from (a.) the center of the sun; (b.) the baseline; and (c.) the calibration signal. The program also computed the variances of the three means.

For the Winter 1966 data, the data processing programs were improved and made considerably more efficient by the following innovations:

1. A preprocessor to FAITH called STARGAZER was written which read all of one days data into drum storage of the PDP-1. The data could then be stepped by the analyst at the CRT scope and completely cleaned up in one operation.

2. All of the cleaned up data could then be sequentially and automatically processed for the means and variances. This contrasted with the one-scan-at-a-time method of the original reduction program.

Average processing time, when all computer components and programs were finally working as desired, was cut from about 45 to 50 minutes per average day's experiment for the summer data to roughly 15 minutes for the winter data. In all, to process the data this far, well over 100 hours of PDP-1 computer time were used.

The results of the processing up to this point gave us the ability to compute the argument of the logarithm term of Equation (4.1-9). The PDP-1 could have been used for this processing but it was desired to do other more sophisticated filtering and for that it was decided

to use the M.I.T. Computation Center IBM 7094.

In order to input the radiometer data to the bigger machine, the PDP-1 tape output was converted to cards. Unfortunately, the coding of the PDP-1 tapes was not the same as standard coding used by IBM. However, the IBM 047 tape to card converter was able to be programmed in a manner which made the proper conversion.

Further information on the quality of each sunscan was encoded with the amplitudes and variances on the data cards. This information was derived from the experiment log book and from some subjective appraisal of the quality of scans. This way data biased by faulty radiometers or other unusual occurrences were easily identified and downgraded in importance or eliminated.

The data was next processed in the 7094 for the slope and intercept of the straight lines formed by plotting the numerator of the right hand side of Equation (4.1-9) against its denominator. The weight each data point carried depended partially on the inverse of its variances as determined from the PDP-1 reduction. All data judged to be below a subjectively determined level of quality was eliminated.

A further condition on the use of data was derived from the breakdown of Equation (4.1-9) because of the sphericity of the earth. A numerical investigation was conducted to see at what elevation angles the planar approximation of the atmosphere was no longer valid. It was determined that if sunscans whose values of secant Θ were no more than 9,

errors of less than 2% would be introduced by the sphericity of the earth. Therefore data was used whose zenith angles were less than $82°49'$ (elevation angles greater than $7°11'$). At these angles, refraction was negligible.

(For a complete mathematical resume of the analysis of error introduced by the radiometer noise, see Appendix A-IV. For a method of estimating and if necessary correcting for atmospheric curvature and atmospheric refraction, see Appendix A-V).

4.2 Computed Atmospheric Absorption Derived from Radiosondes

Thirty two days of radiosonde information were gathered along with solar extinction data. The original plan intended for these radiosonde runs to monitor conditions which the antenna beam was viewing and use the computed spectra therefrom as a standard of comparison. This, of course, assumed that the distance separating the sondes and antenna beams and the time differences between sonde launches and radiometer experiments would introduce errors which would not invalidate the correlations expected. From the comparison of computed to observed spectra these assumptions were proven to be poor in many cases. The conditions during which they break down have been analyzed in a number of cases and they will be documented further on.

Putting aside the question of the accuracy or the relevancy of the radiosonde data to the radiometer data collected, the method of converting the raw radiosonde data to attenuation spectra roughly

followed the following steps:

1. Radiosonde data were received in both raw flight tape form and finished adiabatic chart form. The former data were taken at the Massachusetts Institute of Technology (MIT) some 19 km from the radiometer site, the latter from the Air Force Cambridge Research Laboratories (AFCRL) launch site perhaps 300 meters from the radiometer site. Raw data were reduced to tables of temperature, pressure, and relative humidity values at meteorologically significant points in the atmosphere. Finished data were already in this form.

2. Computer programs took the tables of atmospheric variables and computed the heights of the points, the partial pressures of the points, the mixing ratio of the points, their absolute water vapor densities, and the refractivities of the points. Further, the program computed averages for each layer bounded by two points and in some cases information for interpolated datum points were computed.

3. The average values of each layer were used as input to a computer program which used the absorption coefficients of Chapter 2 to compute attenuation versus frequency. Resonant and non-resonant water vapor absorption, oxygen absorption, and total absorption were computed and printed out at each frequency. In addition numerous atmospheric quantities of special interest were computed and printed by the computer.

The exact equations used for computing and averaging are given in Appendix A-VI.

When computations are made of quantities at exact frequencies, like the computation of absorption which was done from radiosonde data, and it is to be compared with measurements by instruments with finite bandwidths and double sidebands, the question naturally arises as to the effect of the bandwidth and sidebands. In regions of the absorption curve which has a linear slope, the bandwidth-sideband averaged quantities will undoubtedly show little difference from the central value which is being computed. However, when the second derivative of the curve is not zero, how much of an effect can be expected?

To investigate this question a number of calculations were performed to simulate the bandwidth and sidebands for the equipment used in the experiments. The bandwidths of the radiometers were 8 MHz centered ± 30 MHz from the local oscillator frequency. Table 4-1 below presents results which compare several quantities computed for a day which showed above average attenuation and therefore above average first and second derivatives to the absorption curves. The quantities are from left to right: frequency; the average resonant absorption for the low frequency sideband; the average resonant absorption for the high frequency sideband; the average resonant absorption for the two sidebands; and the resonant absorption computed for the local oscillator frequency. The frequencies are in GHz, the absorption values in db.

TABLE 4-I. The effects of sidebands on absorption computations

Frequency	Av. Absorpt. Lower S.B. (db)	Av. Absorpt. Upper S.B. (db)	Av. Absorpt. Both S.B. (db)	Absorpt. Compt. at L.O. Freq. (db)
19.000	0.19827	0.20435	0.20131	0.20096
21.000	0.56009	0.57666	0.56837	0.56742
21.900	0.80366	0.81595	0.80980	0.80863
22.237	0.85598	0.86061	0.85830	0.85710
23.500	0.70963	0.69656	0.70310	0.70196
25.500	0.36084	0.35398	0.35741	0.35681
29.450	0.13821	0.13675	0.13748	0.13725
32.400	0.08994	0.08931	0.08963	0.08948

It is evident that the largest deviation between sideband averages and local oscillator frequency computations is 0.0012 db, a difference which is negligible when other errors are considered. Of the sideband averages, only one of the values differed as much as one unit in the fifth decimal place from the absorption calculated at the center of the band.

4.3 Comparison between Measured Attenuation and Computed Absorption

The radiometer attenuation as computed from Equation (4.1-9) at five frequencies and the absorption as computed from the radiosonde data for each experiment day is plotted in Figures 4-3 to 4-34. The discussion of these figures is separated into three parts: (1) an explana-

tion of the information format; (2) a discussion of the similarities of the observed and computed spectra with reference to the prevailing weather conditions; and (3) a section on the causes of the poor correlation between some radiosonde spectra and observed spectra.

4.3.1 Presentation of the Comparable Spectra

To facilitate discussion of the comparisons, the experiments are not grouped chronologically but by similar prevailing weather conditions. That is, spectra taken on clear days are together, spectra taken during highly unstable conditions are together, etc.

The data on each figure consists of the following: (1) the data of the experiment followed by the time over which radiometer data were taken; (2) the observed weather conditions recorded under the data and time; (3) the radiometer results recorded as single dots in the middle of probable error bars (the errors represent one standard deviation as computed from Equation (A-II-12); (4) a solid spectral curve that has been computed from the data returned by the radiosonde flown on the day of the experiment; and (5) a dashed spectral curve which may be called a matched spectra. This latter spectral curve is derived by taking one of the observed spectral data points (21.9 GHz in the summer data, and 22.235 GHz in the winter data) and multiplying the radiosonde moisture profile by a factor which causes the computed absorption to match the observed attenuation (difference $\leq$ 0.001 db) at this one frequency. Its uses will be apparent as we proceed.

The five general categories which make up the various groupings are the following: (1) stable, mostly clear days; (2) days on which moisture laden air approached the antenna site; (3) days on which dry air was approaching the antenna site; (4) highly unstable conditions manifested by considerable cumulus, towering cumulus and/or thunderstorms; and (5) unknown conditions or conditions in which it was not possible to evaluate in terms of time changes of the local moisture field.

4.3.2 Similarities Between Spectra Pairs within Weather Groups.

The 32 figures labeled 4-3 to 4-34 are broken down into the groupings defined before as follows:

1 $\left\{\begin{array}{l} 4\text{-}3 \longrightarrow 4\text{-}8 \\ 4\text{-}9 \longrightarrow 4\text{-}11 \end{array}\right.$ summer: stable, clear or mostly clear weather
   winter: stable, clear or mostly clear weather

2 $\left\{\begin{array}{l} 4\text{-}12 \longrightarrow 4\text{-}14 \\ 4\text{-}15 \longrightarrow 4\text{-}16 \end{array}\right.$ summer: approaching moist air mass
   winter: approaching moist air mass

3 $\left\{\begin{array}{l} 4\text{-}17 \longrightarrow 4\text{-}22 \end{array}\right.$ summer: approaching dry air mass

4 $\left\{\begin{array}{l} 4\text{-}23 \longrightarrow 4\text{-}28 \end{array}\right.$ summer: unstable, very moist conditions

5 $\left\{\begin{array}{l} 4\text{-}29 \\ \\ 4\text{-}30 \longrightarrow 4\text{-}34 \end{array}\right.$ summer: indeterminate moisture changes during experiment
   winter: unanalyzed conditions due to unavailability of surface weather charts.
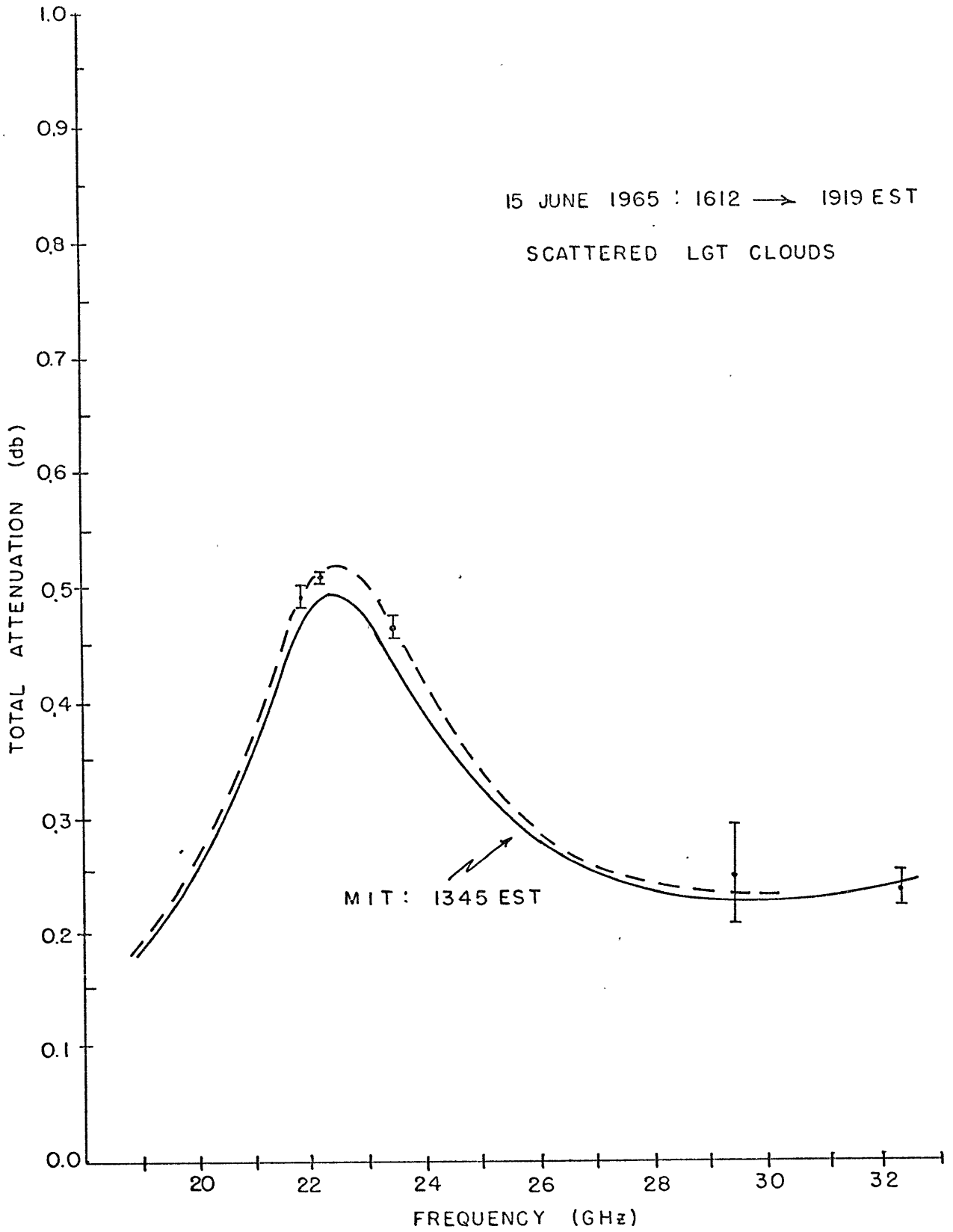
FIGURE 4-3
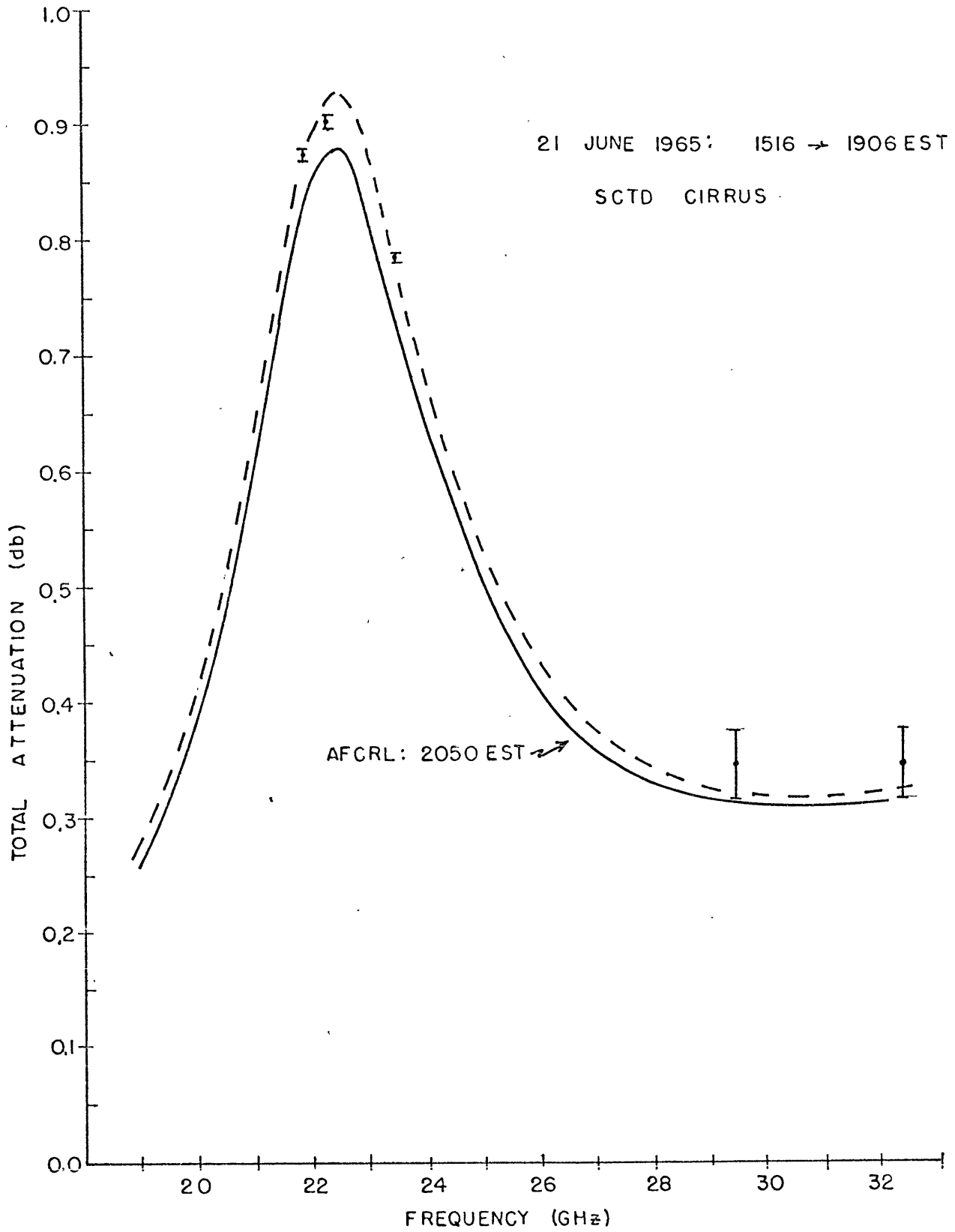
FIGURE 4-4
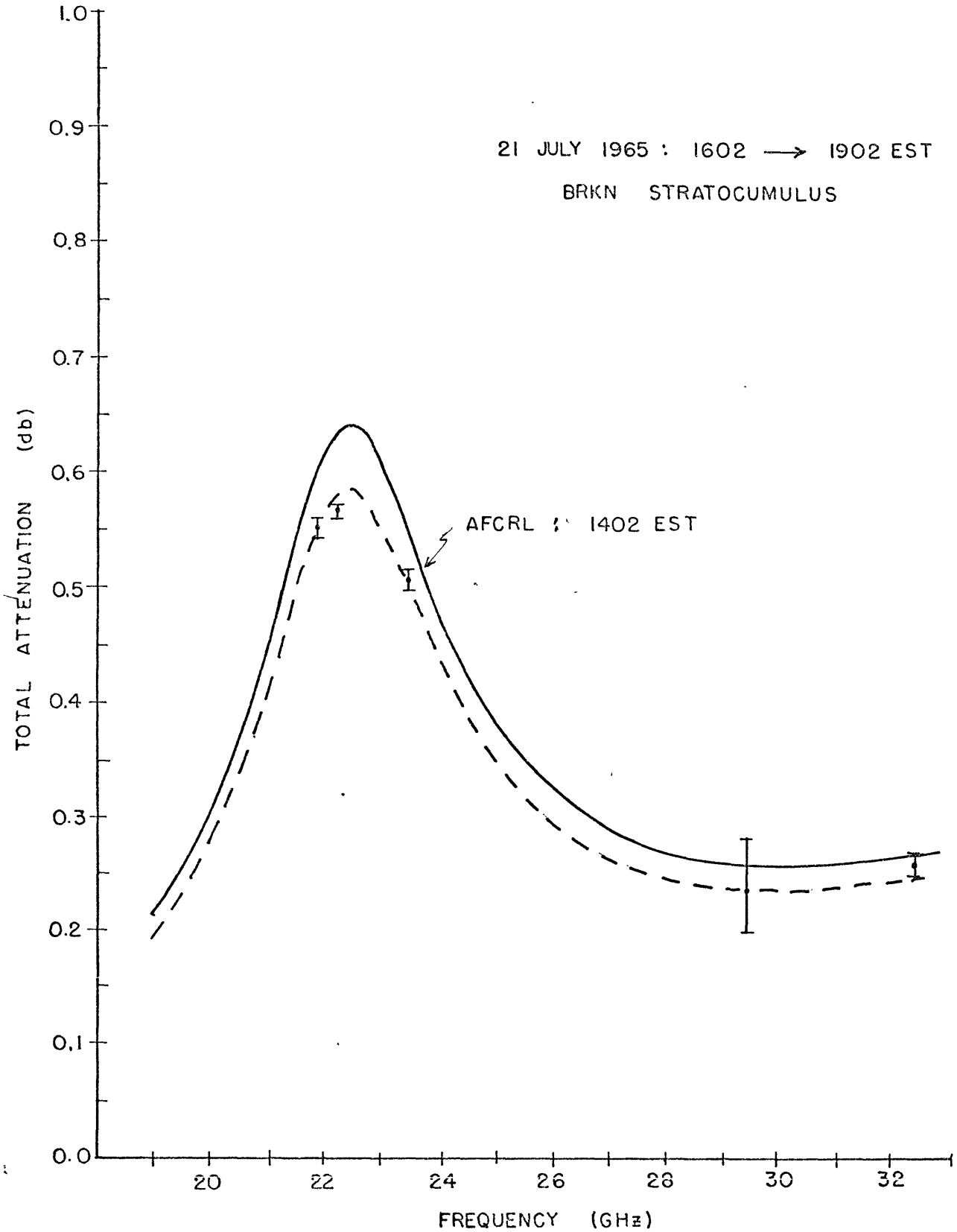
FIGURE 4-5
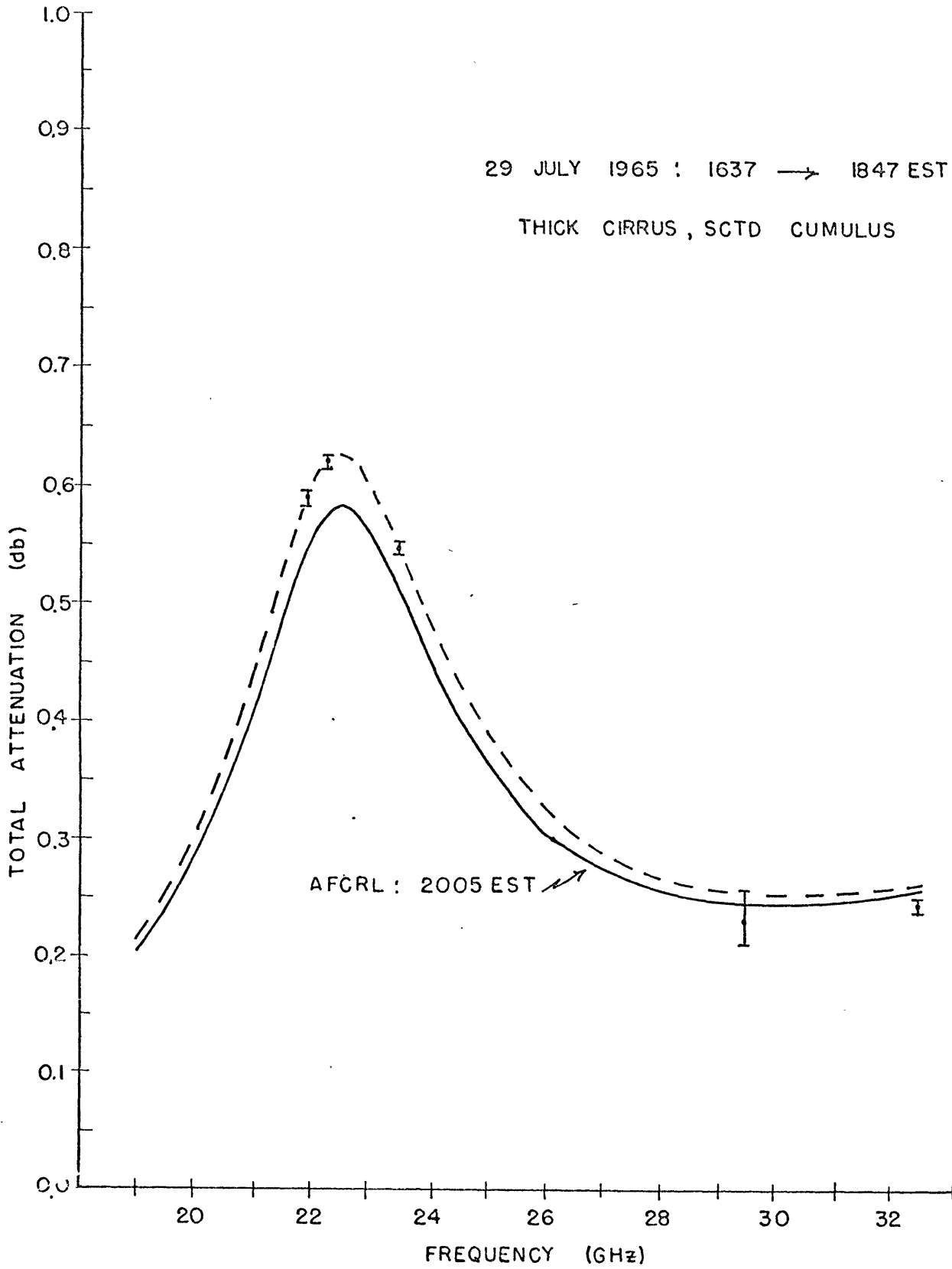
FIGURE 4-6
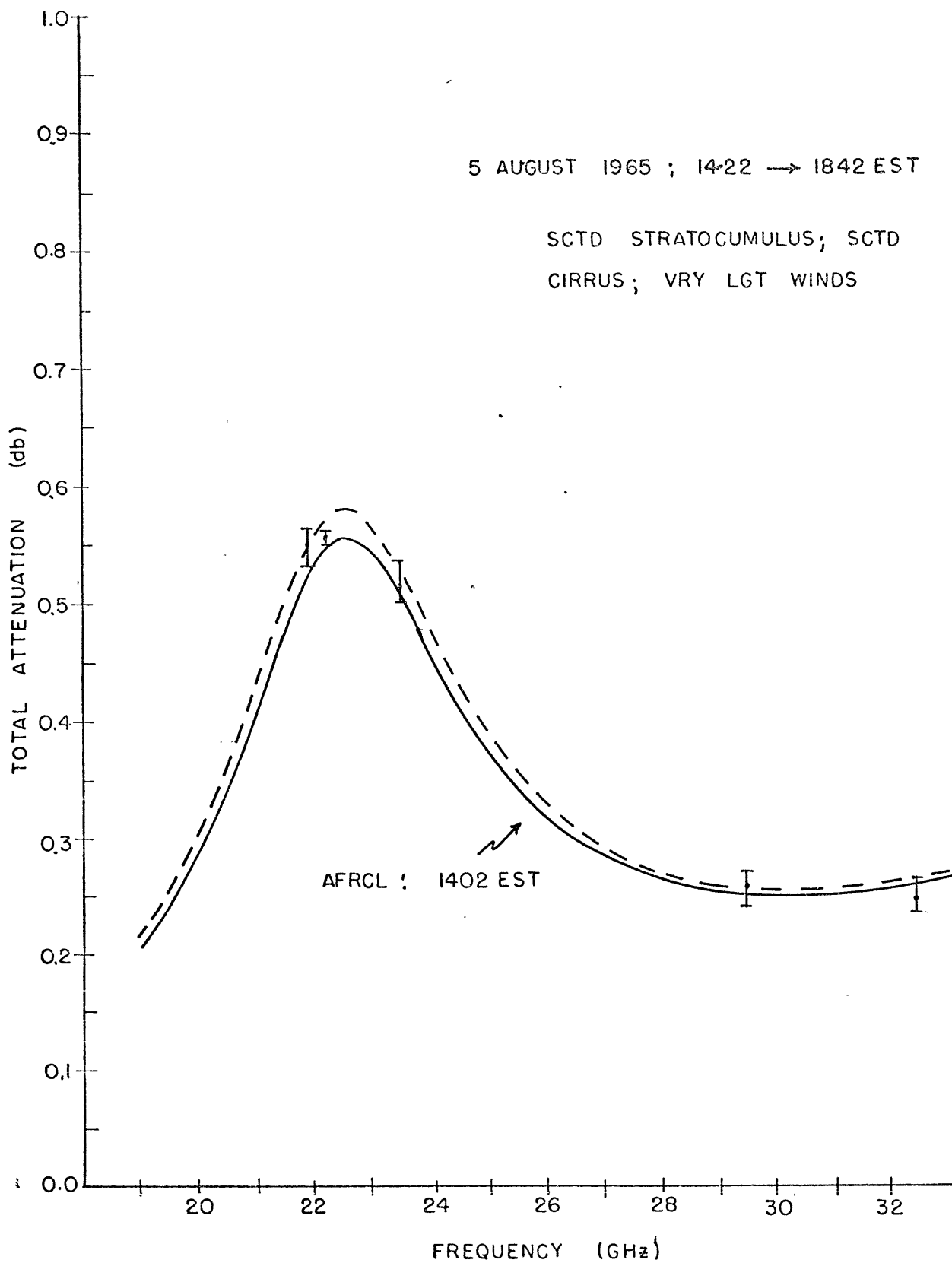
FIGURE 4-7
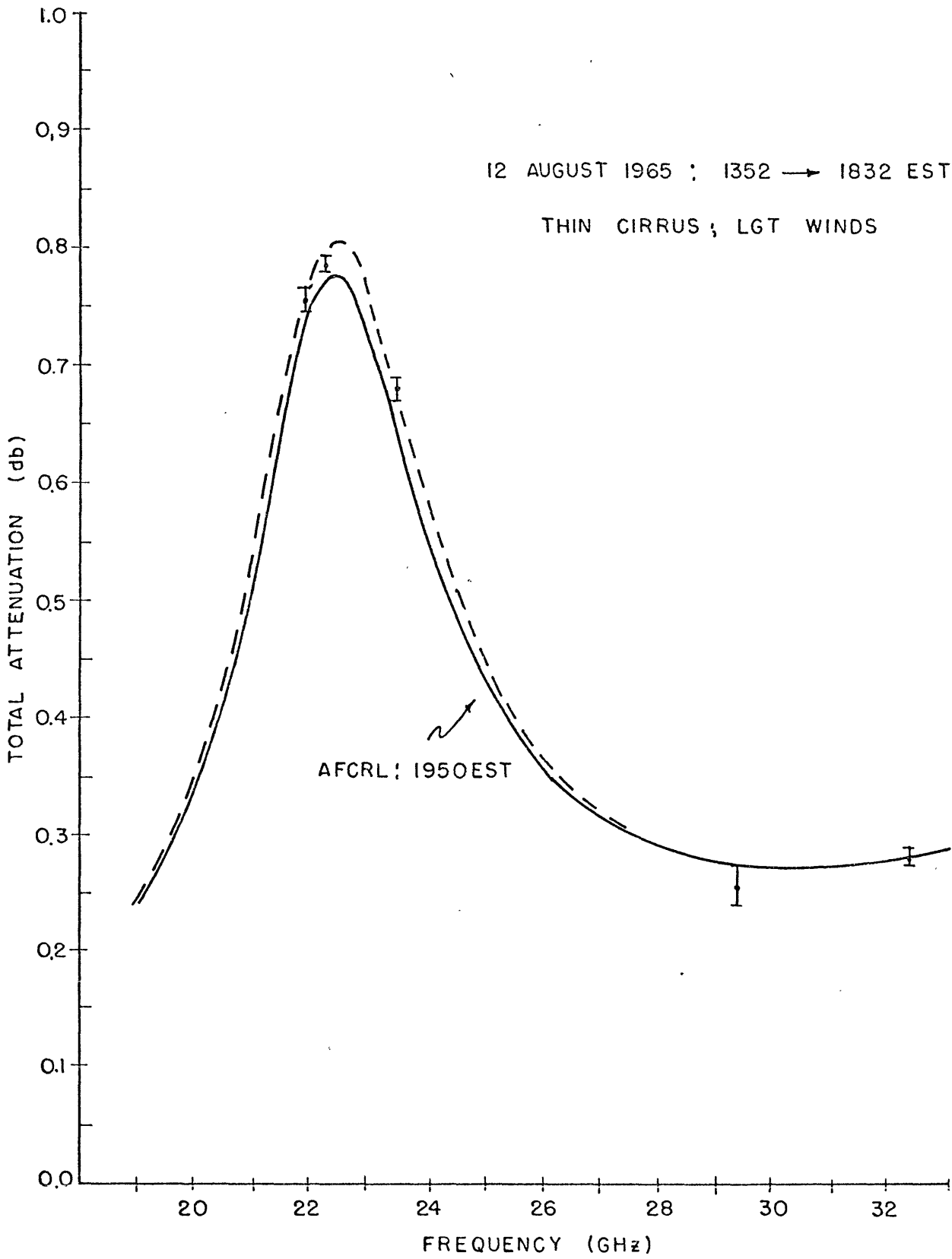
FIGURE 4-8
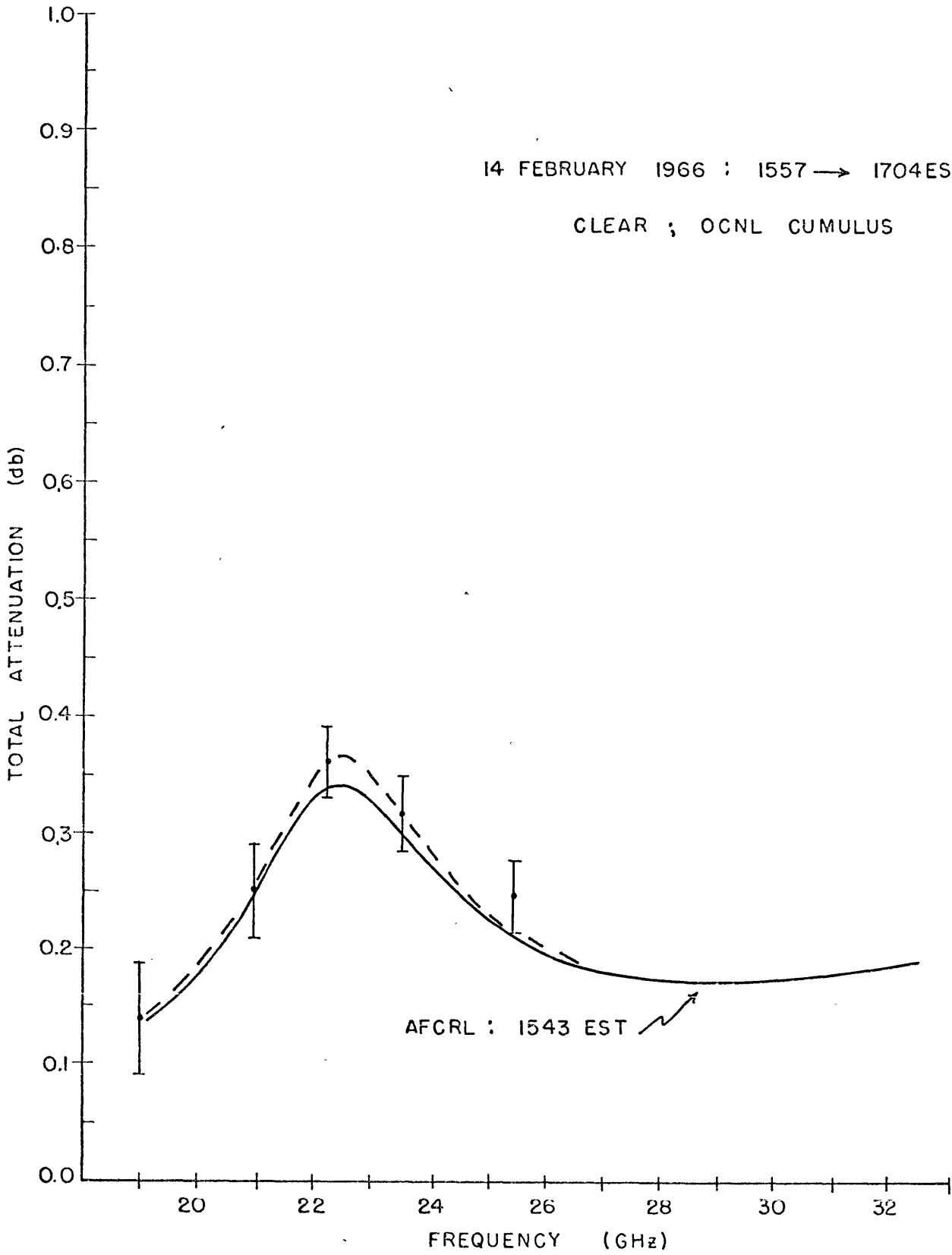
FIGURE 4-9
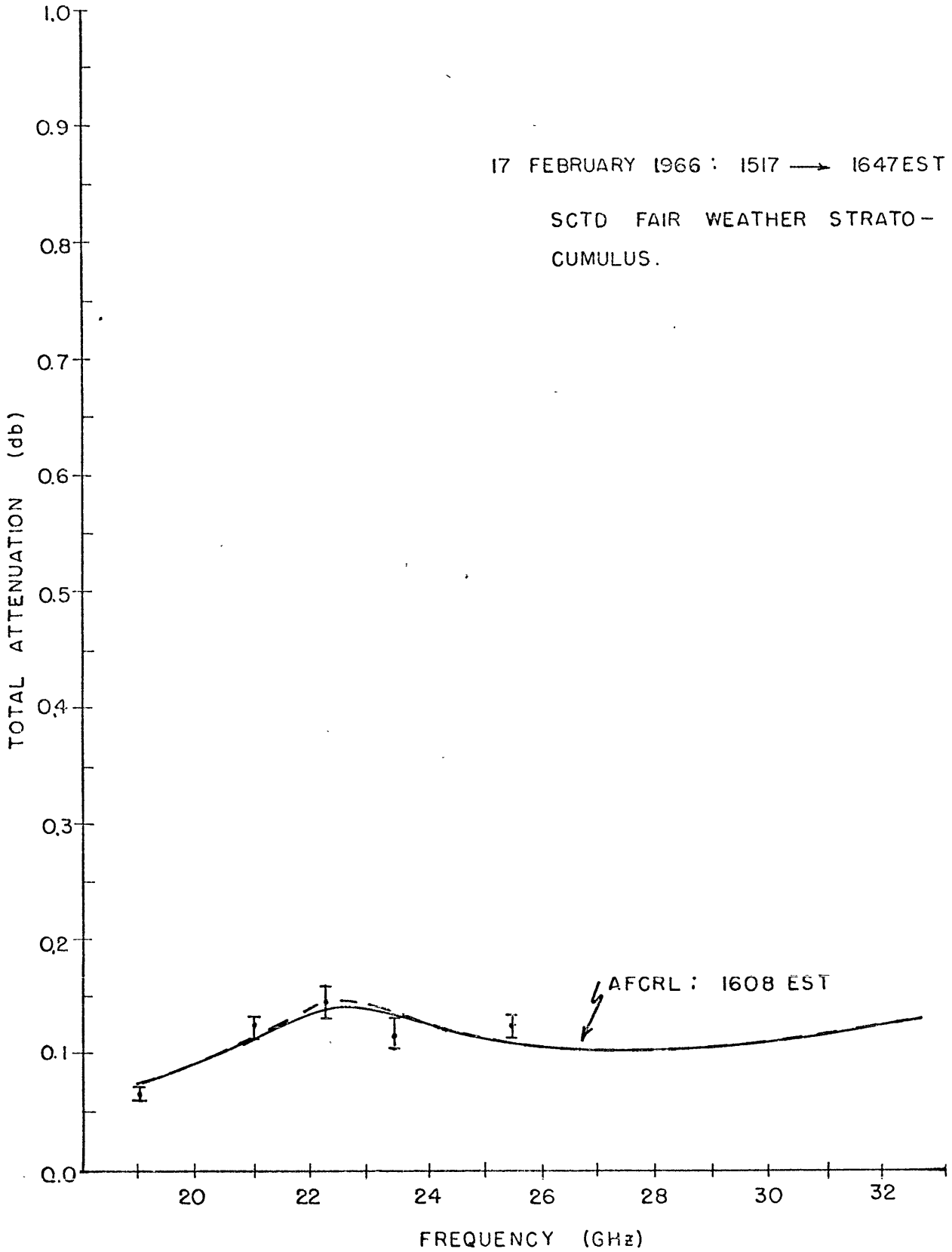
FIGURE 4-10

FIGURE 4-11

FIGURE 4-12

14 JULY 1965 : 1652 → 1902 EST

APPROACHING WARM FRONT ;
CLEAR → CIRRUS SHIELD →
LAYERS, HAZE

MIT : 1458 EST
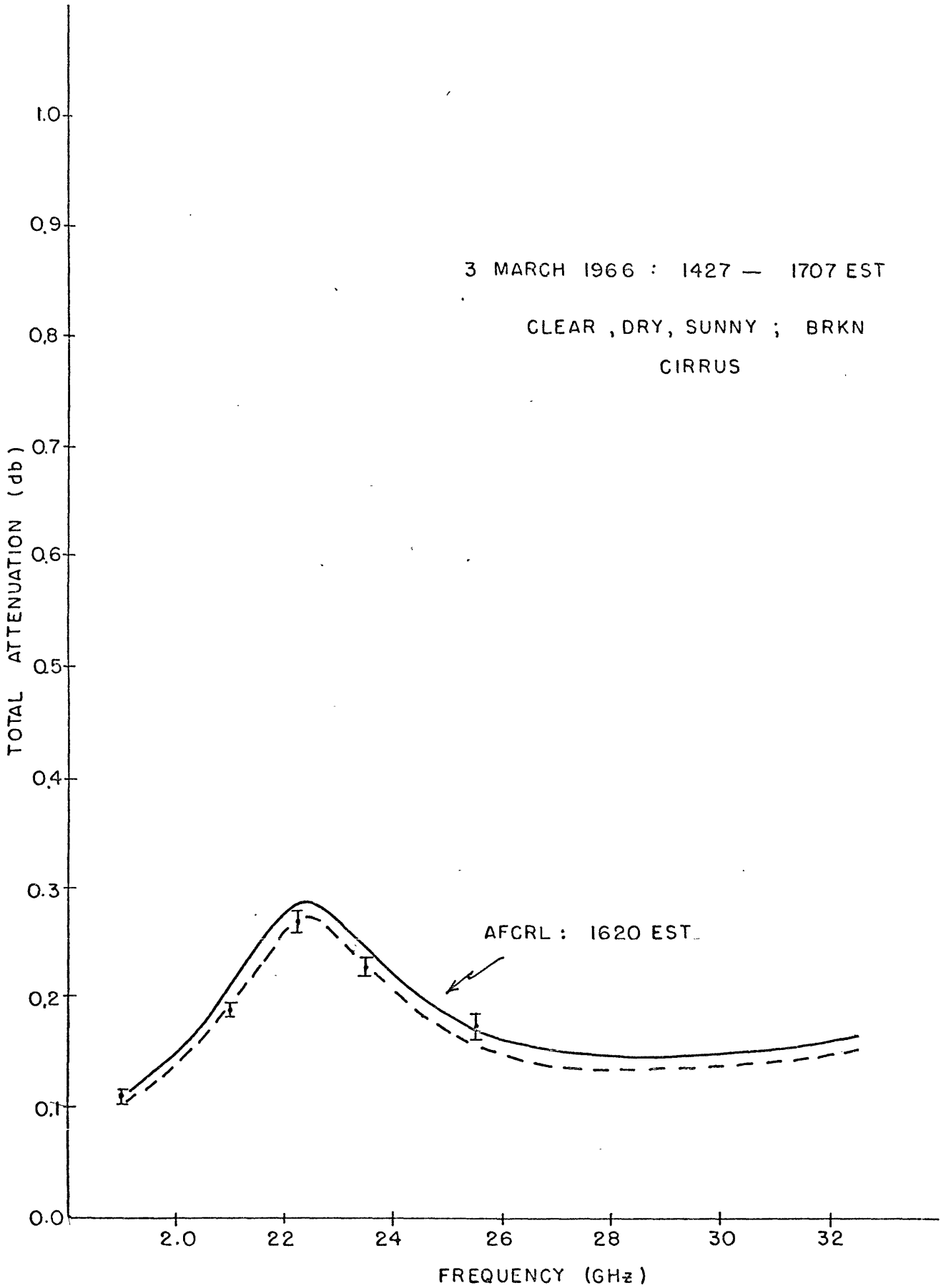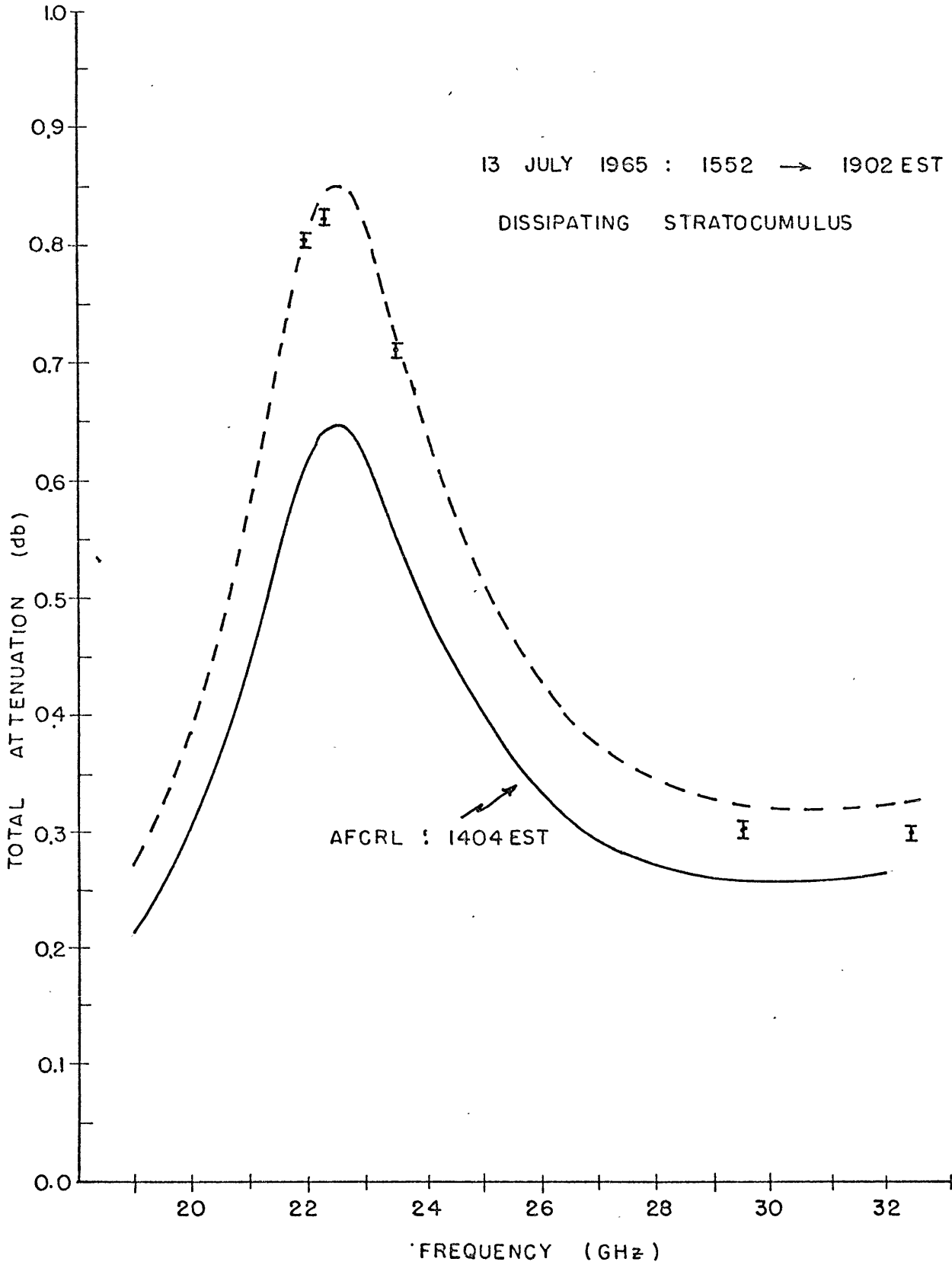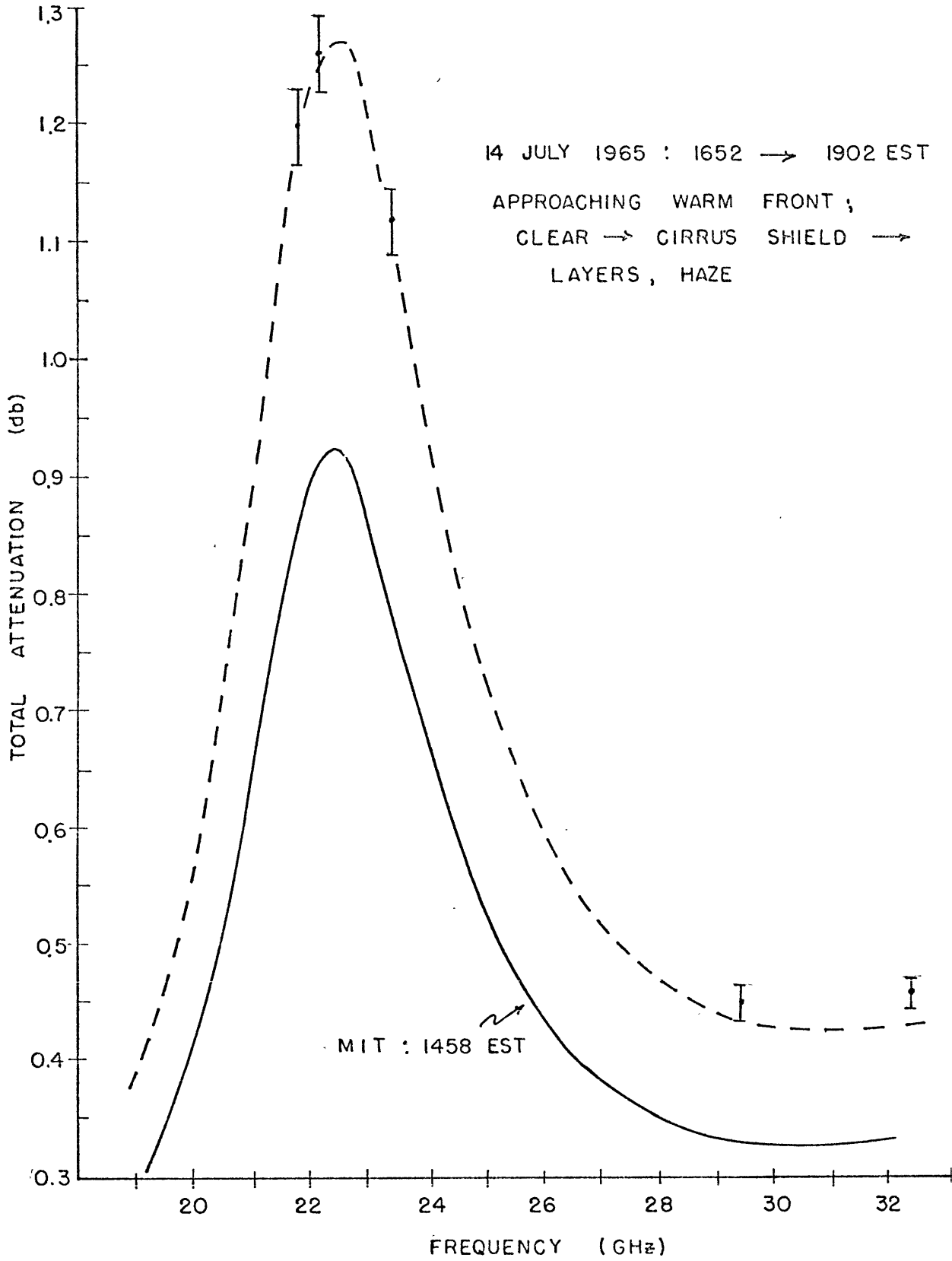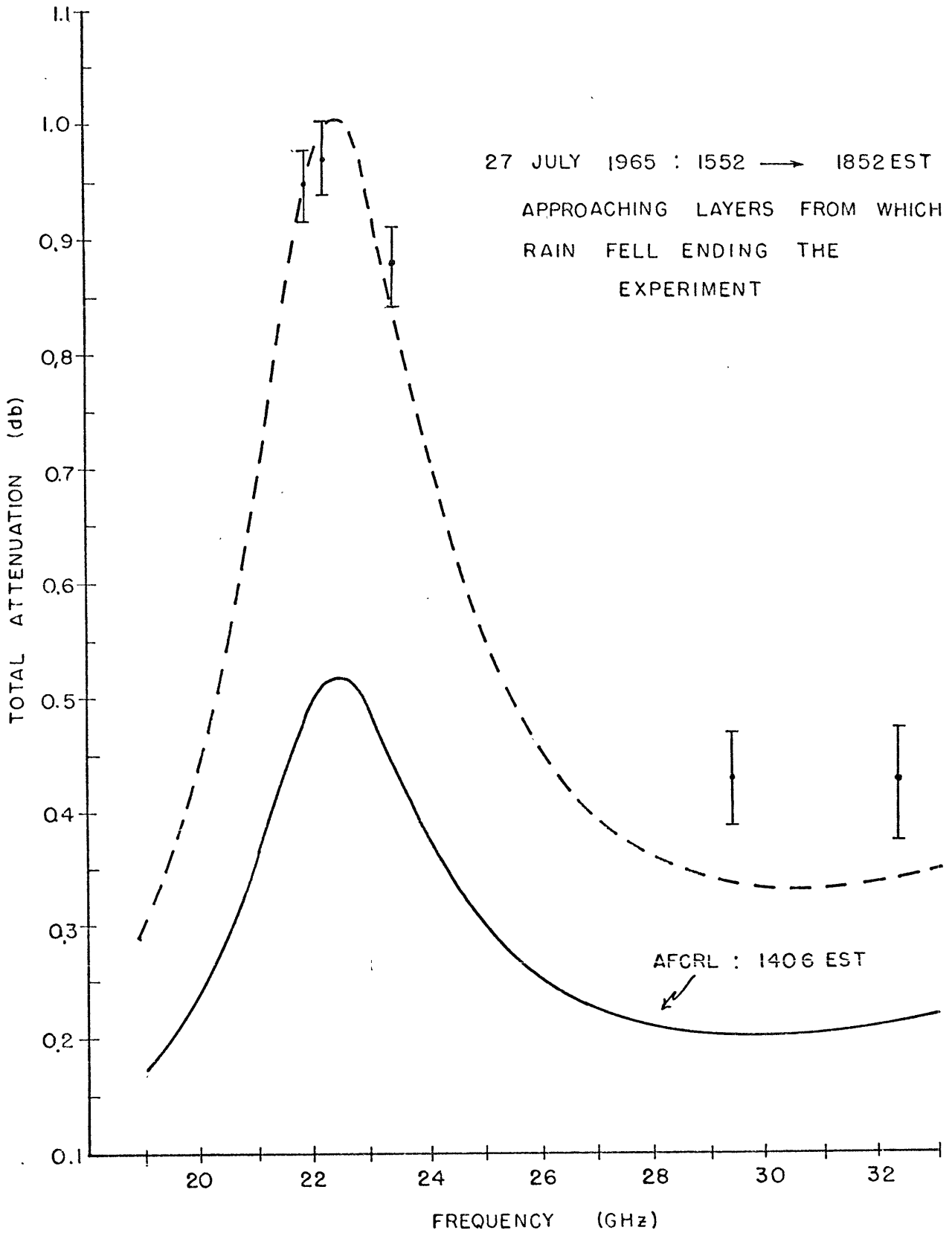
FIGURE 4-13
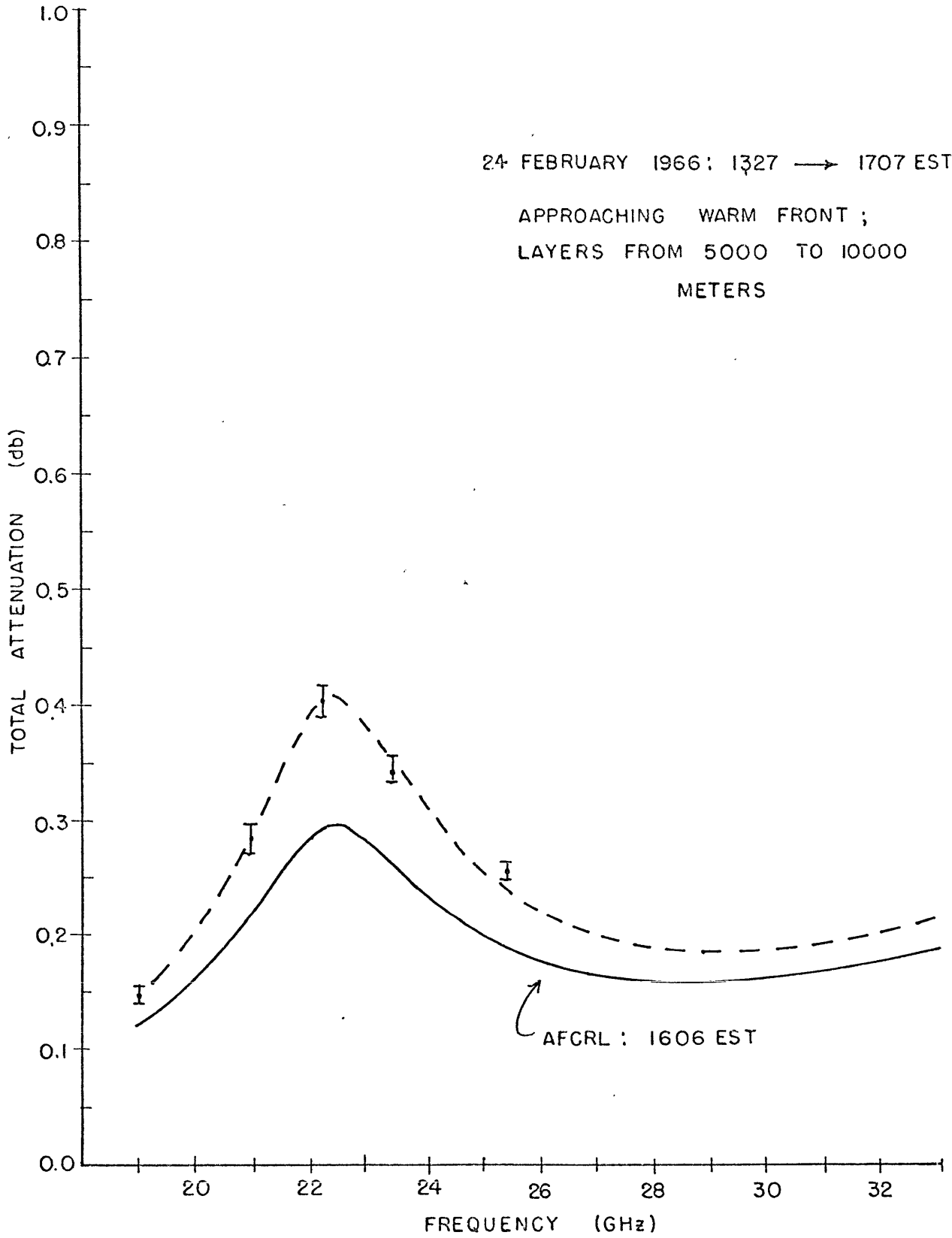
FIGURE 4-14

FIGURE 4-15
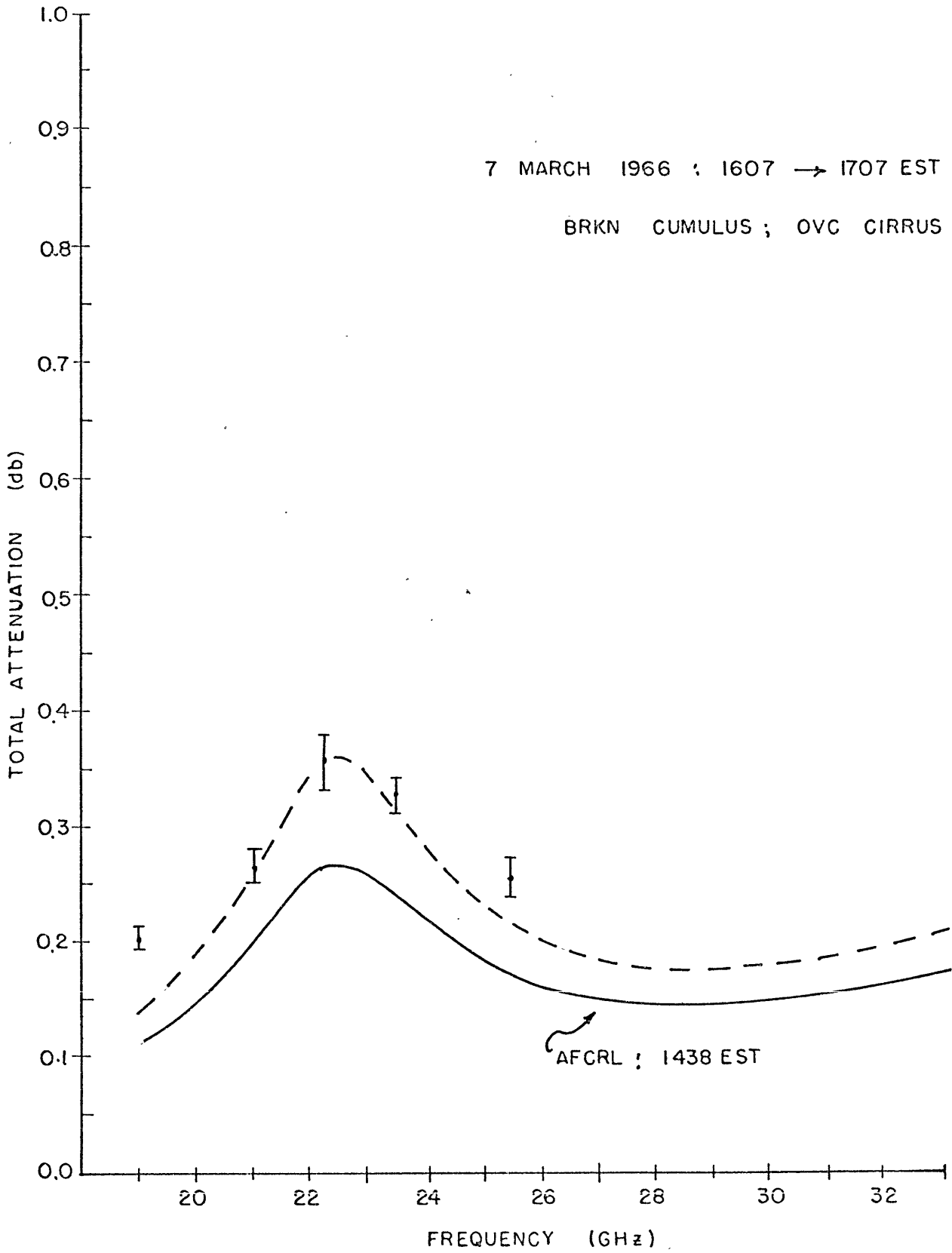
FIGURE 4-16
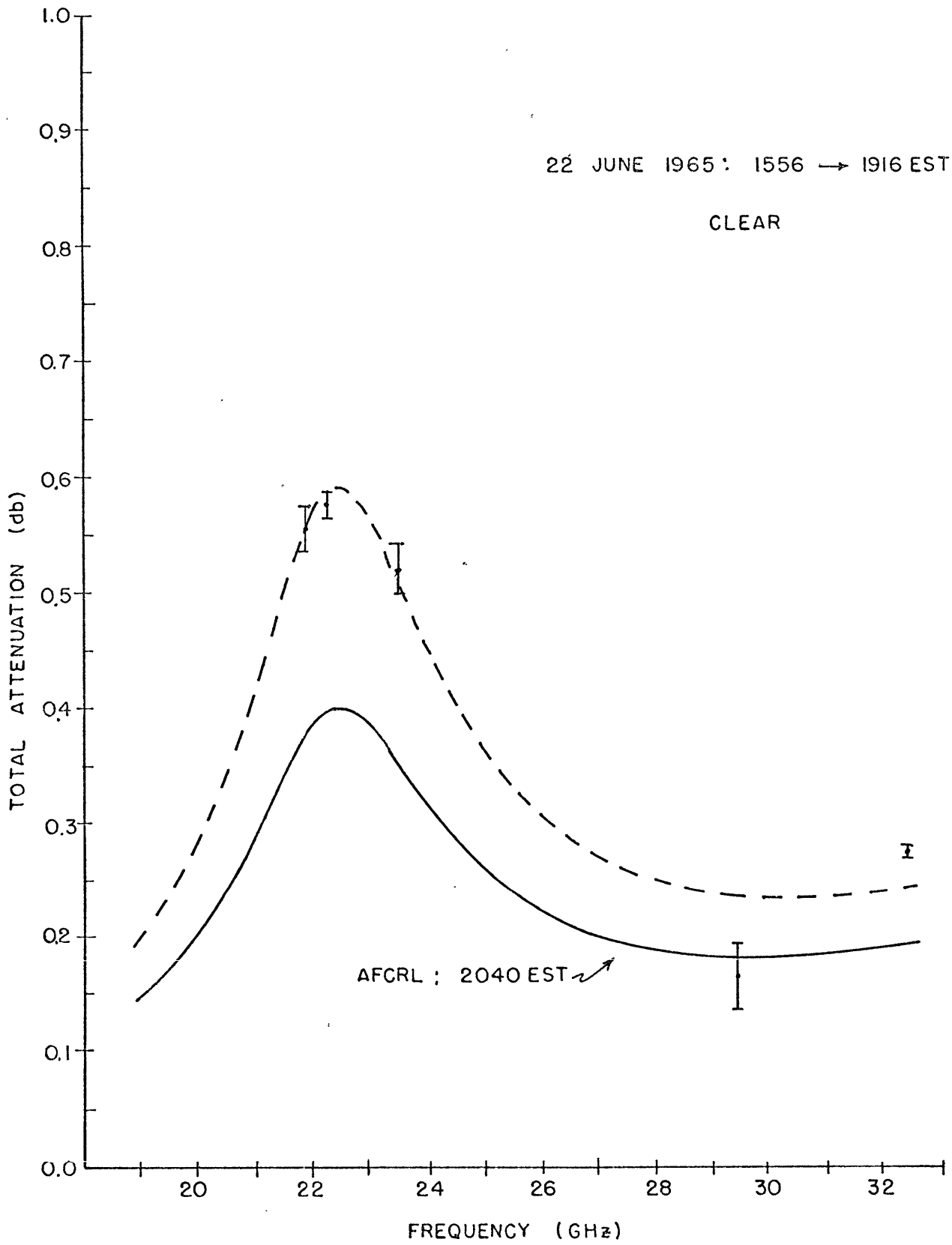
FIGURE 4-17
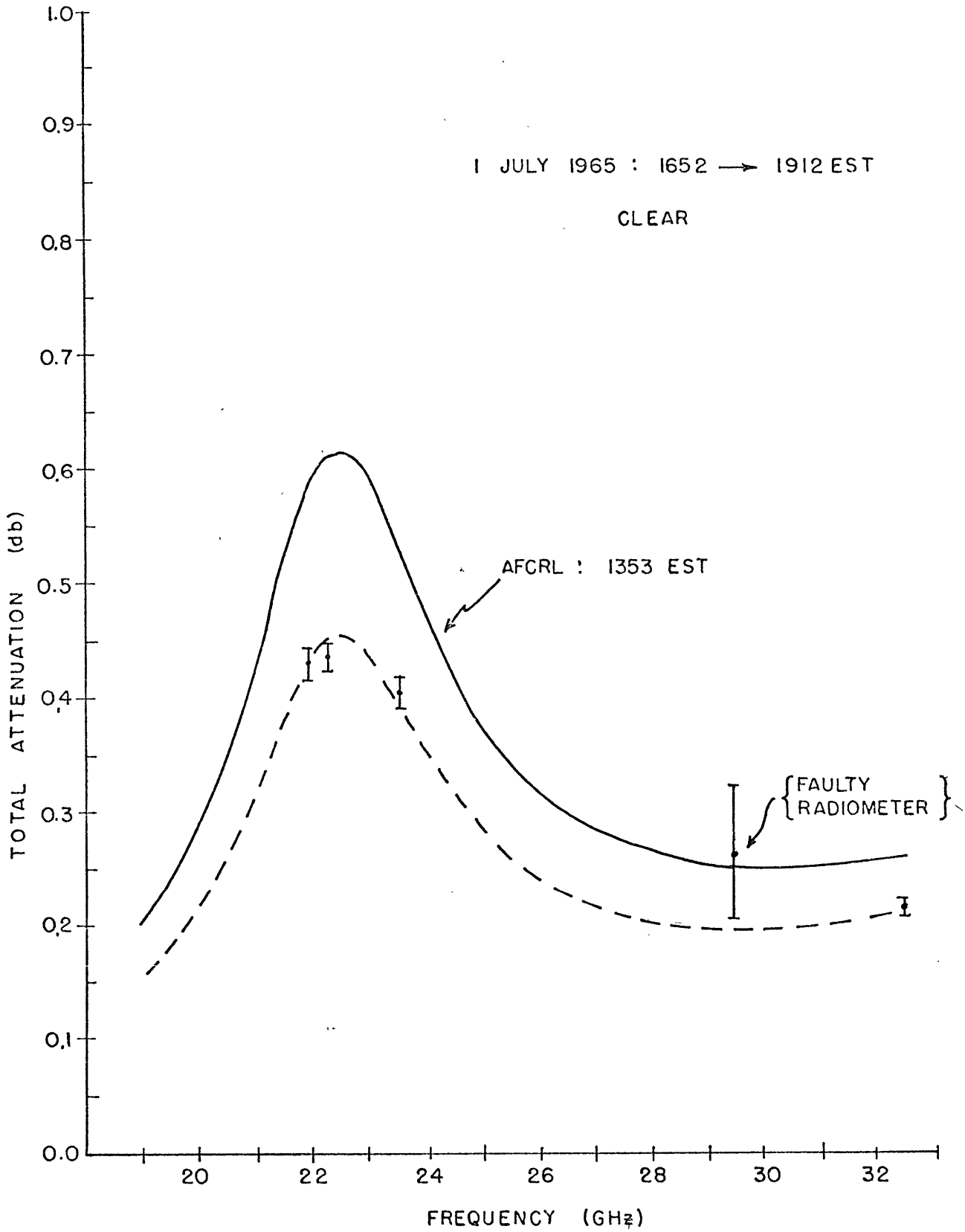
FIGURE 4-18

FIGURE 4-19

FIGURE 4-20

19 JULY 1965 : 1552 ⟶ 1902 EST

SCAT'D STRATOCUM.

AFCRL : 1404 EST

FIGURE 4-21

FIGURE 4-22

22 JULY 1965 : 1542 ⟶ 1902 EST

SCTD STRATOCUMULUS ; BRKN
ALTO CUMULUS ; OVC CIRRUS

.AFCRL : 1402 EST
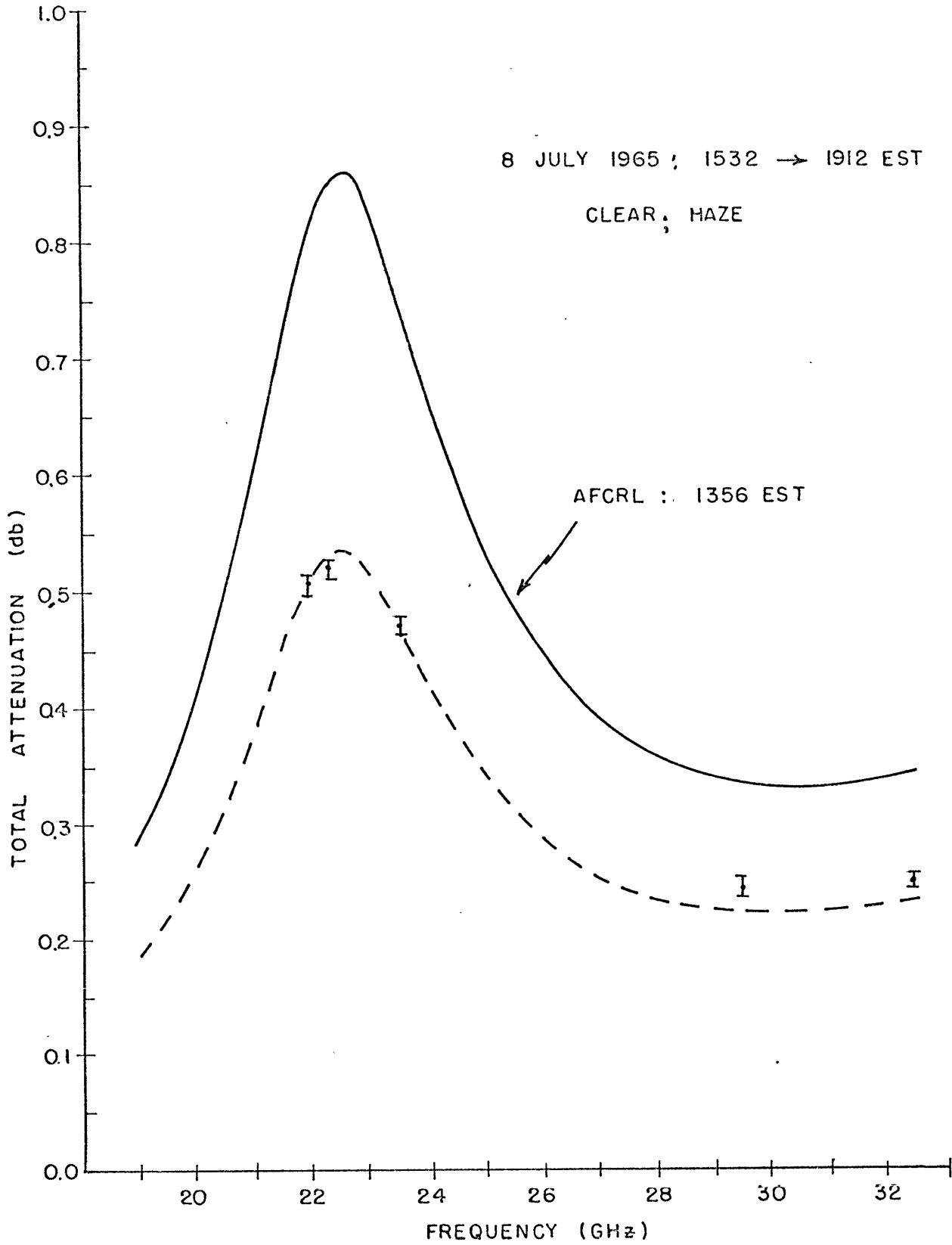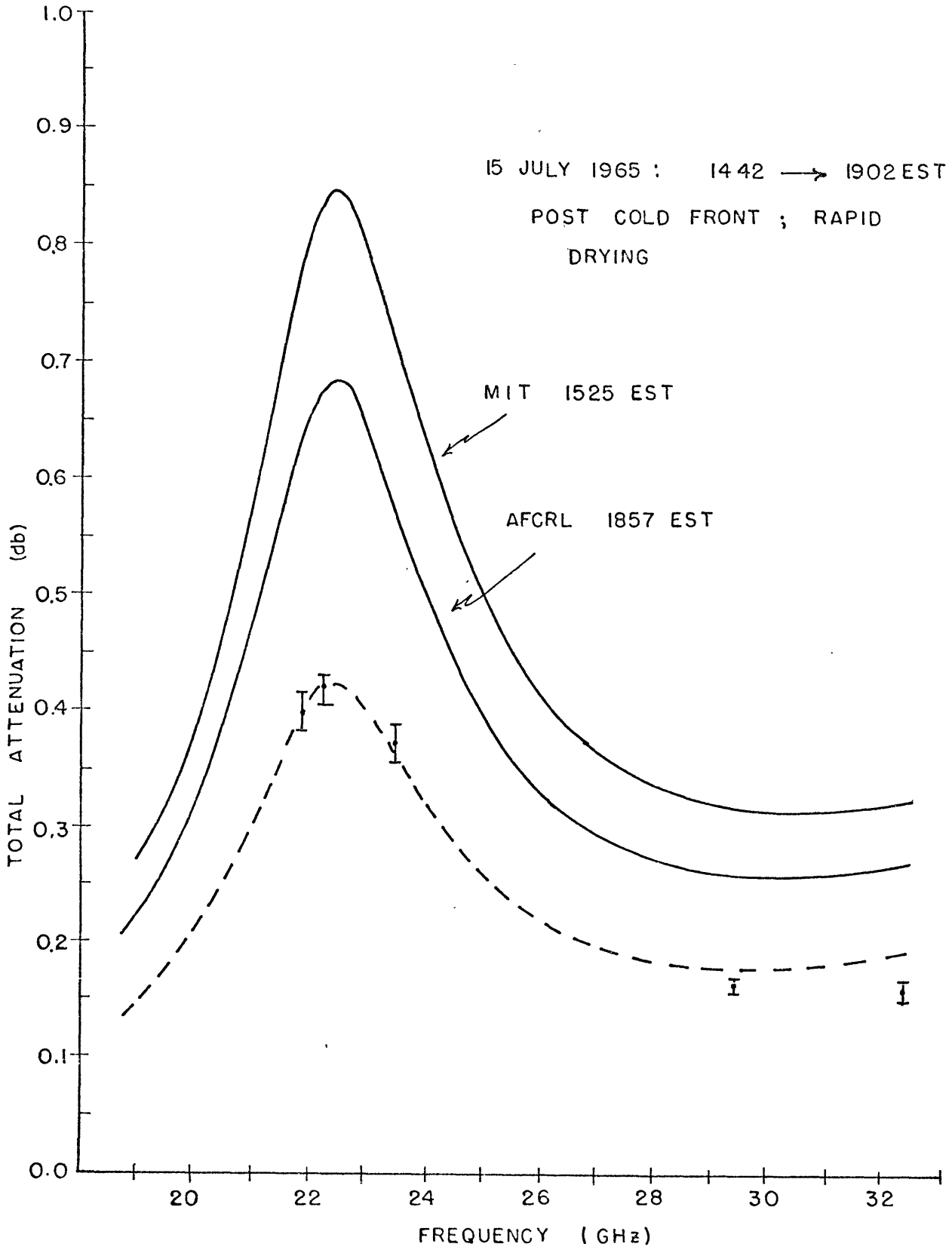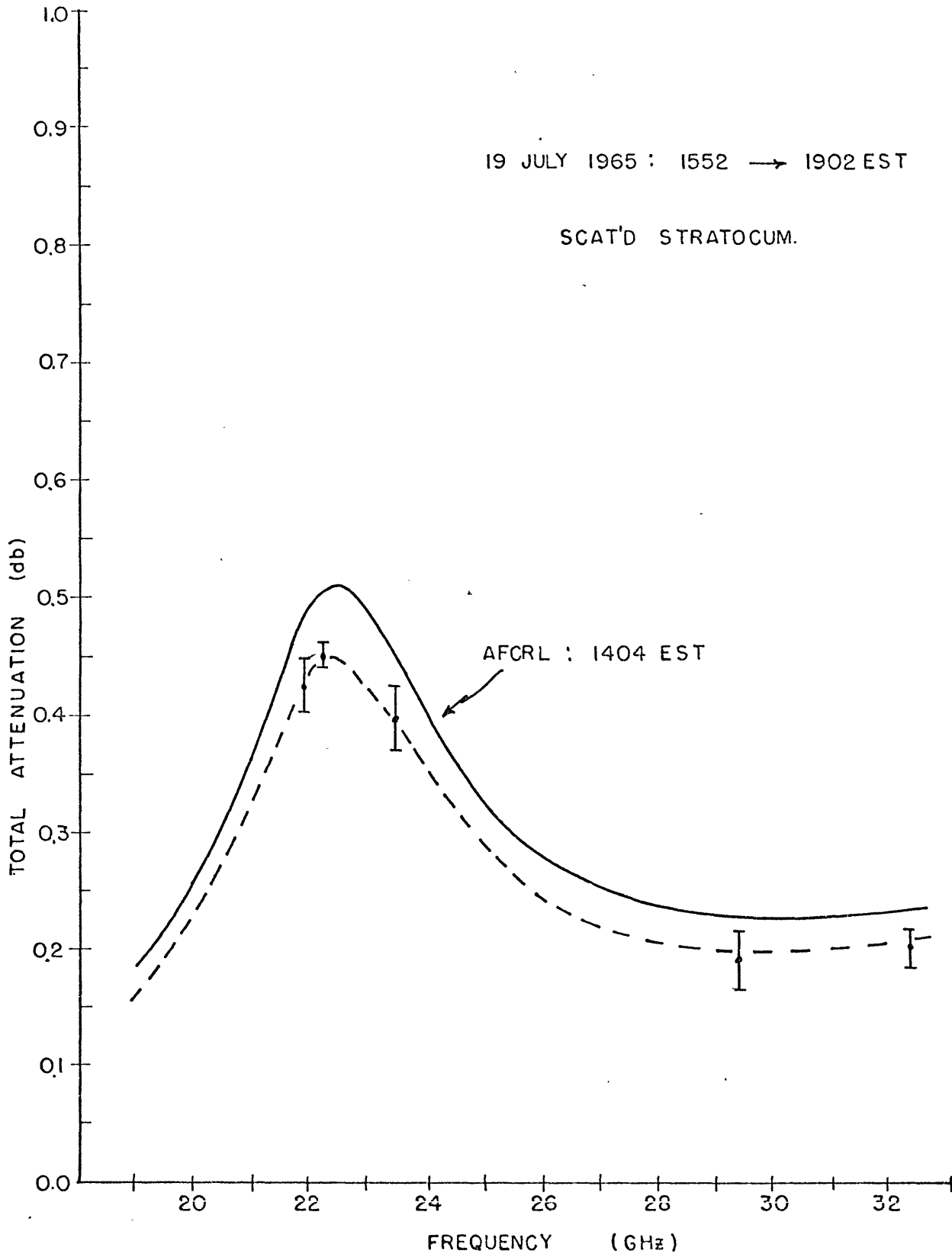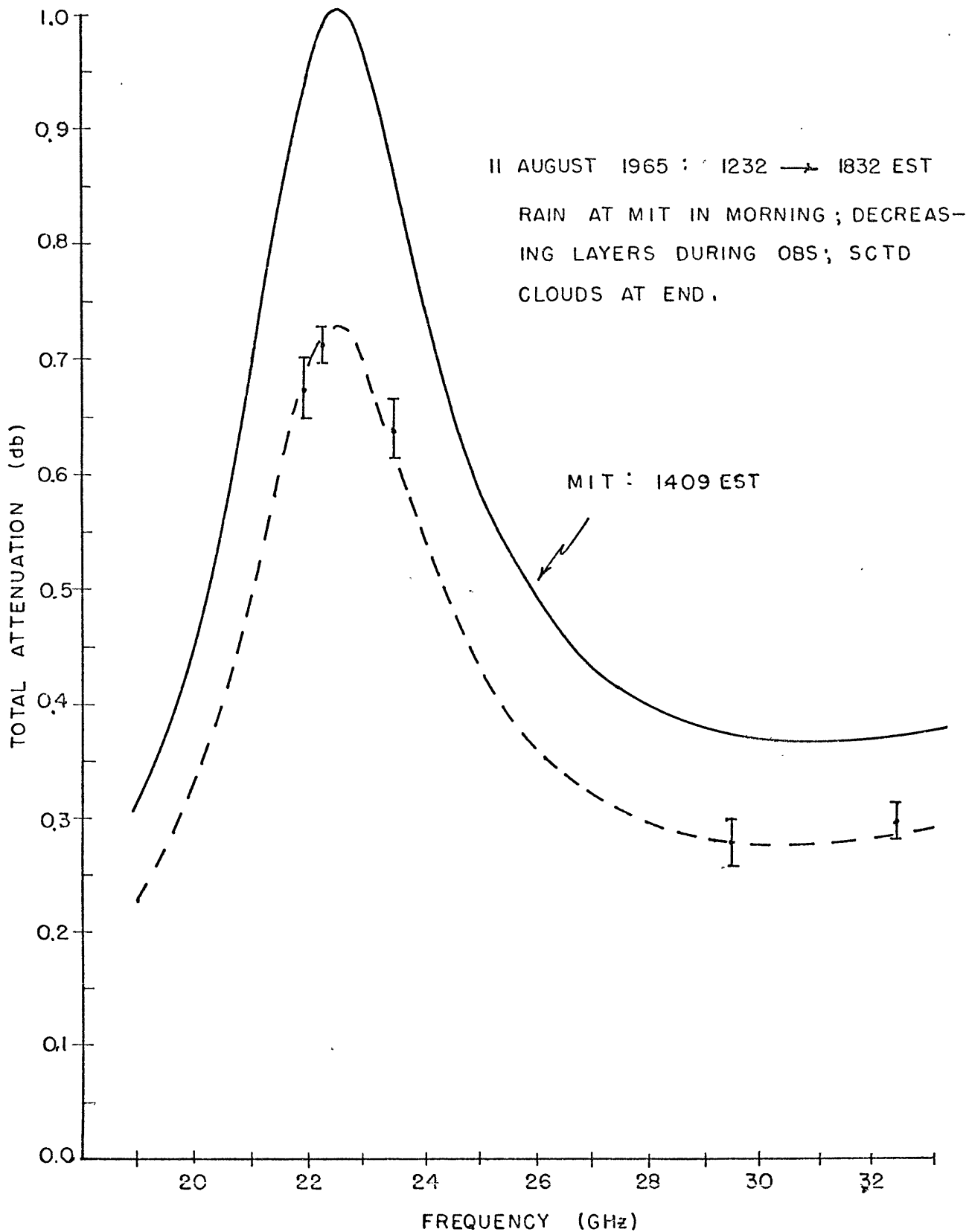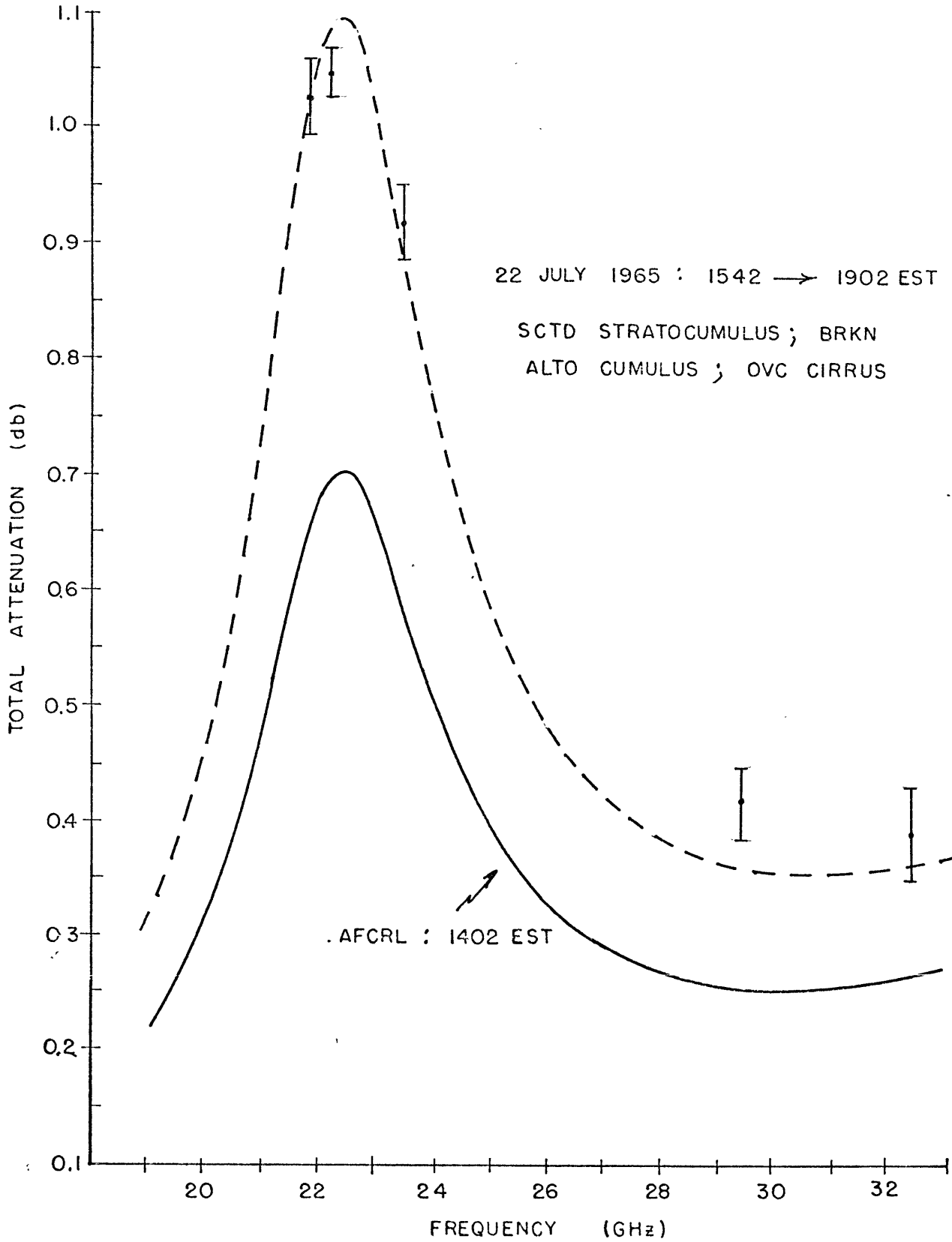
FIGURE 4-23

FIGURE 4-24

FIGURE 4-25

10 AUGUST 1965: 1242 → 1842 EST

HOT, HUMID; MANY TWRG CUM;
THUNDERSTORMS; BRKN STRATO-
CUM; BRKN ALTOCUM; HEAVY
CONTRAILS

MIT : 1305 EST

FIGURE 4-26

10 AUGUST 1965 : 1242 → 1842 EST

HOT, HUMID; MANY TWRG CUM;

THUNDERSTORMS; BRKN STRATO-

CUM; BRKN ALTOCUM; HEAVY

CONTRAILS.

M I T : 1704 EST
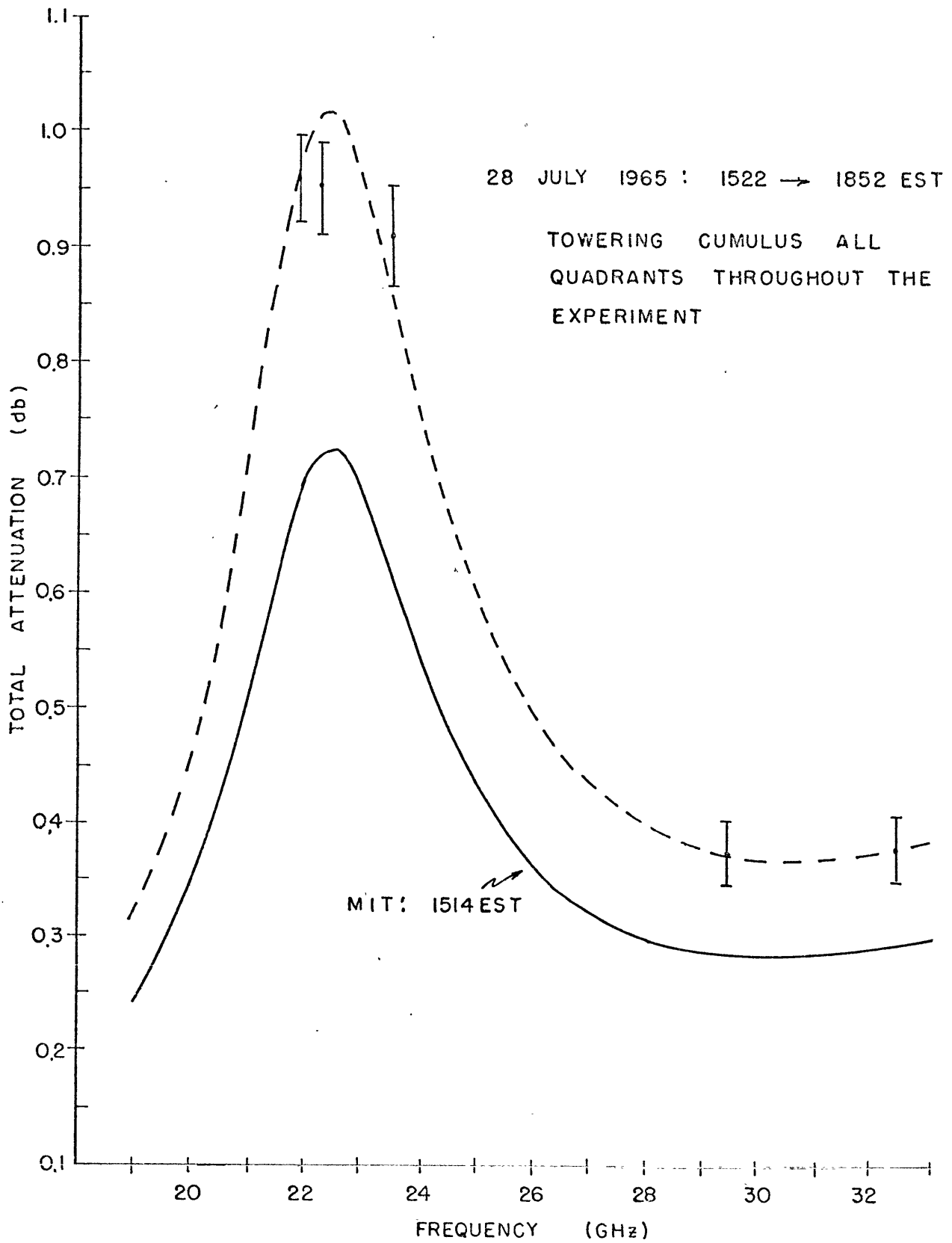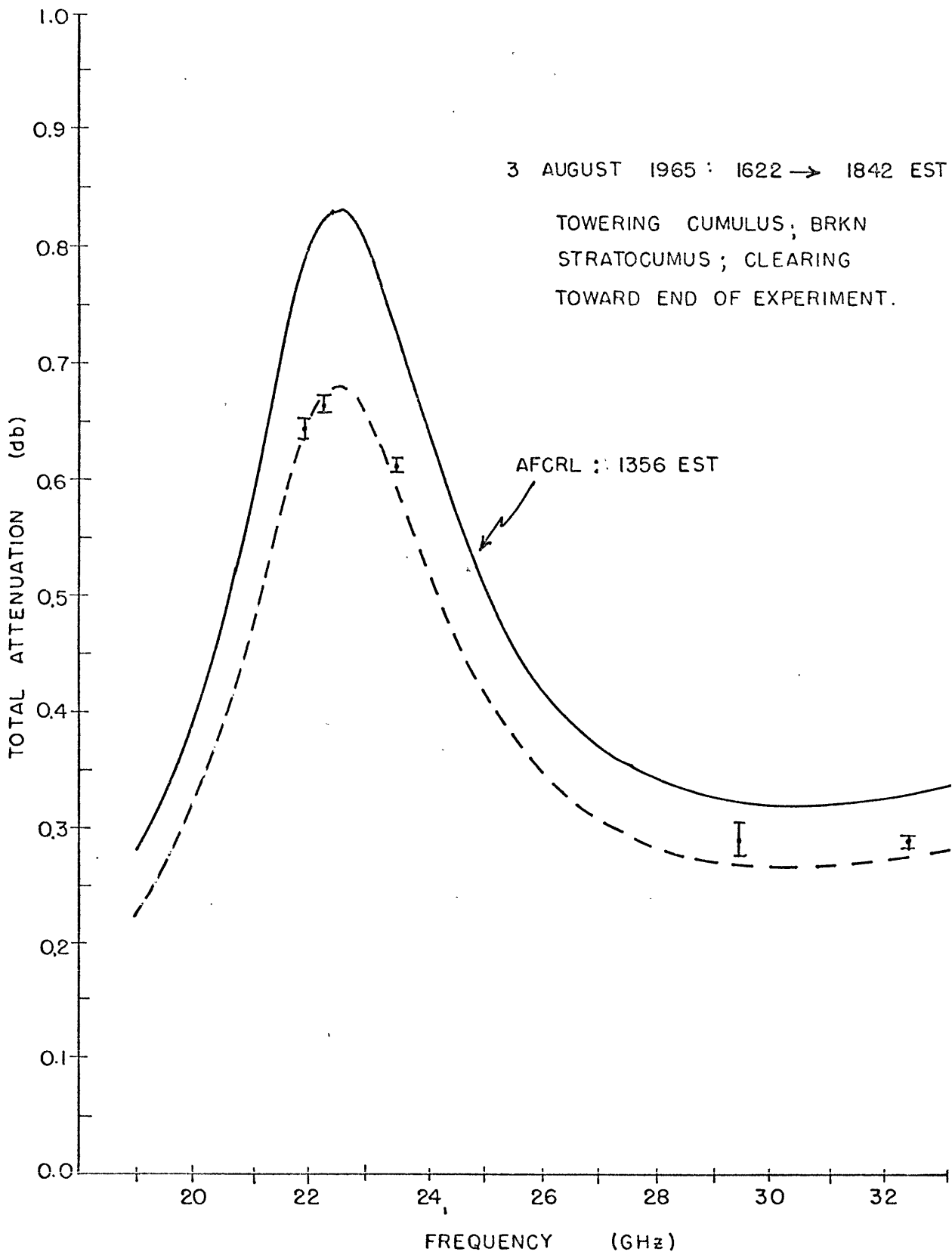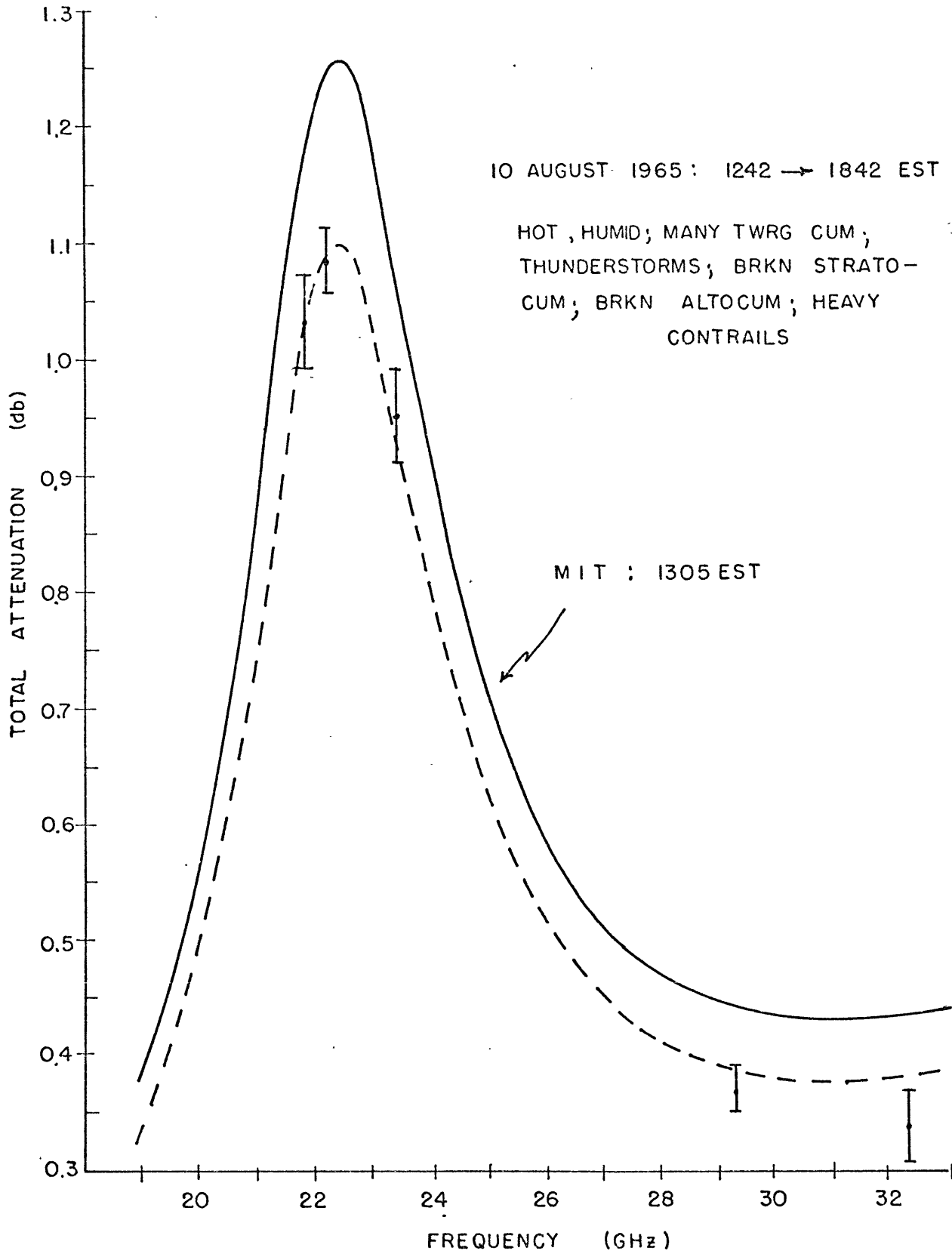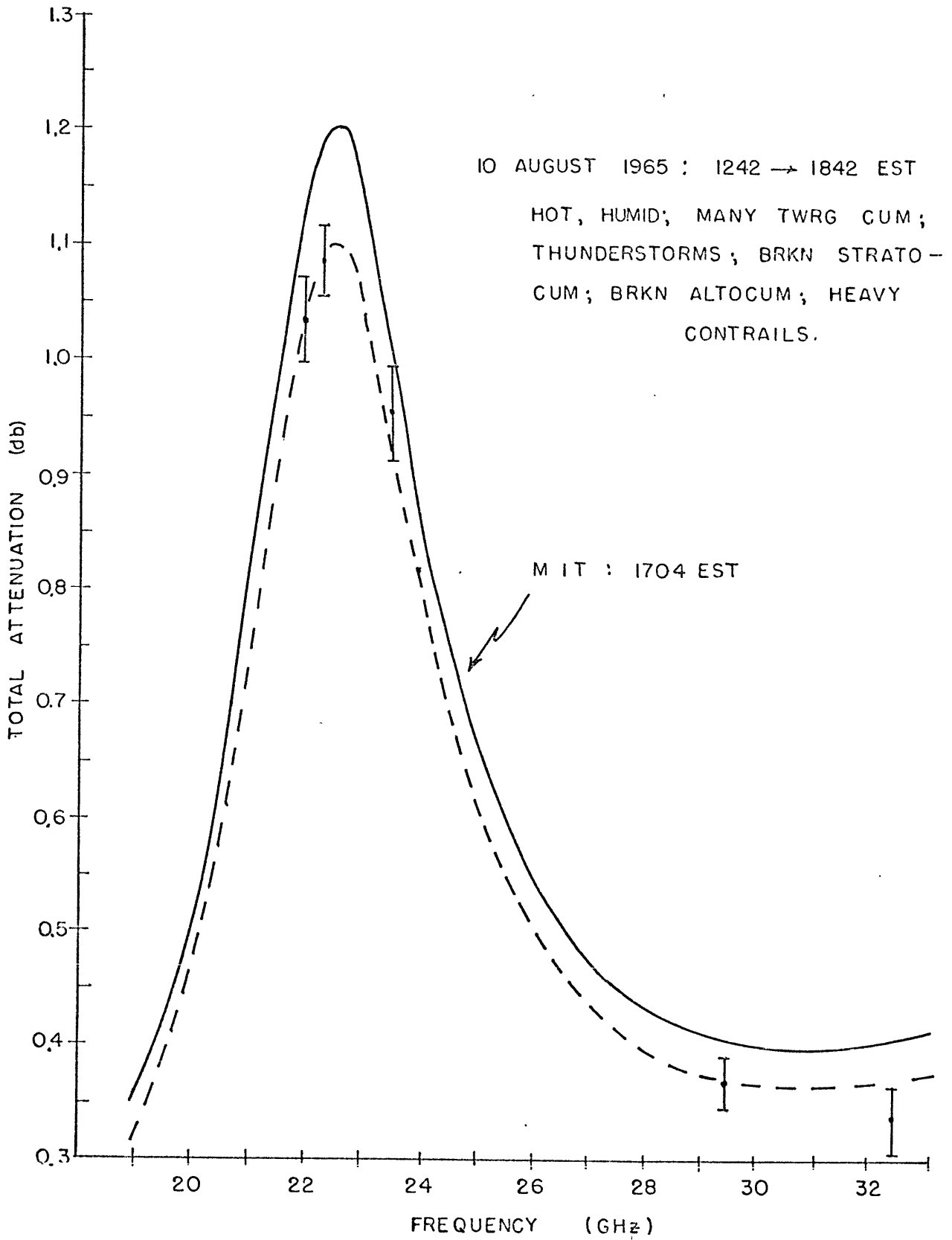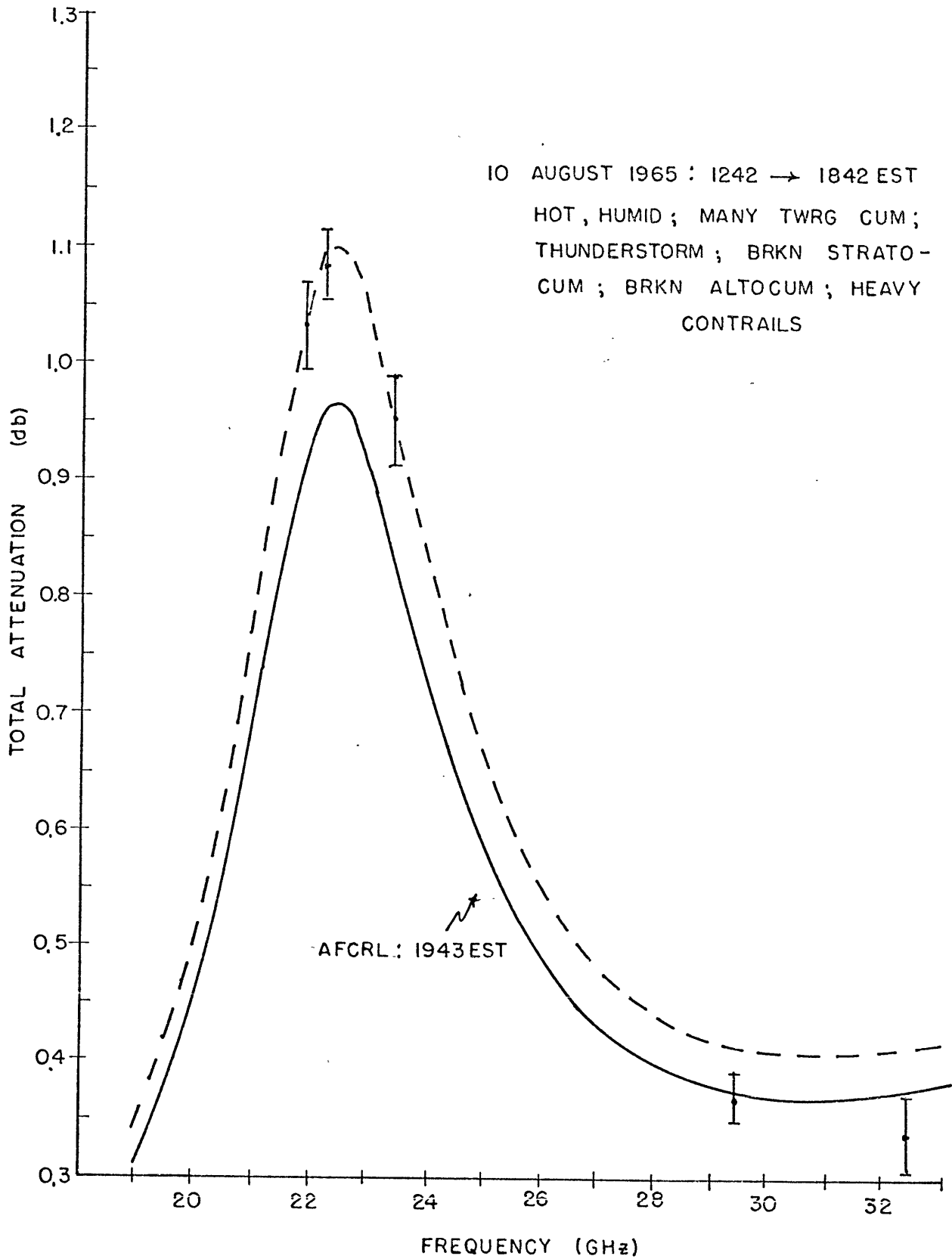
FIGURE 4-27

FIGURE 4-28

FIGURE 4-29

FIGURE 4-30

18 FEBRUARY 1966 : 1507 ⟶ 1647 EST

OVC CIRRUS , CONTRAILS

AFCRL : 1602 EST

FREQUENCY (GHz)

TOTAL ATTENUATION (db)

FIGURE 4-31

23 FEBRUARY 1966 : 1457 ⟶ 1707 EST

SCTD STRATOCUMULUS GOING

CLEAR ; VSBY 50 KM

AFCRL : 1526 EST
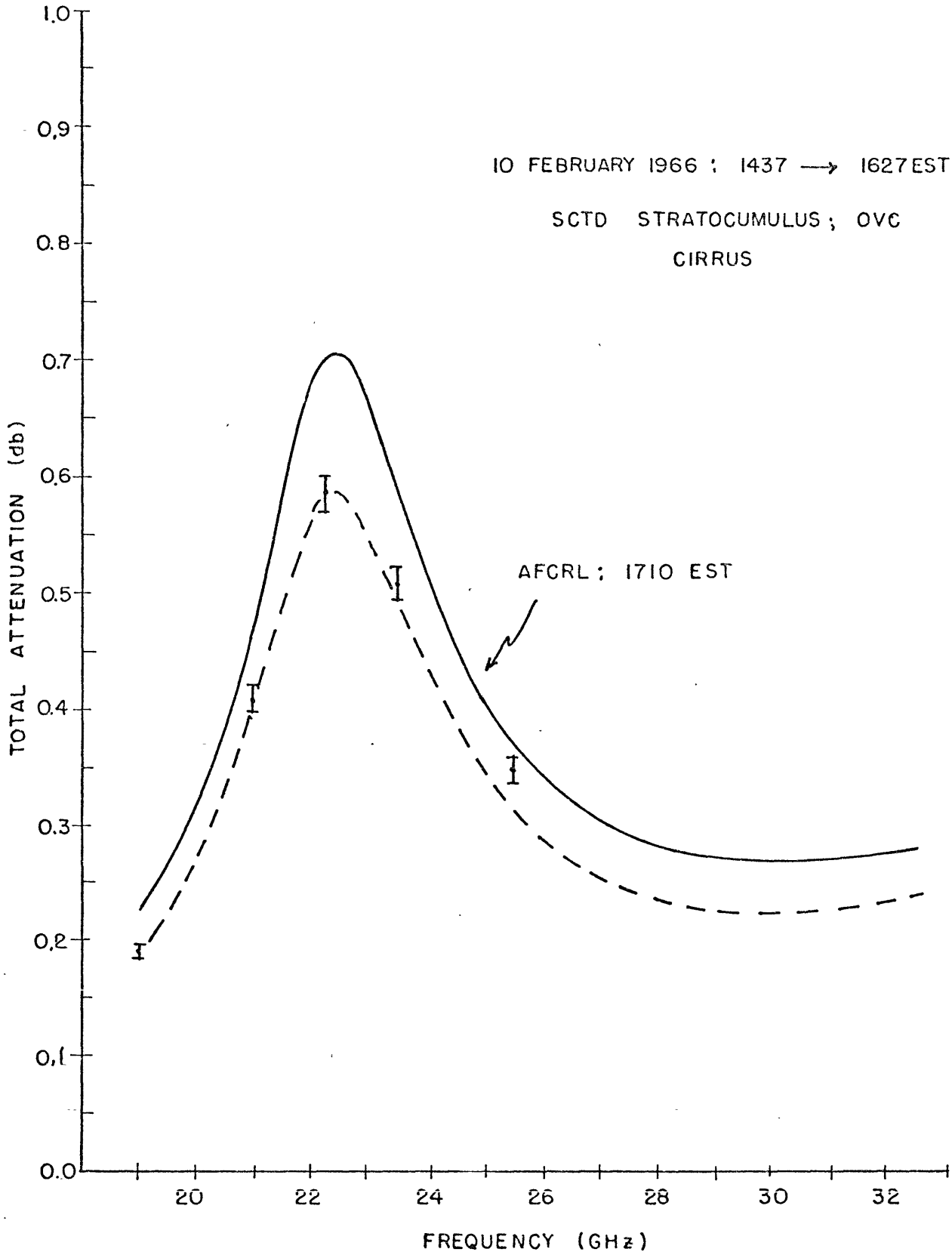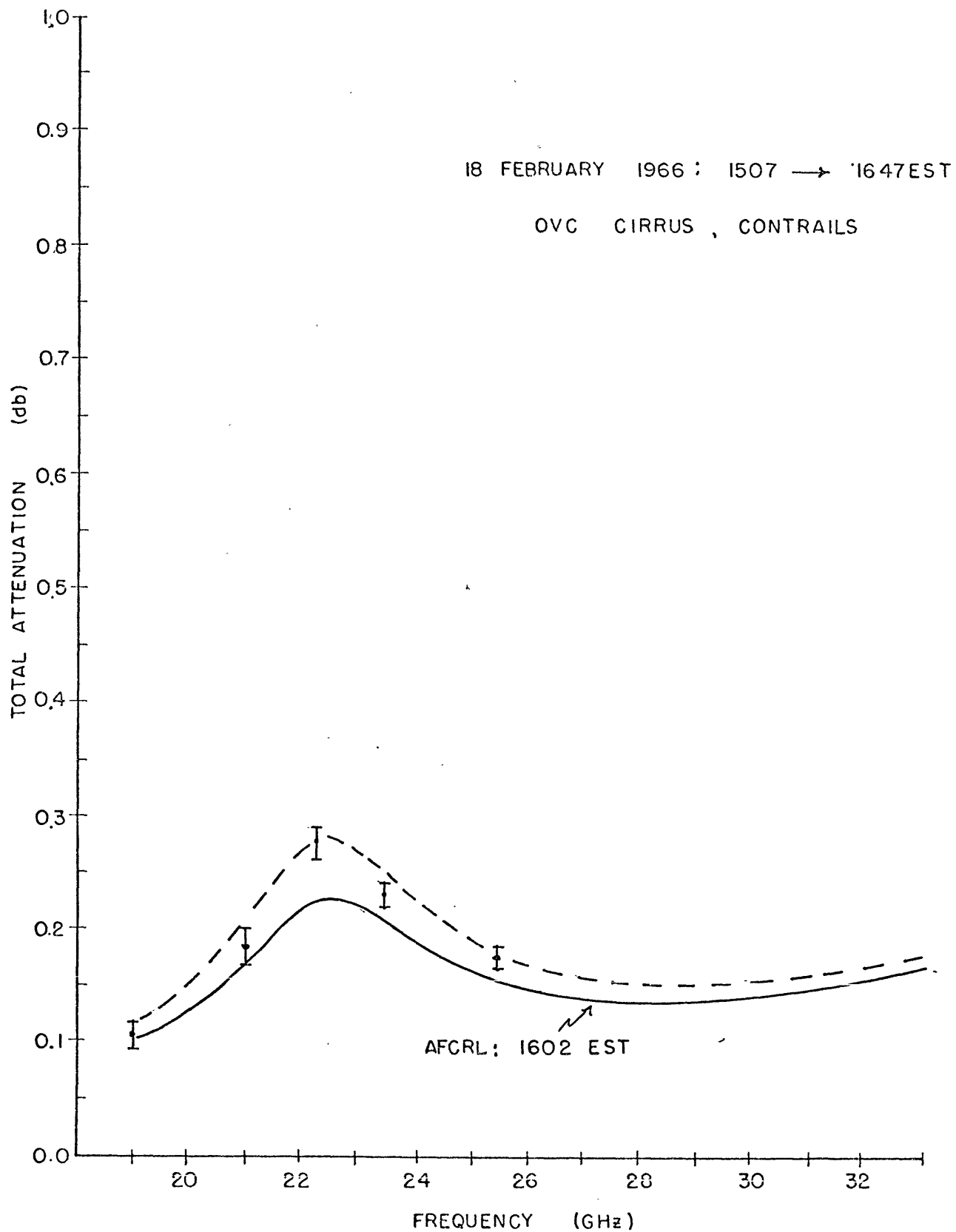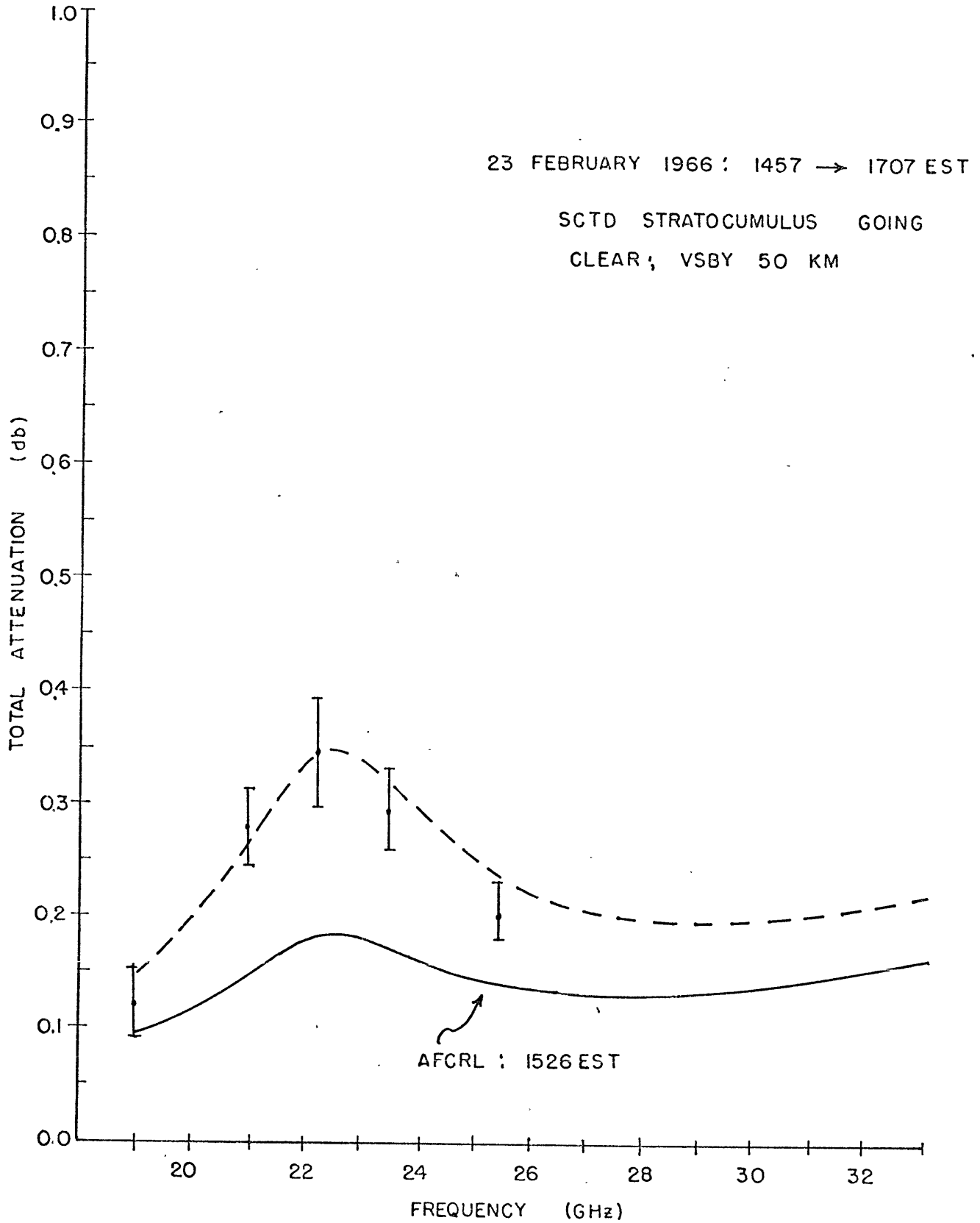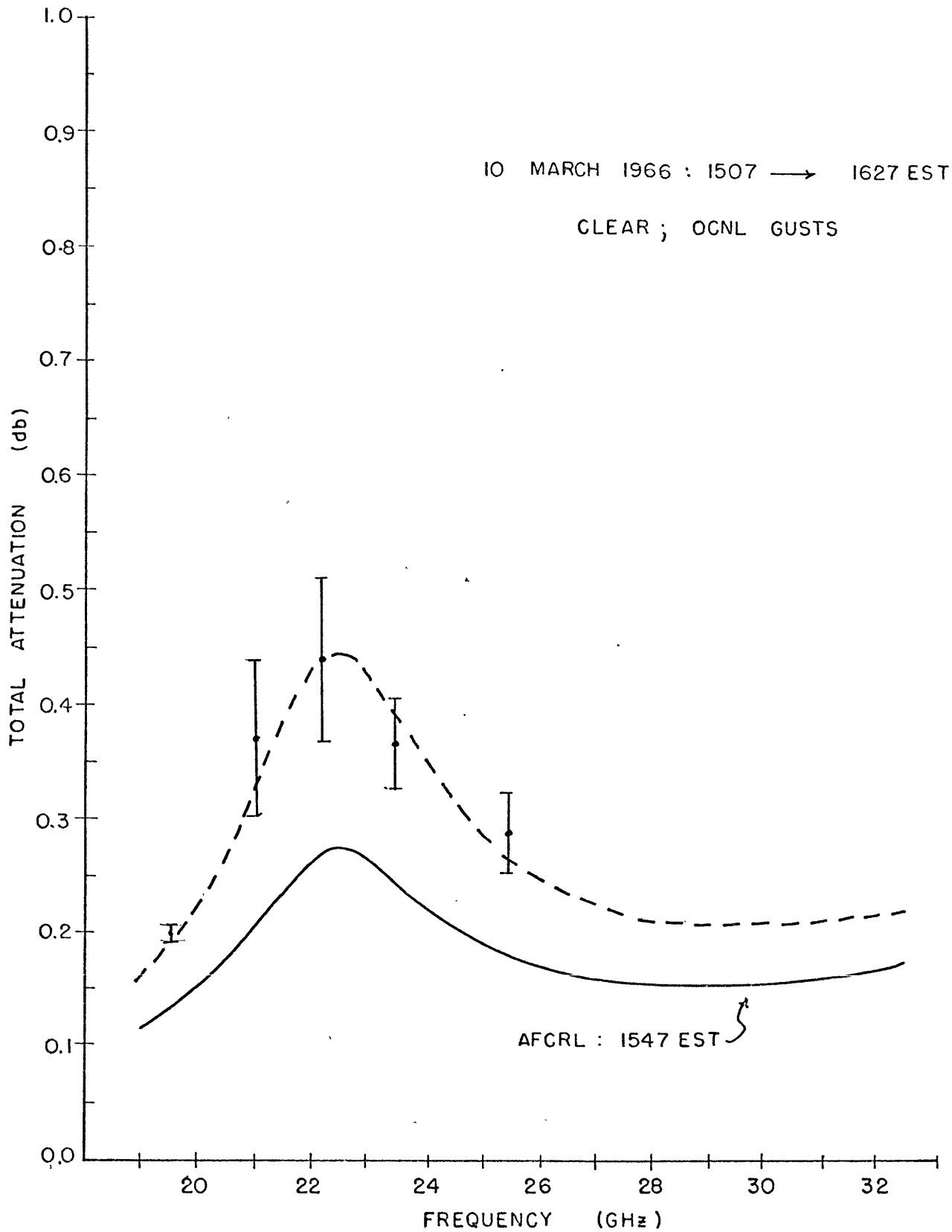
FIGURE 4-32
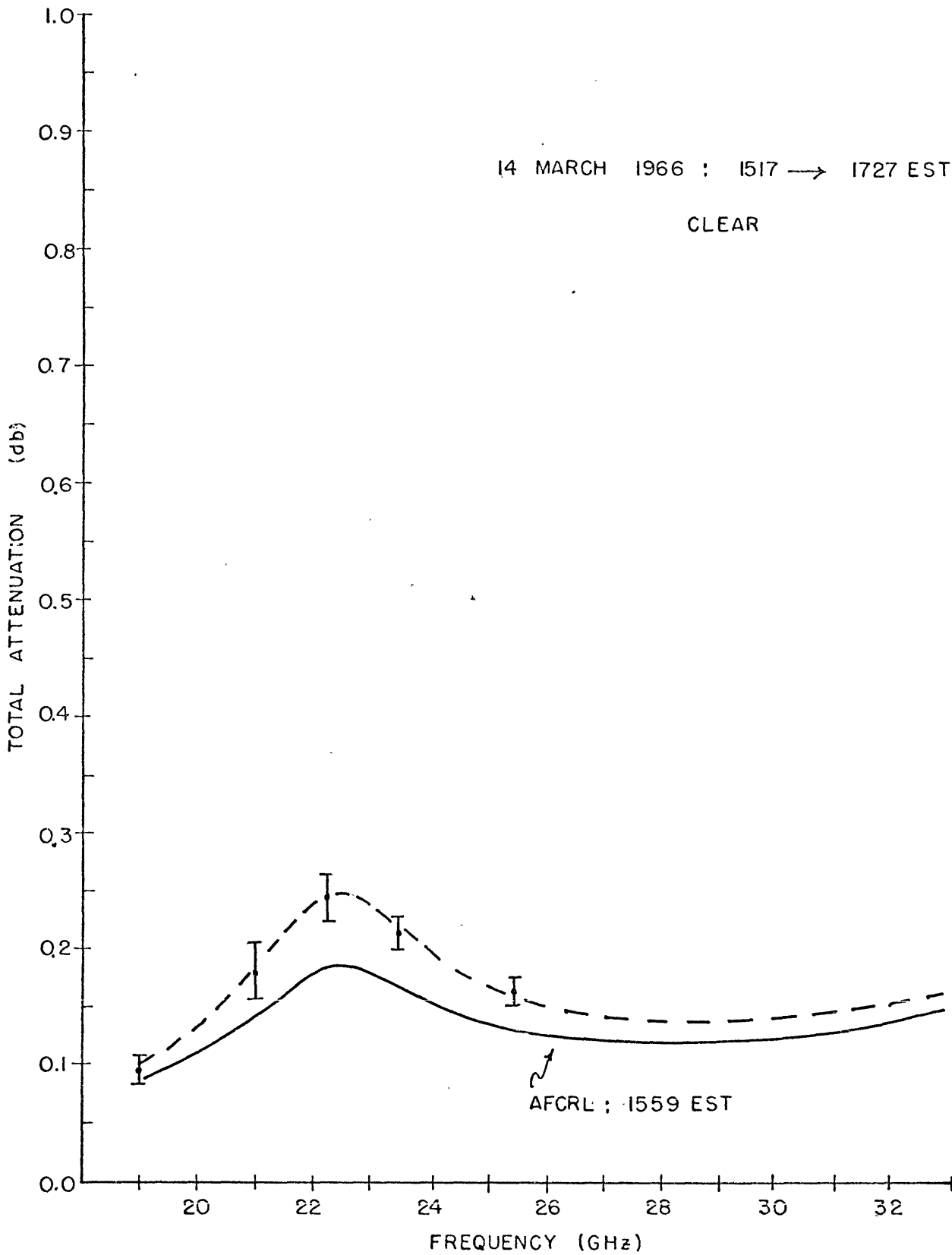
FIGURE 4-33

FIGURE 4-34

The first grouping of spectra (figures 4-3 to 4-11) represents probably the closest correspondence one can expect from radiometer and radiosonde data. They will represent, too, the best data available in this experiment to compare theoretical with true line shape. In this regard the most that can be said is that the theoretical line shape used is certainly adequate within the experimental error. Seven of the nine spectra show observed attenuation to be greater than the computed absorption. This might mean the theoretical line intensities used in the calculations are low, or it might simply mean that radiosondes simply do not detect all the moisture in the atmosphere. We know radiosondes are limited in height and dynamic range so that the latter hypothesis is at least partially true for every radiosonde run. Certainly nothing definite can be said on this point with such a miniscule data sample.

Similarly, the match in the high frequency wing shows about equal numbers of data points above and below the matching spectra. Again, no conclusions can be drawn about the inadequacy of the line shape.

The second grouping of spectra (Figures 4-12 to 4-16) represent conditions where the radiometer is viewing air streaming toward the antenna which contains increasing amounts of moisture. All summer radiosonde data for this series have been taken early in the afternoon and see a drier atmosphere than that measured by the radiometer later in the day. In most instances, the more moist air mass accompanies warm frontal activity. Invariably, the radiosonde is swept in a direction in which the dry air is being taken which heightens the

moisture contrast between the radiosonde and radiometer beam.

Figures 4-17 through 4-22 are days on which dry air masses are replacing more moist ones. In Figure 4-17 the radiosonde was launched after the radiometer observations were completed and therefore sees a considerably drier atmosphere. The remaining days in this series all have radiosonde launches which were earlier than the radiometer observations and therefore show more moisture than do the radiometer attenuation measurements.

The final grouping with analyzed weather conditions is based on days which showed very unstable atmospheric conditions. They are represented by Figures 4-23 through 4-28. Cumulus development in each case was marked, and on some days thunderstorm activity was observed. Gross differences in the observed and computed spectra are apparent, and except for 3 August 1965, radiometer measurements show large probable errors. There are observed spectra whose amplitude is both greater and less than the computed absorption. More will be said about this in Section 4.3.3.

Figures 4-29 through 4-34 are spectra pairs for which the time change of the moisture field could not be ascertained from weather charts or the charts were simply unavailable. Figure 4-29 represents the former case. Figures 4-30 through 4-34 represent the latter.

4.3.3 A Discussion of the Apparent Reasons for Discrepancies
Between Radiosonde and Radiometer Spectra.

To better portray the mechanisms which have caused the rather large discrepancies which appear between some spectra pairs, several of the more thouroughly documented days are reviewed below. One day from each of the four weather groups is analyzed.

For the days of stable weather conditions it is as well to use the spectra taken on the 15th of June 1965, shown in Figure 4-3. The weather prevailing for that day was the result of being near the center of a large high pressure system. Winds were light, only a very lew puffs of clouds existed at low levels and conditions were very steady over the day. The atmosphere was probably the closest to being ideally horizontally stratified on this day as on any day of the experiments. Yet differences between the observed and computed spectra exist. Where do these differences arise? Three possibilities are most likely:

1. Systematic or random errors in the radiosonde and/or the radiometer measurements.

2. Spatial differences in the moisture field between the parts of the atmosphere being measured.

3. Time changes in the atmosphere during the experiment.

Possibilities 2. and 3. are not able to be analyzed under the conditions of the experiment. And, of course, there is no way to measure systematic errors in the radiometer observations. Under the atmospheric conditions which prevailed, systematic errors in the radiometer data should be small; it is thought smaller than the observed

computed spectra difference. This leaves errors in the radiosonde data as a possible source of the discrepancy. This possibility may be fruit-fully analyzed.

Marchgraber[44] has analyzed the carbon type humidity element which was used on all radiosondes flown for the experiments. His conclusions, after exhaustive experimental studies, were that the accuracy of an element to record the relative humidity, if it had not been subjected to extreme conditions during storage and if it had been properly cali-brated before launch, was 5% over the range from 25% to 85% relative humidity and between $-35^{\circ}C$ and $+35^{\circ}C$ ambient temperature. Further, outside the permissible relative humidity and temperature ranges, trend information only, not quantitative information, could be expected. The dynamic response of the element, studied by Grote and Marchgraber[45], appears to be a non-limiting factor for measurements of the type of stable atmosphere whose spectra is given in Figure 4-3.

The humidity range limits of the carbon element immediately produce a bias towards low total atmospheric water vapor for dry cold atmospheres. Relative humidity values below 25% and atmospheric tem-peratures below $-35^{\circ}C$ are quite common. In the atmosphere which produced the curves of Figure 4-3, the relative humidity dropped to levels below the threshold of the sensor at a fairly low altitude and thus for much of the run no moisture was recorded. No bias like this exists for the radiometer and therefore one would expect, for a per-fectly stratified atmosphere, a lower absorption curve than attenuation

curve. This is what is seen not only in Figure 4-3 but in eight out of nine days of the set of stable weather spectra.

To portray the second category of spectra, the data collected on the 14th of July 1965 has been chosen. Its spectra is shown in Figure 4-13. Observations started with clear conditions at 1652 EST. As the experiment progressed cirrus from an advancing warm front moved into the beam of the antenna, haze became apparent at the surface, and the dewpoint steadily increased even though the temperature decreased through the afternoon. By the end of the experiment, the dewpoint had risen to $68^{\circ}F$ ($\sim 291^{\circ}K$) up from $61^{\circ}F$ two hours earlier. This indicated that the water vapor density in the atmosphere around the antenna had increased from 18 to 24 g/m^3 or by one third. By 1900 EST the cirrus had become overcast and altostratus was visible in the west. Heavy haze partially obscured horizontal ground visibility.

The radiosonde for the 14th of July was launched at 1458 EST in clear conditions, two hours before the start of the radiometer exper-iment. The level of moisture detected was substantially below that seen by the radiometer in agreement with the weather trend. There seems no reason to doubt that the discrepancy between the observed and computed spectra are mostly real differences originating in tem-poral changes in the moisture field.

During the morning of the 15th of July, the day after the observation reviewed above was made, a warm front and subsequently a cold front passed the Boston area. During the observations from

that day, shown in Figure 4-20, a northwesterly wind blew bringing in

very dry air. The dew point at the beginning of observations (1442 EST)

was recorded as 56^oF (~ 16 g/m^3 water vapor density) at Hanscom Field,

perhaps a mile distant from the antenna site. Three hours later the

dewpoint was recorded as 47^oF (~ 11 g/m^3), a drop in the moisture content

at the surface of 32%. However, even this decrease does not explain

the difference between the spectra computed from the first radiosonde

of the day launched at MIT at 1525 EST and the radiometer spectrum.

The difference is closer to 50% in total water vapor content. It is

conceivable that upper layers of the atmosphere were drying out faster

than the frictionally slowed surface layers. But this is not borne out

from the second radiosonde launched from AFCRL at 1857 EST quite near

the end of the radiometer observations. The moisture reported by this

flight is about 38% above that observed by the radiometer. The only

other possibility seems to be that the difference stems from the radio-

sondes being carried with the moist air while the antenna was viewing

the source direction of the dry air. Though true, this last possib-

ility is not very quantitatively convincing. We must conclude there-

fore, that the trend towards drying is correctly mirrored by the

difference in spectra amplitudes but there remains an unanswered question

as to why such large discrepancies exist between the radiosonde and

radiometer spectra.

As a last example of particular causes of the differences

between the radiosonde and radiometer spectra, the experiment on the

10th of August 1965 (Figures 4-26, 4-27, and 4-28) has been analyzed.
Three radiosondes were launched that day, two from MIT (1305 EST and
1704 EST) and one from AFCRL (1943 EST). The experiment covered the
period 1242 to 1842 EST. The day was very humid. The atmosphere was
unstable; many towering cumulus and thunderstorms could be seen or were
reported. Broken (> 50% coverage of the sky) stratocumulus, altocumulus
and cirrus covered the sky. The activity accompanied the passage of
a cold front through the area during the experiment.

The first radiosonde (Figure 4-26) was launched as the observa-
tions began and showed perhaps 10-15% more moisture than the radiometer
results. The second radiosonde (Figure 4-27) was launched about in
the middle of the observational period and reported about 8-10% more
moisture than observed. And the third radiosonde was launched approx-
imately one hour after the end of the experiment and reported about
13-15% less moisture than observed.

At least two logical explanations for these differences exist.
One would have the radiosonde on the first two flights penetrate
clouds on ascent and record moisture over a substantial portion of
the flight at levels greater than the average for those levels, since
the clouds covered less than 100% of the sky. Then the third radio-
sonde, during its ascent, passed entirely between clouds recording
less than the average amount of moisture for these levels with clouds.
The antenna beam, on the other hand, always saw some average moisture
level, including cloudy and clear regions, and therefore recorded an

intermediate level of moisture between cloudy and clear radiosonde runs.

The second possible explanation is based on the frontal passage. The first two radiosondes were launched and were carried along with the moist air ahead of and near the front. The third was launched in drier air behind the front. The antenna beam was looking on the average into drier air than the first two radiosondes but considerably more moist air than the third.

It is likely that the last explanation is the more correct of the two, but it is not clear exactly how clouds did affect the results. Therefore, again, we can say that a logical explanation for the differences exist, but without a quantitative foundation.

Chapter 5

DETECTION OF STRATOSPHERIC WATER VAPOR BY MEANS OF

MICROWAVE MEASUREMENTS

On the basis of high altitude balloon measurements of uncondensed

water vapor[64,65,66], Barrett and Chung[31] in 1962 predicted that an anom-

alous emission "spike" should be apparent in ground based microwave

observations of the atmosphere at frequencies very near the 22.237 GHz

water vapor rotational resonance. The spike would be superimposed on

the normal broadened emission line arising from tropospheric water vapor.

It would be the result of excess water vapor in the stratosphere; excess

being determined to be an increase in the water vapor mixing ratio with

height somewhere in the region above about 30 km. Because the line narrows

in direct proportion to the total pressure, any anomalous vapor above 30 km

can only affect a frequency region very near to the line center. And even

though very little total water vapor can exist at high altitude, its con-

tribution is so concentrated (intensity at line center is approximately

proportional to ρ/P , where ρ is the water vapor density and P the

total pressure) that the amplitude of the spike above the gross line

profile was predicted to be a substantial fraction of the total emission

at resonance.

Since Barrett and Chung's paper, at least one attempt has been

made to detect the spike[67] besides the effort reported here. That effort

showed negative results.

In order to further extend our understanding of the spike, and therefore our knowledge of the distribution of water vapor in the stratosphere, this chapter reexamines the problem on the basis of the latest high altitude balloon measurements of water vapor and upon the microwave measurements reported in Chapter 4.

5.1   Stratospheric Water Vapor and its Relationship to Microwave Measurements.

The earliest authoritative measurements of water vapor in the lower stratosphere were done soon after World Warr II in Britain. (For a review of the measurements of stratospheric water vapor before 1961 see Gutnick[68]).   These measurements from aircraft showed a sharp decrease in moisture as one penetrated the tropopause. Later airplane measurements, also done in Britain, tended to confirm this dryness in the lower stratosphere. On the basis of these measurments, a stratospheric water vapor model was predicated which showed the entire stratosphere to be quite dry.

Other investigations of stratospheric water vapor were conducted using balloons and humidity sensors. The results from many of these flights contradicted the British model by showing that, even though a dry region existed just above the tropopause, the absolute density of water vapor at altitudes above approximately 20 km many times did not decline, and on some occasions even increased with height. The resonant spike predicted by Barrett and Chung was based on such measurements.

Because of the large discrepancy between the measurements
mentioned above, several attempts have been made in the last several
years to measure stratospheric water vapor with a fidelity which would
answer the question of whether the stratosphere was "wet" or "dry".

One of the major problems which had to be overcome for balloon
measurements was outgassing of water vapor from the measuring apparatus.
As equipment ascends into the stratosphere, water vapor normally ad-
sorbed onto the exposed surfaces begins to evaporate. In the tropo-
sphere, this outgassing constitutes a negligible percentage of the
total water vapor being measured. In the stratosphere, however, where
extremely dry conditions can occur, outgassing water vapor apparently
can become the major contributor to the water vapor being measured.
Such conditions, of course, invalidate the results from any measure-
ments made. (For a discussion of the contamination problem see
Mastenbrook[69]).

As apparatus and techniques have become more sophisticated,
especially with respect to the contamination problem, the very wet
stratospheres measured in the nineteen-fifties and early nineteen-
sixties have not been repeated. Measurements below 30 kilometers
at low, middle and high latitudes in 1964 and 1965 by Mastenbrook[70]
and at midlatitudes by Sissenwine, et al.[71] tend to confirm a generally
dry stratosphere. Some of the runs do, however, show trends near
their peak altitudes which have interesting implications for the region
above 30 kilometers.

5.5.1 Model Atmospheres for the Simulation of Stratospheric
Microwave Absorption and Emission.

In order to better understand the origin and nature of the stratospheric water vapor spike, a number of model atmospheres have been constructed and will be investigated. They are presented in Figures 5-1, 5-2, and 5-3. Their temperature profiles are the Standard Atmosphere, 1962, (midlatitude), and the Tropical and Subarctic (summer) supplements thereto, as presented in the Handbook of Geophysics and Space Environments[41]. (An Arctic supplemental atmosphere appears with the subarctic atmosphere, but extends only to 30 km. The distribution of temperature above this level was not available. The profile is included because it has been used for analyses appearing in Chapter 3). The moisture curves for the atmospheres (represented as dew point-frost point curves) up to the 10 km level are means for the latitudes represented. They are also reported in the Handbook of Geophysics and Space Environments.

Above 10 kilometers, distributions of moisture have been extended to 28 kilometers based on the profiles reported in either Mastenbrook or Sissenwine, et al. Five hypothetical distributions of water vapor above the 28 kilometer level have been suggested for the Tropical and Midlatitude atmospheres and four for the Subarctic.

The moisture distribution in each case is smoothly extended to 90 kilometers. This neglects the possibility that photochemical reactions above the 70 kilometer level may deplete the available water vapor
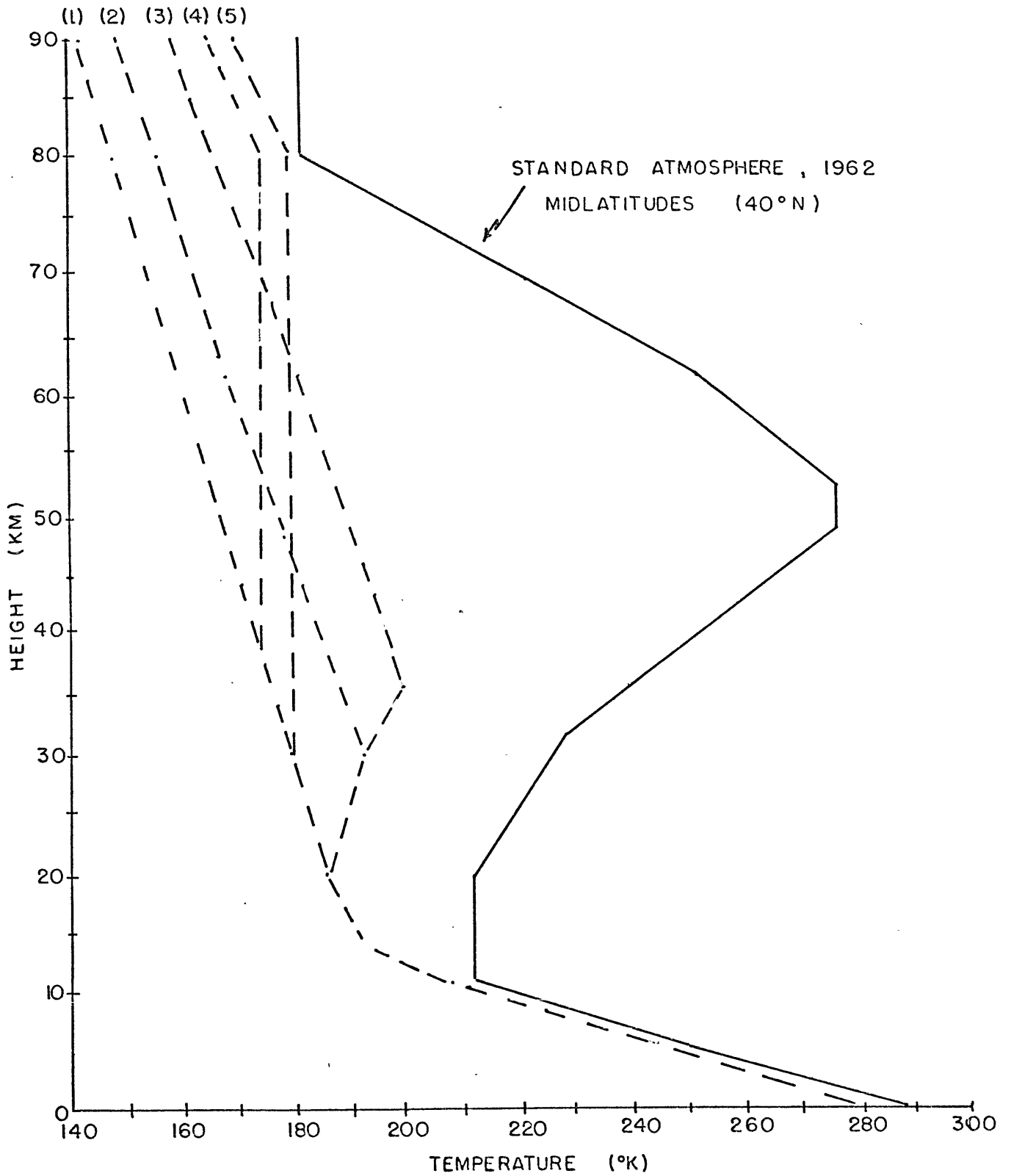
Figure 5-1. Standard Atmosphere (midlatitude), 1962, with five hypo-
thetical moisture distributions.
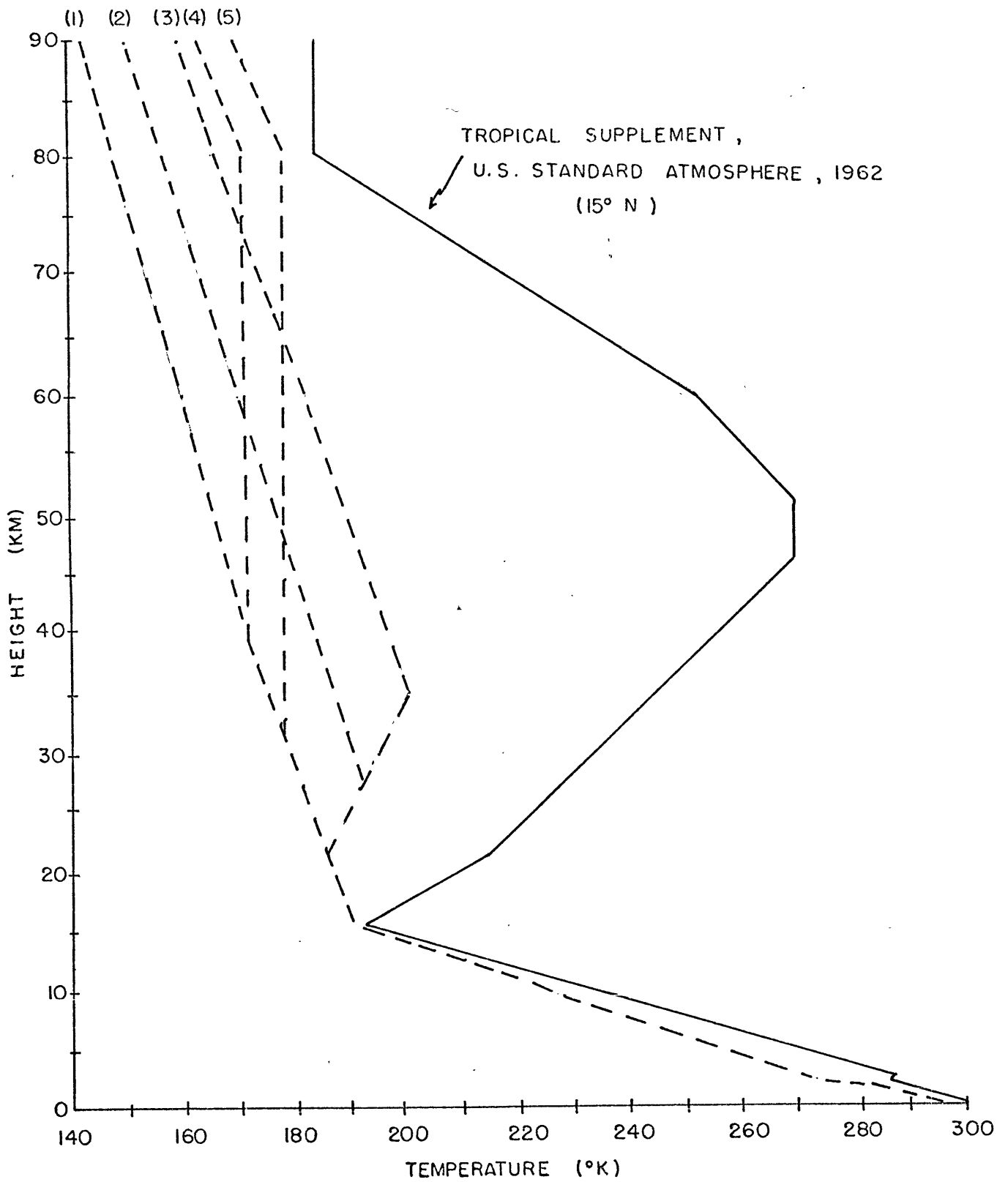
Figure 5-2. Tropical supplemental standard atmosphere with five hypo-
thetical moisture distributions.
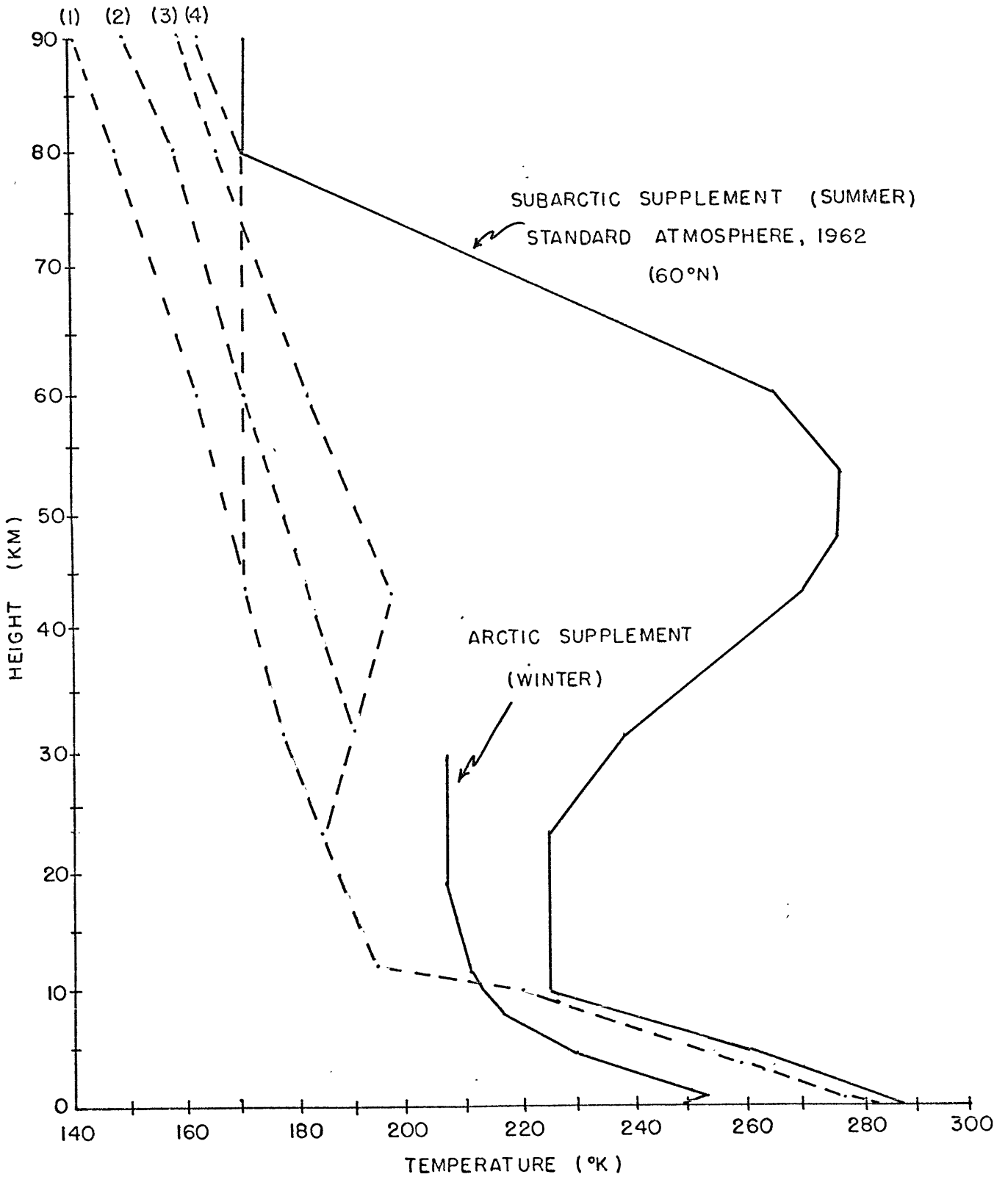
Figure 5-3. Subarctic (summer) supplemental standard atmosphere with four hypothetical moisture distributions.

supply, as suggested by Hunt[72]. However, the effects of excess water vapor above the 70 km level will show up in our calculations as a very narrow extension of the spike we are investigating. Its presence will alter the results we are most interested in very little, i.e., those in which the finite bandwidth of the radiometer is taken into consideration. And they leave open the question of whether saturation does occur in the region of 80 km where noctilucent clouds have been observed. The particles making up the clouds may be meteoric dust with coatings of ice[73]. The Subarctic Supplemental Atmosphere, which has the lowest temperature at the mesopause of all the model atmospheres and is representative of the latitudes and season for noctilucent clouds, has one hypothetical moisture distribution which is saturated at the 80 km level.

All of the moisture profiles below 30 km for the atmospheres presented do not exceed in absolute water vapor density the wettest atmospheres reported in Mastenbrook. The water vapor profiles above 30 km attemp to follow some of the trends which were evident in the observed data near the top of their ascents. The exact profiles are necessarily subjectively determined.

In the Tropical and Midlatitude Atmospheres the profiles are constructed with the approximate scheme of having constant mixing ratios of 2×10^{-6} grams of water vapor per gram of dry air for profile (1), 2×10^{-5} g/g for profile (2), 2×10^{-4} g/g for profile (3), and two profiles, (4) and (5), which have constant water vapor densities above a certain level. The constant mixing ratio profiles, when these ratios are greater

than the mixing ratios in the lower stratosphere, have been achieved by increasing the water vapor just above the 30 km level.

The Subarctic atmosphere is similar except that there is only one constant vapor density case. This case, however, provides for saturation at the mesopause. Whether or not saturation occurs at the mesopause during the existence of noctilucent clouds is not known. If the only source of moisture is from diffusion from the troposphere through the extreme cold of the tropopause, it appears that a constant mixing ratio of water vapor to air would be expected throughout the stratosphere. However, several mechanisms which might upset this are: (1) strong localized intrusions of moisture into the stratosphere from the troposphere and circulation patterns which eventually carry the moisture upward (for an account of large thunderstorms which penetrate the tropopause see Long[72]); and (2), a secondary source of water vapor at high altitudes[73].

For each of the model atmospheres the integrated water vapor above 30 km is listed in Table 5-I below, ML stands for midlatitude, TS for Tropical Supplement, and SS for Subarctic Supplement.

TABLE 5-I. Integrated water vapor above 30 kilometers in microns of precipitable water for the various models discussed in the text.

Model	ML	TS	SS
1	0.26	0.26	0.31
2	2.6	2.6	3.0
3	18.	19.	11.
4	0.79	0.81	0.66
5	1.97	1.96	-
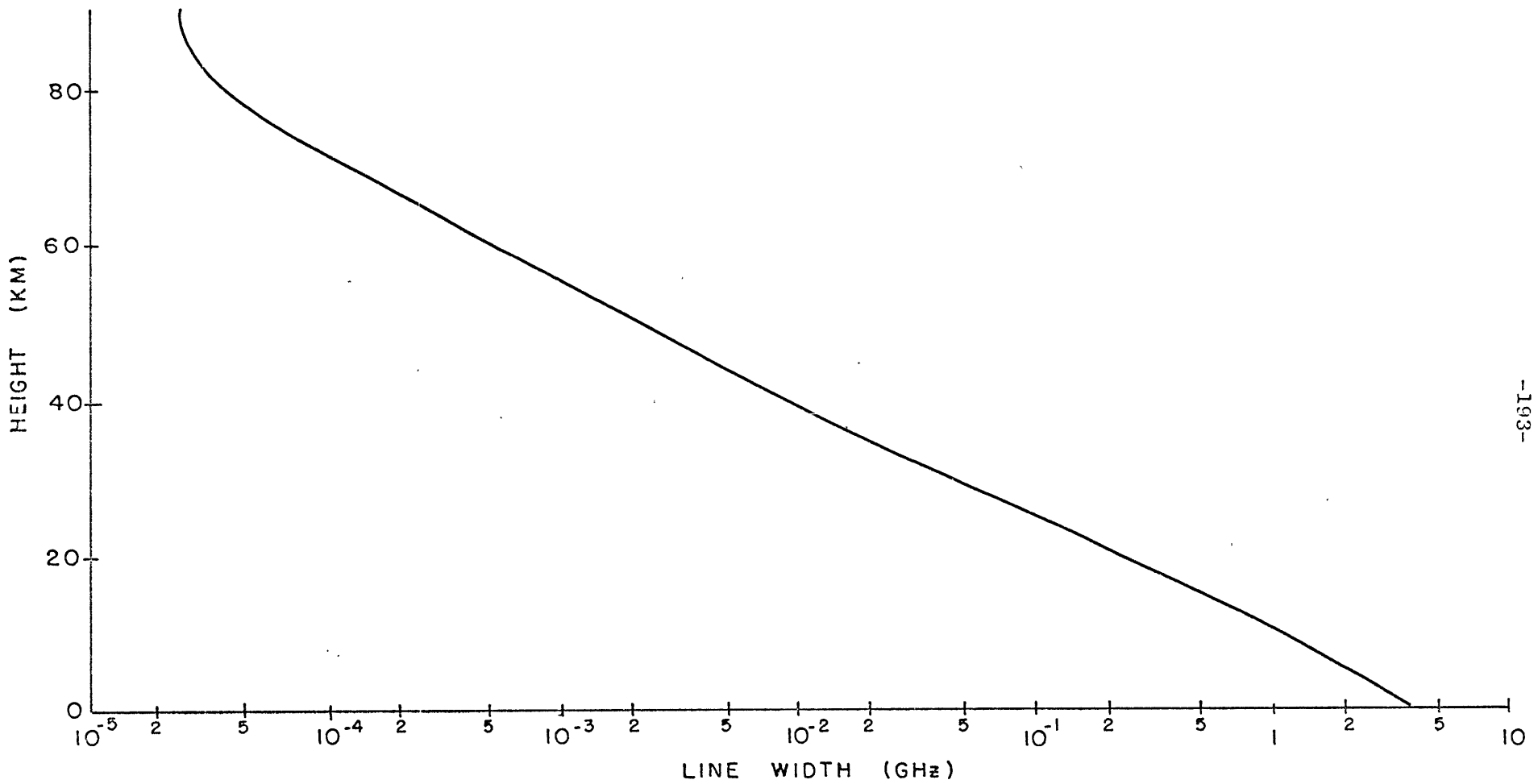
Figure 5-4.   The line width of 1.35 cm water vapor resonance as a function of height in the atmosphere.

The values compare with 17 and 44 μ of precipitable water vapor above

30 km for the atmospheric models used by Barrett and Chung.

5.1.2 The Line Widths for the Model Atmospheres.

The existence of the stratospheric spike is based upon the extreme

narrowing of the spectral line at low pressures. How this line width

varies with height is shown for all the atmospheres in Figure 5-4. The

slight upturn at 75 to 80 km is due to the relatively increasing impor-

tance of Doppler broadening at these levels. It depends only upon the

square root of the temperature and therefore fluctuates over the entire

lower 100 km of the atmosphere less than one order of magnitude. It

should be noted that at about 72 km, the line half-width has narrowed

to 100 KHz, and by 90 km is roughly 25 KHz.

5.1.3 The Stratospheric Water Vapor Spike Produced by
Model Atmospheres.

If we compute the absorption which the midlatitude Standard Atmo-

sphere of Figure 5-1 would produce, we would obtain the spectrum which

is plotted in Figure 5-5. This is the spectrum which a radiometer of

infinitely small bandwidth would see. The normal line shape due to

pressure broadening of tropospheric water vapor is pierced by an extremely

thin spike due to the vapor above approximately the 28 to 30 km level.

The designations ML1, ML2, etc. are indicators of the height of the

spike for each of the stratospheric vapor variations numbered in Figure
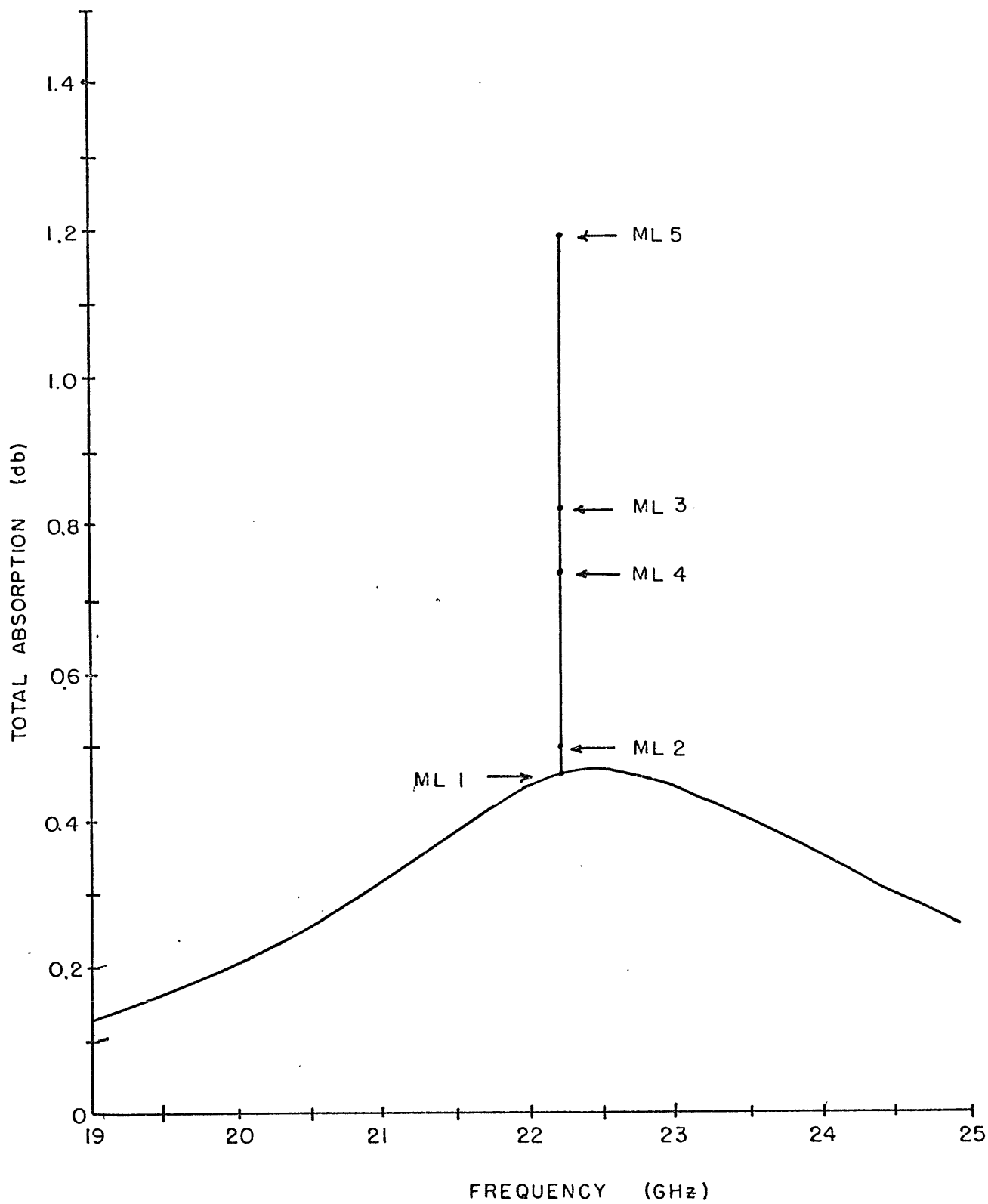
Figure 5-5. The opacity spikes caused by the milatitude atmospheres.

5-1. The constant mixing ratio case for the driest atmosphere

(w = $2x10^{-6}$ g/g) shows no spike at all. The most pronounced spike is

produced by the atmosphere which shows a constant frost point (and

therefore a constant water vapor density) above 30 km. This is quite

expected after considering that this model places the greatest amount

of water vapor at the highest levels. It will be seen that the mag-

nitudes of the spike shown in Figure 5-1 will be altered significantly

when we consider finite bandwidth radiometers.

In Figure 5-6, the narrowness of the spikes are brought out more

clearly by the expanded frequency ordinate. For even greater detail,

a one MHz plot of the region about resonance is shown in Figure 5-7.

It is much more clear in this figure how very narrow the spikes produced

by the model atmospheres really are. The width of the ML4 and ML5

spikes are less than 100 KHz. The larger width of the ML3 spike results

from the large amount of water vapor immediately above 30 km.

5.1.4 The Effects of a Finite Bandwidth on the Amplitudes

of the Stratospheric Spikes Computed for the Model

Atmospheres.

It is clear from Figure 5-5 that even with a radiometer with

infinite bandwidth resolution, we could not detect the presence of

water vapor in the stratosphere if it were distributed as it is in

ML1 i.e., an overall small amount of water vapor decreasing with height

so as to maintain a uniform mixing ratio from tropopause to mesopause.
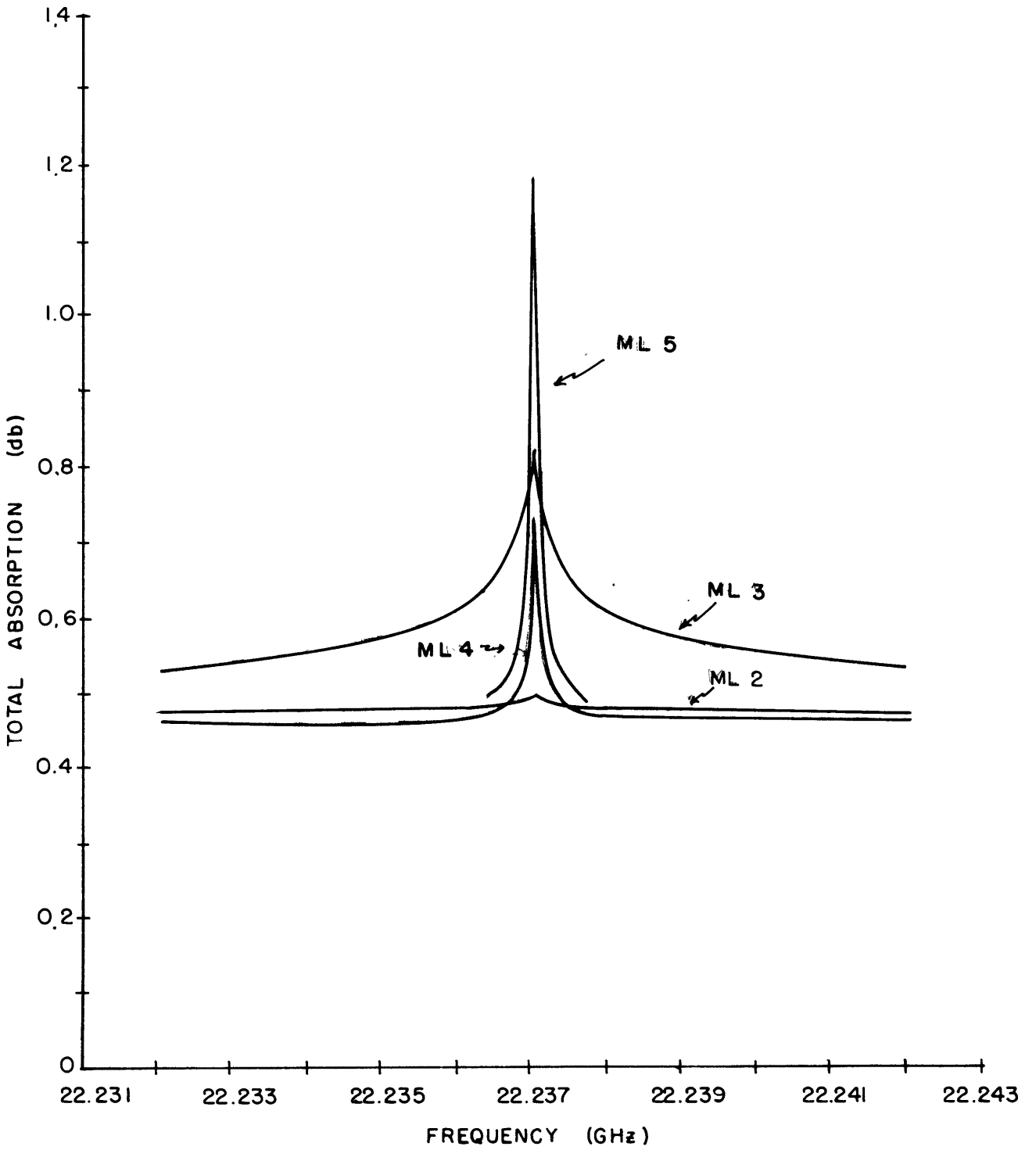
Figure 5-6. The midlatitude opacity spikes on a 12 MHz scale.
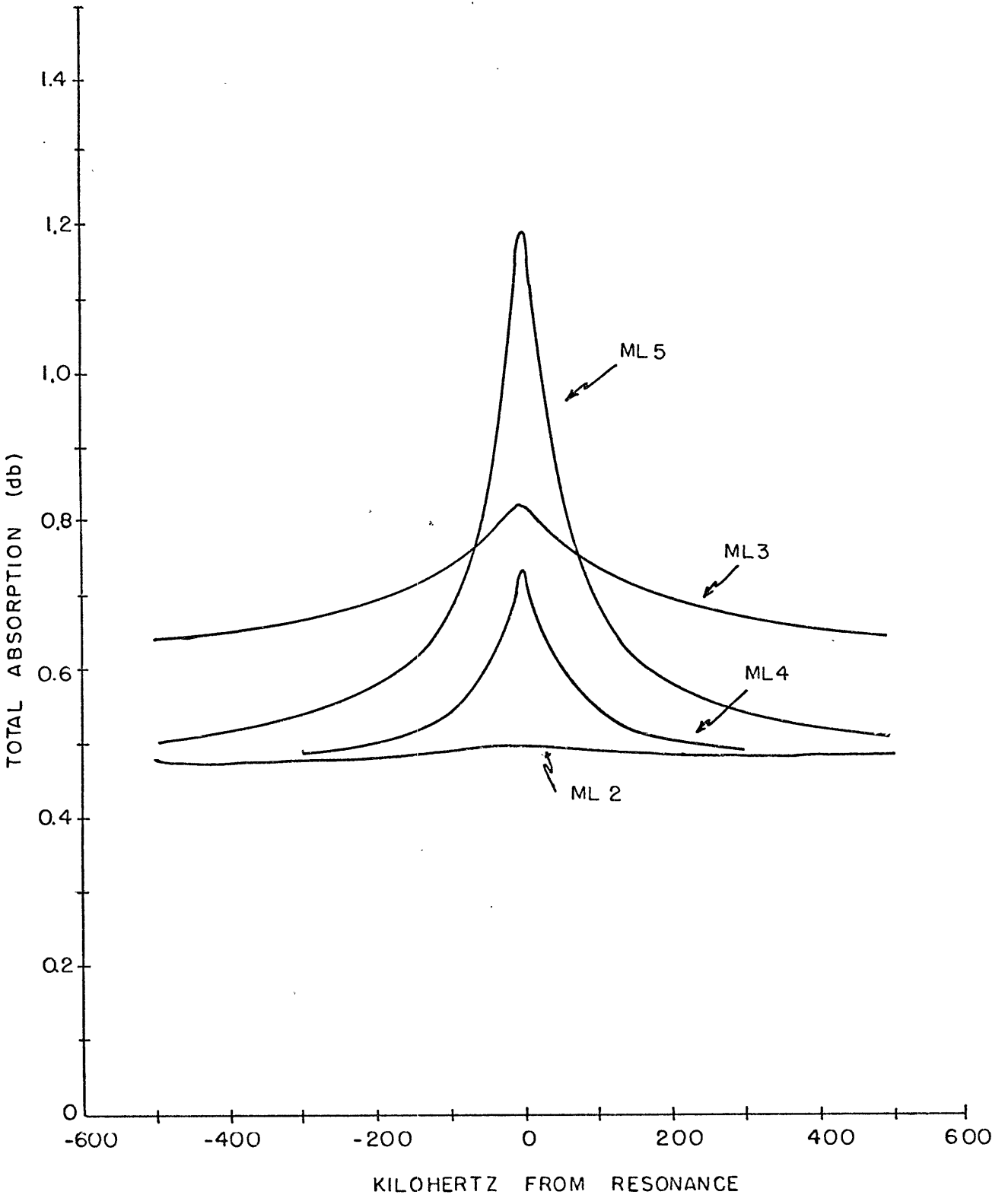
Figure 5-7. The midlatitude opacity spikes on a 1 MHz scale.

The amplitudes for the other spikes would most likely be detectable
with an infinite resolution radiometer, but, since such an instrument
cannot exist, the effect of bandwidth must be considered.

The newest equipment being built at the Massachusetts Institute
of Technology to study the resonance region of water vapor uses filters
to achieve a one MHz bandwidth. For such resolution, the spikes of
Figure 5-6 would be reduced to those seen in Figure 5-8. For amplitude
comparisons on and off the center of the line, the atmospheres repre-
sented by ML3, ML4, and ML5 have a reasonable chance of detection.
With ideal atmospheric conditions, and a well tuned radiometer, the
smallest amplitude variation detectable is in the vicinity of 0.01 db.
The resonant enhancement in the ML2 atmosphere is only 0.02 db and it
is very broad; it must be considered, therefore, to be a very marginal
stratospheric distribution to detect by opacity measurements.

For the observations reported in Chapter 4, the nominal band-
width of each radiometer was 8 MHz in each sideband. The sidebands
were separated by 60 MHz. The spike produce by the midlatitude model
atmosphere would appear as in Figure 5-9 for an 8 MHz bandwidth for
a single sideband radiometer. The vertical scale has been increased
by a factor of four in Figure 5-9 over that used in Figure 5-8. The
spikes are greatly smeared by the large bandwidth-to-spike-half-width
ratio, and their detectability has been further reduced from the one
MHz resolution case.

For a synopsis of the effect of the bandwidths discussed,
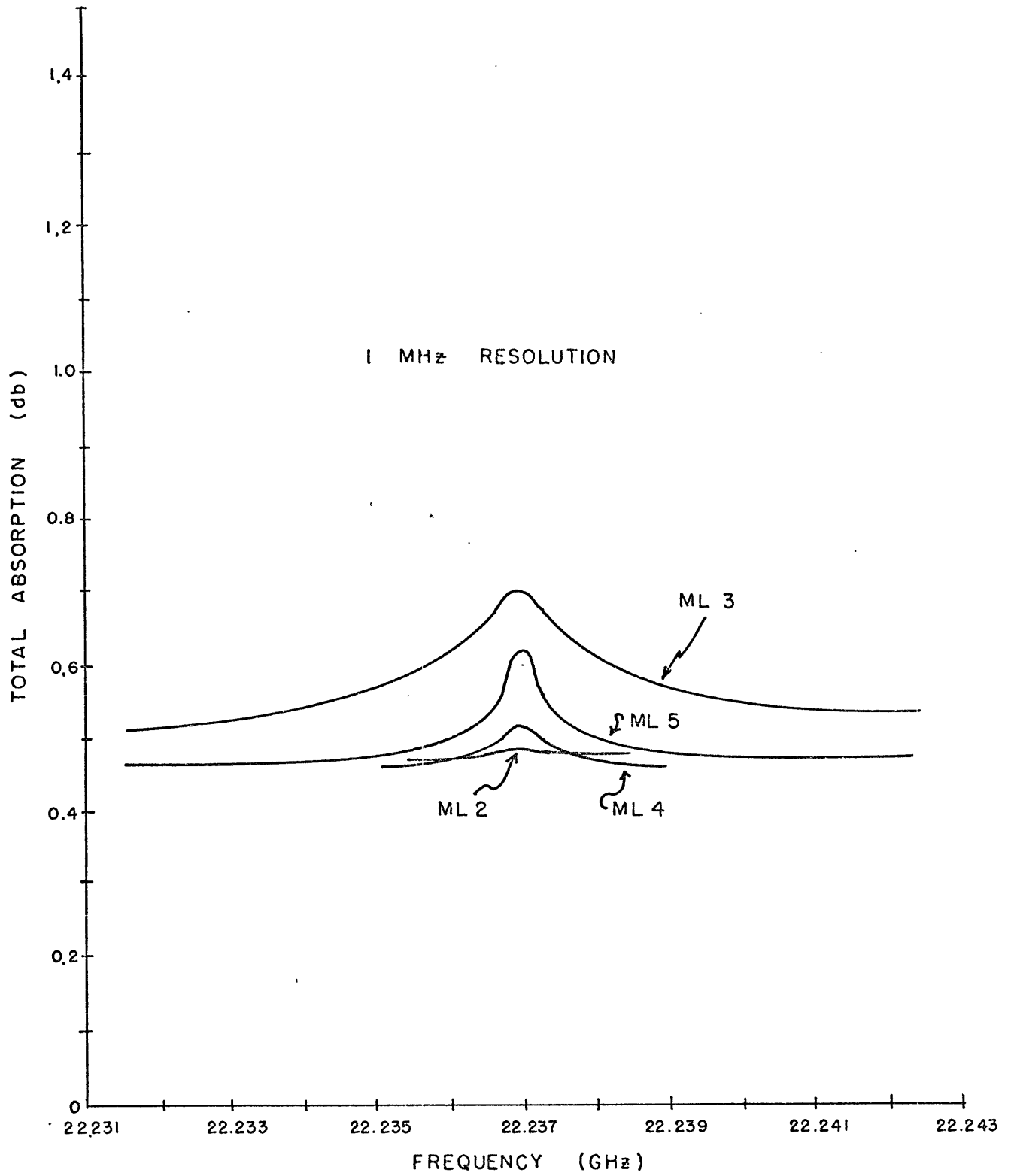
Figure 5-8.   The midlatitude opacity spikes seen by 1 MHz bandwidth
radiometer.
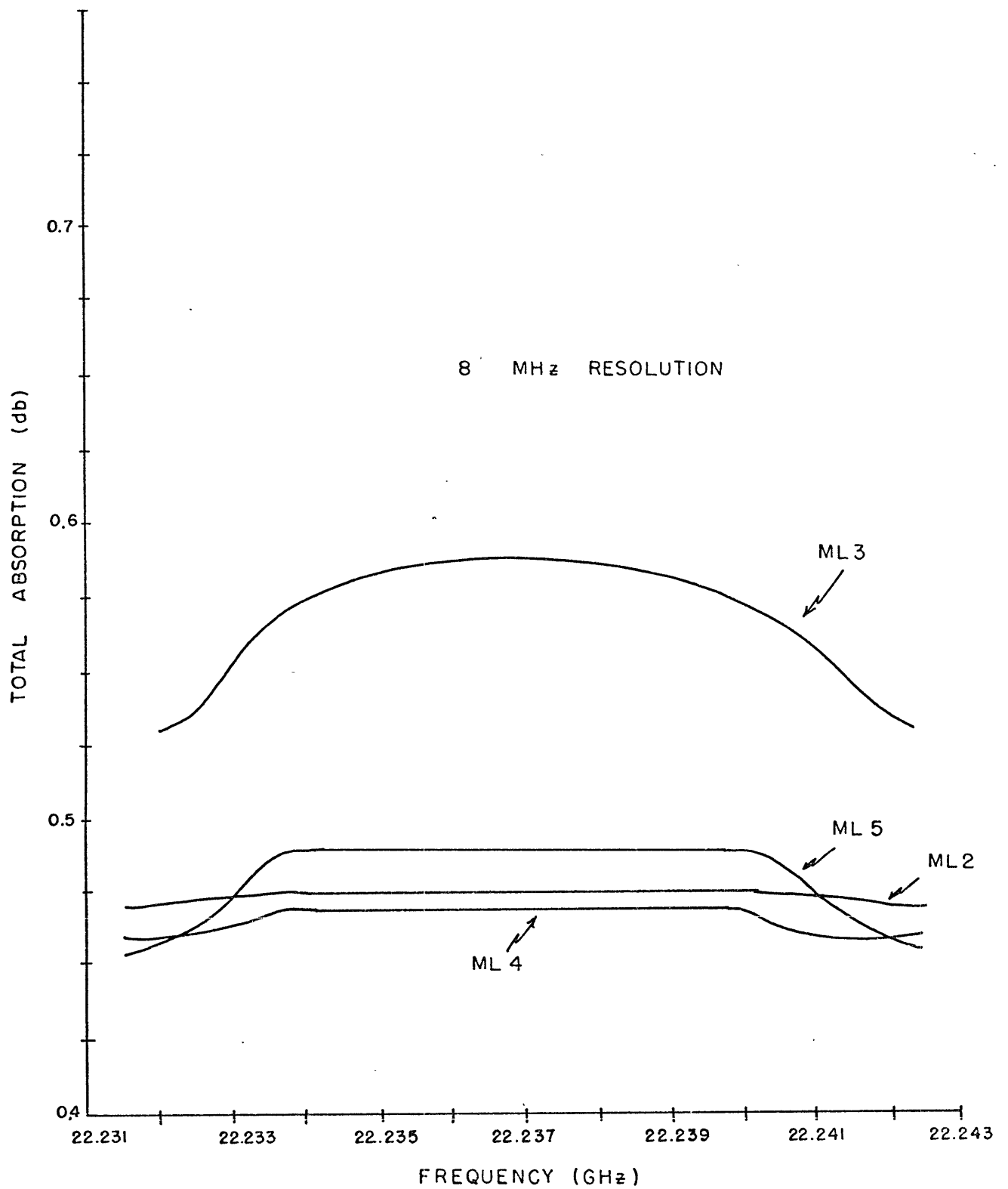
Figure 5-9. The midlatitude opacity spikes seen by an 8 MHz bandwidth
radiometer.

Figure 5-10 compares the amplitudes of the spikes for infinite, 1 MHz,

and 8 MHz resolutions. The spikes which at first looked so promising

to detect with infinite resolution, have, in the 8 MHz resolution case,

been reduced to one easily detectable case, three marginal cases, and

one for which there is no chance of detecting.

And finally, for a double sideband radiometer as used to obtain

the data reported in Chapter 4, all of the amplitudes must be reduced

by one half. Therefore, under the most ideal atmospheric conditions

and with the most finely tuned radiometer, ML1, ML2, and ML4 disappear

into the noise; the spike from ML5 is of marginal detectability; and

only the water vapor of the atmosphere depicted by the ML3 curve of

Figure 5-1 is apparently safely detectable. Its amplitude would be

approximately 0.06 db above the absorption measured at nearby frequencies.

5.1.5   The Results of Opacity Measurements at 22.237 GHz.

One of the purposes of the summer observations reported in

Chapter 4 was to search for the stratospheric water vapor spike.

Accordingly, one of the five radiometers was tuned so that one of its

two sidebands covered the frequency region at and near 22.237 GHz.

From the discussion in 5.1.4 about double sideband, 8 MHz resolution

radiometers, it must not be unexpected that results were negative.

The one fact that was established was that on only one day (14 July

1965) did the absorption at 22.237 exceed the value which might have

been expected from water vapor in the troposphere alone. The matched

spectra always equalled or exceeded the absorption observed at 22.237 GHz
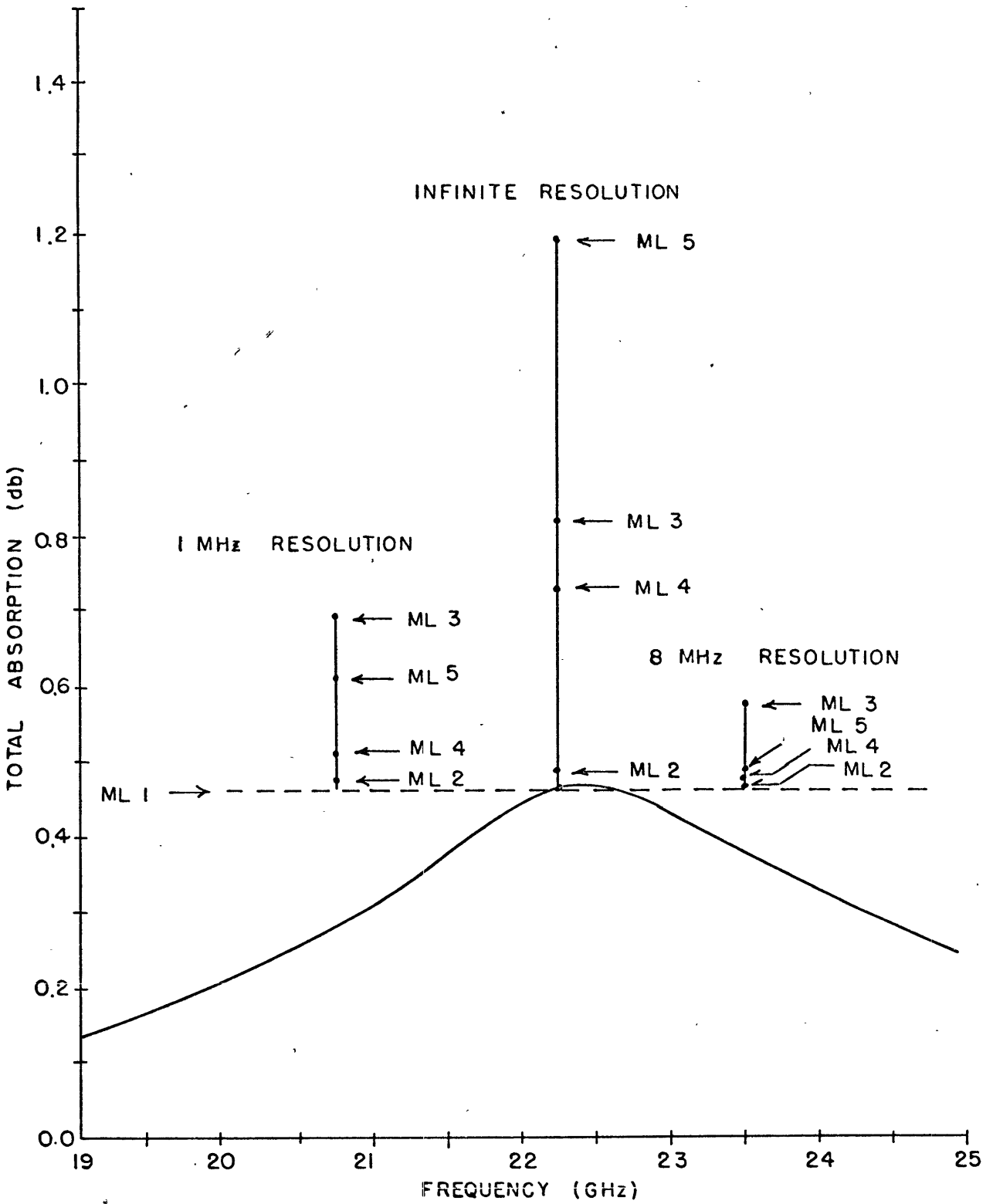
Figure 5-10. Comparison between opacity spikes seen by radiometers
with zero, 1 MHz, and 8 MHz bandwidths.

when at 21.9 GHz the observed attenuation and computed absorption were numerically equal.

Besides those shortcomings of the experiment design which were brought out in section 5.1.4, other experimental problems reduced the chances of detecting a spike, if it existed: (1) the local oscillator for the resonant frequency radiometer drifted in frequency, how much during any one experiment is uncertain; and (2) atmospheric inhomogeneities and variability increased the noise levels on many days well above 0.01 db.

Indeed, from the results of the observations reported in Chapter 4, and the opacities computed from more realistic distributions of water vapor in the stratosphere given in this chapter, it appears that a considerably more sophisticated approach to measurements near resonance must be used if a spike will ever be detected.

5.2 The Stratospheric Water Vapor Spike Expected for Climatic Regions other than Midlatitude and Measurements other than Ground Based Opacity.

So far we have analyzed only midlatitude model atmospheres and ground based opacity measurements for evidence of the stratospheric water vapor spike. This was done quite obviously to say something about the negative results which were recorded from the radiometer observations of Chapter 4. For measurements which might be done in other climates and by other methods, it is of interest to determine

what variations in the amplitude one can expect in the spike for the
same bandwidths analyzed in section 5.1.4. That will be done in the
remainder of this section of Chapter 5.

5.2.1 Ground Based Opacity Measurements near Resonance
in Tropical and Subarctic Climates.

Figures 5-11 and 5-12 depict, respectively, the spikes which
one would measure for the five Tropical atmospheres of Figure 5-2,
and for the Subarctic atmospheres of Figure 5-3. In each diagram the
effect of 1 MHz and 8 MHz bandwidths is assessed.

Even though the base absorption is quite different for the
spikes of the three climatic zones, closer examination reveals that
the amplitudes of analogous stratospheric cases are quite similar.
In fact, the small differences can almost all be accounted for by
the small differences in integrated moisture brought out in Table 5-I.
The changes in stratospheric temperatures between different climatic
zones have little effect on the production of a spike.

5.2.2 Ground Based Brightness Temperature Measurements
near 22.237 GHz.

Figure 5-13 shows the spikes one would measure if he were moni-
toring atmospheric emission in the model midlatitude atmospheres.
The relative amplitudes of the spikes are not changed substantially
from the opacity cases. Line widths of the various spikes remain
similar to those in the opacity computations, and, therefore, the
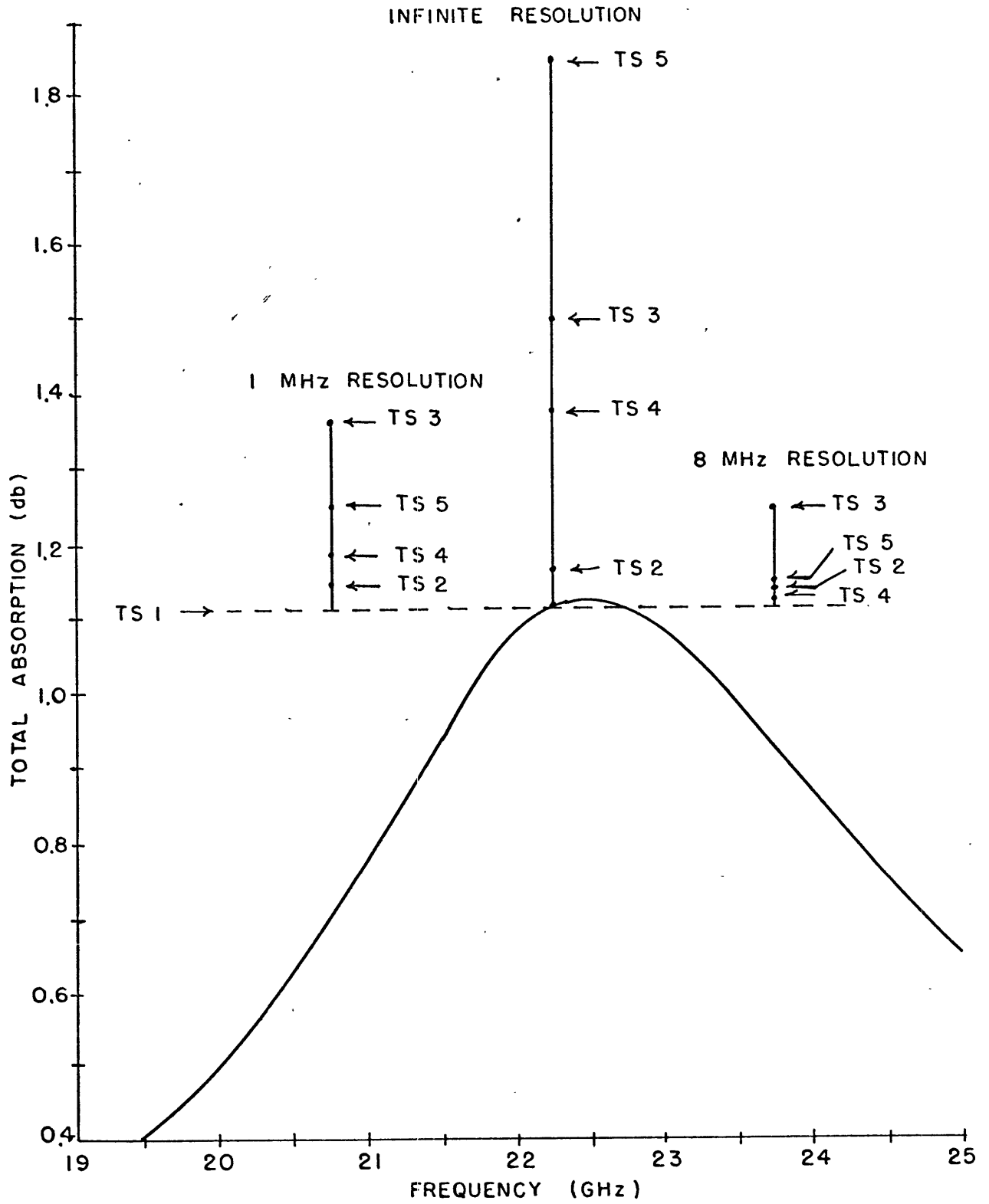
Figure 5-11. Stratospheric water vapor opacity spikes in the tropical atmospheres.
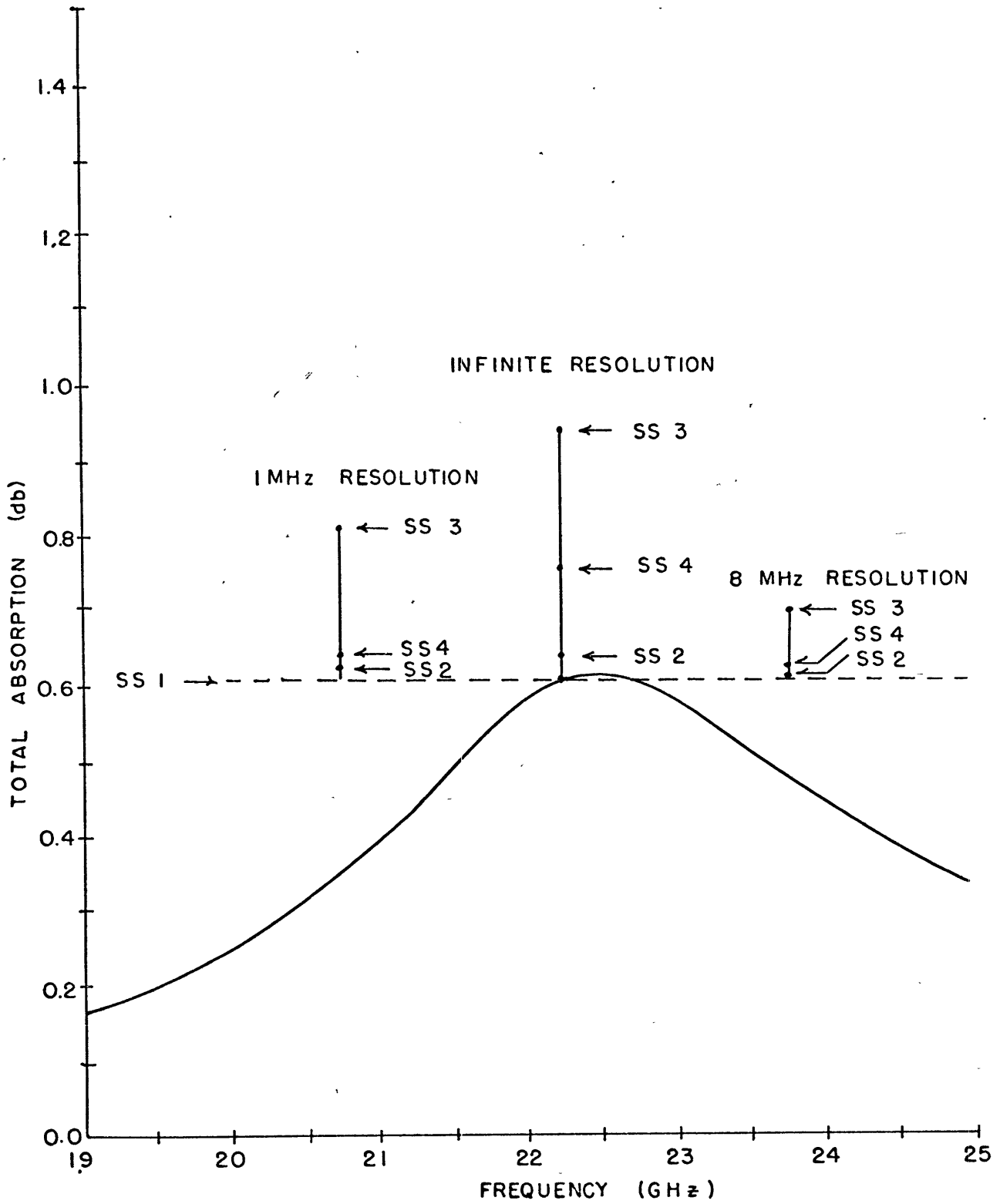
Figure 5-12. Stratospheric water vapor opacity spikes in the subarctic summer atmospheres.
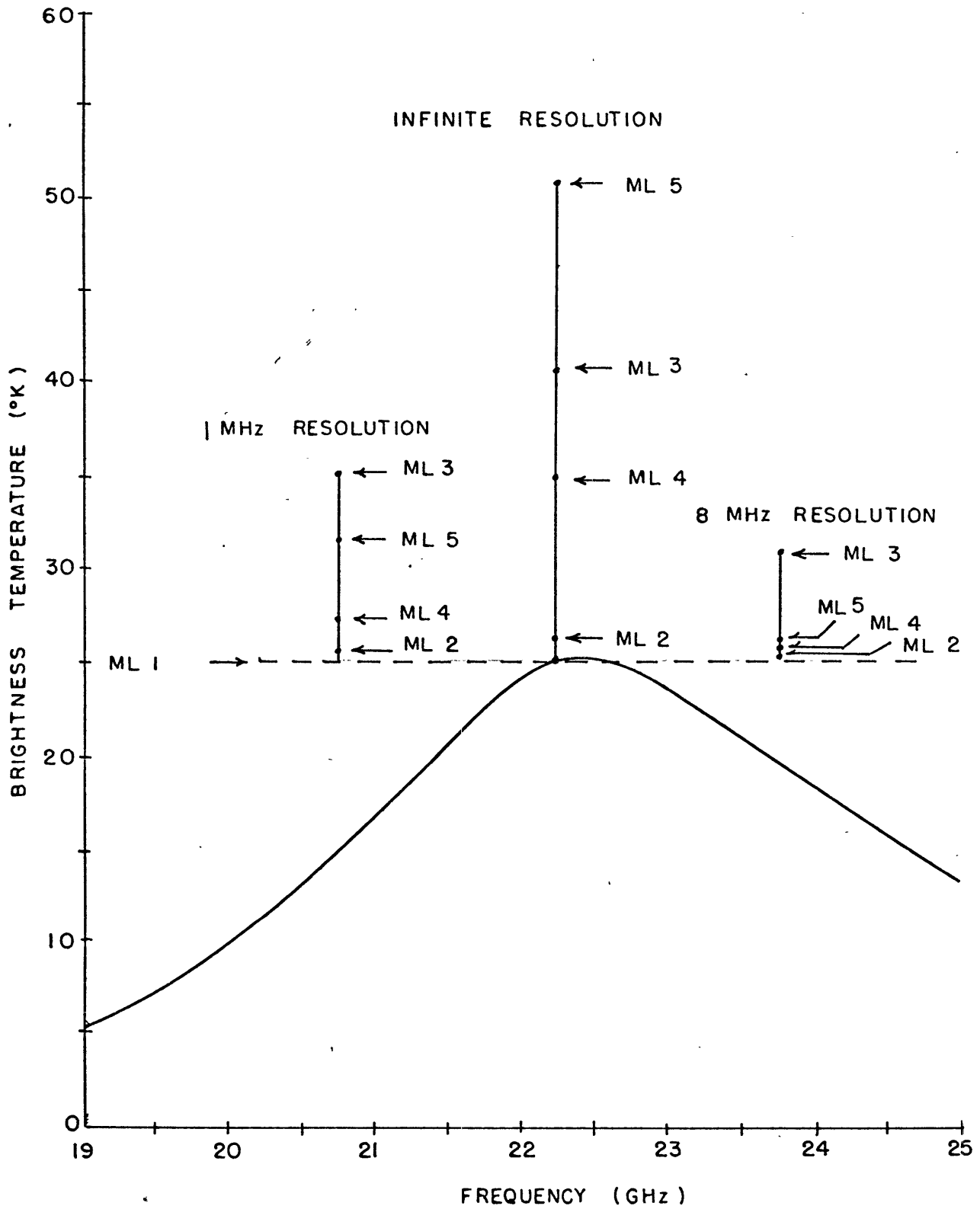
Figure 5-13. Emission spikes seen from the ground in the midlatitude atmospheres.

effects that a finite bandwidth radiometer produces is similar to those documented in Figures 5-8 and 5-9 for opacity measurements. Likewise, the opacity variations evident between Figures 5-10, 5-11, and 5-12 due to climatic differences are repeated for brightness temperature and therefore they have not been plotted.

5.2.3 Opacity and Brightness Temperature Measurements from a Balloon.

Calculations were carried out on the various stratospheric water vapor distributions to simulate the measurements which a balloon borne radiometer at 28 km would collect. They can be very easily visualized for the opacity measurements by simply removing the broad tropospheric absorption base upon which all spikes analyzed so far have been perched. The only perceivable change occurs to the amplitudes of the brightness temperature spikes. They have been raised by a factor of approximately 15 percent because of the decreased attenuation between the region in which the spike emission originates and the level of the antenna.

5.2.4 Brightness Temperature Measurements from Space near 22.237 GHz.

When a radiometer looks down at the earth, it sees the background emission attenuated by the atmosphere plus the reflected and direct atmospheric contributions. When the atmosphere is more opaque, the atmospheric contributions increase, but the background radiation

is diminished; this compensation reduces the amplitude at resonance

from that seen for measurements from the ground at the same frequen-

cies.

Such compensation significantly reduces the spike amplitude as

seen from space over a background whose temperature is $288^{\circ}K$ and which

has a power reflection coefficient of 0.6. This is illustrated in

Figure 5-14. The comparable upward looking amplitude was plotted in

Figure 5-13.

The amount of compensation and therefore the amplitude of the

spike will vary greatly as the background temperature and emissivity

change. For lower reflection coefficients (higher emissivities), the

background compensation is greater and the amplitude of the spike is

reduced further. Qualitatively similar results were reported by May

and Kahle[73] and by Croom[74].

5.3 Measurements of Stratospheric Attenuation and Emission

near the 183.310 GHz Water Vapor Rotational Resonance.

The 22.237 GHz water vapor resonance is nearly two hundred

times weaker for similar conditions than the next lowest frequency

rotational resonance at 183.310 GHz. As a result, the sensitivity

for monitoring very small amounts of water vapor, such as are found

in the stratosphere, would be greatly increased for measurements near

the higher frequency line.

In this section, we will investigate what results might be
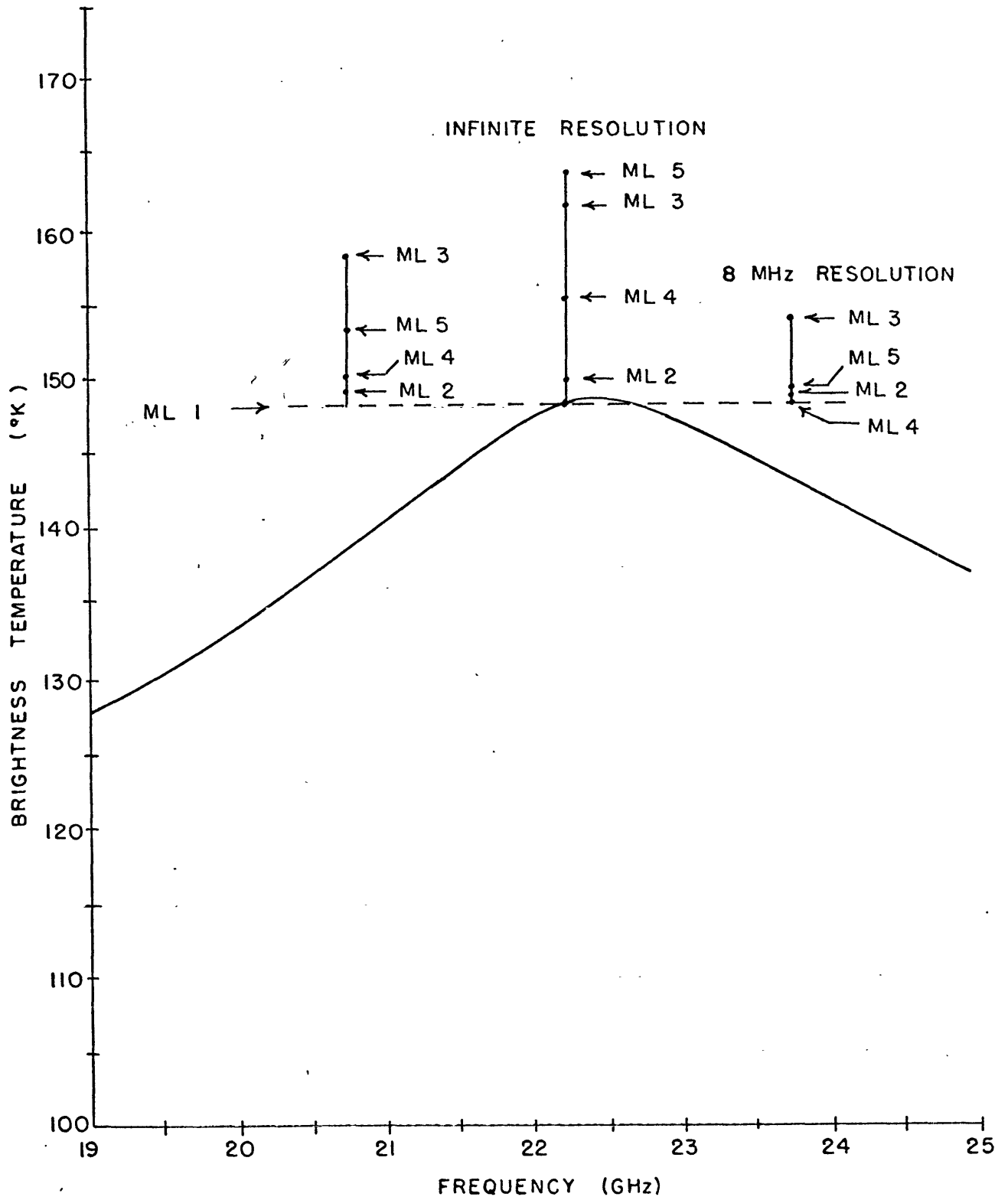
Figure 5-14. Emission spikes seen from space in the midlatitude atmospheres.

expected from atmospheric measurements near 183.310 GHz.

    5.3.1 Stratospheric Absorption and Emission Near 183.310 GHz

        as Measured from a Balloon at an Altitude of 28 kilo-

        meters.

The 183 GHz line is so intense that measurements from low levels
in the troposphere produce brightness temperatures equal to the kinetic
temperature of the nearby atmosphere. However, at 28 kilometers, a
convenient level for a balloon borne radiometer to attain, well over
99% of the total water vapor in an atmospheric column is below the balloon.
The 22.2 GHz resonance is not capable of measuring emission from the
small water vapor above 28 km except in those stratospheres postulated
to be very moist. On the other hand, the 183.3 GHz is sensitive to the
water vapor in even the driest of the proposed model stratospheres.

In Figure 5-15, the zenith absorption near resonance is plotted
for the five midlatitude atmospheric models (Figure 5-1) which a radio-
meter would measure from a height of 28 kilometers. For the stratos-
phere which contained the maximum integrated water vapor of the five
models (ML3), and for the atmosphere with considerable moisture near
the mesopause (ML5),the absorption on resonance attains values near 70 db!
Even the driest stratosphere proposed (ML1) has a peak absorption of
0.79 db. This is often more than the total zenith absorption measured
at the ground at 22.237 GHz.

If emission measurements were made in the same atmospheres, the
spectra plotted in Figure 5-16 would be obtained. The sharp peaks of
the absorption spectra are now blunted because the coldest temperatures
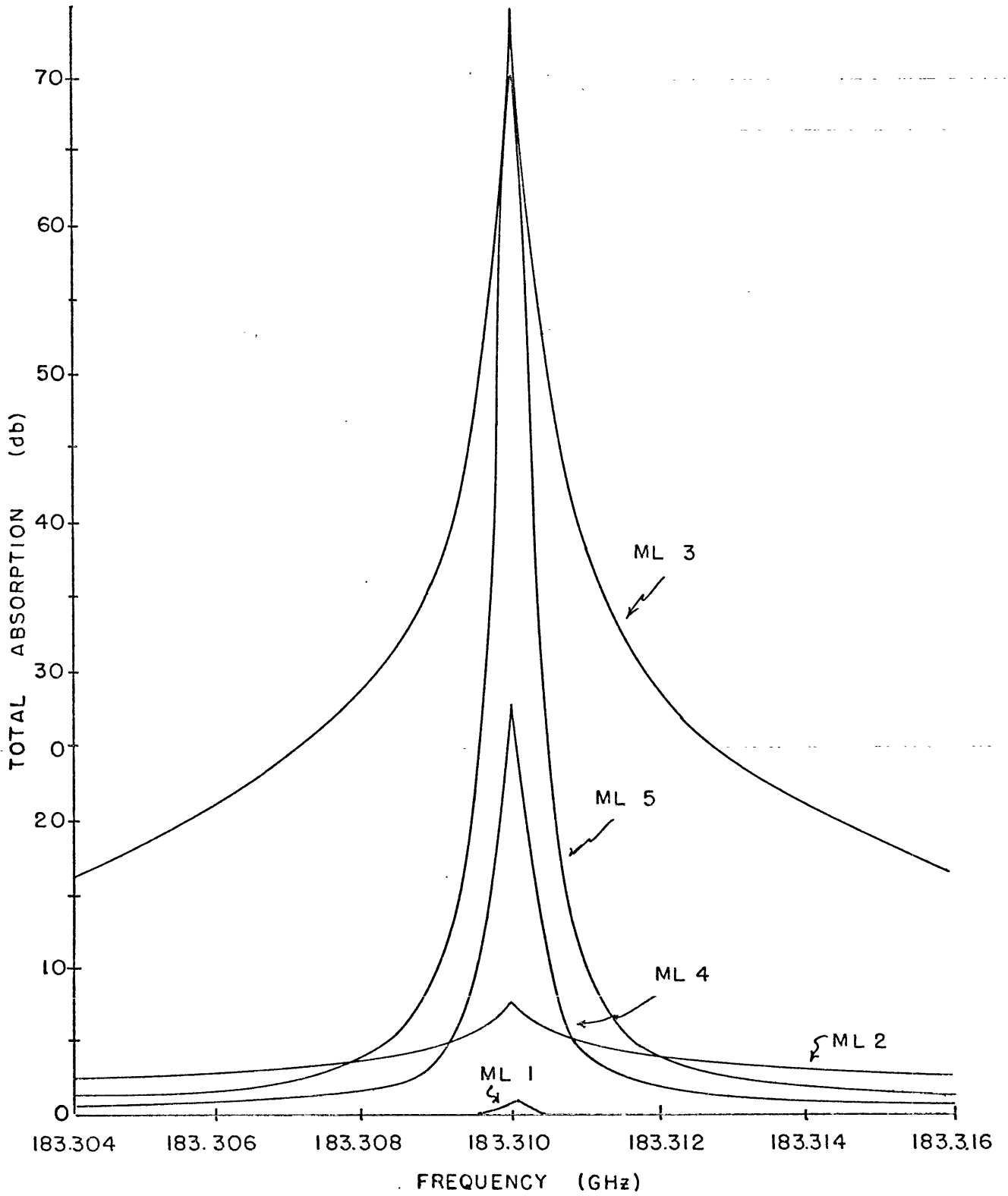
Figure 5-15. Possible total zenith opacity in midlatitudes,
above 28 km, near the water vapor resonance
centered at 183.310 GHz.
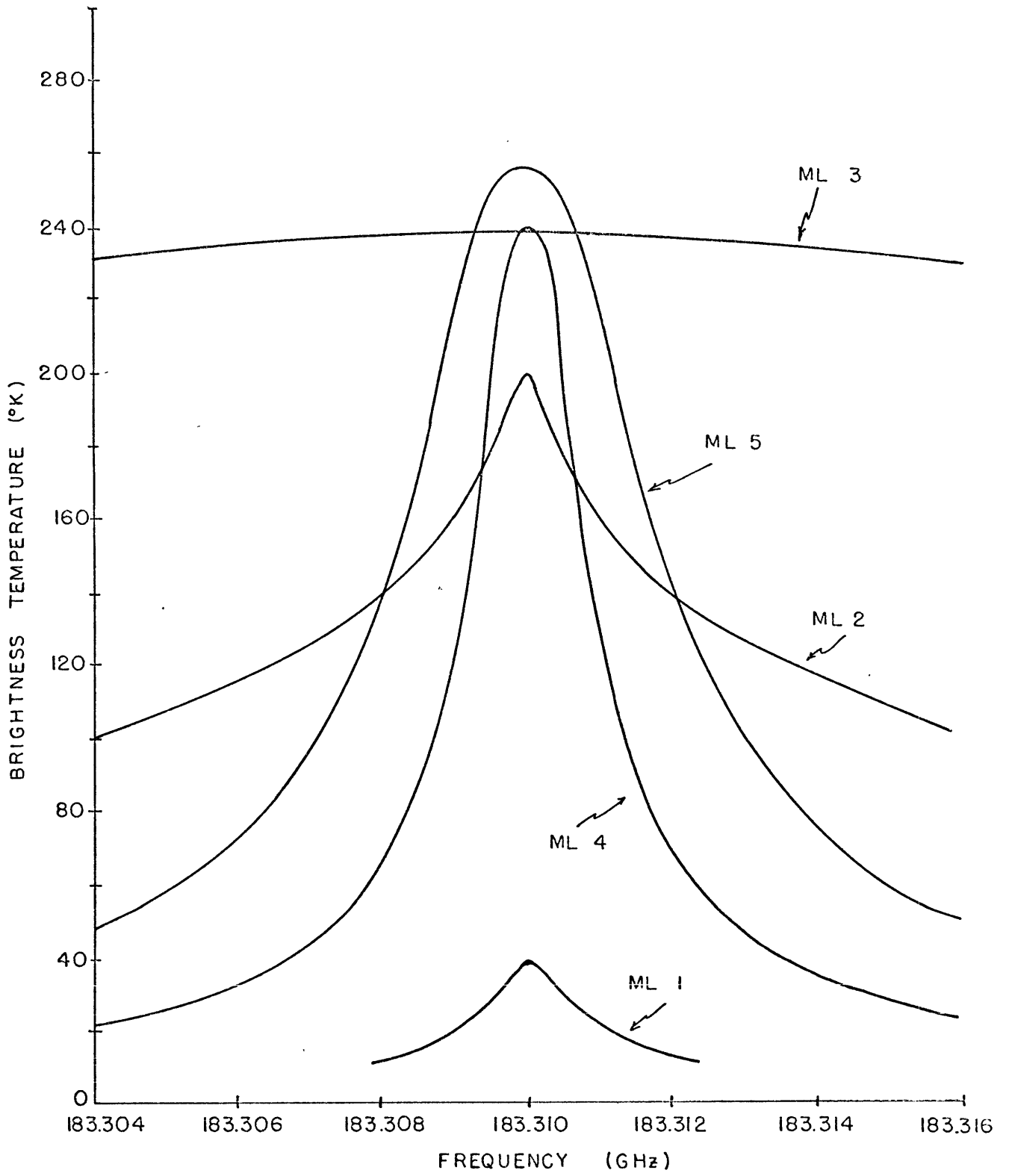
Figure 5-16. Emission spectra in midlatitudes, near 183.310 GHz,
looking up from a height of 28 km.

of significance are near the radiometer; higher opacity brings the effective origin of the radiation being measured closer to the radiometer and therefore into colder source temperatures. The result is to effectively broaden the lines.

A suitable bandwidth for the detection of the 183.3 GHz spike from a balloon would be considerably greater (by approximately 8 to 10) than the bandwidth necessary at 22.2 GHz. This is offset, of course, by the difficulties in building narrow band radiometers at such frequencies.

5.3.2 Spectra near 183.3 GHz Obtained from Simulated Measurements Made from Space.

Looking down at the Tropical and Midlatitude atmospheres near 183 GHz, one would see spectra for the direct stratospheric cases as plotted in Figure 5-17. The level of the effective origin of the radiation rises as one nears resonance. For atmosphere ML1, on resonance, 90% of the radiation arises between the levels of 4000 and 11,000 meters; off resonant frequencies see further into the atmosphere and therefore warmer effective temperatures. The Tropical atmosphere contains more moisture than the midlatitude model and therefore the effective origin of radiation is at higher and colder levels near resonance explaining the deeper minimum.

The level of the effective origin of radiation at resonance continues to rise as the moisture concentration in the stratosphere increases. Eventually, for enough water vapor, the effective origin of radiation measured at a satellite moves above the tropopause and the atmospheric temperature, and therefore the brightness temperature
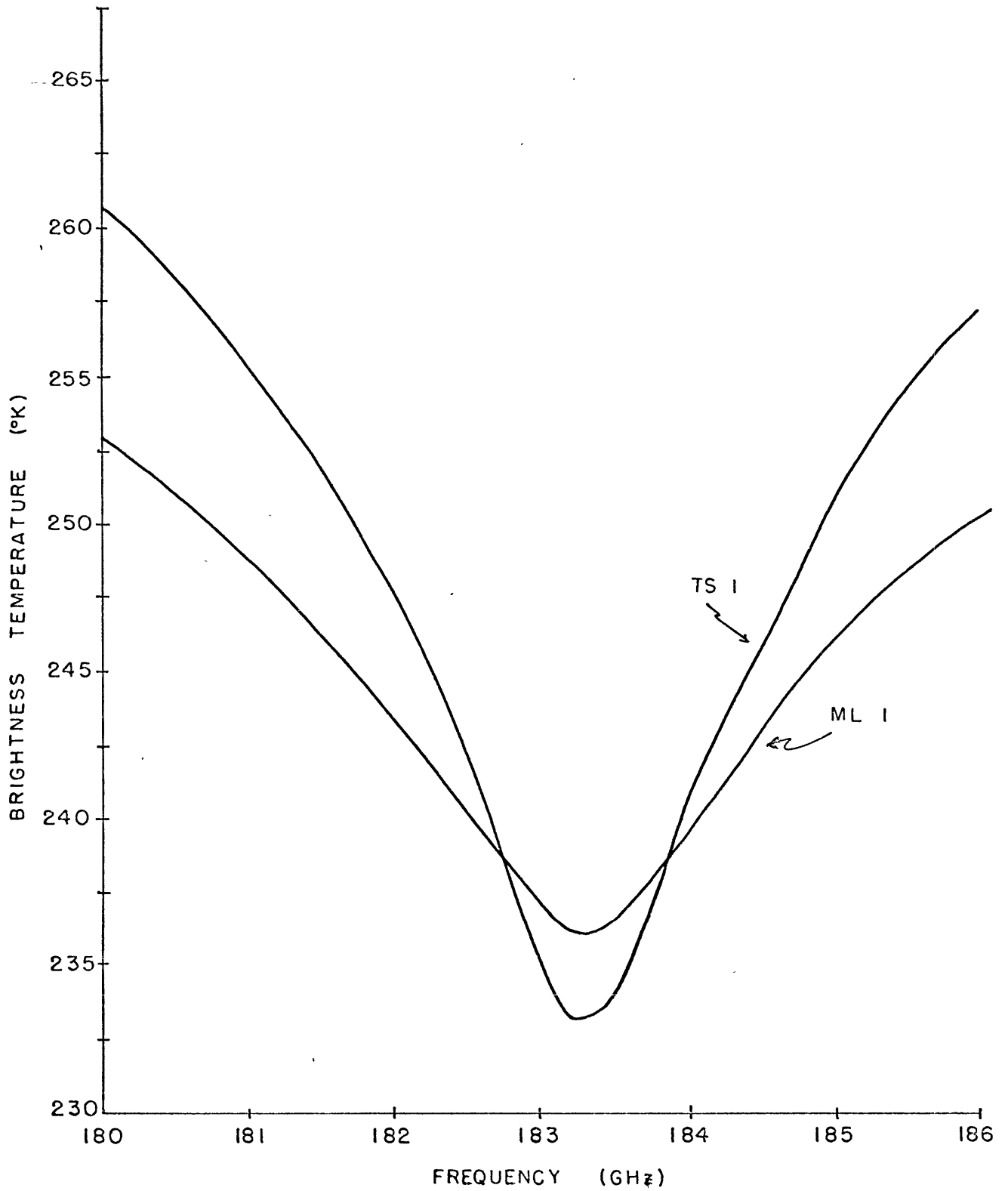
Figure 5-17. Emission spectra from space near 183 GHz above a tropical and midlatitude atmosphere.

measured at the satellite, begins to increase. Superimposed on the minima of Figure 5-17, near resonance, would be a secondary maxima. And if even more moisture is added to the stratosphere, the level of the effective origin of radiation being measured can move above the stratopause and into declining temperatures again in the mesosphere. Superimposed on the secondary maximum would now appear a spike pointing towards lower temperatures. Such a situation is depicted in the final Figure 5-18. The secondary maxima a few MHz off resonance are almost equal to the temperatures at the stratopause. The resonant minima have begun to plunge toward the very low mesopause temperatures.

The obvious conclusion to be drawn from the previous discussion and figures is that measurements near the 183 GHz line offer a potentially powerful tool to explore the amount and distribution of stratospheric water vapor given an approximate knowledge of the temperature distribution as a function of height. When radiometers are built with suitable bandwidths and noise factors, and whose physical dimensions and weight are adequate for satellites, they undoubtedly can be coupled with radiometers which monitor the spectrum in and near the complex of oxygen lines near 5 mm, and from which one can determine the temperature distribution in the stratosphere. Such a combination will be a very effective means of mapping, on a synoptic basis, the amount and distribution of stratospheric water vapor.
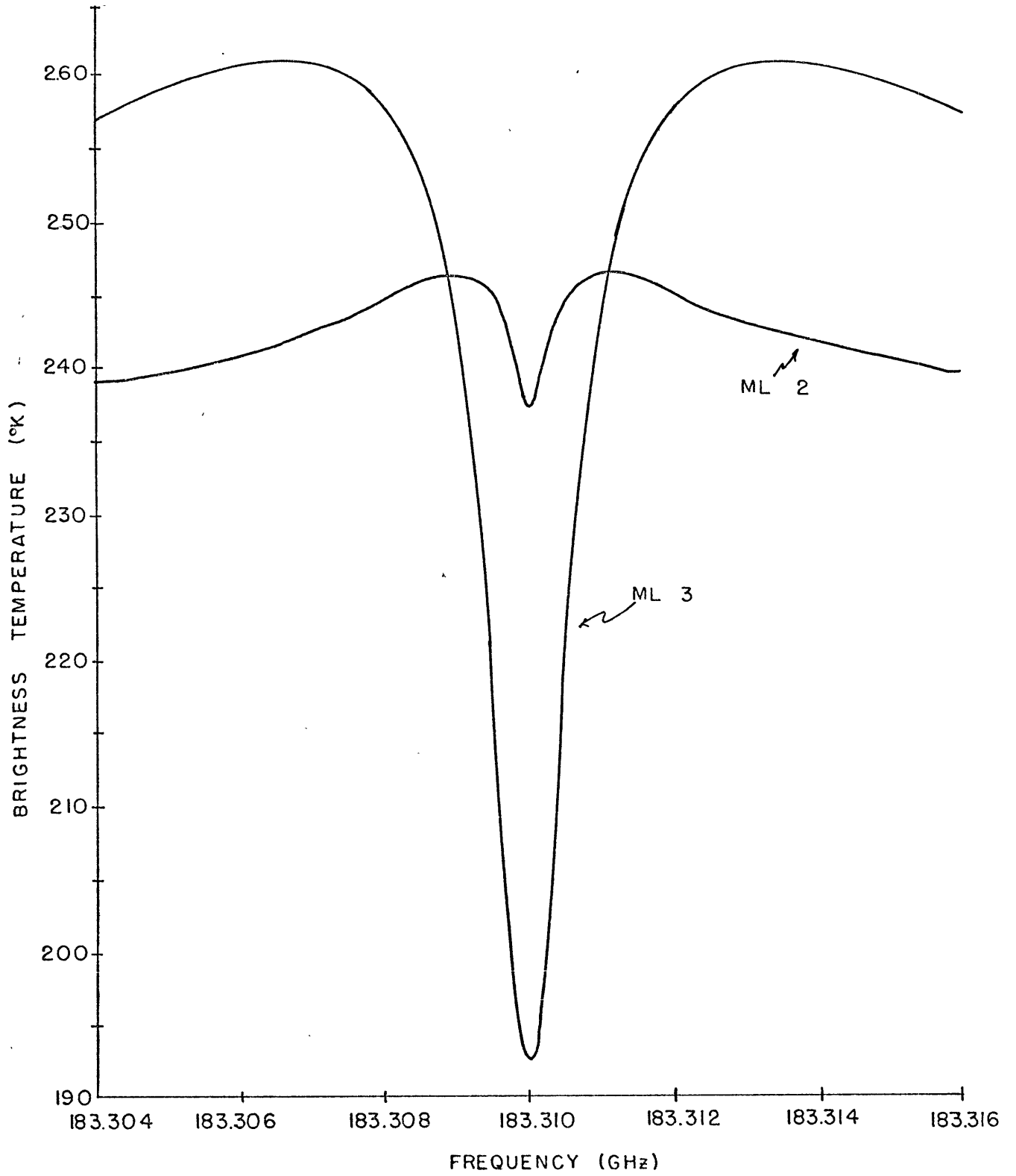
Figure 5-18. Possible emission spectra seen from space
near 183.310 GHz over moist stratospheres.

Chapter 6

INTEGRATED ATMOSPHERIC WATER VAPOR

As shown in Chapter 4, solar attenuation measurements reveal significant day to day variations in the shape and intensity of the 1.35 cm water vapor spectral line. Further, these variations have been shown to arise from changes in the total amount and the vertical distribution of water vapor. A question which naturally arises is: given the spectral data, what meteorological information important to every day forecasting may be extracted from it? In this chapter, the possibility that spectral measurements can give accurate information about the vertically integrated atmospheric water vapor content will be investigated.

The problem may be approached from any of the sets of spectral measurements which were presented in Chapter 3. However, because there are data which exists for total zenith opacity, the problem will be analyzed from the standpoint of such measurements.

6.1 Statement of the Problem

For any given set of atmospheric conditions, the total zenith opacity has been defined in Equation (3. 1-19) as

$$\tau_{max} (\nu) = \int_0^H \gamma_r (\nu, z) \, dz \qquad (6.1\text{-}1)$$

In Equation (6.1-1), $\tau_{max}(\nu)$ is the attenuation which would be

measured at the zenith, $\gamma_T(\nu, z)$ represents all the mechanisms of attenuation and will depend upon the frequency and where the observer is located in the atmosphere. H is, as before, a height above the levels of significant attenuation.

If we restrict ourselves to a frequency region sufficiently close to the 1.35 cm rotational resonance of water vapor, the γ_T may be conveniently broken down into several parts, each of which represents separate physical mechanisms of attenuation. This separation can be symbolically written as

$$\gamma_T = \gamma_{RES} + \gamma_{NON} + \gamma_{O_2} + \gamma_R \qquad (6.1-2)$$

where γ_{RES} represents the attenuation due to the 1.35 cm resonance alone, γ_{NON} represents the attenuation from the wings of all higher frequency water vapor lines, γ_{O_2} is the attenuation coefficient for oxygen (Appendix A-II), and γ_R represents the attenuation from all sources not specified above. For the analysis which follows, it will be assumed that γ_R is negligible. On clear days, this is a safe assumption; on days with heavy clouds, however, γ_R can contribute significantly to γ_T.

Similar to the breakdown of γ_T, τ_{max} may be thought of as consisting of separate contributions from each part of γ_T so that we may write

$$\tau_{RES}(\nu) = \int_0^H \gamma_{RES}(\nu, z)\, dz \qquad (6.1-3)$$

where $\tilde{\tau}_{RES}$ is the zenith opacity arising from the 1.35 cm resonance

alone. For the moment, it will be assumed that τ_{RES} can be determined

from measurements of $\tilde{\tau}_{max}$; our problem then becomes one of understand-

ing how $\tilde{\tau}_{RES}$ is related to the integrated atmospheric water vapor.

The full equation of γ_{RES} is represented by Equation (2.3-6).
It may be conveniently expressed as

$$\gamma_{RES} \left(\nu, P, T, \rho \right) = C \rho \, \nu^2 \, f_1(T) \, S \tag{6.1-4}$$

where C is an appropriate constant, ρ is the absolute density of water

vapor, ν is the frequency of observation, $f_1(T)$ is given by

$$f_1(T) = \exp \left\{ -\frac{644}{T} \right\} \Big/ T^{5/2} \tag{6.1-5}$$

and S is a derivative from the line shape factor. S is not perfectly

known, but can be adequately approximated for our purposes from the

van Vleck-Weisskopf expression of Equation (2.2-14). Fully written out

S is given by

$$S = \Delta\nu \left[\frac{1}{(\nu - \nu_0)^2 + \Delta\nu^2} + \frac{1}{(\nu + \nu_0)^2 + \Delta\nu^2} \right] \tag{6.1-6}$$

in which ν_0 is the resonant frequency for the transition (22.237 GHz)

and $\Delta\nu$ is the half width at half maximum for the spectral line.

For pressures between about one atmosphere ($\sim$ 1000 mb) and per-

haps 1.5×10^{-3} mb, $\Delta\nu$ has been shown to be quite accurately approximated

for the 1.35 cm line by

$$\Delta \nu = B \, \frac{P}{T^{0.625}} \left(1 + \alpha_{1.35} \, \frac{\rho T}{P} \right) \qquad (6.1-7)$$

where B is an appropriate constant, P represents total atmospheric pressure in mb, T the kinetic temperature in degrees Kelvin, and the water vapor density in g/m^3. Neglecting the small contribution of ρ to $\Delta \nu$, it is apparent from the above equations and the discussion accompanying Figure 3-6 that for homogeneous conditions, the line becomes narrower and more intense as the pressure is reduced. In the atmosphere, the pressure diminishes logarithmically with height and therefore the spectrum of τ_{H_2O} is composed of a complex combination of many different line shapes.

To overcome the problem of changing line shapes, it is desirable to formulate a solution which either does not depend upon $\Delta \nu$ at all or, at the very least, restricts its importance. At least two methods are available which will accomplish the above mentioned goal. One is to utilize a modification of the so-called integrated line intensity; the other is to take advantage of the properties of the zenith opacity weighting functions. The discussion will begin with the integrated line intensity approach.

6.2 The Modified Integrated Line Intensity as a Measurement of

Total Atmospheric Water Vapor

The unmodified or normal integrated line intensity I is defined as follows:

$$I \equiv \int_0^\infty \frac{\tau_{RES}}{\gamma^2} \, d\nu \qquad (6.2\text{-}1)$$

It is clear that, if τ_{RES} can be measured as a function of frequency, then I may be evaluated from these measurements.

Using Equations (6.1-3) and (6.1-4), the integrated line intensity may be related to the water vapor distribution as

$$I = C \int_0^H \rho F_1(T) \left\{ \int_0^\infty S \, d\nu \right\} dz \qquad (6.2\text{-}2)$$

The modified line shape factor, S, is a normalized function which when integrated from zero to infinity equals π. Therefore (6.2-2) can be restated as

$$I = C \pi \int_0^H \rho F_1(T) \, dz \qquad (6.2\text{-}3)$$

The line width is eliminated, and the expression for the integrated line intensity is greatly simplified.

If, further, we choose a mean temperature $\bar{T}$ such that

$$F_1(\bar{T}) = \frac{\int_0^H \rho F_1(T) \, dz}{\int_0^H \rho \, dz} \qquad (6.2\text{-}4)$$

then we can write

$$I = C \pi F_1(\bar{T}) \int_0^H \rho \, dz \qquad (6.2\text{-}5)$$

an expression equivalent to Equation (13) in Barrett[55]. Rearranging terms leads to

$$V = \int_0^H \rho \, dz \quad = \quad \frac{I}{C \, \pi \, F_i(\bar{T})} \tag{6.2-6}$$

The problem of finding the integrated water vapor is reduced to the determination of a suitable water vapor averaged temperature $\bar{T}$ and the evaluation of the area under the curve of τ_{RES}/ν^2 versus frequency.

6.2.1 The Problem of Restricted Measurements.

Since it would be impossible to measure τ_{RES} over the entire frequency spectrum, a more realistic problem would restrict our knowledge of τ_{RES} to a region near resonance. This means that the limits for ν in Equations (6.2-1) and (6.2-2) must be modified. As it happens, no set of limits are possible which cause the integration to be independent of the half width. Therefore, since some knowledge of the effective half width is necessary, it is easiest to take the limits for ν as $\nu_0 \pm \Delta\nu$. Then the integration of S proceeds as

$$\int_{\nu_0 - \Delta\nu}^{\nu_0 + \Delta\nu} S \, d\nu \quad = \quad \pi/2 \; + \; \delta_{\nu\nu} \tag{6.2-7}$$

where $\delta_{\nu\nu}$ is dependent upon $\Delta\nu$ but is $\leq$ 0.7% of $\pi/2$ for any reasonable choice of the half width.

Equation (6.2-6) can be modified, as a consequence of Equation (6.2-7) to read

$$\gamma = \frac{2I'}{C_1 \pi P_1(\bar{T})} \qquad (6.2\text{-}8)$$

where now I' is understood to be the value of the integral in Equation
(6.2-1) with limits modified from 0 and ∞ to $\nu_o - \overline{\Delta\nu}$ and $\nu_o + \overline{\Delta\nu}$
where $\overline{\Delta\nu}$ is some water vapor weighted line width average over height.

δ_{vv} has been neglected because the error introduced by disregarding
it is in no way limiting. The determination of $\overline{\Delta\nu}$ and subsequently
I' will certainly be less accurate than the errors associated with δ_{vv} .

6.2.2 The Evaluation of $f_1(T)$

The temperature factor $f_1(\bar{T}) = \exp\left\{-644/\bar{T} \ /\bar{T}^{5/2}\right\}$ may now
be profitably analyzed. Equation (6.1-5) shows it to be the water vapor
weighted average of $f_1(T)$ in the vertical. Figure 6-1 is a plot of
$f_1(T)$ as a function of temperature. A maximum occurs in the vicinity
of 260°K which fortuitously causes the value of $f_1(T)$ to vary only
slowly over temperatures in the atmosphere where atmospheric water vapor
predominates. In particular, if one chooses $f_1(\bar{T}) = 7.67\text{x}10^{-8}$, then an
error equal to or less than 0.5% will occur if the actual weighted aver-
age temperature in the atmosphere is between 235°K and 282°K. An error
equal to or less than 1.0% will be caused if we choose $f_1(\bar{T}) = 7.63\text{x}10^{-3}$
and the actual weighted average temperature is between 228°K and 293°K.
These errors are less than those to be expected from the evaluation of
$\overline{\Delta\nu}$ and I' .
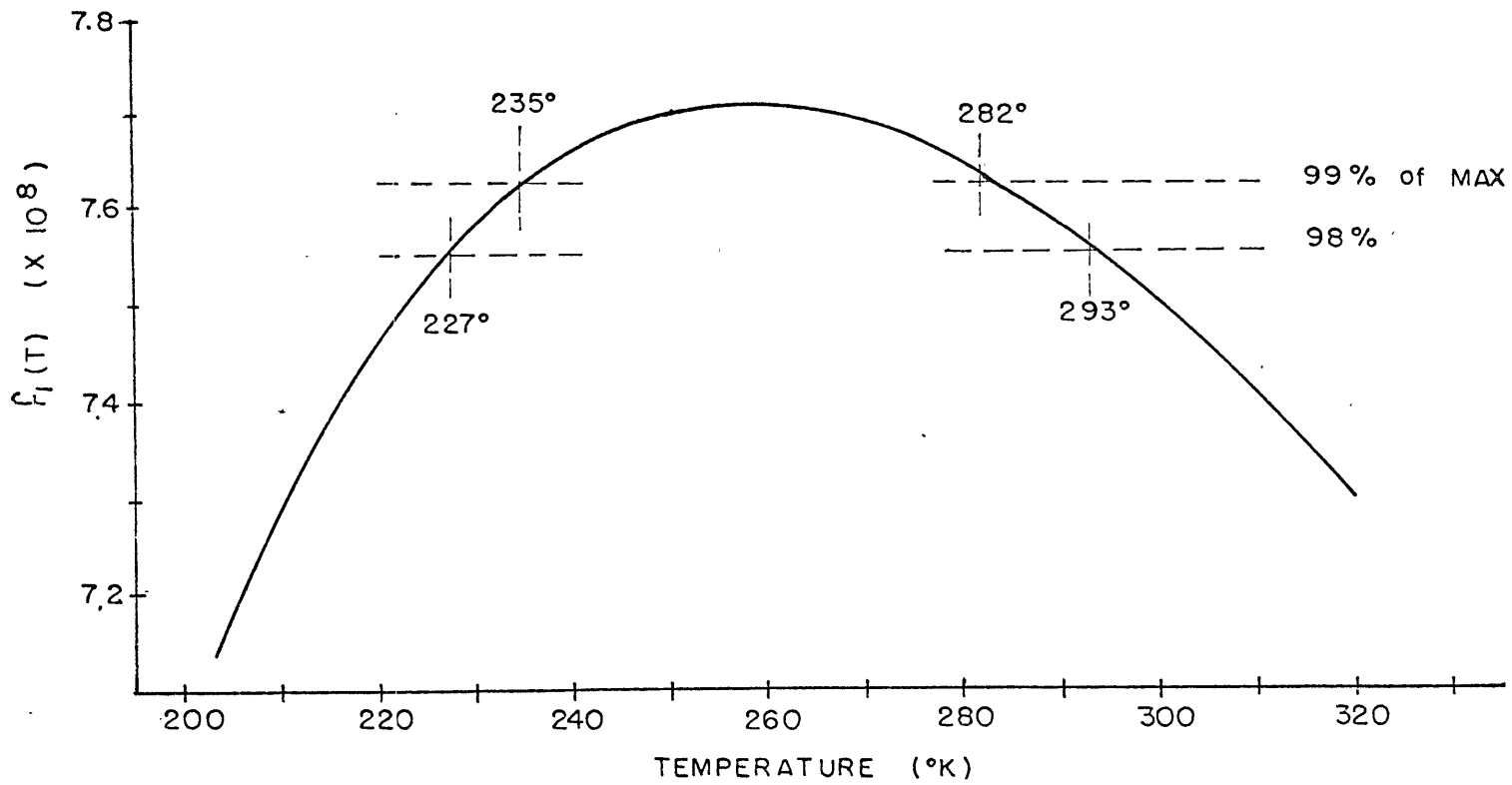
Figure 6-1. The function $f_1(T)$ versus temperature.

6.2.3 Evaluation of I' .

The modified line intensity I' is computed from the area with

diagonal hashing in Figure 6-2. To evaluate it, one needs to know the

line shape, the effective half width, and the contributions of oxygen

and the non-resonant part of γ_{H_2O} . The oxygen contribution, as

will be seen in section 6.4, can be estimated with fair accuracy. The

non-resonant contribution is not so easily deduced.

To give some perspective to what accuracies can be expected if

we knew all of the line parameters well, I' was evaluated for the

spectrum in Figure 6-2. The area was determined in each 1 GHz column

and divided by the square of the mid-frequency for that block. The

effective half width of the line was taken as the water vapor weighted

average half width for the atmosphere on that day, i.e.,

$$\overline{\Delta\nu} = \frac{\int_0^H \rho \, \Delta\gamma \, dz}{\int_0^H \rho \, dz} \qquad . \qquad (6.2-9)$$

By using I' as determined above in Equation (6.2-8), along with

a value of $f_1(\overline{T})$ equal to 7.67×10^{-8}, the integrated water vapor was

computed to be 1.76 g/cm^2 versus a value of 1.73 g/cm^2 computed directly

from the radiosonde data. Better accuracy is no doubt attainable by

a more careful computation of I'.

The dilemma posed by the contribution to τ_{max} of the non-

resonant part of γ_{H_2O} may be approached from at least two differ-

ent directions. The first would be to attempt to determine τ_{NON} and
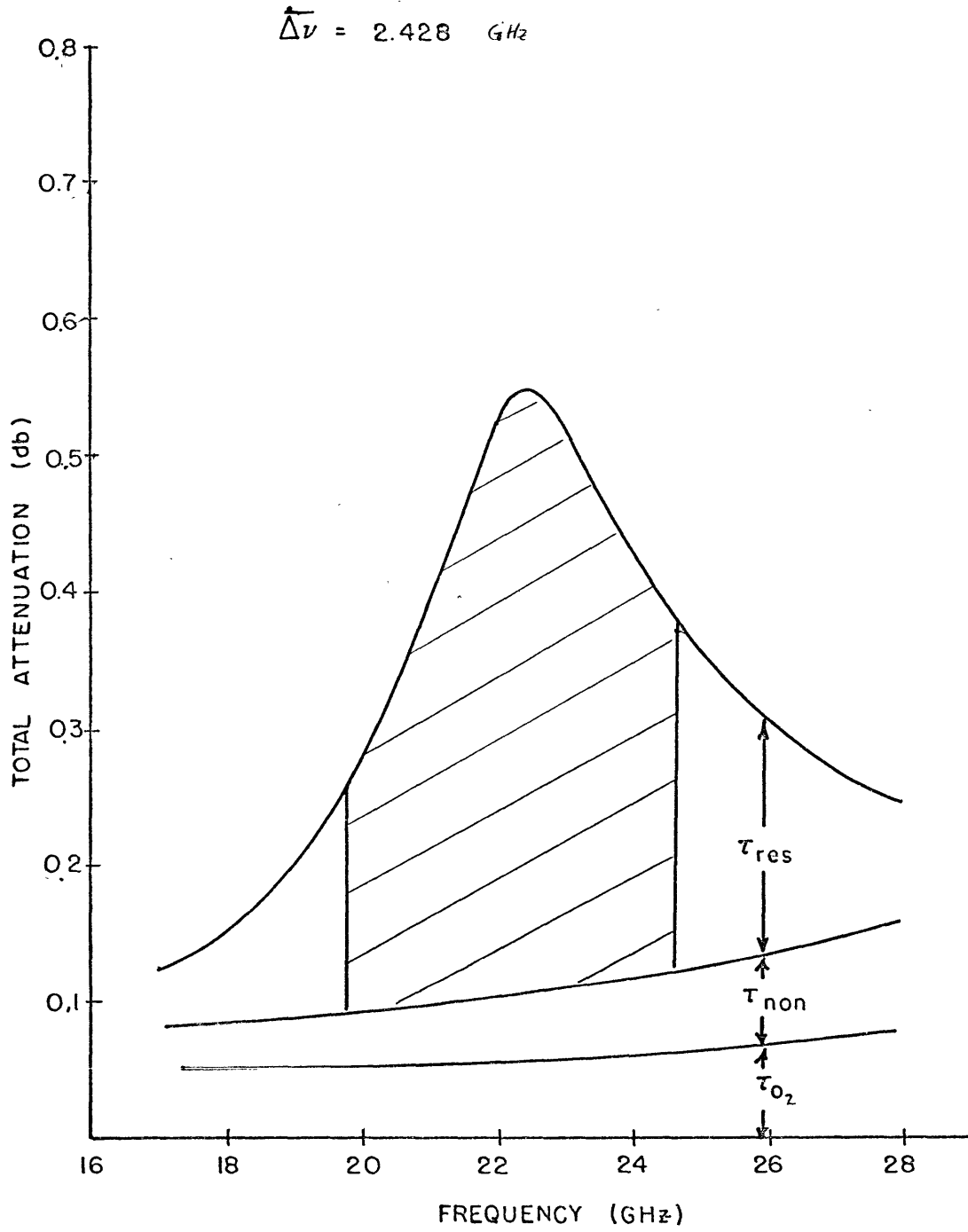
Figure 6-2. A water vapor absorption spectrum from which the integrated water vapor in the beam may be determined.

subtract it from τ_{H_2O} . However, there are many approximations necessary when this approach is used. It appears, in fact, that besides the approximations, an iterative procedure is also needed to accurately determine τ_{NON} .

A second method of approach is to combine τ_{NON} with τ_{RES} and derive a new I'. If I_1' is the integrated intensity using τ_{RES} and I_2' is the equivalent using τ_{NON} , then

$$I_T' = I_1' + I_2' = \int_{\nu_0 - \bar{\Delta\nu}}^{\nu_0 + \bar{\Delta\nu}} \frac{\tau_{RES}}{\nu^2} d\nu + \int_{\nu_0 - \bar{\Delta\nu}}^{\nu_0 + \bar{\Delta\nu}} \frac{\tau_{NON}}{\nu^2} d\nu \qquad (6.2\text{-}10)$$

The non-resonant absorption may be expanded as (see Equation 2.3-11)

$$\tau_{NON} \doteq \int_0^H \gamma_{NON} \, dz = k_1 \nu^2 \int_0^H \frac{\rho \Delta\nu}{T^{3/2}} \, dz \qquad (6.2\text{-}11)$$

where K_1 is a constant and the remaining variables retain their normal meaning. Substituting Equations (6.2-11) and the restricted interval modification of (6.2-5) into (6.2-10) gives

$$I_T' = \frac{c}{2} \pi F_1(\bar{T}) \int_0^H \rho \, dz + k_1 \int_{\nu_0 - \bar{\Delta\nu}}^{\nu_0 + \bar{\Delta\nu}} d\nu \int_0^H \frac{\rho \Delta\nu}{T^{3/2}} \, dz \qquad (6.2\text{-}12)$$

$$\doteq \int_0^H \rho \, dz \left[\frac{c}{2} \pi F_1(\bar{T}) + k_1 \frac{2 \bar{\Delta\nu}^2}{\bar{T}^{3/2}} \right] \qquad (6.2\text{-}13)$$

The integrated water vapor is therefore given by

$$V = \int_0^H \rho \, dz = \frac{I_T'}{c/2 \, \pi \, F_1(\bar{T}) + k_1 \frac{2 \bar{\Delta\nu}^2}{\bar{T}^{3/2}}} \qquad (6.2\text{-}14)$$

Instead of the necessity of only estimating a function which varies slowly with T as in Equation (6.2-8), i.e., $f_1(T)$, Equation (6.2-14) requires a precise estimate of $\overline{T}$ because the right hand term in the denominator is inversely proportional to $\overline{T}^{3/2}$. Further, the same term is directly proportional to $\overline{\Delta\nu}^2$; the importance of correctly estimating $\overline{\Delta\nu}$ is therefore also increased.

No doubt statistical techniques or a technique using correlations with easily measured surface variables could be used to estimate values for $\overline{T}$ and $\overline{\Delta\nu}$ for any given day's observations. However, the accuracy of the integrated water vapor estimate V derived from Equation (6.2-14) would probably not be greater than that value derived from the technique to be presented in the next section; and that technique is a great deal more straightforward to implement. We will therefore leave this analysis of the integrated line intensity approach for estimating integrated water vapor and proceed to outline the composite weighting function method.

6.3 Total Integrated Atmospheric Water Vapor by the Method of Composite Weighting Functions

The discussion in Chapter 3 of water vapor weighting functions for various microwave measurements pointed out and illustrated the property of "sensitivity". That is, at a given frequency there exists a height at which a unit density of water vapor contributes most effectively toward increasing the value of the parameter being measured.

From Figure 3-4 the maximum sensitivity for 19.0 GHz occurred at the ground, for 21.9 GHz the maximum was near 16 km, and for 22.237 GHz the sensitivity was greatest at the top of the atmosphere.

For the purpose of measuring the total integrated water vapor, the ideal weighting function would be a constant with height. For such a weighting function, a given amount of water vapor at any altitude would produce an exactly similar effect on measuring apparatus at the ground; the parameter being measured would be directly proportional to the integrated water vapor.

An approximation to such an ideal weighting function may be constructed from a combination of real weighting functions by considering the following analysis:

Using the weighting function notation, the total zenith opacity for a given set of atmospheric conditions is

$$\tau_{H_2O} (\nu) = \int_0^H \rho (z) \, W_\tau (\nu, z) \, dz \qquad (6.3\text{-}1)$$

We define a new function L which is given by

$$L (z) \equiv \int_0^\infty a (\nu) \, W_\tau (\nu, z) \, d\nu \qquad (6.3\text{-}2)$$

Further, we choose the $a(\nu)$ such that

$$L (z) = \text{constant}. \qquad (6.3\text{-}3)$$

Equation (6.3-1) can be rewritten, as a consequence, as

$$\int_0^\infty a(\nu)\,\tau(\nu)\,d\nu \;=\; \int_0^H \rho(z)\int_0^\infty a(\nu)\,W_\tau(\nu,z)\,d\nu\,dz$$

$$= L\int_0^H \rho(z)\,dz \qquad\qquad (6.3\text{-}4)$$

The integrated water vapor V can be separated out and written as

$$V \;=\; \frac{\displaystyle\int_0^\infty a(\nu)\,\tau_\nu\,d\nu}{L} \qquad\qquad (6.3\text{-}5)$$

It is clear from Equations (6.2-1), (6.2-4) and (6.2-6) that a(ν) and L exist and have the following proportionalities:

$$a(\nu) \;\sim\; \frac{1}{\nu^2} \qquad\qquad (6.3\text{-}6)$$

$$L \;\sim\; f_1(\bar{T}) \qquad\qquad (6.3\text{-}7)$$

The restatement of the solution for V using (6.3-5), however, has introduced an entirely new possibility for approximating the answer without becoming involved with the complexities which were evident from the directly integrated line intensity approach.

This may be seen more clearly by restating the problem in terms of a set of discrete measurements of total zenith water vapor opacity. Let L(z) be written now as

$$L(z) = \sum_i a(\nu_i) W_\tau(\nu_i, z) \delta \nu_i \qquad (6.3\text{-}8)$$

where the $\delta \nu_i$ are small frequency intervals in which the average value of the weighting function is W_τ . Choose the a_i such that

$$\int_0^H \left\{ L(z) - \bar{L} \right\}^2 dz \qquad (6.3\text{-}9)$$

is a minimum, where

$$\bar{L} = \frac{\int_0^H L(z) \, dz}{H} \qquad (6.3\text{-}10)$$

Then the best approximation possible for the integrated water vapor using only the set of i opacity measurements is given by

$$V = \frac{\sum_i a(\nu_i) \, \tau(\nu_i) \, \delta \nu_i}{L} \qquad (6.3\text{-}11)$$

The value of using Equation (6.3-11) is that since the W_i are nearly constant over widely occurring atmospheric conditions, then the a_i and L will also be nearly constant. And also, a very important improvement over the integrated line intensity approach is that the weighting functions include γ_{NON} , i.e., the only separation which must be made after measuring τ_{max} is that between the oxygen and water vapor contributions. The only task remaining is to find frequencies which best satisfy Equation (6.3-9).

Several composite weighting functions L(z) are presented in Figure 6-3. They are constructed from combinations of weighting functions whose frequencies were those monitored for the observations reported in Chapter 4. Two of the curves in the figure (labeled 21.9 and 29.45) are for combinations of 21.9 GHz and 29.45 GHz weighting functions. The third curve (labeled 22.237, 23.5, and 29.45) was derived from the weighting functions at 22.237 GHz, 23.5 GHz, and 29.45 GHz. The first two composite weighting functions show considerable deviations from $\overline{L}$ in the critical first two kilometers of the atmosphere. Undoubtedly these can be improved by optimizing the two frequencies used in the synthesis.

The two-frequency curve which shows a deviation from $\overline{L}$ of about 5% in the first 4 to 5 kilometers was arrived at by using an exponential weighting function to emphasize the region of the atmosphere near the surface of the earth where water vapor predominates. Expression (6.3-9) was modified in that case so that

$$\int_0^H \left\{ L(z) - \overline{L} \right\} e^{-z/H_s} \, dz \qquad (6.3\text{-}12)$$

was minimized, where H_s is some adjustable scale height which can be used to determine the emphasis placed on the layers near the surface. In the examples of Figure 6-3, H_s was 5 kilometers. When Expression (6.3-12) is used, then (6.3-10) must also be modified to read

$$\overline{L} = \frac{\int_0^H L(z) e^{-z/H_s} \, dz}{\int_0^H e^{-z/H_s} \, dz} \qquad (6.3\text{-}13)$$
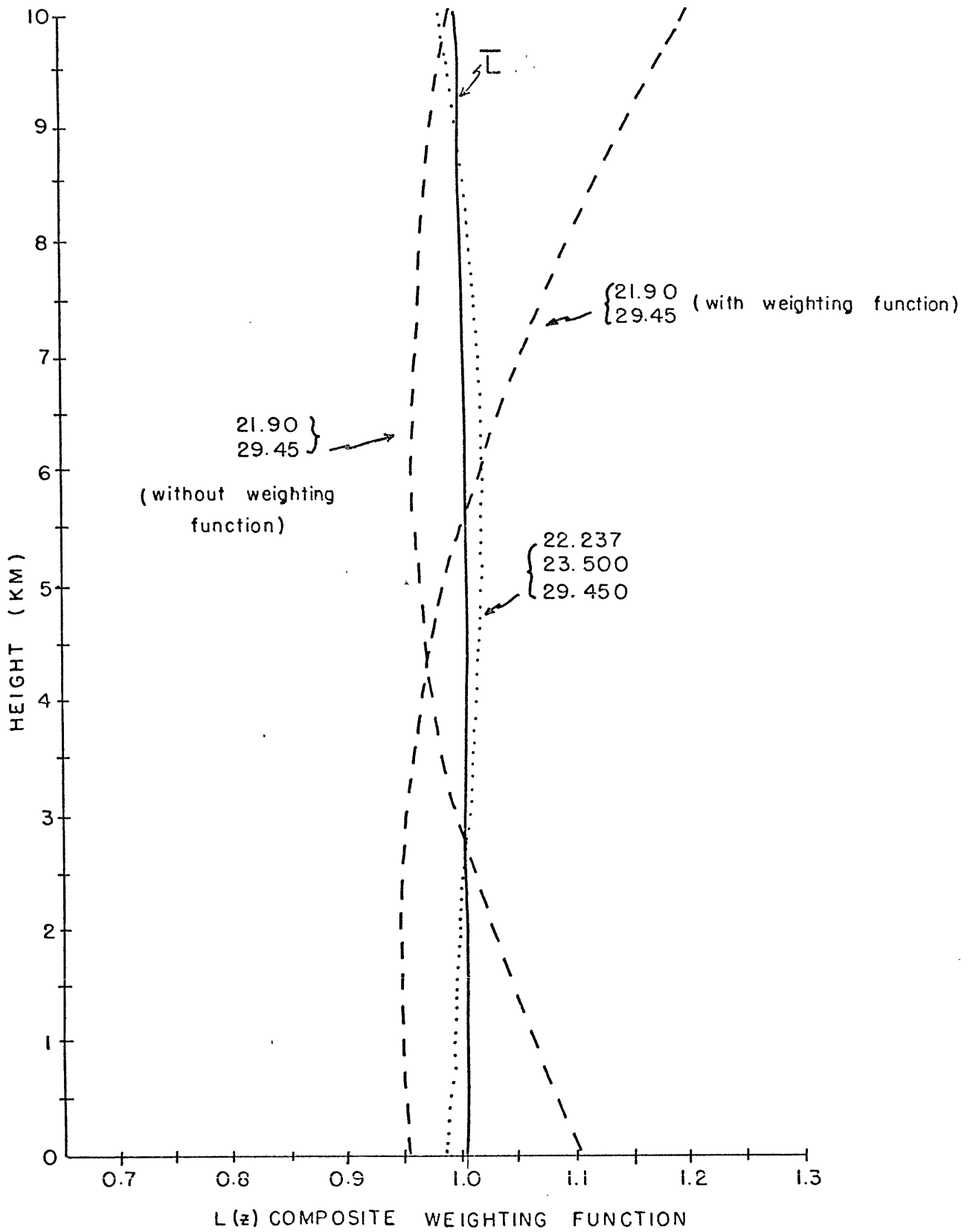
Figure 6-3. Several composite weighting functions L(z).

Summer

DATE OF EXPERIMENT	INT. H_2O RADIOS. (g/cm^2)	INT. H_2O 2 FREQ. (g/cm^2)	% DISC.
15 June 1965	1.564	1.563	-0.0
16 " "	1.565	1.559	-0.0
21 " "	2.771	2.688	-3.0
22 " "	1.227	1.187	-3.2
1 July 1965	1.950	1.918	-1.6
8 " "	2.881	2.799	-2.8
13 " "	2.067	2.011	-2.7
14 " "	3.016	2.892	-4.1
(MIT) 15 " "	2.775	2.706	-2.5
(AFCRL) 15 " "	2.158	2.106	-2.4
19 " "	1.644	1.607	-2.2
21 " "	2.004	1.976	-1.4
22 " "	2.107	2.071	-1.7
27 " "	1.525	1.495	-2.0
28 " "	2.344	2.291	-2.3
29 " "	1.869	1.832	-2.0
3 Aug. 1965	2.758	2.701	-2.0
5 " "	1.886	1.834	-2.8
(1405) 10 " "	4.241	4.118	-2.9
(1804) 10 " "	3.908	3.804	-2.7
(2043) 10 " "	3.280	3.200	-2.4
11 " "	3.299	3.216	-2.5
12 " "	2.405	2.333	-3.0
		Average:	-2.3

Winter

DATE OF EXPERIMENT	INT. H_2O RADIOS. (g/cm^2)	INT. H_2O 2 FREQ. (g/cm^2)	% DISC.
10 Feb. 1966	1.752	1.743	+0.5
14 " "	1.102	1.117	+1.3
17 " "	0.318	0.321	+0.9
18 " "	0.815	0.838	+2.8
23 " "	0.631	0.652	+3.3
29 " "	1.159	1.186	+2.3
3 Mar. 1966	0.691	0.694	+0.4
4 " "	3.540	3.539	-0.0
7 " "	1.134	1.110	-2.1
10 " "	0.845	0.816	-3.4
14 " "	0.643	0.626	-2.6
		Average:	+0.3

Table 6-I. A comparison between the integrated water vapor as determined by using computed absorption and Equation (6.3-14), and the integrated water vapor actually observed by radiosondes.

Summer

DATE OF EXPERIMENT	INT. H_2O RADIOS. (g/cm^2)	INST. H_2O 3 FREQ. (g/cm^2)	% DISC.
15 June 1965	1.564	1.617	+3.4
16 " "	1.565	1.625	+3.8
21 " "	2.771	2.794	+0.8
22 " "	1.227	1.223	-0.1
1 July 1965	1.950	1.984	+1.7
8 " "	2.881	2.908	+1.0
13 " "	2.067	2.078	+0.5
14 " "	3.016	3.013	-0.1
(MIT) 15 " "	2.775	2.798	+0.8
(AFCRL) 15 " "	2.158	2.181	+1.1
19 " "	1.644	1.666	+1.3
21 " "	2.004	2.045	+2.0
22 " "	2.107	2.135	+1.3
27 " "	1.525	1.547	+1.4
28 " "	2.344	2.378	+1.4
29 " "	1.869	1.904	+1.9
3 Aug. 1965	2.758	2.804	+1.7
5 " "	1.886	1.909	+1.2
(1405) 10 " "	4.241	4.271	+0.7
(1804) 10 " "	3.908	3.941	+0.8
(2043) 10 " "	3.280	3.306	+0.8
11 " "	3.299	3.330	+0.9
12 " "	2.405	2.415	+0.4

Average: +1.3

Winter

10 Feb. 1966	1.752	1.813	+3.5
14 " "	1.102	1.160	+5.3
17 " "	0.318	0.340	+6.9
18 " "	0.815	0.864	+6.0
23 " "	0.631	0.671	+6.3
29 " "	1.159	1.219	+5.2
3 Mar. 1966	0.691	0.714	+3.3
4 " "	3.540	3.660	+3.4
7 " "	1.134	1.193	+5.2
10 " "	0.845	0.882	+4.4
14 " "	0.643	0.673	+4.7

Average: +4.9

Table 6-II. A comparison between the integrated water vapor as determined by using computed absorption and Equation (6.3-15), and the integrated water vapor actually observed by radiosondes.

The three-frequency curve in Figure 6-3 deviates from $\overline{L}$ no more than 2% at any level. It represents a remarkably constant L(z). It was also derived by emphasizing the lower regions of the atmosphere, but it is apparent that this was probably unnecessary.

The $a\left(\nu_i\right)$ from the weighted two-frequency curve in Figure 6-3 and the $a\left(\nu_i\right)$ from the three-frequency curve were used on radiosonde absorption computations to determine how accurately integrated water vapor could be estimated if the spectral data were perfect. The results are listed in Tables 6-I and 6-II.

The first table shows the results from using two frequencies only. The $a\left(\nu_i\right)$ for these two frequencies were found empirically and have the values

$$a(21.9) \quad = \quad 1.672 \ g/cm^2 \ db^{-1}$$

$$a(29.45) \quad = \quad 6.015$$

The equation giving the integrated water vapor is therefore

$$V \quad = \quad 1.672 \cdot \tau (21.9) \quad + \quad 6.015 \cdot \tau (29.45) \ g/cm^2 \qquad (6.3\text{-}14)$$

where the $\tau's$ are in db and the a's have been adjusted such that $\overline{L} = 1 \ \delta \nu$.

It will be noticed that all the errors for the estimated summer integrated water vapor are low by an average of -2.3%, which of course is to be expected since L(z) for this case is less than $\overline{L}$ in the lowest 5 kilometers. However, L(z) is low by approximately 5% in this region

where most of the water vapor is and one must therefore draw the con-
clusion that the weighting functions which were used to construct

$L(z)$ were probably a few percent lower than the average weighting

functions of the summer atmospheres examined in Table 6-I to explain

some of the difference between -5% and -2.3%. This will be shown to

be more likely when we investigate the three-frequency case. If all

the estimated integrated water vapor values are increased by 2.3 per-

cent, then only three days would show errors greater than 1.0 percent.

The same cannot be said of the winter two-frequency estimations. The

error spread is from -3.4 percent to plus 3.3 percent reflecting the

effect of colder temperatures on the weighting functions.

From the results above, it is reasonable to expect that for

only two frequencies and no adjustments of the $a(\nu_i)$ for temperature,

accuracies within ±5 percent of the true value are obtainable year

round in a climate such as exhibited by Massachusetts. Using $a(\nu_i)$

adjusted for temperature, the accuracy can probably be increased to

± 2 percent, with the average error approaching zero in each season.

The results for the three-frequency estimation are listed in

Table 6-II. The $a(\nu_i)$ for this composite weighting function are

$$a(22.237) \ = \ 0.385 \ g/cm^2 \ db^{-1}$$

$$a(23.5) \ = \ 2.161$$

$$a(29.45) \ = \ 4.322$$

As in the case of the a's for the two-frequency $L(z)$, the constants

above are adjusted such that $\bar{L} = 1 \ \delta\nu$ and therefore

$$\mathcal{V} = 0.385 \cdot \mathcal{C}(22.235) + 2.161 \cdot \mathcal{C}(23.5) + 4.322 \cdot \mathcal{C}(29.45) \qquad (6.3\text{-}15)$$

Surprisingly enough, despite the considerable improvement in the constancy of L(z) for the three-frequency case, the summer estimates are not substantially better than the two-frequency estimates. If the ± 1.3 percent bias is removed, there are actually more days where the error is greater than 1.0 percent than in the two-frequency summer results. However, the spread of the winter data is considerably smaller than in the two-frequency winter results, even though a much stronger bias is evident. Without seasonal or temperature adjustments of the $\alpha\ (\mathcal{V}_i)$, there is no reason to expect better results over several seasons than with two frequencies. With seasonal adjustments only, some slight advantage probably lies with the three-frequency method. More statistics are necessary to properly decide whether two- or three-frequency observations are better and by how much.

The above results were quoted for perfect data and errors reflect deviations of L(z) from $\bar{\text{L}}$ and fluctuations in the weighting functions with varying atmosphere conditions. More error must be expected from imperfect spectral data.

Some general remarks are in order about the errors introduced by observational data. If obtaining optimum integrated water vapor estimates is the only criterion upon which frequencies for observation are chosen, then they should be chosen to be as low in frequency as possible for two reasons: (1) the effects of clouds are diminished;

and (2), equipment is more reliable. For instance, the 19.0 GHz weighting function is very similar to the 29.45 GHz weighting function used in our experiments and would be a much wiser choice. This is especially true when one realizes that the same absolute errors are multiplied by a factor of four more at the off resonance frequency, i.e.,

$$\frac{a\,(29.45)}{a\,(21.9)} \approx 4$$

Three frequencies do help to alleviate the problem of having noisy data at one frequency. This redundancy will probably be the most important reason to have three rather than two frequencies for observations.

No attempt has been made to evaluate the integrated water vapor from the observations of Chapter 4 mainly because no standard of comparison exists for the results. However, an error analysis of a sort can be done by using the quoted errors on observations to estimate the uncertainty of the integrated water vapor estimates. The error which one would expect in V when errors exist in τ can be approximately written as

$$d V = \left\{ \sum_i \left(a_i |d\tau_i| \right)^2 \right\}^{1/2} \qquad (6.3\text{-}15)$$

For a day of good observing $|d\tau_i|$ can be expected to be near 0.01 db on all channels. Therefore, for the two-frequency case

$$d V_2 = \left\{ \left[1.672\,(0.01) \right]^2 + \left[6.015\,(0.01) \right]^2 \right\}^{1/2}$$

$$= 0.062 \text{ g/cm}^2$$

This must be considered a lower limit to the error expected due to observational errors. For a typical day, one might expect 2 g/cm^2 of integrated water vapor so that this would represent about a 3 percent error, somewhat greater than that expected from variations of L(z). It would appear that the limiting factor for most observations will certainly be the accuracy of the spectral data.

6.4 The Oxygen Contribution to $\hat{\tau}_{max}$

Even with the substantial simplifications which Equation (6.3-11) incorporates over Equation (6.2-8) there still remains the separation of τ_{H_2O} from τ_{max}.

If Equation (6.1-2) is recalled, the attenuation of radiation from an extraterrestrial source may be attributed to several constituents in the atmosphere. We are interested in only one of these constituents, τ_{H_2O}. Following the example of Equation (6.1-2), for any given set of atmospheric conditions, τ_{max} may be broken up as follows:

$$\tau_{max} = \tau_{H_2O} + \tau_{O_2} + \hat{\tau}_{R} \qquad (6.4\text{-}1)$$

As before τ_{R} will be considered to be negligible. The contribution from τ_{O_2} is small but never negligible, and in some cases of extremely dry conditions (the Arctic for instance) will exceed $\hat{\tau}_{H_2O}$. Similar to Equation (6.1-3), τ_{O_2} may be expressed as

$$\tau_{O_2} = \int_{o}^{H} \gamma_{O_2} \, dz \qquad (6.4\text{-}2)$$

γ_{o_2} may be conveniently expressed (see Appendix A-II for the full equation) as

$$\gamma_{o_2} = C_1 P T^{-3} \nu^2 \sum_n S_n e^{-E_n/kT} \qquad (6.4\text{-}3)$$

where γ_{o_2} is in db/m if P is the total pressure in mb, T is the kinetic temperature in degrees Kelvin, ν is the frequency of the penetrating radiation in GHz and C_1 is a constant equal to 2.015×10^{-3}. E_n is the energy in the same units as kT of the lower rotational state of a given transition, each of which is designated by n, and k is Boltzmann's constant. The summation is carried out over all transitions which link signficantly populated energy states at atmospheric temperatures.

The meaning of the S_n is given in Appendix A-II. However, a common factor to all the terms of the S_n is the half width (assumed to be the same for all transitions) $\Delta \nu_{o_2}$. Therefore, we can write

$$\sum_n S_n e^{-E_n/kT} = \Delta \nu_{o_2} \sum_n S_n' e^{-E_n/kT} \qquad (6.4\text{-}4)$$

where

$$\Delta \nu_{o_2} \simeq C_2 P T^{-0.85} \qquad (6.4\text{-}5)$$

$\Delta \nu_{o_2}$ is given in GHz when C_2 is 7.75×10^{-2} GHz/mb and P and T are in millibars and degrees Kelvin respectively.

By removing the common factor of $\Delta \nu_{o_2}$, the S_n' in the region of 22 GHz are now almost independent of $\Delta \nu_{o_2}$. This follows from

Equation (A-II-4) and the inequalities $\nu_n \geq 2\nu$ and $\nu \geq 7 \Delta \nu_{O_2}$ where the ν_n are the resonant frequencies of the oxygen transitions. The summation remaining is a function of temperature through the Boltzmann term. Figure 6-4 is presented to illustrate how the value of the summation from the r.h.s. of Equation (6.4-4) behaves as a function of temperature. It is very closely approximated by a linear function of T . Therefore, from Equation (6.4-5) and the discussion above, Equation (6.4-3) may be rewritten as

$$\gamma_{O_2}' \; (\nu = \text{constant}) \; = \; C_3 \; P^2 \; T^{-3.85} \{ C_4 + C_5 T \} \qquad (6.4\text{-}6)$$

where, for γ_{O_2}' in db/m, C_3 is given by

$$C_3 \; = \; C_1 C_2 \nu^2 \; = \; 1.55 \times 10^{-4} \nu^2 \qquad (6.4\text{-}7)$$

and ν is in GHz. At 19 GHz

$$C_4 \; = \; 0.012$$
$$C_5 \; = \; 1.725 \times 10^{-3} \; .$$

Up to Equation (6.4-6), the approximations may have been quite accurate, introducing very little error. Figure 6-5 compares the computations of total zenith opacity due to oxygen by the full equation (6.4-3) to that from (6.4-6) for a number of radiosonde runs. The small systematic error of 0.0008 db results from ignoring the pressure dependence of β from Equation (A-II-8).

Despite the simplifications of Equation (6.4-6), we are in no better position to simply estimate the oxygen zenith opacity of the
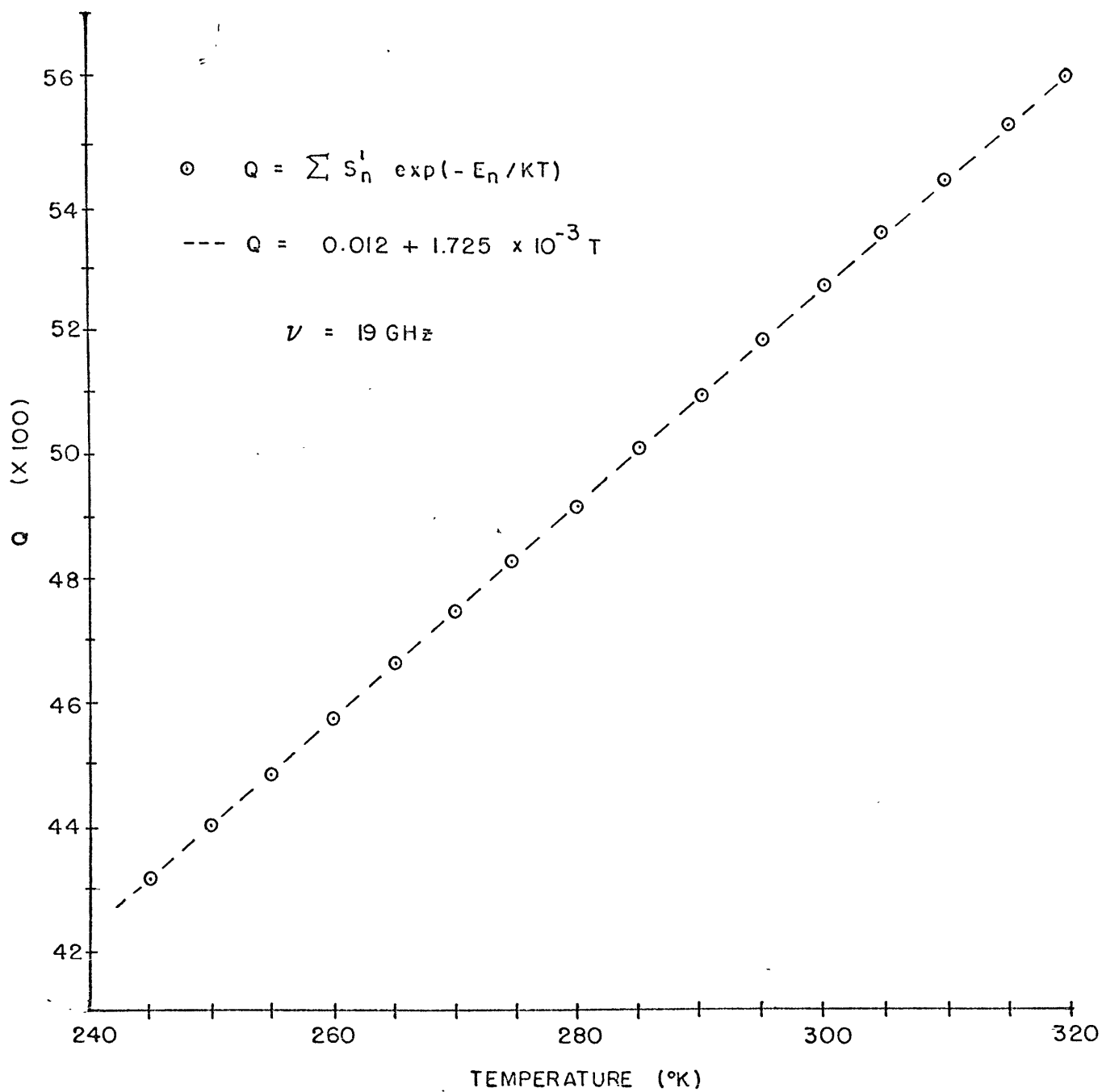
Figure 6-4. The summation from γ_{O_2} and its approximation.
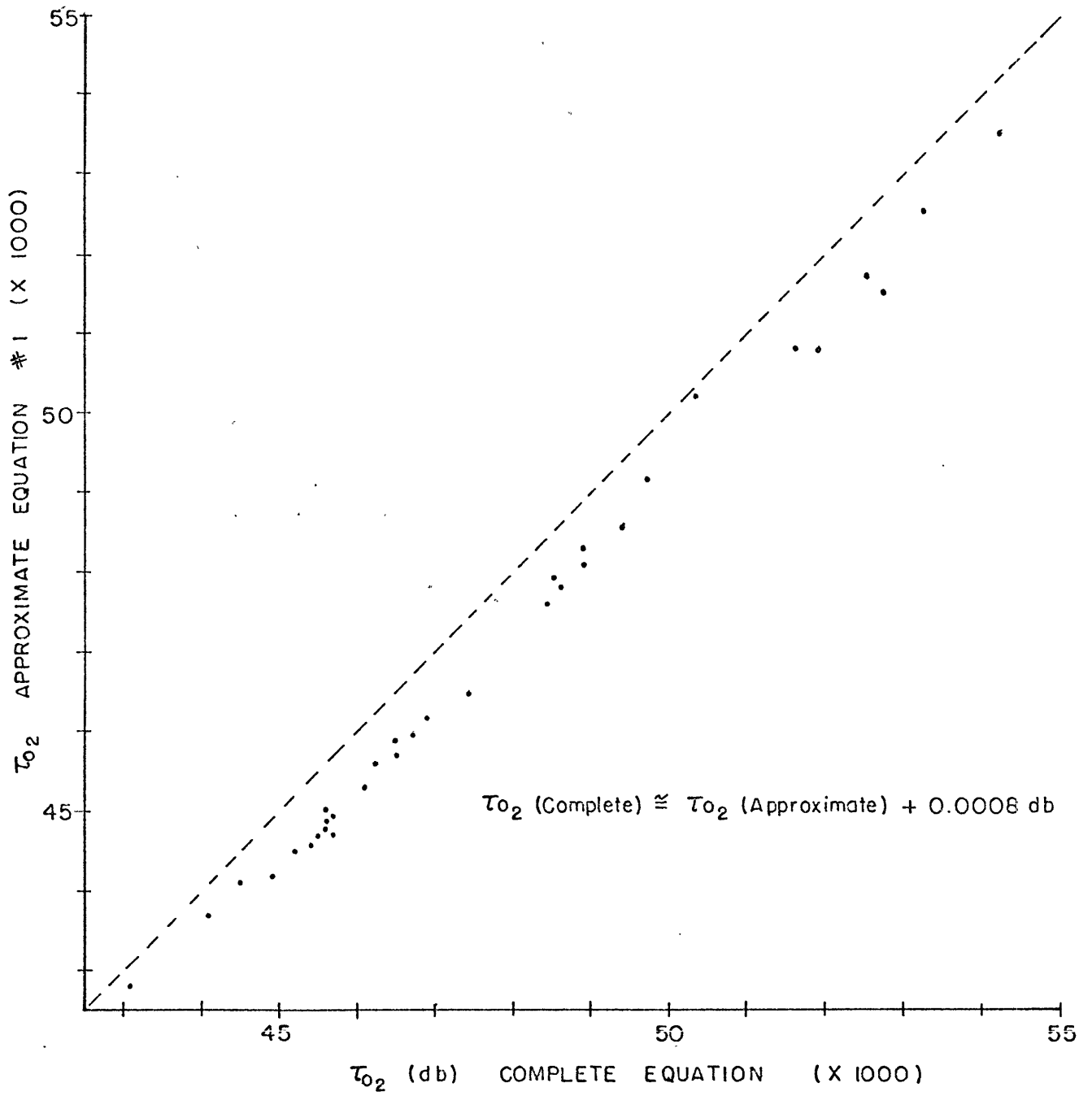
Figure 6-5. The first approximation to τ_{O_2}.

atmosphere. Certainly if measurements of the vertical profile of temperature and pressure can be made in order to use (6.4-6), the water vapor can be measured also. The only convenient parameters which will be measurable at a radiometer site will be surface pressure and temperature. Therefore it will be necessary to use these as inputs to any scheme which estimates the contribution of τ_{O_2} to τ_{max} .

In order to produce such a scheme, several assumptions are necessary. First, we assume that all of the attenuation due to oxygen near 22.2 GHz occurs in the lowest 12 km of the atmosphere. This is reasonable for two reasons: (1) at the height of 12 kilometers in the Standard Atmosphere, 1962, the pressure is about 20 percent of the sea level value. This introduces a factor of 1:5 for attenuation in regions above and below this level. (2) the effective pressures in the two regions are approximately in the ratio of 1:4 introducing another factor of 1:20 in the strength of γ_{O_2} above and below 12 km because of its dependence on pressure squared. The two factors taken together represent roughly an effective attenuation in the two regions of about 1:100 disregarding temperature effects.

Second, we assume that pressure decreases exponentially with altitude with a scale height of 8 km, i.e.,

$$P(z) = P_s e^{-z/H_p} \qquad (6.4-8)$$

where H_p = 8 km, and P_s is the surface pressure. The average pressure over this region is approximately given by

$$\bar{P} = \frac{\int_0^{12} P_s\, e^{-z/H_p}\, dz}{\int_0^{12} dz} = \frac{H_p\, P_s}{12}\left(1 - e^{-12/H_p}\right)$$

$$\cong P_s/2 \qquad\qquad (6.4\text{-}9)$$

The validity of the assumption of an exponential decrease in pressure is investigated in Figure 6-6. The two radiosonde curves mark the extreme summer and winter profiles of pressure versus height. For the first four to six kilometers the approximation appears to be a good average of the extremes. At higher levels the scale height changes because of decreasing temperature and the fit is not as good. Nevertheless, we will retain the approximation at all levels.

The third approximation will be that the temperature decreases linearly with height at a rate near 6.5°K per kilometer up to the 12 km limit. This is approximately true for mean atmospheric conditions. To establish an average temperature which is meaningful for Equation (6.4-6), we must take into consideration that its importance is associated with the pressure squared.

If

$$T(z) = T_s + \eta z \qquad\qquad (6.4\text{-}10)$$

in which T_s is the surface temperature, η is the vertical gradient of the temperature equal approximately to -6.5°K/km, and $T(z)$ is the temperature at the height z, then a pressure squared weighted temperature is given by
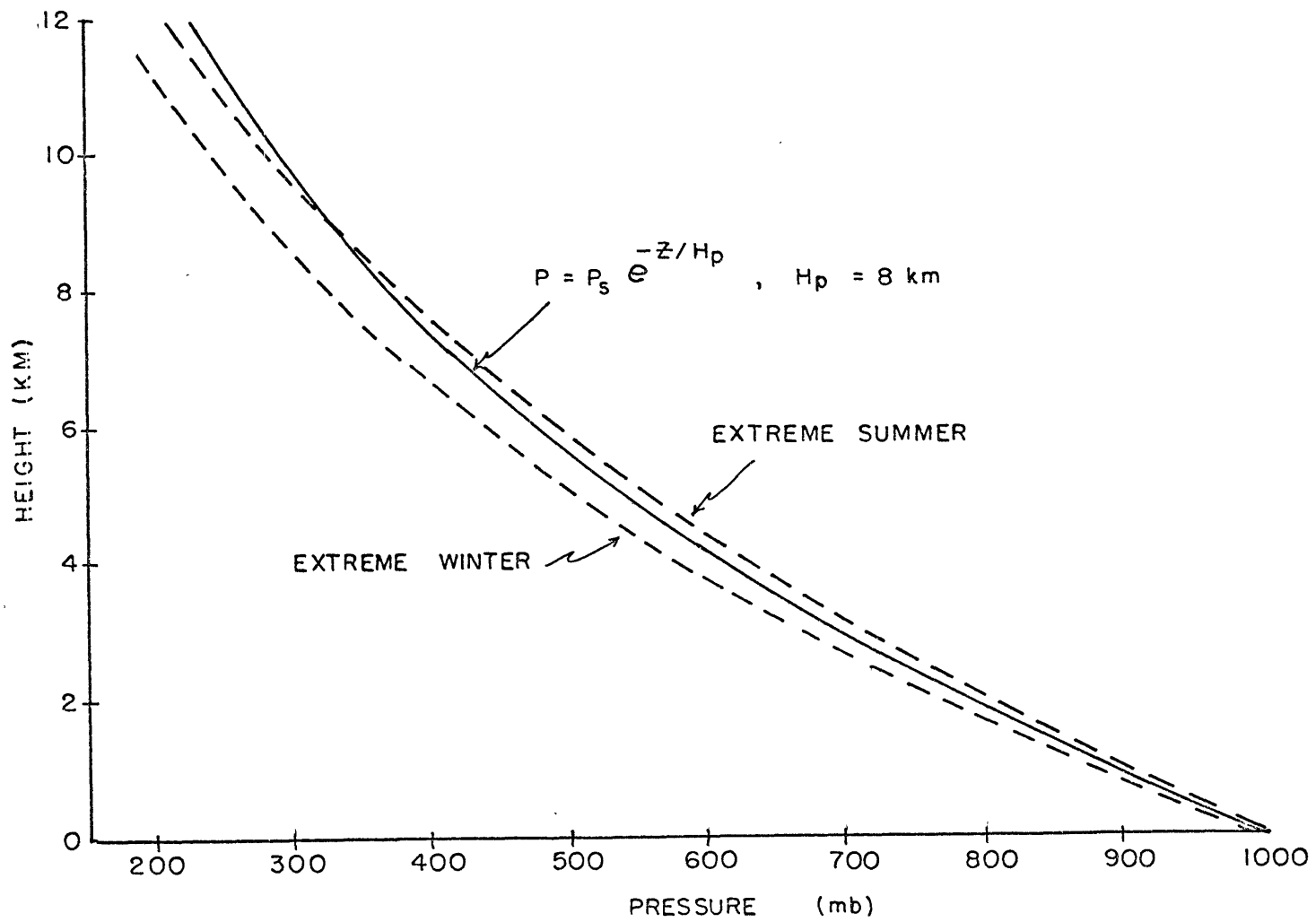
Figure 6-6. The exponential approximation to the dependence of pressure with height.

$$\overline{T} = \frac{\int_o^{12} P_s^2 \, e^{-2z/H_p} \left(T_s + \eta z \right) dz}{\int_o^{12} P_s^2 \, e^{-2z/H_p} \, dz}$$ (6.4-11)

$$= T_s - b$$

where b $= 22^{\circ}$K for an atmosphere whose vertical temperature gradient

is -6.5° K/km.

If we substitute these average quantities for P and T into

Equation (6.4-6) and the result into (6.4-2) with the full realization

that the averages ignore such possibilities as systematic correlations

between themselves, deviations from the model, and are, therefore, only

rough approximations to the real averages, we have a tentative approx-

imation for the oxygen attenuation. It requires only that we know the

pressure and temperature at the observation site. The general expres-

sion is

$$\mathcal{T}_{o_2} \left(\nu = const \right) = \left\{ \gamma_{o_2}' \left(\overline{P}, \overline{T} \right) \right\} \cdot h$$ (6.4-12)

$$= \left\{ c_3 \frac{P_s}{a^2} \left(T_s - b \right)^{-f} \left[c_4 + c_5 \left(T_s - b \right) \right] \right\} \cdot 12 \times 10^3 \, db$$ (6.4-13)

$\widehat{\mathcal{T}}_{o_2}$ at 19 GHz is in db when $C_3 = 5.60 \times 10^{-2}$ and C_4 and C_5 are the

same as before. The constants a, b, and f are, from our previous

analysis, approximately equal numerically to 2, 22°K and 3.85 respect-

ively.

Empirical values of a, b, and f were found which produced the

best overall correlation between the approximate $\hat{\tau}_{0_z}$ calculated

from Equation (6.4-13) above and the full equation from Appendix II

for the 34 radiosonde runs reported in Chapter 4. The results showed

that it was necessary to change the temperature exponent from 3.85 to

a lower value. This changed the value of C_3 considerably. The final

approximate equation, valid only at a given frequency ν , can be

written as

$$\hat{\tau}_{0_z} (\nu = const) \cong C_6 P_s^2 (T_s - b)^{-f} \left[C_4 + C_5 (T_s - b) \right] \qquad (6.4-14)$$

In the equation, C_6 incorporates the constants C_3 and a, and the inte-

gration height of 12×10^3 meters from Equation (6.4-13). For $\nu = 19$ GHz,

and $\hat{\tau}_{0_z}$ in db, then pressure is in millibars, temperature is in

degrees Kelvin, and the various constants have the following values:

$$
\begin{aligned}
C_4 &= 0.012 \\
C_5 &= 1.725 \times 10^{-3} \\
C_6 &= 6.7 \times 10^{-2} \\
b &= 21^\circ K \\
f &= 2.40
\end{aligned}
\qquad \Big\} \quad 19 \ GHz
$$

A comparison between $\hat{\tau}_{0_z}$ as calculated from Equation (6.4-14)

and the full equations in Appendix II is shown in Figure 6-7. The max-

imum deviation between the approximated and non-approximated values is

2.4×10^{-3} db for all of the summer and winter radiosondes reported in

COMPLETE:

$$\tau_{O_2} = \int_0^h C_1 \, P^2 \, T^{-3.85} \left(\sum_n S_n' \, e^{-En/KT} \right) d\bar{z}$$

APPROXIMATE:

$$\tau_{O_2} = C_6 \, P_s^2 \, (T_s-b)^{-f} \left[C_4 + C_5 (T_s-b) \right]$$

τ_{O_2} FINAL APPROXIMATE EQUATION (X 1000)

τ_{O_2} (db) COMPLETE EQUATION (X 1000)
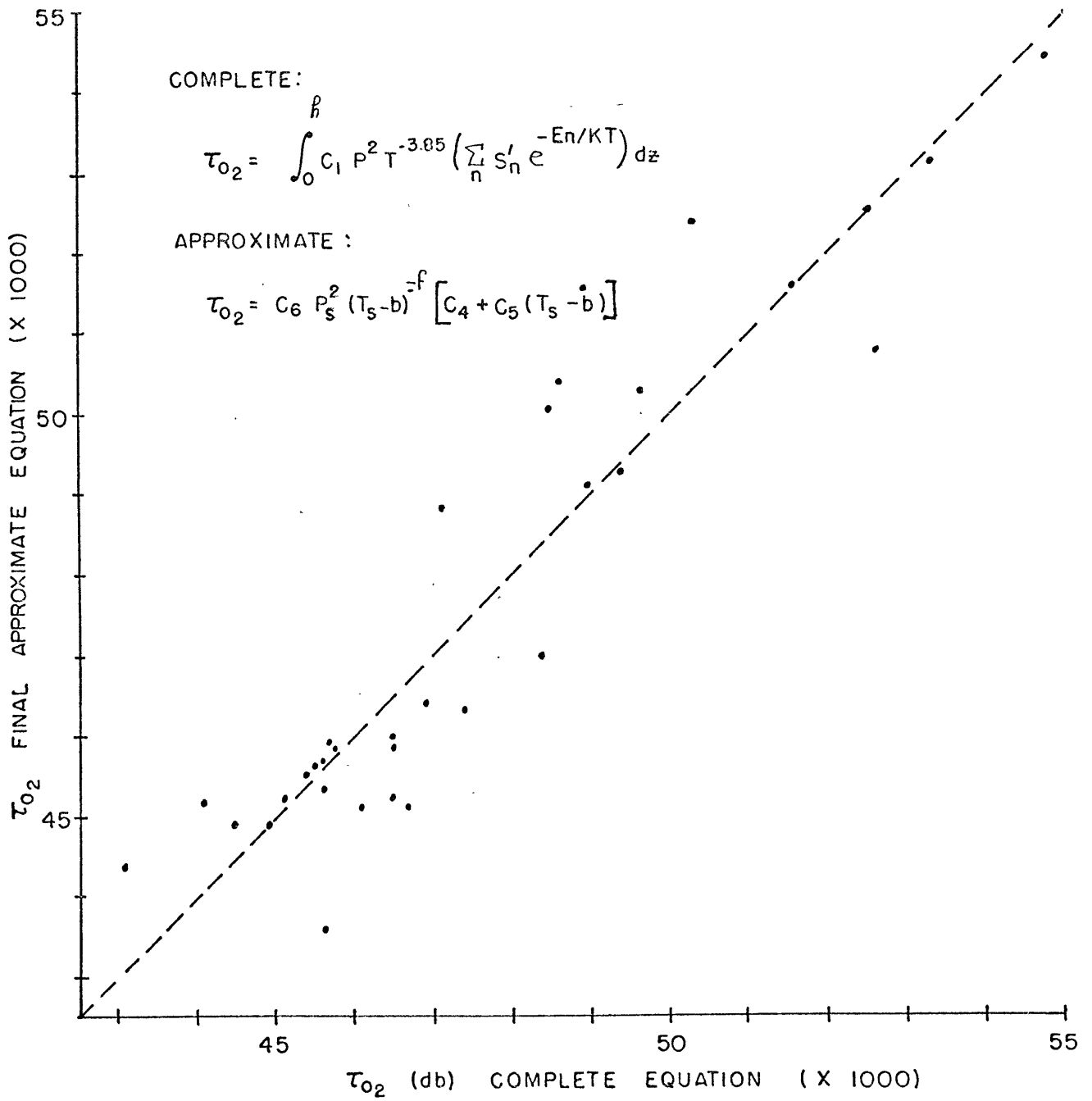
Figure 6-7. A comparison between τ_{O_2} as computed
from the final approximate equation and
τ_{O_2} computed from the full equation.
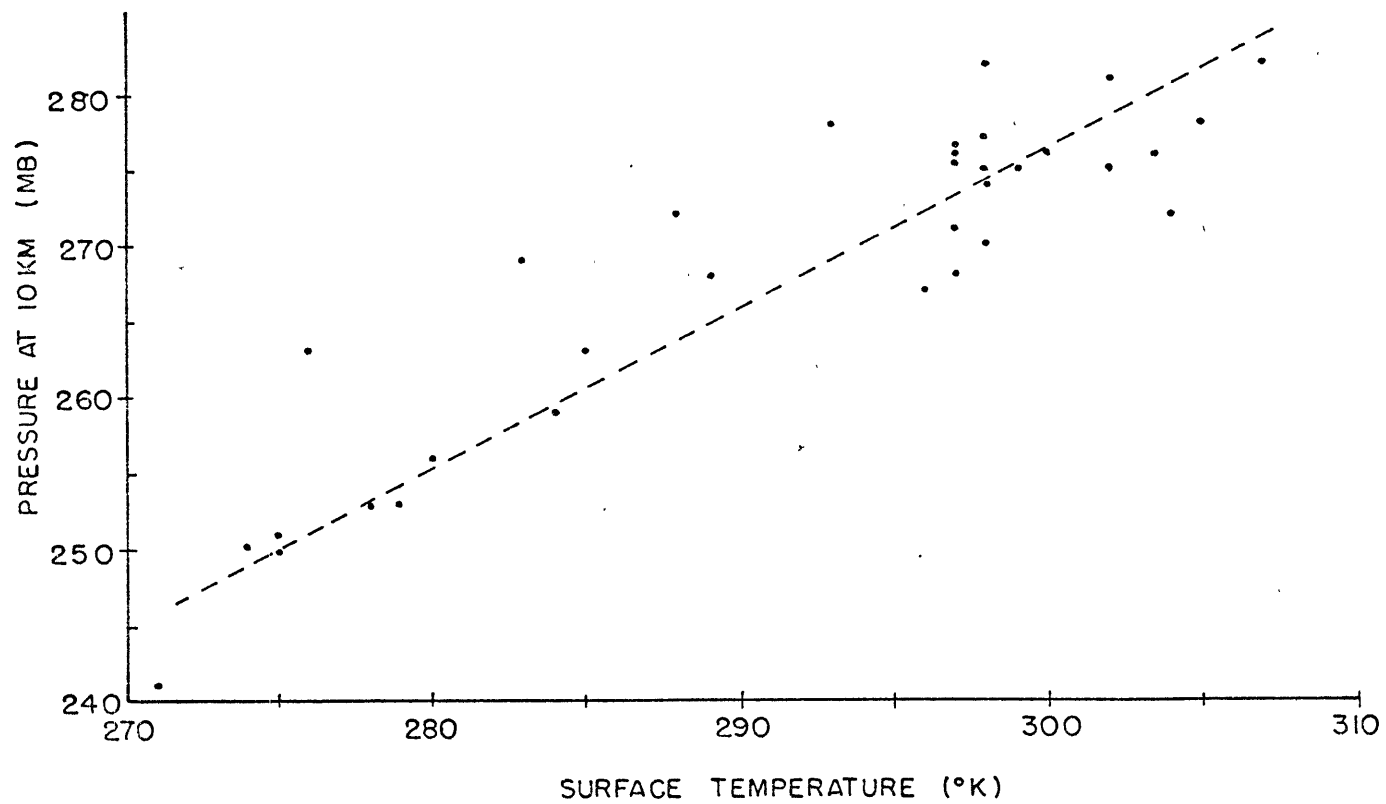
Figure 6-8. The relationship between surface temperature and the pressure at 10 km.

Chapter . The root-mean-square error is approximately 1×10^{-3} db.
The mean value of τ_{o_2} is about 50×10^{-3} db so that a mean error of
about 2% can be expected from using Equation (6.4-14) around the
Boston area. For other regions, C_6 , b, and f will no doubt need to
be optimized again.

The decrease in the temperature exponent f from 3.85 in Equa-
tion (6.4-6) to 2.40 in (6.4-14) can be attributed to systematic cor-
relations between surface temperature and: (1) the pressure scale
height; (2) the vertical lapse rate of temperature; and (3) the opti-
mum surface temperature.

The most obvious correlation is between surface temperature
and the vertical scale height of pressure H_p . When the surface tem-
perature is cool the entire atmosphere tends also to be cool. And
since the separation of constant pressure surfaces is directly pro-
portional to the mean temperature in the layer, the pressure drops
more rapidly in height for cooler atmospheres, i.e., the scale height
diminishes. This may be seen in Figure 6-8. The pressure is lower
at 10 kilometers for lower surface temperatures.

The effect produced by such a correlation can be seen from
Figure 6.6. Everywhere the approximate exponential value of P(z) is
greater than the P(z) measured for the cold winter atmosphere. The
average pressure is therefore lower for the cool atmosphere than in
the exponential approximation and τ_{o_2} estimated from Equation
(6.4-14) is too high. Therefore, for low surface temperatures τ_{o_2}

estimated from (6.4-14) is too high; and conversely, high surfaces temperatures result in an estimation of τ_{o_2} from (6.4-14) which is too low. To correct this the exponent of (1/T) must be reduced.

The second correlation exists between the temperature lapse rate and the surface temperature and is plotted in Figure 6-9. The tropopause temperature variations are less than the surface temperature variations. Therefore the average temperature lapse rate must be higher for higher surface temperatures. That is what appears in Figure 6-9. The average temperature which Equation (6.4-14) assumes is always given by $(T_s - b)$ where b is a constant. Quite obviously, b should be greater for larger lapse rates and less for smaller lapse rates. The effect of leaving b constant is to provide average temperature estimates to Equation (6.4-14) which are too high for high surface temperatures and too low for low surface temperatures. The effect on τ_{o_2} estimated from (6.4-14) is the same as for the pressure-surface temperature correlation. The remedy is also the same: decrease the temperature exponent f.

Finally, even if all lapse rates were constant, the use of the surface temperature T_s as measured at the observation site will not be an optimum value for the lower boundary of a constant lapse rate approximation. Shallow inversions in winter, for instance, will produce a value of T_s which is much too low to be representative of the entire atmosphere. Also, in summer, many times there are shallow layers which have a lapse rate considerably greater than the average
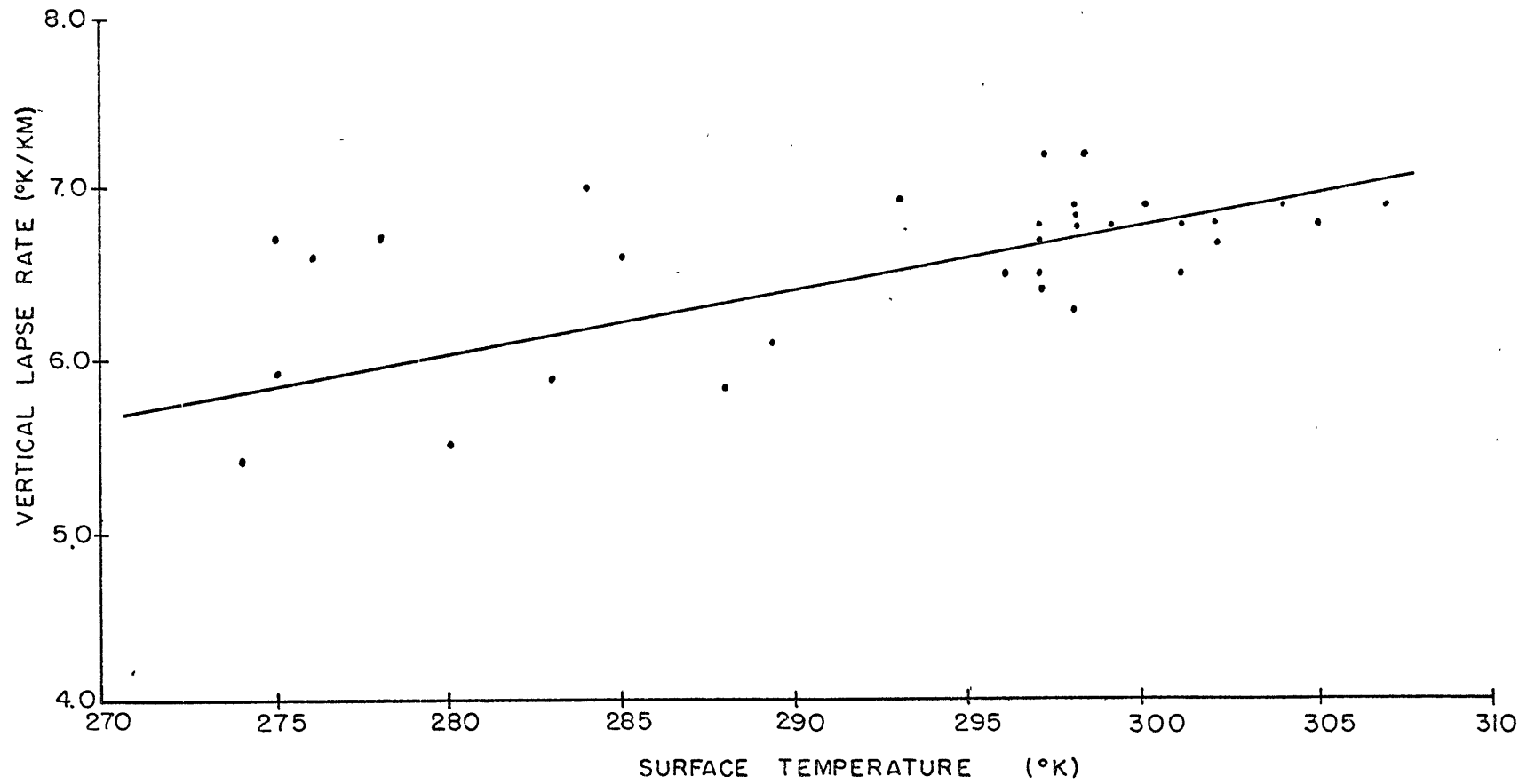
Figure 6-9. The relationship between surface temperature
and vertical lapse rate.

for the remainder of the atmosphere, again causing the surface temperature to be unrepresentative of the mean temperature. This misrepresentation is correlated with surface temperature as shown in Figure 6-10. An optimum surface temperature was determined by extrapolating to the surface the best straight line fit through a day's temperature profile. Systematically, the surface temperature tended to be lower than this optimum in cold surface temperature days and above the optimum on warm surface temperature days. The effect on τ_{o_2} estimated by Equation (6.4-14) is again to reduce τ_{o_2} below its true value on warm days and to increase it above its true value on cold days. The remedy is once more to reduce the exponent f.

The result of all three correlations has led to the adoption of the exponent of (1/T) as 2.40.

Equation (6.4-14), with the values of the constants quoted, is valid at 19 GHz only. To extend it to values through 32 GHz, the following empirical formula is accurate to within 0.001 db:

$$\tau_{o_2}(\nu) = \tau_{o_2}(\nu = 19\,GHz)\left\{2.229 - 2.715\left(\frac{\nu}{19}\right) + 1.486\left(\frac{\nu}{19}\right)^2\right\} \quad (6.4-15)$$

where the frequency ν is in GHz.
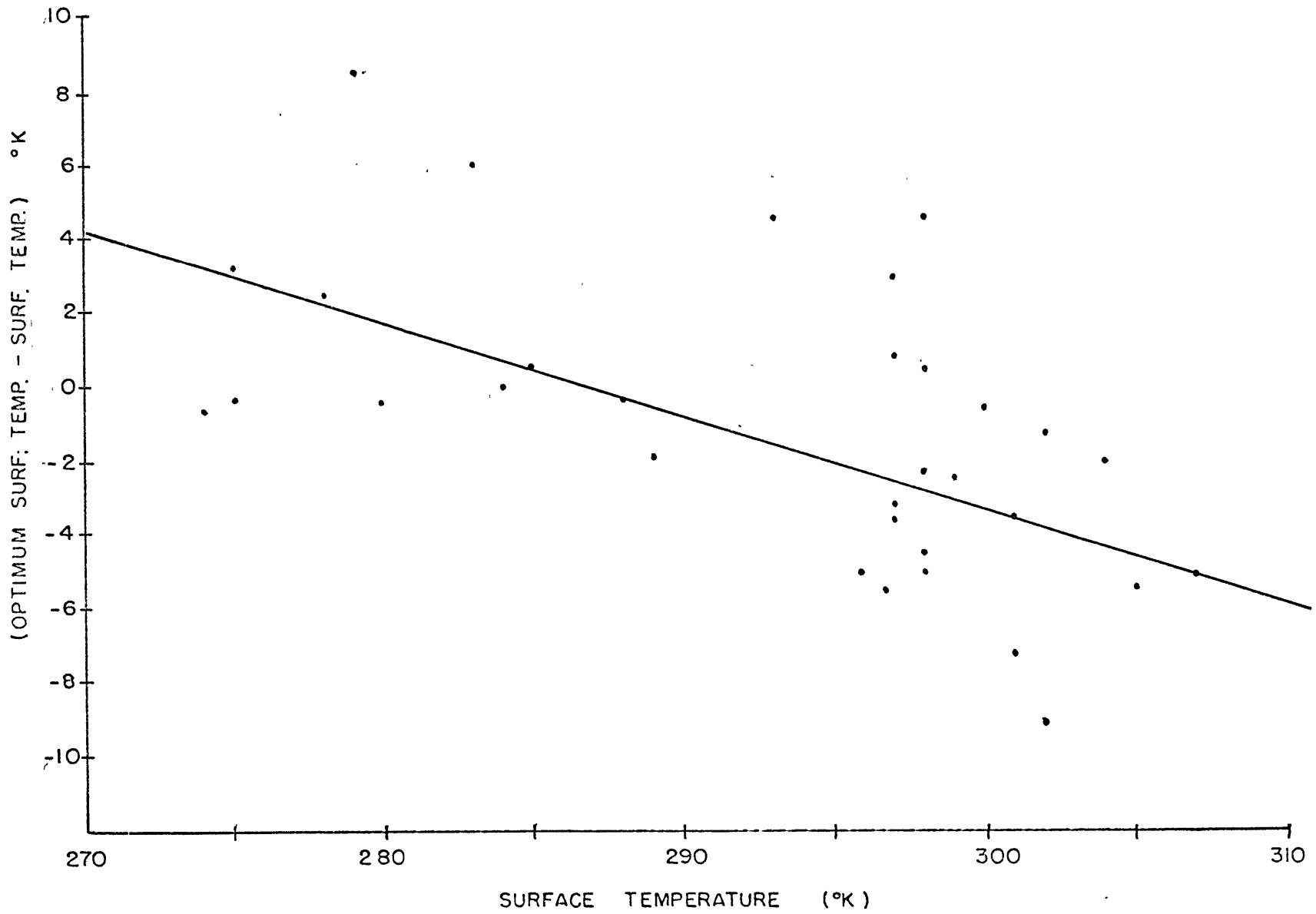
Figure 6-10. The relationship between the measured surface temperature
and the optimum surface temperature.

Chapter   7

THE ABUNDANCE AND VERTICAL DISTRIBUTION OF WATER VAPOR FROM

TOTAL ZENITH OPACITY SPECTRAL MEASUREMENTS NEAR 22.2 GHz

Before the full potentialities of satellites are achieved for

meteorological surveillance, satisfactory schemes must be perfected

which relate the radiation data which a satellite might measure to

the parameters of interest to the meteorologist.

A great deal of work on inversion schemes has already been

done. Geophysical quantities which appear to be recoverable from radia-

tion data are: atmospheric temperature[35,49,50,51,52,54]; the amount

and vertical distribution of ozone[55]; the amount and vertical distri-

bution of water vapor[31,56,57,60]; the spatial extent and liquid water

content of clouds[56,61]; surface temperature[57,62]; sea "state"[58]; the

thickness of constant pressure difference layers[51]; and the existence

of trace gases[63].

The work so far accomplished to recover information about atmo-

spheric water vapor from satellites has been done mostly in the infrared,

primarily because instrumentation has been available for a long time

and because the instrumentation is simple and compact lending itself

to satellite packaging. Möller[60] for instance, has shown how to relate

the radiation received at a satellite in the 5.8 to 6.8 micron band to

the mean relative humidity of the troposphere if the temperature profile

is known. Modifications of this method have been used by Rashke[57] to

evaluate radiation data from Tiros IV in order to provide global mean

relative humidity maps of the upper troposphere (above 500 mb).

The infrared spectral region, however, suffers from a serious

limitation when it is used to study atmospheric water vapor. The

limitation is imposed by clouds. Even thin clouds are opaque to

infrared radiation and therefore limit the region of the troposphere

able to be explored by infrared sensors. When hemispheric pictures

of the earth taken from space are analyzed for percent cloud cover,

it is quickly evident how much of a handicap this is.

The microwave region of the spectrum, on the other hand, has

the advantage of spanning a zone of frequencies within which clouds

at the lower frequencies are essentially transparent and at the higher

frequencies are opaque. Below about 30 GHz (1 cm) clouds rapidly lose

their ability to absorb and scatter radiation; at higher frequencies

they rapidly become opaque. Quite fortuitously, the lowest frequency

water vapor resonance is centered near 1.35 cm and is therefore little

affected by ordinary cloud cover.

This has naturally led to the suggestion that microwave radio-

metry eventually should be the most useful tool for determining infor-

mation about atmospheric water vapor from satellites. This is probably

true, but first, a satisfactory inversion scheme must be perfected

to relate the measurements to the water vapor distribution. This is

not an easy problem. Besides the inherent problems of stability from

which many inversion schemes suffer, there are the added problems of the background radiation and clouds, both of which must be properly handled if accurate water vapor information is to be extracted from the data.

The former problem has been touched upon in Chapter 3 and Appendix A-III. The problem of clouds has been studied by Staelin[56]. He has shown that the weighting functions for certain frequencies above and below the 22.2 GHz resonance are almost identical in the absence of clouds. However, the spectral effect of clouds is proportional to $1/\lambda^2$. Therefore, measurements which would otherwise be similar at the two frequencies are modified in the presence of clouds. The modifications contain information about the clouds which may be used to correct the spectral data.

Of the types of microwave measurements presented in Chapter 3, the satellite measurements for the reasons given above will be the most difficult to invert for information about atmospheric water vapor. The surface based measurements of the brightness temperature spectrum will be the next most difficult to invert. They do not have the complex question of a variable background to contend with, but they are inherently non-linear because of the role of temperature in the absorption coefficient and in the source function. The brightness temperature can never exceed the temperature of the atmosphere; therefore, as the water vapor abundance increases, the brightness temperature near the center of the line will at first increase approximately linearly,

then asymptotically approach the kinetic temperature of the atmospheric water vapor. However, the brightness temperature observed at frequencies in the wings of the line will seldom, if ever, depart from a linear relationship with water vapor. The result is a nonlinear spectrum.

The simplest of the measurements discussed in Chapter 3 to invert must be the zenith opacity measurements; they are very nearly linear in water vapor density for the concentrations found in the atmosphere. Despite their relative simplicity, they retain many of the difficulties and problems which must be overcome if any set of spectral measurements are to be inverted for the vertical distribution of water vapor. Therefore, the problem of the inversion of opacity measurements has been chosen as the subject of investigation for this chapter.

7. 1   The Optimum Linear Estimator

The scheme outlined below was suggested by Rodgers[43] for the problem of inverting infrared spectral data to yield a profile of the atmospheric temperature. The form which will be presented for water vapor was suggested by Staelin[84].

Recall the shape of the zenith opacity weighting functions. Certain frequencies are more sensitive to water vapor at a given height than other frequencies. That is, if the water vapor is increased at say 16 km, the opacity measured on the ground at 21.9 GHz will be relatively strongly affected whereas the opacity measurement at 19.0 GHz will be relatively weakly affected. If, on the basis of

measurements at these two frequencies alone, we were forced to choose

a water vapor distribution, the choice at 16 km would naturally rely

more heavily on the 21.9 GHz measurement. At levels near the surface,

we would most likely rely just as heavily on both frequencies. Using

the same reasoning and utilizing the quasi-linear nature of γ_{H_2O}

with respect to water vapor density, we can write for any given level

z_i in the atmosphere a best estimate of the water vapor at that level

based upon measurements of zenith opacity at j frequencies at the

ground, i.e.,

$$\rho_i^* = \sum_j D_{ij} \, d_j \tag{7.1-1}$$

where ρ_i^* is the estimated mean density in the i th layer in the

atmosphere, the d_j are the opacity measurements and, D_{ij} is some linear

operator which transforms the spectral data to an estimate of water

vapor. The D_{ij} change with height not only because ρ diminishes with

height but also because the sensitivity of the various frequencies

change with height.

Equation (7.1-1) as it stands does not provide a unique solution

for the ρ_i^* because for every set of d_j opacity measurements there

can be an infinite manifold of water vapor distributions which would

produce those measurements. What is needed is a condition on the D_{ij}

which defines the optimum estimate of the water vapor distribution

given a set of spectral measurements d_j . A logical condition which

suggests itself is to choose the D_{ij} such that the most probable water

vapor distribution which will produce a given set of d_j's is estimated.
This condition can be written symbolically as the minimization of the
expression

$$E\left[\left(\underline{\rho}^* - \underline{\rho}\right)^t \left(\underline{\rho}^* - \underline{\rho}\right)\right] = E\left[Q\right] \qquad (7.1\text{-}2)$$

where the once underlined quantities are column vectors, the symbol E
represents the expected value or statistical average of the square
bracketed quantity, the superscript t stands for a matrix transpose,
and ρ_i^* and ρ_i are the estimated and real water vapor densities
in the i th layer in the atmosphere. Simply stated, Equation (7.1-2)
requires that the mean squared error between the estimated water vapor
and actual water vapor density be a minimum in the statistical sense.

In order to utilize the condition established in expression
(7.1-2), rewrite $\underline{\rho}^*$ in terms of the matrix $\underline{\underline{D}}$ (double underline
identifies a matrix) and the data vector $\underline{d}$:

$$Q = \left[\underline{d}^t \underline{\underline{D}}^t \underline{\underline{D}} \underline{d} - \underline{\rho}^t \underline{\underline{D}} \underline{d} - \underline{d}^t \underline{\underline{D}}^t \underline{\rho} + \underline{\rho}^t \underline{\rho}\right] \qquad (7.1\text{-}3)$$

The condition for minimization becomes

$$\frac{\partial E[Q]}{\partial D_{ij}} = 0 \qquad (7.1\text{-}4)$$

The result for any given ij is

$$0 = E\left[d_j \underline{\underline{D}} \underline{d} + \underline{d}^t \underline{\underline{D}}^t d_j - \rho_j d_i - d_i \rho_j\right] \qquad (7.1\text{-}5)$$

which can be restored to full matrix notation as

$$0 = E\left[\underline{\underline{D}}\,\underline{d}\,\underline{d}^t - \underline{\rho}\,\underline{d}^t\right] \quad . \tag{7.1-6}$$

For the equality to be satisfied Equation (7.1-6) requires that

$$\underline{\underline{D}}\,E\left[\underline{d}\,\underline{d}^t\right] = E\left[\underline{\rho}\,\underline{d}^t\right] \quad . \tag{7.1-7}$$

$\underline{\underline{D}}$ is not a random variable and therefore has been removed to the outside of the statistical average brackets. If we define a data correlation matrix $\underline{\underline{C}}_d$ such that

$$\underline{\underline{C}}_d = E\left[\underline{d}\,\underline{d}^t\right] \tag{7.1-8}$$

then a formal solution to the operator $\underline{\underline{D}}$ may be written as

$$\underline{\underline{D}} = \underline{\underline{C}}_d^{-1}\,E\left[\underline{\rho}\,\underline{d}^t\right] \tag{7.1-9}$$

A straightforward method of evaluating the r.h.s. of Equation (7.1-9) would be to simply simultaneously monitor the spectral features of the atmosphere and its water vapor distribution in some suitable manner to establish the statistical averages of the required correlations. This would not require any knowledge of the atmosphere-spectral data relationship but would be a costly and time consuming endeavor.

Another method which would eliminate the necessity of the simultaneous radiometer measurements would rely on the known relationship between atmospheric conditions and the spectral data to establish

the needed correlations in (7.1-9). Old radiosonde data would be as usable as new data to establish approximations to the statistical averages. Further simplification ensues if the quasi-stationary nature of the weighting functions are utilized. For that case a noiseless data vector can be written as

$$\underline{d}_o = \underline{\underline{W}} \, \underline{\rho}$$ (7.1-10)

where $\underline{\underline{W}}$ is composed of elements W_{ij} which are average values of the weighting function at a given frequency ν_j , over a vertical interval in which the average water vapor density is ρ_i , multiplied by that vertical interval Δz_i .

The total noisy data vector can be written as

$$\underline{d} = \underline{d}_o + \underline{n}$$ (7.1-11)

where the n_j are the expected noise levels in each radiometer channel. The data correlation matrix becomes

$$\underline{\underline{C}}_d = E\left[\underline{d}\,\underline{d}^t\right] = E\left[(\underline{d}_o + \underline{n})\,(\underline{d}_o + \underline{n})^t\right]$$

$$= E\left[\underline{d}_o\,\underline{d}_o^t + 2\,\underline{n}\,\underline{d}_o^t + \underline{n}\,\underline{n}^t\right]$$ (7.1-12)

If there is no correlation between the noise and data, then Equation (7.1-12) reduces to

$$\underline{\underline{C}}_d = E\left[\underline{d}_o\,\underline{d}_o^t\right] + E\left[\underline{n}\,\underline{n}^t\right] = \underline{\underline{C}}_o + \underline{\underline{C}}_n$$ (7.1-13)

in which $\underline{\underline{C}}_o$ and $\underline{\underline{C}}_n$ are the noiseless data correlation matrix and the noise correlation matrix, respectively. If the noise is uncorrelated

from channel to channel then

$$\underline{\underline{C}}_n = \left[n_r n_s \delta_{rs} \right] \tag{7.1-14}$$

where δ_{rs} is the Kronecker delta.

Using Equation (7.1-10) $\underline{\underline{C}}_o$ may be written as

$$\underline{\underline{C}}_o = E\left[\underline{d}_o \underline{d}_o^t \right] = E\left[\underline{\underline{W}} \underline{\rho} \underline{\rho}^t \underline{\underline{W}} \right]$$

$$= \underline{\underline{W}} \, E\left[\underline{\rho} \, \underline{\rho}^t \right] \underline{\underline{W}} = \underline{\underline{W}} \, \underline{\underline{C}}_\rho \, \underline{\underline{W}} \tag{7.1-15}$$

where a water vapor correlation matrix $\underline{\underline{C}}_\rho$ has been implicitly defined.

Finally, the statistical average of the water vapor data correlation required in Equation (7.1-9) may be found from radiosonde data alone by making the substitution

$$E\left[\underline{\rho} \, \underline{d}^t \right] = E\left[\underline{\rho} \, (\underline{d}_o + \underline{n})^t \right]$$

$$= E\left[\underline{\rho} \underline{\rho}^t \underline{\underline{W}} + \underline{\rho} \underline{n}^t \right]$$

$$= \underline{\underline{C}}_\rho \, \underline{\underline{W}} \tag{7.1-16}$$

The last expression results if there is no correlation between the water vapor distribution and the noise in the measurements.

If we draw everything together, the solution of $\underline{\underline{D}}$ may be rewritten as

$$\underline{\underline{D}} = \left(\underline{\underline{C}}_o + \underline{\underline{C}}_n \right)^{-1} \underline{\underline{W}} \, \underline{\underline{C}}_\rho \tag{7.1-17}$$

where $\underline{\underline{C}}_n$, $\underline{\underline{C}}_o$, $\underline{\underline{W}}$, and $\underline{\underline{C}}$ are defined in Equations (7.1-14), (7.1-15),

(7.1-10), and (7.1-15) respectively.

Equation (7.1-1) together with the definition of $\underline{\underline{D}}$ given in (7.1-17) will be known as the Optimum Linear Estimator (OLE).

7.2 The Implementation of and the Results from the Optimum Linear Estimator.

Several of the important features of the OLE include: (1) data need not be only radiometer data; it can be anything which is correlated in some manner with the distribution of water vapor; and (2), no relationship between the number of data points and the number of estimation levels is implied.

The first feature has been utilized for the results presented further on by using the measured surface water vapor density as a data point. This would normally be easily measured and is certainly an important piece of information in the estimation of the water vapor profile.

The second feature is helpful in easily establishing the optimum number of data channels to use.

The proper evaluation of the expected values of the various correlations which are part of the solution to $\underline{\underline{D}}$ require an infinite number of atmospheric soundings. Unfortunately, for the analysis which ensues, there were available only 34 atmospheric soundings, a rather small statistical sample to say the least. Nevertheless,

it is possible to portray the characteristics of the OLE in broad terms even with such a small sample.

Most of the atmospheric water vapor is in the lowest two or three kilometers of the troposphere, and therefore we have extended our predicted values of ρ to only 10 kilometers. The water vapor estimates are the average values over one kilometer slabs plus sometimes the surface value. Therefore the index i runs normally from 1 to 10, or 1 to 11.

The number of data channels is varied from two to five. For illustration, if five channels are used and eleven layers, then the size of the various matrices would be the following:

$$\underline{d} : \quad 5 \times 1$$

$$\underline{\rho} : \quad 11 \times 1$$

$$\underline{\underline{D}} : \quad 11 \times 5$$

$$\underline{\underline{C}} : \quad 11 \times 11$$

$$\underline{\underline{C}}_o, \, \underline{\underline{C}}_o : \quad 5 \times 5$$

$$\underline{\underline{W}} : \quad 5 \times 11$$

The weighting functions used throughout the analysis are averages of the weighting functions for all of the days with radiosonde data in a given season. In Figure 7-1, these average values are plotted. For the summer data, mostly information from channels at frequencies of 21.9 GHz, 23.5 GHz and 29.45 GHz were used. They appear as solid curves in the figure. For the winter data, mostly
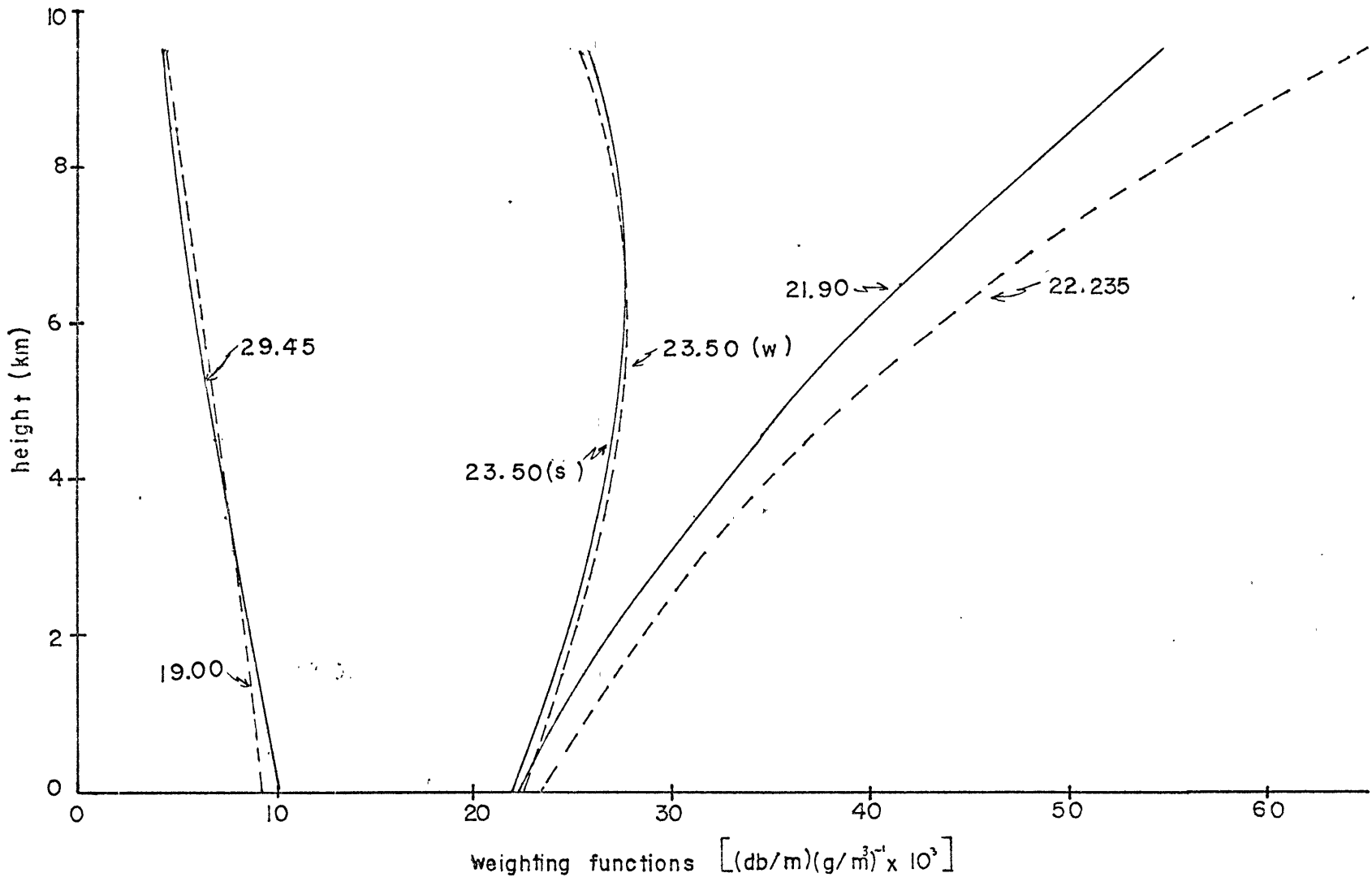
Figure 7-1. The average weighting functions computed for use in the Optimum Linear Estimator.

information from channels at frequencies of 19.0 GHz, 22.235 GHz and 23.5 GHz were used. They appear as dashed lines in Figure 7-1. The summer to winter variation in the 23.5 GHz weighting function may be noted; also to be noted is the close similarity between the 19.0 and 29.45 GHz weighting functions.

There are several parameters which can be varied in the OLE scheme: the amount of expected noise; the number of data channels; and the atmospheric statistics. We will investigate, in a series of subsections, the effects of varying each of these parameters. And finally, several days of real data from the observations reported in Chapter 4 will be inverted and analyzed.

7.2.1 The Effects of Expected Noise on the Results of the Optimum Linear Estimator.

The data which is recovered from atmospheric spectral observations is never perfect. Even if the atmosphere were perfectly stratified and unchanging in time, random noise would still be introduced by the radiometer. Therefore, of utmost importance is to know how any inversion scheme reacts to the errors which are inevitably introduced.

The OLE considers noise as a quasi-weighting function for the data received. If the scheme expects no noise, then the inversion will use the data to produce the most detailed estimate of the water vapor distribution of which it is capable. If noise is expected in

the data, the OLE treats the data more skeptically, relying more on the mean statistics of the atmosphere which are contained in $\underline{\underline{C}}$.

To illustrate the effect of expected noise on the $\underline{\underline{D}}$ operator, consider Figures 7-2 and 7-3. Figure 7-2 plots the $\underline{\underline{D}}$ matrix when no noise is expected. At any level, it is evident that the difference between values which contain large numerical factors will determine the estimated value of the water vapor. Small errors in any one channel will cause large variations in these estimates.

In Figure 7-3, the $\underline{\underline{D}}$ matrix has been calculated under the assumption that the statistical average of the random noise in each channel is 0.005 db. Notice the drastic reduction in the abscissa scale. The expectation of a little noise has stabilized the solution substantially. Small errors in any one channel are much less impor- tant if the noise stabilized $\underline{\underline{D}}$ operator were to be used.

To illustrate the effect which noise has on the water vapor estimate itself, Figure 7-4 has been prepared. The solid curve is the radiosonde profile; the dotted curve is a result of using the $\underline{\underline{D}}$ operator which expects no noise; and the dashed curve portrays the expected water vapor profile when noise is expected in the data. The data input was that calculated from the radiosonde information; it was therefore essentially noiseless data.

The noiseless inversion is particularly good. It picks up the inversion near the surface and faithfully follows the abrupt change in the vertical gradient between three and four kilometers in height.
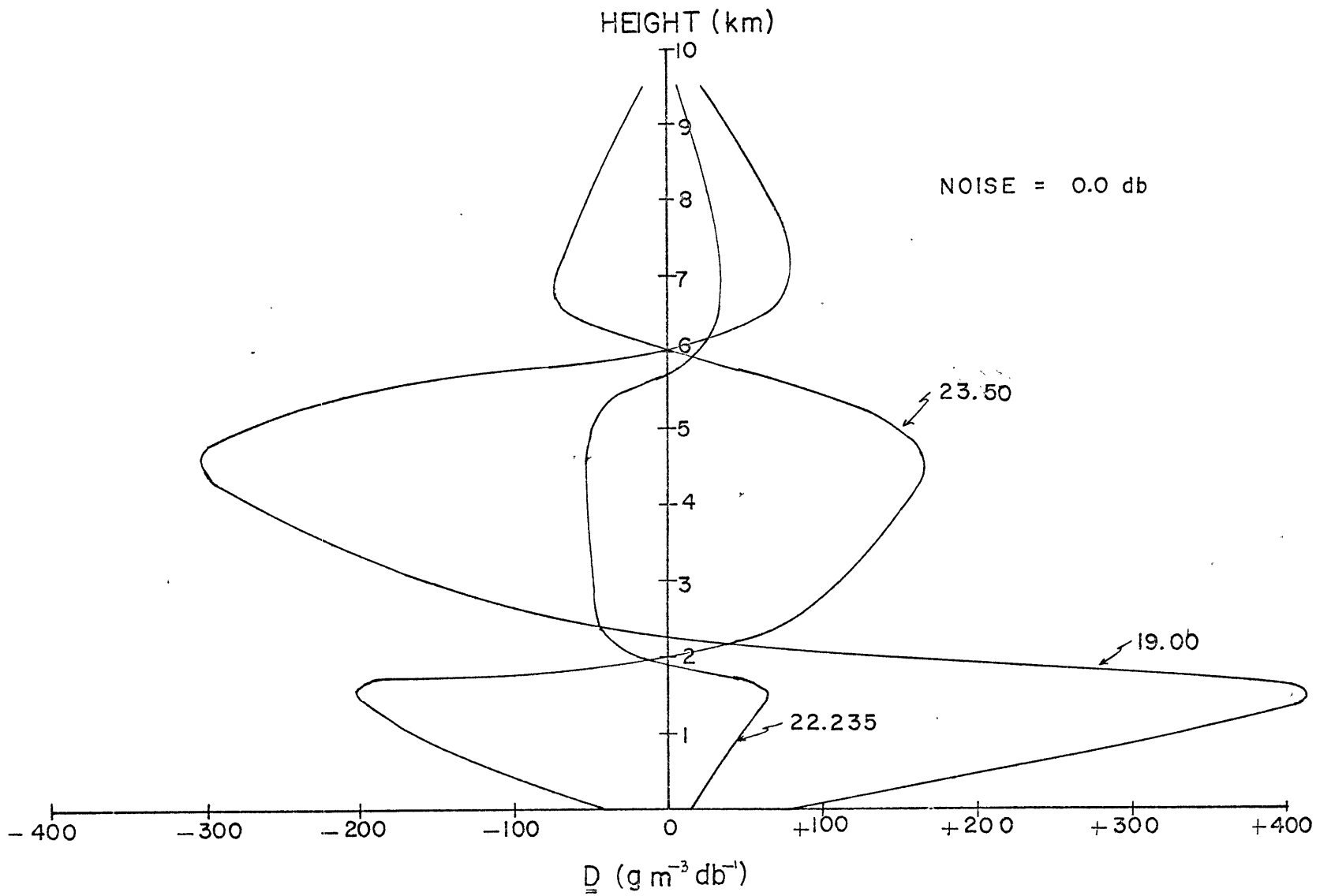
Figure 7-2. The $\underline{\underline{D}}$ matrix which expects no noise.
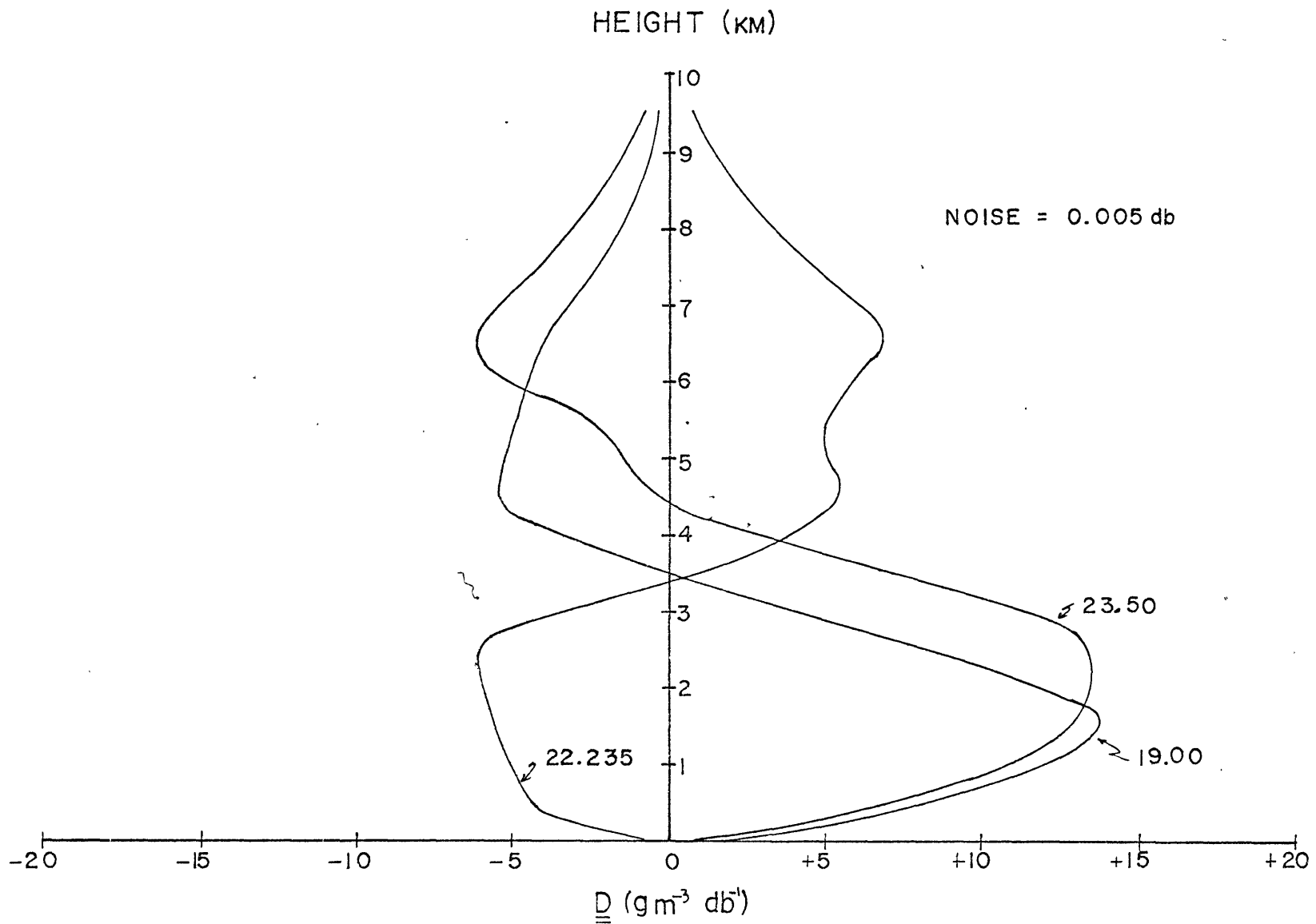
Figure 7-3. The $\underline{\underline{D}}$ matrix which expects 0.005 db of noise in each radiometer channel.

It even follows the trend of the data in the highest four kilometers.
The noisy inversion is good but many details are lost: the inversion
is gone, and the profile is considerably smoothed.

A general feature is evident in the smooth profile: for small
values of noise the noisy inversion always tends to the shape of the
mean profile of water vapor contained in the diagonal terms of $\underline{\underline{C}}\varphi$.
This can be understood by realizing that the noise correlation matrix
$\underline{\underline{C}}_n$ contains only diagonal terms, and when added to $\underline{\underline{C}}_o$ tends, for small
values of noise, to enhance the diagonal terms of $\underline{\underline{C}}_o$. These contain
information about the mean profile. Infinite noise would drive the
solution to zero everywhere. This last feature is undesirable and
can be remedied by predicting only deviations from the mean profile
instead of the complete water vapor curve. Then a $\underline{\underline{D}}$ operator which
assumes infinite noise merely returns the mean profile, as it should
when no new information is available.

The integrated water vapor may be easily computed from the
estimation of the water vapor profile and compared to the radiosonde
results. In Figure 7-4, it can be noted that the radiosonde reported
3.28 g/cm^2 of integrated water vapor, the noiseless estimation pre-
dicted 3.26 g/cm^2, and the noisy inversion showed 3.24 g/cm^2 of inte-
grated water vapor. The reduced estimation by the noisy inversion is
a result of forcing the solution toward zero. A scheme predicting
deviations from the mean profile would always force the integrated
water vapor toward the mean value.
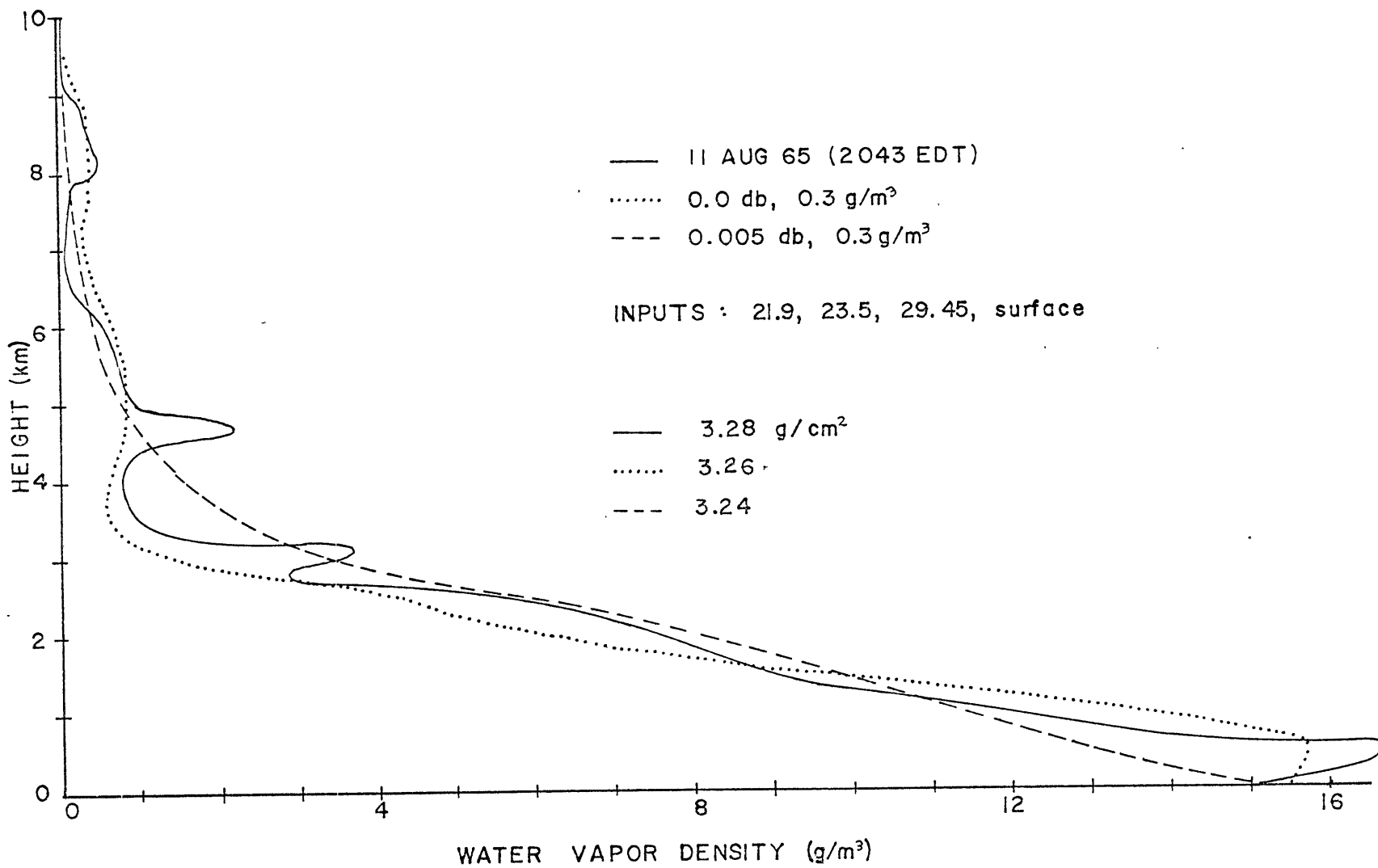
Figure 7-4. The effect of expected noise on the inversion of noiseless spectral data.
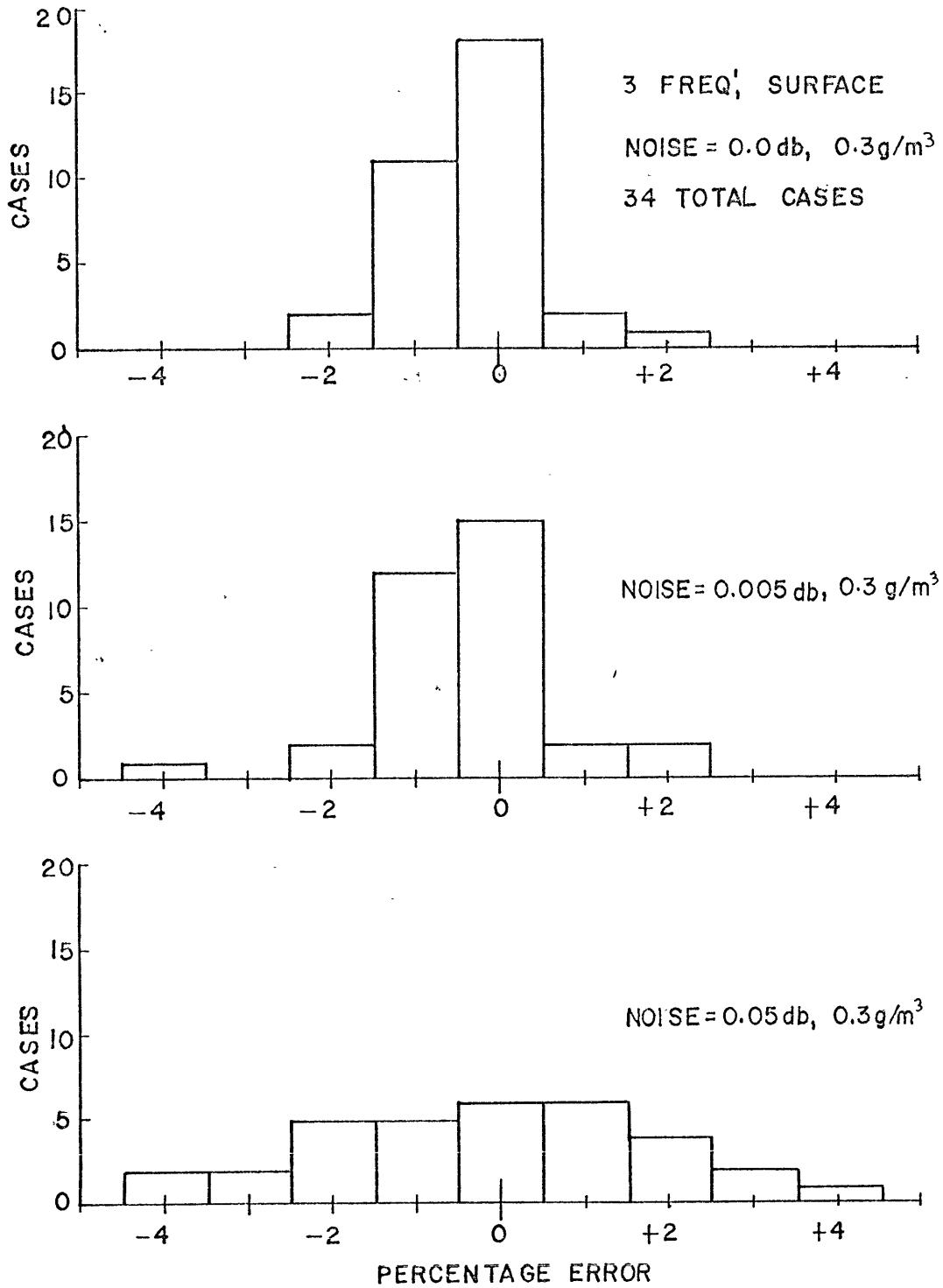
Figure 7-5.   The effect of noise on the estimation of integrated water vapor.

Figure 7-5 compiles the statistics of the effect of noise on integrated water vapor. As noise increases from zero in the radiometer data and 0.3 g/m^3 for the surface value, to 0.05 db in each radiometer channel, the scatter between estimated values and radiosonde values becomes greater, but not drastically.

The effect of noise on the accuracy of the vertical distribution of water vapor may be assessed in Figure 7-6. The average integrated water vapor in a one kilometer slab determined from the radiosonde information was compared to the predicted values of average water vapor density in each slab. The average absolute percent discrepancy is plotted for each one kilometer slab. The changes due to increased noise show mostly as a change in the maximum error from the top of the profile to a level nearer five or six kilometers.

A winter profile of moisture with two matching inversions is shown in Figure 7-7. Again, noise tends to cause a loss in the ability of the inversion to follow the original profile and drives the integrated estimate towards zero.

7.2.2 The Effects of the Number of Data Channels
on the Results from the Optimum Linear Estimator.

The information which one obtains about the atmosphere from one channel is, of course, a statistically independent parameter. However, the information from two or more channels is obviously correlated and therefore there is redundancy. The degree to which channels are inde-
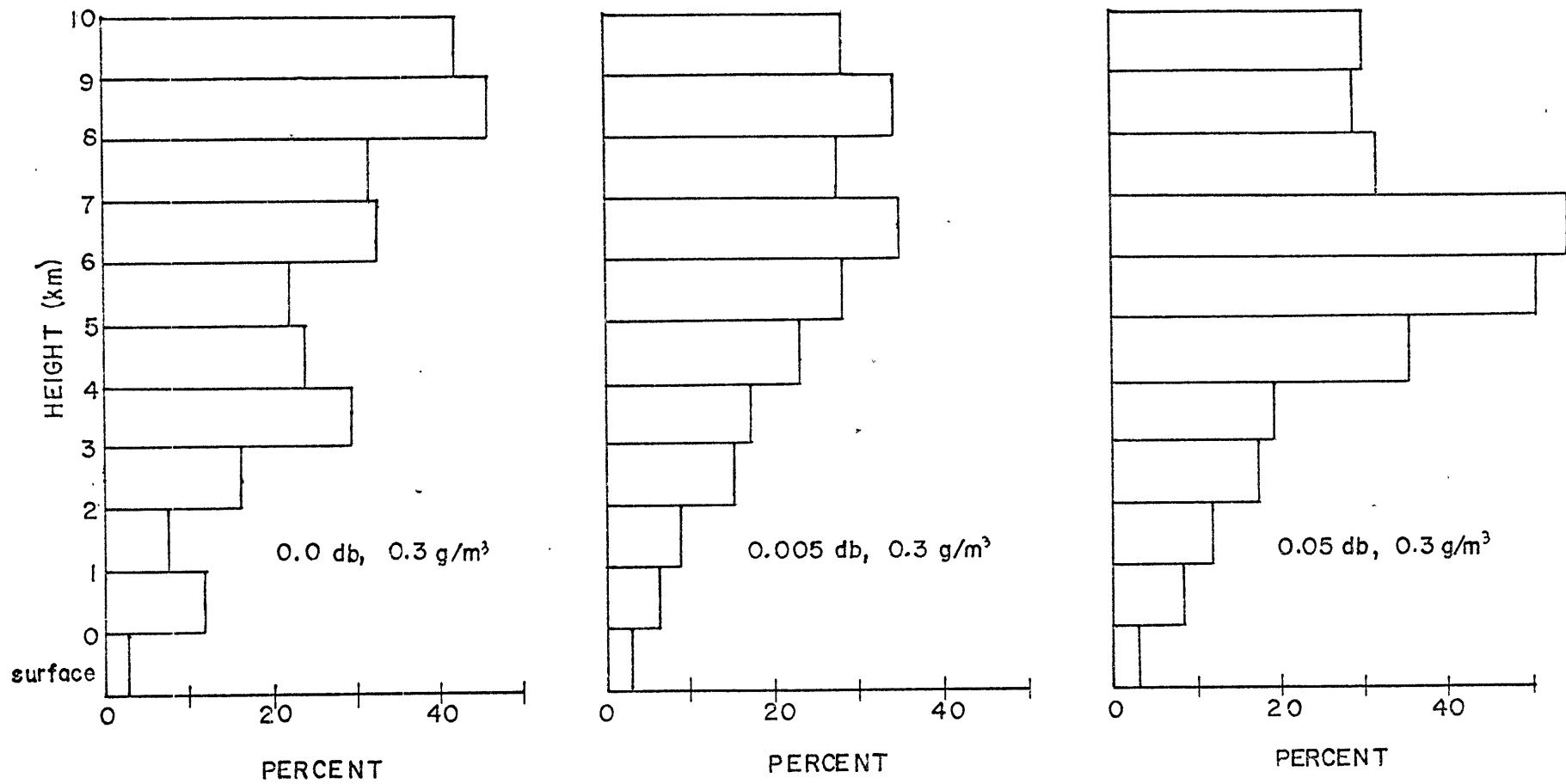
Figure 7-6. The effect of noise on the accuracy of estimation of the vertical distribution of water vapor. The average absolute percentage error in 1 km layers is plotted versus height.
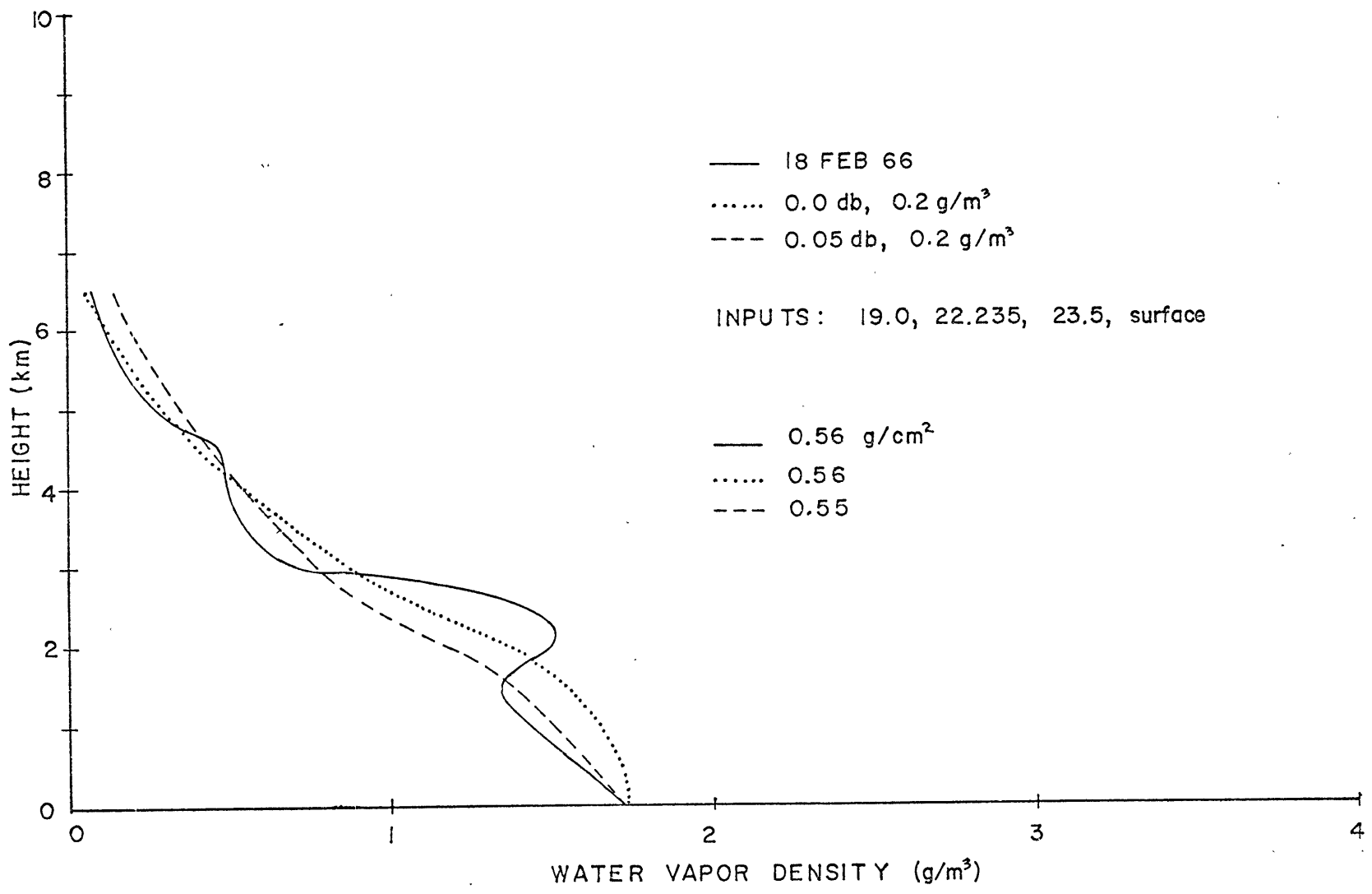
Figure 7-7. The effects of noise on a winter inversion.

pendent of each other may be qualitatively assessed from the weighting

functions of Figure 7-1. The channels near resonance (21.9 and 22.235

GHz) emphasize the upper parts of the troposphere whereas the channels

in the wings (29.45, 19.0 GHz) emphasize surface layers. Any combina-

tion of channels which are in the wings and near resonance should show

a maximum of statistical independence and therefore provide the most

information possible with just two channels. The weighting function

at 23.5 GHz is quite obviously not a linear combination of the extreme

weighting functions, but the broadness of its maximum precludes it

from adding a great deal of new information to the other channels.

If the surface pseudo-weighting function were to be plotted, it would

appear in Figure 7-1 at the surface as a one meter thick slab. It

therefore carries little redundant information and is a valuable data

input.

The effect of having the surface data point is illustrated in

Figure 7-8. A strong inversion of moisture occurred on this day.

Without the surface data point the inversion would have been undetected

and a large error would have occurred in the estimation of the surface

water vapor concentration. It should be noticed, however, that the

integrated water vapor estimate is slightly better for the scheme which

does not use the surface data point, a fact which is generally true.

Figure 7-9 compiles the effect of reducing the number of data

channels from four including the surface, to three and then to two,

the last two without the surface data point. An interesting effect
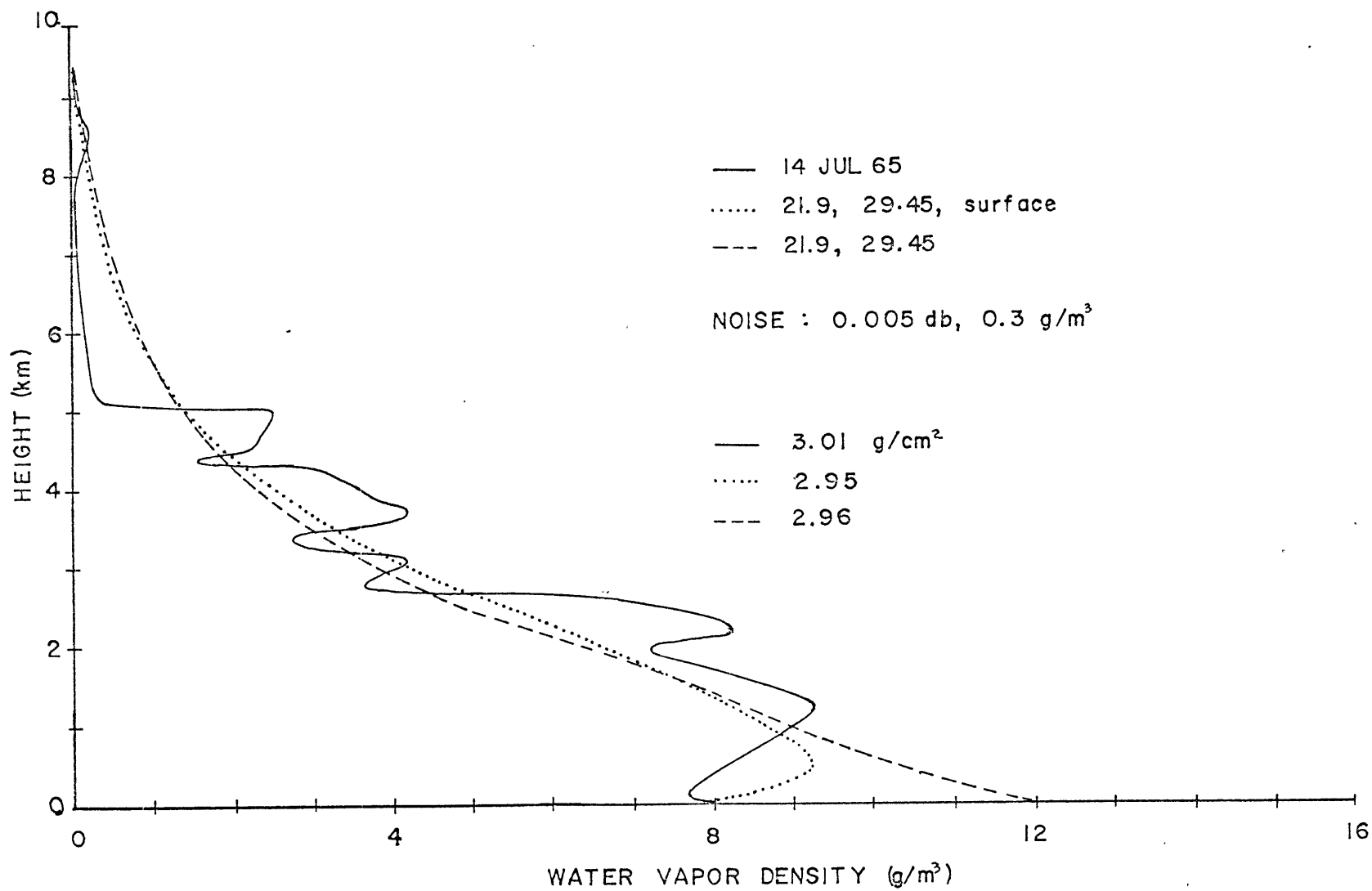
Figure 7-8. The effect on inversion accuracy of a surface data point.
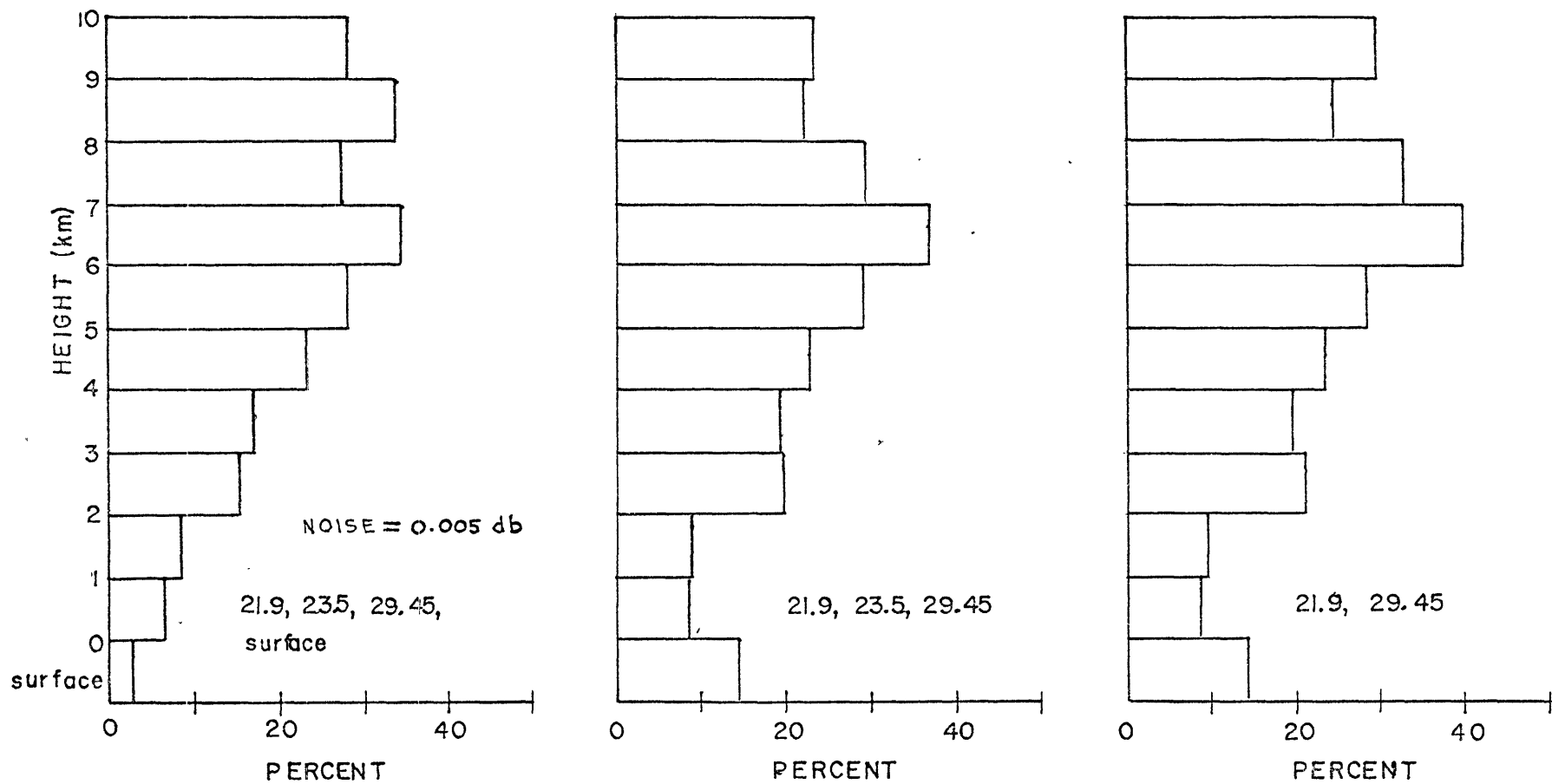
Figure 7-9. The effect of reducing the number of data channels on inversion accuracy. The average absolute percentage error in 1 km layers is plotted versus height.
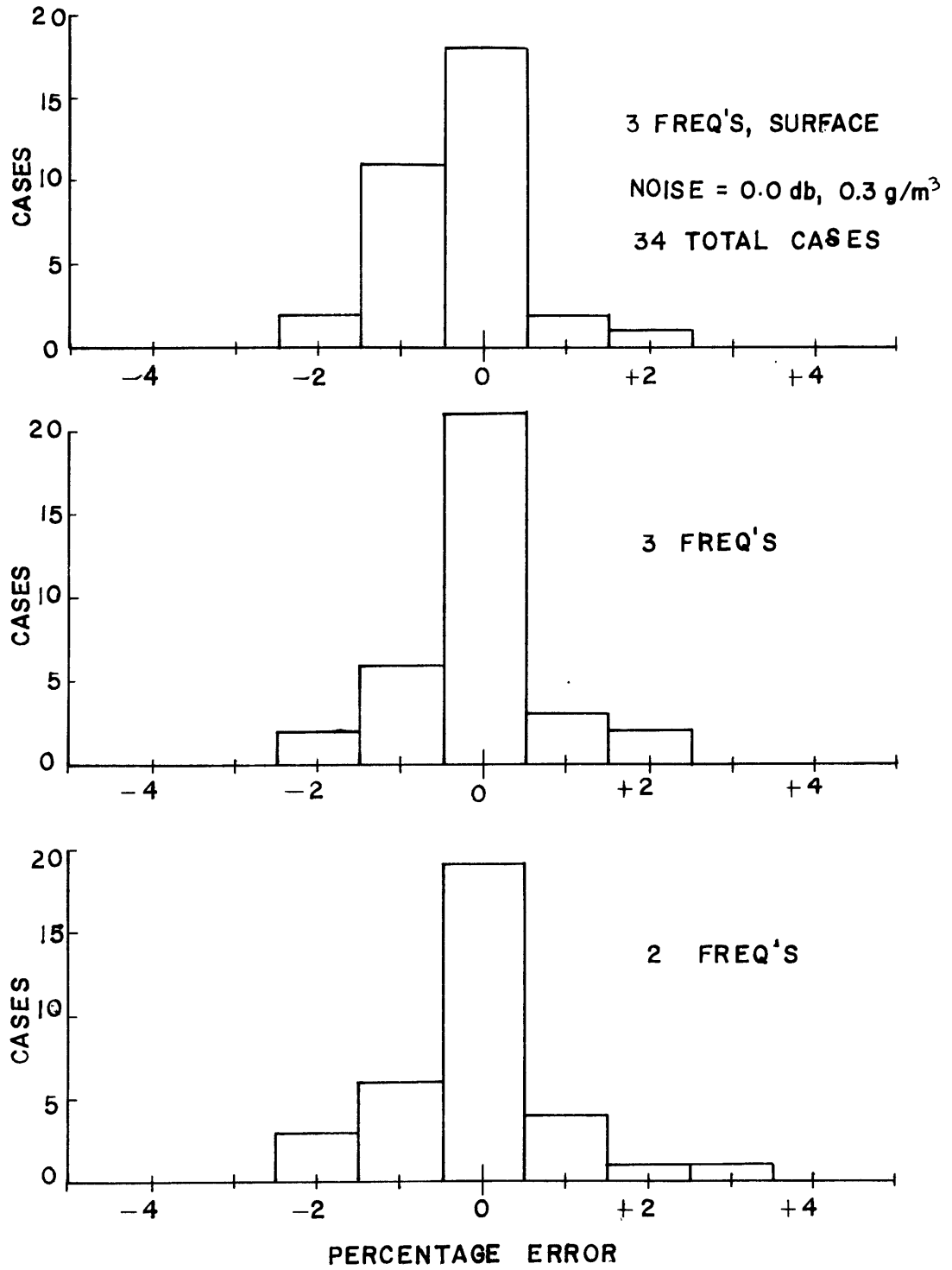
Figure 7-10.   The effect of the number of input data points on the estimation of integrated water vapor.
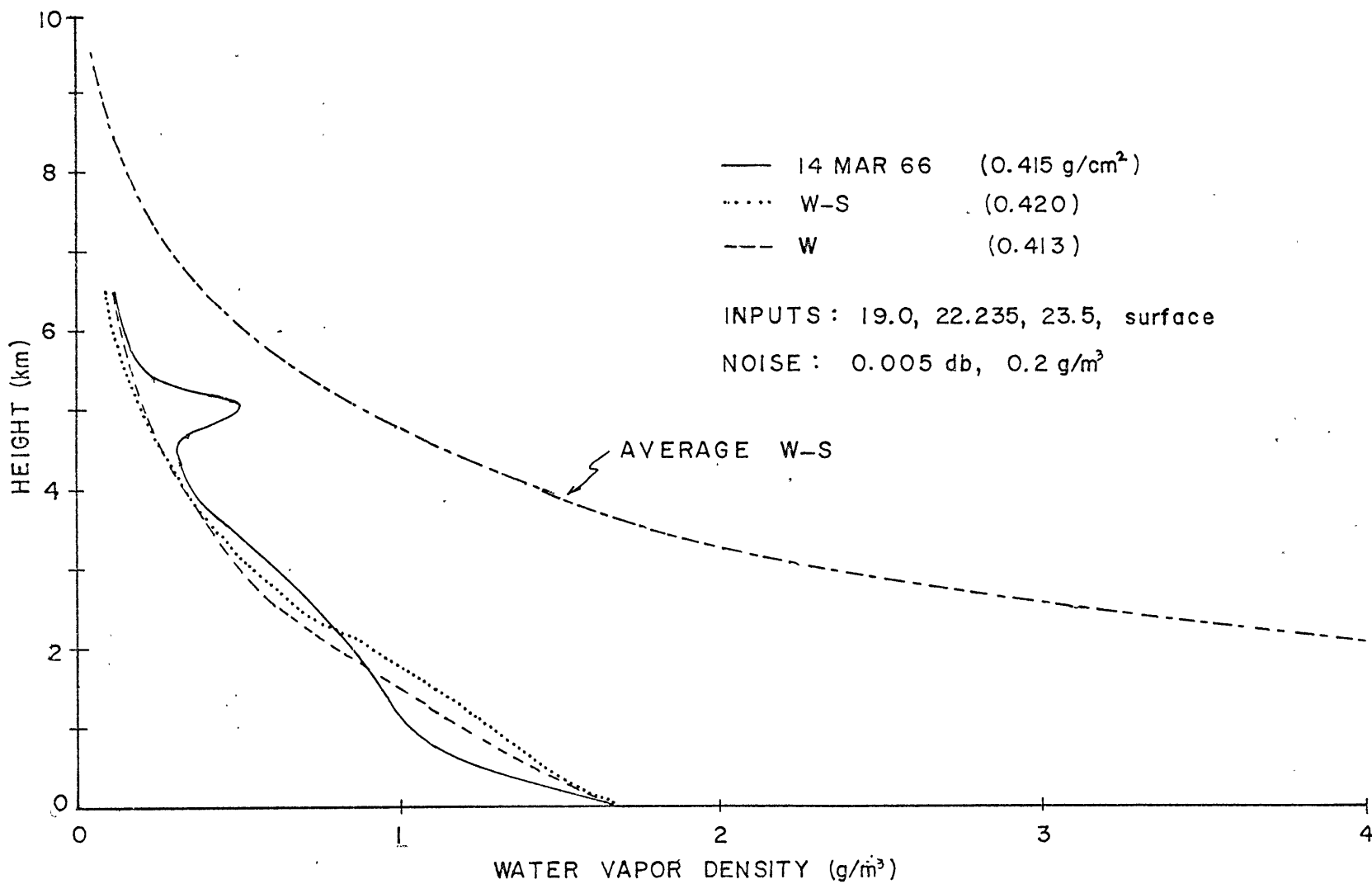
Figure 7-11. The effect of biased atmospheric statistics on inversion accuracy.

occurs when the surface data point is dropped. The absolute average percentage error at the surface is almost twice as large as in the two one-kilometer layers just above the surface. This is due, of course, to the effect which the solid earth has upon the water vapor in the boundary layer. Little differences of significance occur above the surface indicating the small effect which both the surface data point and 23.5 GHz data point have in this region. The maximum error remains near six or seven kilometers for all three cases.

The variation of the number of input channels for the noiseless case has little effect on the estimation of integrated water vapor. In Figure 7-10, the inversion using three frequencies (21.9, 23.5, 29.45 GHz) and the surface water vapor density shows a slightly larger spread of errors than the three frequency case without the surface. Also, little deterioration occurs when the 23.5 GHz channel is dropped.

7.2.3 The Effect of Imperfect Atmospheric Statistics on
the Results from the Optimum Linear Estimator

To investigate the role which the atmospheric statistics play in the inversion scheme, a winter set of radiosonde absorption data was inverted using statistics which were heavily weighted towards a summer situation. In Figure 7-11, data from a day in the winter which had a very small amount of water vapor was inverted using weighting functions, mean profiles, and statistics which were derived from mostly summer radiosondes. The results show some degradation in the

estimates of the vertical distribution and total amount of water vapor, but surprisingly little. An inversion using winter statistics and weighting functions is also plotted for comparison.

7.2.4 Inversion of Real Radiometer Data

If one were to simply invert the spectral data collected and reported in Chapter 4, it would be difficult to evaluate the results since, as has been shown in Chapter 4, the radiosonde data is not a good standard of comparison. Therefore two days of spectral data which have reasonably closely matched radiosonde absorption spectra, have been chosen to illustrate the inversion of real data. One day is in the summer, the other is a winter day.

Figure 7-12 shows the inversion of real radiometer data for the summer day. The inversion profile is derived from a $\underline{\underline{D}}$ matrix which expected 0.05 db of noise per channel and an error in the ground measurement of water vapor density of 0.3 g/m^3. Because of the high level of noise expected, the inversion shape approximates the mean profile and therefore misses most of the secondary variations in the curve of the real profile. The integrated water vapor estimate is high by 4.7%. However, the radiosonde absorption was about 3.3% below the observed attenuation. This could mean that the integrated water vapor estimation error might have been less than 4.7%.

The winter inversion is shown in Figure 7-13. Two large inversions of water vapor are not detected. Again the shape of the inversion
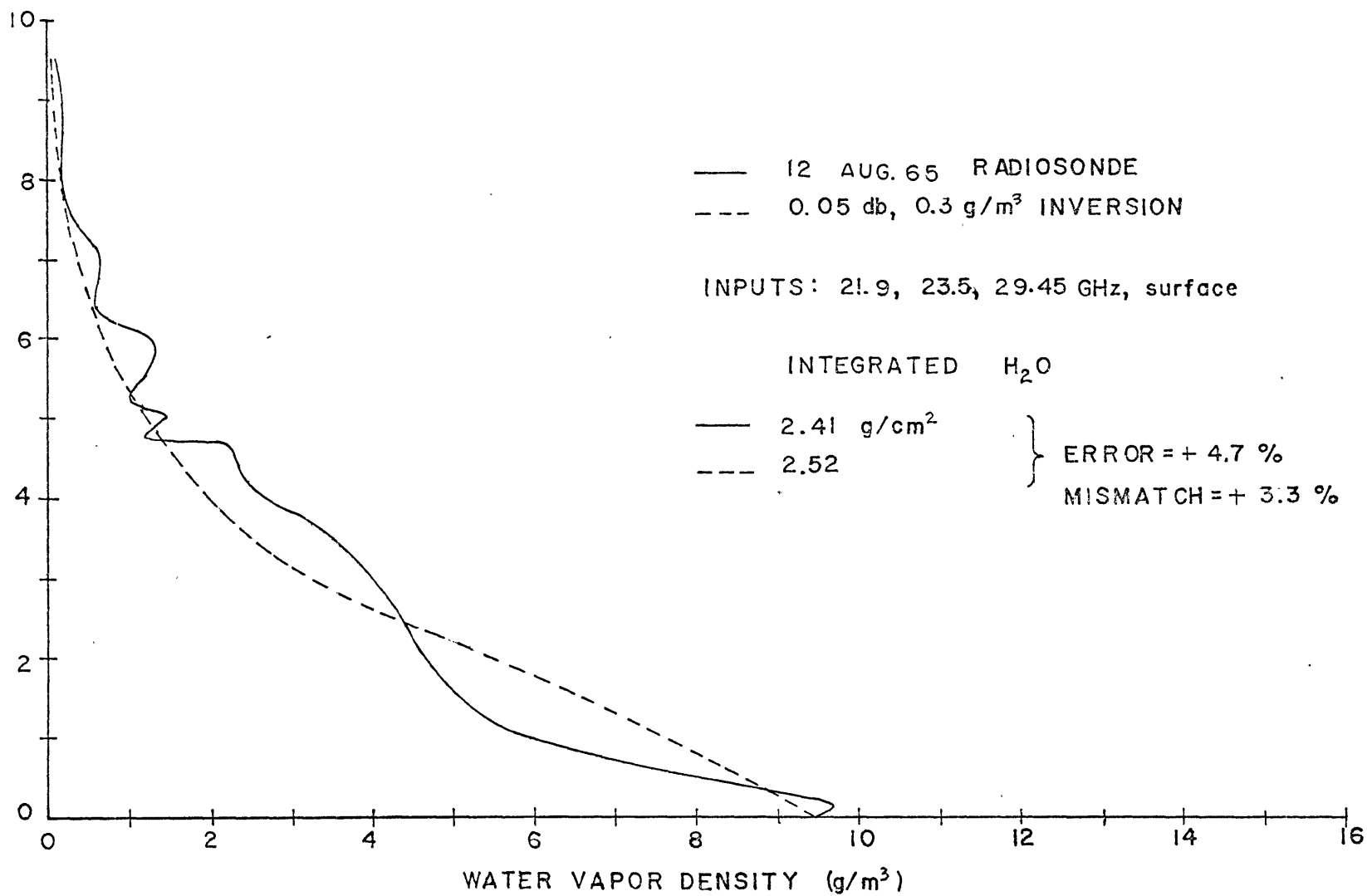
Figure 7-12. Inversion from observed spectral data taken on a summer day.
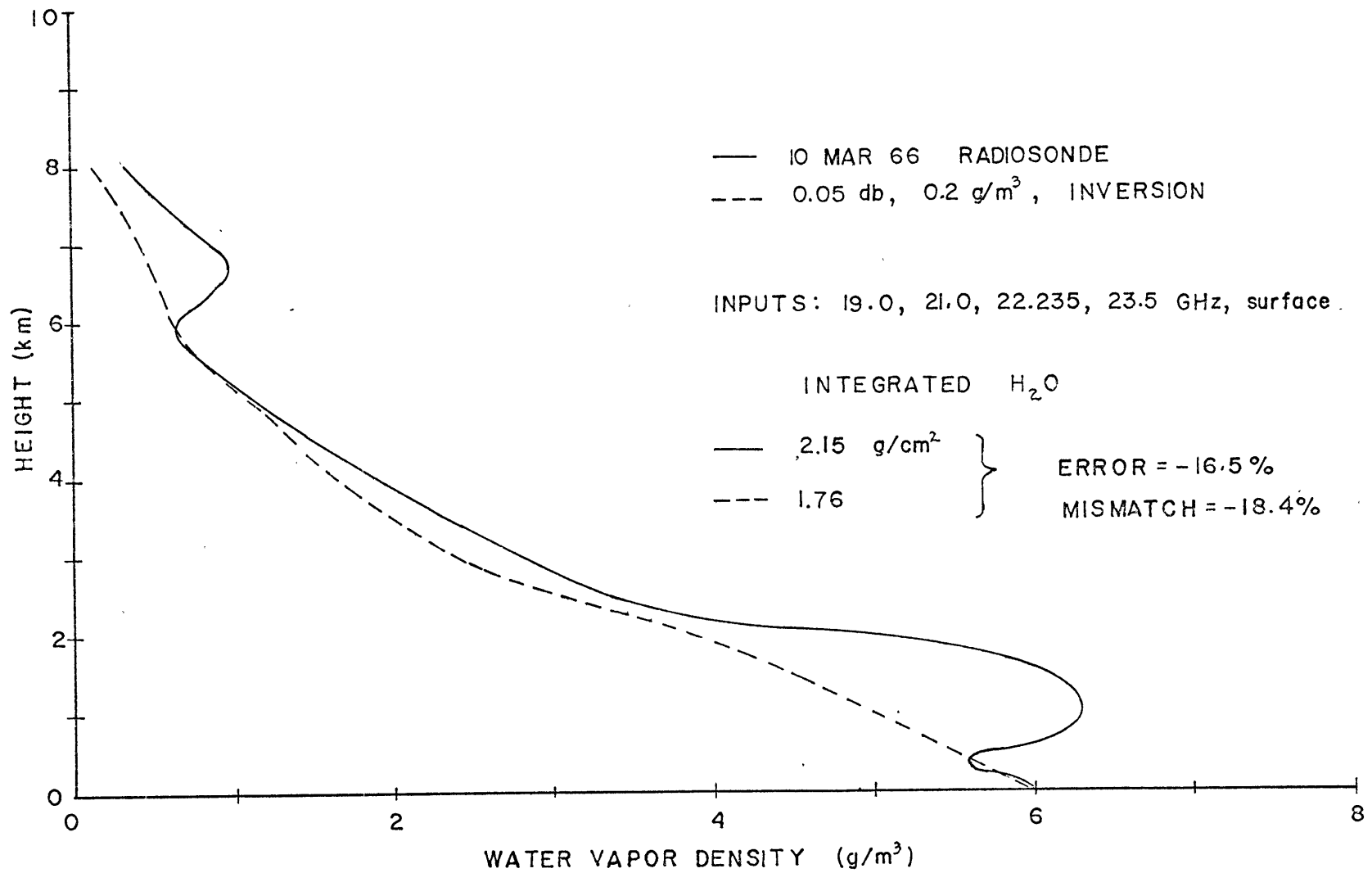
Figure 7-13. Inversion from observed spectral data taken on a winter day.

curve is constrained by the expected noise to a profile similar to the mean. The integrated water vapor is low by 16.5%. However, the mismatch between observed attenuation and radiosonde absorption amounted to approximately 18.4% so that it is difficult to assess the true significance of this poor estimation.

It is clear that the fine structure in the atmospheric water vapor profiles will not be recoverable from the radiometer data. And, it is clear that with noisy data, most of the major variations from the mean profile will also be difficult to detect. However, the integrated water vapor and general profile, even with noisy data, should be generally accurate and for most meteorological purposes quite useful.

Chapter 8

SUGGESTIONS FOR FUTURE RESEARCH

A great deal of work remains before the full potential of micro-wave measurements applied to meteorological problems is achieved. However, the outline of where we should go from here seems rather clear.

A number of major problems, both theoretical and experimental, need to be investigated. Among the theoretical problems, perhaps the most basic one is: what is the true expression for the line shape? We have built up semi-empirical expressions in order to approximate and interpret the measurements we can and do make. The application of any theory to the atmosphere eventually rests on the assumption that the line shapes we use are adequate when we know, in certain cases at least, that they are not. It seems that the fine experimental work of Becker and Autler on the line shape, done now over twenty years ago, should be repeated, refined and extended.

A second major problem is associated with our inadequate know-ledge of the true statistics of atmospheric water vapor. What are the mean spatial and temporal fluctuations of the moisture field during given weather and climatic regimes? Information of these quantities could give some idea of the optimum performance which we can expect from any radiometer measurements and hence a realistic goal to work toward in radiometer design. The answers are of equal importance to radio astronomers who intend to build and operate large spatial arrays

of antennas and who further want to correlate the signals from these arrays. Random fluctuations in the moisture field over scale sizes small with respect to the array size means random fluctuations in the relative phases of the received signals. There may be some atmospheric regimes which are highly unfavorable to such measurements.

There are several ways of getting an idea of the statistics which we need. There exist data which consists of many closely spaced (~10 minutes apart) radiosonde runs. The correlation of data from flight to flight can give us some idea of the spatial fluctuations of the moisture field for the scale size represented by the wind speed times the delay between flights, and of the temporal fluctuations on time scales greater than the delay time. More satisfactory for accuracy and resolution would be measurements taken by any one of the several refractometer equipped aircraft over the U.S. Flight patterns could be tailored to provide the best possible coverage for a given situation.

The use of radiometers mounted on satellites to monitor water vapor over the oceans introduces several unsolved theoretical problems. One concerns an adequate method of treating the background radiation from the sea. We are not entirely clear on the microwave properties of the sea under ideal observational conditions, especially the dependence of emissivity on temperature. And for rough, frothy, seas, we are as yet unable to satisfactorily predict what a radiometer would see, or conversely, what a given observed spectra should be interpreted as in terms of the state of the sea surface. Measurements of actual

ocean water under carefully controlled laboratory conditions seems
necessary to answer the emissivity problem. Correlation between obser-
vations and sea conditions might throw some light on the sea state-
expected spectra relationship.

Further, when the background radiation problem has been solved,
there remains the task of integrating it into an adequate inversion
scheme for space based observations. The Optimum Linear Estimator out-
lined in the previous chapter is an important step forward in the
direction of eventual solution to this problem. Even though its linear
nature is a great simplification in any inversion procedure, some of
its basic features no doubt will be important features in the inversion
of the brightness temperature spectra measured from the ground and from
space. In particular, the feature which uses atmospheric statistics and
expected noise to stabilize the solution is no doubt applicable to the
more general nonlinear inversion scheme, the feature is a most satis-
factory means of incorporating the enormous amount of information about
the atmosphere which we have so assiduously collected over the last one
hundred years or so.

Improvement of the OLE is also a distinct possibility. As men-
tioned in Chapter 7, the solution as outlined drives the estimated
water vapor profile toward zero instead of the mean for increased noise.
This is undesirable. The solution can be and was reformulated in one
of the several ways in which the estimation approaches the mean atmo-
spheric profile for large expected noise levels in the radiometer data.

The estimations resulting from the scheme were very much inferior to the scheme outlined in Chapter 7. The reasons for this are not clear. More should be done to bring the solution to the form which returns the mean profile for infinite noise.

Another area for future theoretical, numerical, and experimental work is with the interpretation of spectral observations taken in the presence of clouds. In this thesis clouds were treated rather cavalierly; almost as if they did not exist. They do exist; they existed on many days of the observation taken in Chapter 4; and they will always be part of the spectral data which will be taken from satellites. No doubt considerable information of the role of clouds in spectral observations near 1 cm is still contained in the data collected and reported in Chapter 4. A good starting place might be to reevaluate that data for information about how cloudy situations should be interpreted. And certainly, numerical experiments using theoretical cloud models can be devised to explore further the role which clouds will play in a satisfactory spectral data inversion scheme for opacity or brightness temperature. The most logical place to start is with OLE and the data of Chapter 4.

Bibliography

1. Lorenz, E.N.; A Study of the Predictability of a 28-Variable Atmospheric Model, Tellus, 17, 3, (1965).

2. Townes C.H., and A.L. Schawlow; Microwave Spectroscopy. McGraw-Hill, New York, (1955).

3. Herzberg, G.; Molecular Spectra and Molecular Structure: II. Infrared and Raman Spectra of Polyatomic Molecules. D. Van Nostrand Co., Princeton, (1945).

4. van Vleck, J.H.; The Absorption of Microwaves by Oxygen, Phy. Rev., 71, No. 7, (1947).

5. van Vleck, J.H.; The Absorption of Microwaves by Water Vapor, Phy. Rev., 71, No. 7, (1947).

6. van Vleck, J.H.; In Propagation of Short Radio Waves, ed. Kerr, Dover Pub., Inc., (1951).

7. King, G.W., R.M. Hainer, and P.C. Cross; Expected Microwave Absorption Coefficients of Water and Related Molecules, Phy. Rev., 71, 7, (1947).

8. Dennison, D.M.; Infra-Red Spectra of Polyatomic Molecules, Rev. of Mod. Phy., 12, 175, (1940).

9. Wacker, P.F., and M.R. Pratto; Microwave Spectral Tables; Line Strengths of Asymmetric Rotors, NBS Mono. 70, Vol. II, U.S. Govt. Pr. Off., (1964).

10. van Vleck, J.H., and V.F. Weisskopf; On the Shape of Collision Broadened Lines, Rev. Mod. Phys., 17, Nos. 2,3, (1945).

11. Birnbaum, G., and A.A. Maryott; J. Ch. Phys., 21, 1774, (1953).

12. Nethercot, A.H., J.A. Klein, J.H.N. Loubser, and C.H. Townes; Nuovo Cimento, 9, Supp. 3, 358, (1952).

13. Gordon, R.G.; On the Pressure Broadening of Molecular Multiplet Spectra, J. Ch. Phys., 46, 2, pp. 448-455, (1967).

14. Breene, R.G.; The Shift and Shape of Spectral Lines, Pergamon Press, New York, (1961).

15. Anderson, P.W.; Pressure Broadening in the Microwave and Infra-Red Regions, Phys. Rev., 76, 5, (1949).

16. Ben-Reuven, A.; Transition from Resonant to Nonresonant Line Shape in Microwave Absorption, Phys. Rev. Lett., 14, 10, (1965).

17. Zhevakin, S.A., and A.P. Naumov; Izvestiya Vuzov (Radiofizika), 6, 4, P. 674, (1963).

18. Debye, P.; Polar Molecules, Dover Public., New York.

19. Benedict, W.S., and L.D. Kaplan; Calculation of Line Widths in H_2O-N_2 Collisions, J. Chem. Phys., 30, 2, (1959).

20. Benedict, W.S., and L.D. Kaplan; Calculation of Line Widths in H_2O-H_2O and H_2O-O_2 Collisions, J. Qu. Spec. and Rad. Trans., 4, pp. 453-469, (1964).

21. Becker, G.E., and S.H. Autler; Water Vapor Absorption of Electromagnetic Radiation in the Centimeter Wave-Length Range, Phy. Rev., 70, Nos. 5 and 6, (1946).

22. Hodgman, C.D., (editor); Handbook of Chem. and Phys., Chem. Rub. Pub. Co., 38th ed., (1956).

23. Townes, C.H., and F.R. Merritt; Water Spectrum Near One-Centimeter Wave-Length, Phy. Rev., 70, 558L, (1946).

24. Lorentz, H.A.; Proc. Amst. Akad. Sci., 8, 591, (1906).

25. Frenkel, L. and D. Woods; The Microwave Absorption by H_2O Vapor and its Mixtures with Other Gases Between 100 and 300 Gc/s, Proc. IEEE, 54, 4, (1966).

26. Rusk, J.R.; J. Chem. Phy., 42, 493, (1965). (See also Letters, J. Chem. Phy., 43, 8, p. 2919, (1965)).

27. Hemmi, C.; Pressure Broadening of the 1.63 mm Water Vapor Absorption Line, Tech. Rep. 1, El. En. Res. Lab., Mm Wave Sc., Univ. of Tex., (1966).

28. Straiton, A.W., and C.W. Tolbert; Anomalies in the Absorption of Radio Waves by Atmospheric Gases, Proc. IRE, 48, 5, (1960).

29. Tolbert, C.W., L.C. Krause, and A.W. Straiton; Attenuation of the Earth's Atmosphere between 100 and 140 Gigacycles per Second, J. Geo. Res., 69, 7, (1964).

30. Tolbert, C.W., A.W. Straiton, R.A. Simons; Attenuation and Emission of the Earth's Atmosphere between the Frequencies of 100 GC and 160 GC, Rep. 5-55, El. Eng. Res. Lab., Univ. of Texas, (1964).

31. Barrett, A.H., and V.K. Chung; A Method for the Determination of High Altitude Water Vapor Abundance from Ground Based Microwave Observations, J. Geo. Res., 67, 11, (1962).

32. Dicke, R.H., R. Beringer, R.L. Kyhl, and A.B. Vane; Atmospheric Absorption Measurements with a Microwave Radiometer. Phys. Rev., 70, Nos. 5 and 6, p. 340, (1946).

33. Bean, B.R., and E.J. Dutton; Radio Meteorology, Nat. Bur. St., Mono. 92, U.S. Govt. Pr. Off., Washington, D.C., (1966).

34. Smart, W.M.; Spherical Astronomy, Cambridge Univ. Press, Cambridge England, (1962).

35. Meeks, M.L., and A.E. Lilley; The Microwave Spectrum of Oxygen in the Earth's Atmosphere, J. Geo. Res., 68, 6, (1963).

36. Chandrasekhar, S.; Radiative Transfer, Dover, New York, (1960).

37. Aller, L.H.; The Atmospheres of the Sun and Stars, Ronald Press, New York (1963).

38. Planck, M.; The Theory of Heat Radiation, Dover Pub., New York (1959).

39. Goody, R.M.; Atmospheric Radiation: I - Theoretical Basis, Oxford Press, (1964).

40. Staelin, D.H.; in Meteorological Experiments for Manned Earth Orbiting Missions, Final Rep. Contr. No. NASW-1292 by Geo. Corp. of Am. (G. Ohring, principal invest.). NASA, Washington, D.C. (1966).

41. Valley, S.L.; Handbook of Geophysics and Space Env., Air Force Cambridge Res. Labs., Bedford, Mass., (1965).

42. Woolley, R. v.d. R., and D.W.N. Stibbs; The Outer Layers of a Star, Oxford University Press, London, England, (1953).

43. Bacon, R.H.; Am. J. Phys., 21, 428 (1953).

44. Marchgraber, R.M.; Carbon Type Humidity Element, Resistance ML-476 ( )/AMT, U.S. Army Sig. Res. and Dev. Lab., Tech. Rep. 2052, Fort Monmouth, N.J., (1959).

45. Grote, H.H., and R.M. Marchgraber; The Dynamic Behavior of the Carbon Humidity Element ML 476, U.S. Army Elect. Res. and Dev. Labs., Fort Monmouth, New Jersey, (1963).

46. von Hippel, A.R.; Dielectrics and Waves, John Wiley, London, England, (1962).

47. Hasted, Ritson, and Collie; J. of Chem. Phy., 16, 1, (1948).

48. American Institute of Physics Handbook, 2nd Ed., McGraw Hill, N.Y., (1963).

49. Kaplan, L.D.; J. Opt. Soc. Am., 49, 10, (1959).

50. Lenoir, W.B.; Ph.D. Thesis, Mass. Inst. of Tech., (1965).

51. Rodgers, C.D.; A Discussion of Inversion Method, Clarendon Lab. Mem. 66.13, Univ. of Oxford, England, (1966).

52. King, J.I.F.; Atm. Sci., 21, 3, 324-326, (1964).

53. Yamamoto, G.; J. Met., 18, 5, 581-588, (1961).

54. Wark, D.Q.; J. Geo. Res., 66, 1, 77-82, (1961).

55. Goody, R.M.; The Physics of the Stratosphere, London, Cambridge Univ. Press, (1958).

56. Staelin, D.H.; J. Geo. Res., 71, 12, 2875-2881, (1966).

57. Raschke, E.; NASA Contractor Rep. 595, God. Sp. Flt. Cntr., Wash., D.C., (1966).

58. Cox, C.S., and W.H. Munk; J. Opt. Soc. Am., 44, 838-850, (1954).

59. Barrett, A.H.; Mem. Soc. Roy. Soc. Liege, Cinq Ser., 7, P. 197, (1962).

60. Moller, F.; Plan. Space Sci., 5, 202-206, (1961).

61. See for example: Nordberg, W., A.W. Mc Culloch, L.L. Foshee, and W.R. Bandeen; Bull. Am. Met. Soc., 47, 11, (1966).

62. Nordberg, W.; Science, 150, 3696, 559-572, (1965).

63. Barrett, A.H.; Microwave Studies of the Terrestrial Atmosphere, unpublished manuscript, Mass. Inst. of Tech., (1964).

64. Barrett, E.W., L.R. Herndon, and H.J. Carter; Some Measurements of the Distribution of Water Vapor in the Stratosphere, Tellus, 2, 302-311, (1950).

65. Murcray, D.G., F.H. Murcray, W.J. Williams, and F.E. Leslie; J. Geo. Res., 65, 3641-3650, (1960).

66. Mastenbrook, H.J., and J.E. Dinger; Distribution of Water Vapor in the Stratosphere, J. Geo. Res., 66, 1437-1444, (1961).

67. Bonvini, L.A., D.L. Croom, and A. Gordon-Smith; their results are referred to in Croom, D.L.; J. Terr. Atm. Phys., 28, pp. 323-326, (1966).

68. Gutnick, M.; How Dry the Sky? J. Geo. Res., 66, 9, pp. 2867-2871, (1961).

69. Mastenbrook, H.J.; Frost Point Hygrometer Measurements in the Stratosphere and the Problem of Moisture Contamination, from Humidity and Moisture, Vol. 2, Rheinhold Pub. Corp., (1965).

70. Mastenbrook, H.J.; Water Vapor Observations at Low, Middle, and High Latitudes During 1964 and 1965, NRL Report 6447, Nav. Res. Lab., Washington, D.C., (1966).

71. Sissenwine, N., D.D. Grantham, and H.A. Salmela; Mid-Latitude Stratospheric Humidity Regime to 30 Km, Interim Notes on Atm. Properties No. 73, Air Force Canbridge Res. Lab., Bedford, Mass., (1966).

72. Long, M.J.; A Preliminary Climatology of Thunderstorm Penetrations of the Tropopause in the United States, J. of Ap. Met., 5, pp. 467-473, (1966).

73. May, E.C., and A.B. Kahle; The Satellite Determination of High Altitude Water Vapor, NASA Contractor Rep. CR-70, Off. of Tech. Ser., Washington, D.C., (1964).

74. Croom, D.L.; J. Atm. and Terr. Phys., 28, pp. 323-326, (1966).

75. Croom, D.L.; J. Atm. and Terr. Phys., 27, pp. 217-233, (1965).

76. Croom, D.L.; J. Atm. and Terr. Phys., 27, pp. 235-243, (1965).

77. Ghosh, S.N., and H.D. Edwards; Rotational Frequencies and Absorption Coefficients of Atmospheric Gases, A.F. Surv. in Geo., 82, A.F. Camb. Res. Lab., Bedford, Mass., (1958).

78. Goff, I.A., and Gratch, S.; Trans. Am. Soc. Heat. and Vent. Eng., 52, pp. 95, (1946).

79. Baranger, M.; Phys. Rev., 111, p. 481 (1958); Phys. Rev., 111, p. 494 (1958); Phys. Rev., 112, p. 855 (1958).

80. Kolb, A.C., and H. Griem; Phys. Rev., 111, p. 514 (1958).

81. Fano, U.; Phys. Rev., 131, p. 259 (1963).

82. See for example: Yap, B.K.; Wind Velocity and Radio Emission from the Sea, S.M. Thesis, Mass. Inst. of Tech., (1965).

83. Staelin, D.H.; Quart. Prog. Rep. No. 76, Res. Lab. of Elect., Mass. Inst. of Technology, 15 January 1966.

84. Staelin, D.H.; private communication.

Appendix A-I

Water Vapor Rotational Spectral Line Parameters

On the following pages, all the needed constants appear which are necessary to compute the absorption for the 54 lowest frequency rotational spectral lines of water vapor. An asterisk means the frequencies have been experimentally determined. Otherwise they are taken from Ghosh and Edwards[77]. Term values are taken from Dennison[8]. Line strengths are those computed by King, et al.[7] Line widths for air are those which Benedict and Kaplan[19] computed for nitrogen without correction. The temperature exponents are also from Benedict and Kaplan[19]. The line widths in water vapor are from the later work of Benedict and Kaplan[20] on oxygen and water vapor. Values in parentheses in the Line Strength column are estimates from graphs drawn on the basis of the tables of line strengths for various asymmetry parameters computed by Wacker and Pratto[9]. The numbers in parentheses in the last three columns are estimates for the lines involved based on averages over similarly arising lines.

TABLE OF WATER VAPOR ROTATIONAL SPECTRAL LINE PARAMETERS

FREQUENCY (MHz)	TRANSITION	PARITY	LOWER TERM VALUE $(cm)^{-1}$	UPPER TERM VALUE $(cm)^{-1}$	LINE STRENGTH	LINE WIDTH (AIR) $cm^{-1} atm^{-1}$	LINE WIDTH (AIR) TEMP. EXP.	LINE WIDTH (WATER VAPOR) $cm^{-1} atm^{-1}$
22,235.22*	$5_{23} \rightarrow 6_{16}$	eo → oe	446.39	447.17	0.0549	.09019	.626	0.4777
183,310.12*	2_{20} 3_{13}	ee → oo	136.15	142.30	0.1015	.09600	.649	0.4937
323,158.5	9_{36} 10_{29}	oe → eo	1283.02	1293.80	(0.087)	.07652	.42	0.4012
323,758.1	4_{22} 5_{15}	ee → oo	315.70	326.50	0.0891	.09292	.619	0.5071
377,418.0	3_{21} 4_{14}	eo → oe	212.12	224.71	0.1224	.09480	.63	0.5280
389,708.8	$11_{2,10}$ 10_{37}	ee → oo	1525.31	1538.31	(0.068)	.0702	.33	0.3807
435,874.3	6_{44} 7_{53}	ee → oo	1045.14	1059.68	(0.082)	.0500	.29	0.2648
437,673.0	5_{50} 6_{43}	oe → eo	742.18	756.78	0.0987	(.059)	(.36)	(0.348)
441,570.0	6_{61} 7_{52}	eo → oe	1045.14	1059.87	(0.082)	.05023	.332	0.2709
445,766.9	3_{30} 4_{23}	oe → eo	285.46	300.33	0.1316	.08247	.510	0.4748
465,851.9	5_{51} 6_{42}	oo → ee	742.18	757.72	0.0990	.0629	.38	0.3521
470,948.1	4_{40} 5_{33}	ee → oo	488.19	503.90	0.1165	.0690	.38	0.3987
487,136.0	7_{17} 6_{24}	oo → ee	586.46	602.71	(0.033)	.0861	.51	0.4926
498,527.5	7_{70} 8_{63}	oe → eo	1394.96	1411.59	(0.077)	.0424	.32	0.2051
498,527.5	7_{71} 8_{62}	oo → ee	1394.96	1411.59	(0.072)	.0424	.34	0.205
557,583.4	1_{01} 1_{10}	eo → oe	23.76	42.36	1.5000	.11115	.645	0.4889
617,838.3	4_{41} 5_{32}	eo → oe	488.19	508.80	0.1193	.07606	.60	0.4262
641,520.6	8_{80} 9_{73}	ee → oo	1789.36	1810.76	(0.066)	.0380	.40	0.172
641,520.6	8_{81} 9_{72}	eo → oe	1789.36	1810.76	(0.066)	.0380	.40	0.1715
752,737.5	2_{02} 2_{11}	ee → oo	70.08	95.19	2.0739	.10440	.69	0.4648
833,077.5	8_{35} 9_{28}	oo → ee	1052.72	1080.51	(0.157)	.0798	.51	0.4297
857,958.9	11_{29} 10_{56}	eo → oe	1690.74	1719.36	(0.067)	(.055)	(.20)	(0.309)
859,158.0	9_{90} 10_{83}	oe → eo	2225.87	2254.53	(0.059)	.0357	.48	(0.1535)
859.158.0	9_{91} 10_{82}	oo → ee	2225.87	2254.53	(0.059)	.0357	.48	0.1535
912,518.1	3_{31} 4_{22}	oo → ee	285.26	315.70	0.1613	.08638	.676	0.4689
961,381.6	4_{31} 5_{24}	oo → ee	383.93	416.00	0.2622	.08262	.56	0.4722
987,462.1	1_{11} 2_{02}	oo → ee	37.14	70.08	0.7557	.10316	.660	0.5069

FREQUENCY (MHz)	TRANSITION	PARITY	LOWER TERM VALUE $(cm)^{-1}$	UPPER TERM VALUE $(cm)^{-1}$	LINE STRENGTH	LINE WIDTH (AIR) $cm^{-1}\ atm^{-1}$	LINE WIDTH (AIR) TEMP. EXP.	LINE WIDTH (WATER VAPOR) $cm^{-1}\ atm^{-1}$
1,077,394.9	$12_{2,11}$ 11_{38}	eo → oe	1774.85	1810.79	(0.042)	.061	.25	0.3476
1,098,379.3	3_{03} 3_{12}	eo → oe	136.74	173.38	2.1809	.09944	.701	0.5590
1,107,672.3	10_{29} 9_{55}	ee → oo	1438.19	1475.14	(0.050)	(.061)	(.25)	(0.631)
1,113,368.1	0_{00} 1_{11}	ee → oo	0.00	37.14	1.0000	.10034	.689	0.5026
1,142,746.1	$10_{10,0}$ 11_{93}	ee → oo	2702.61	2740.73	(0.054)	(.03434)	(.503)	(0.1297)
1,142,746.1	$10_{10,1}$ 11_{92}	eo → oe	2702.61	2740.73	(0.054)	.03434	.503	0.1297
1,145,743.9	8_{18} 7_{25}	oe → eo	744.20	782.42	(0.025)	.08008	0.498	0.4563
1,154,137.6	2_{21} 3_{32}	eo → oe	134.88	173.38	0.3003	.09515	0.61	0.5485
1,159,833.3	5_{41} 6_{34}	eo → oe	610.34	649.03	0.2784	.07131	.399	0.4229
1,161,332.2	3_{12} 3_{21}	oe → eo	173.38	212.12	2.5434	.09487	.682	0.5060
1,163,430.7	7_{61} 8_{54}	eo → oe	1216.38	1255.19	(0.223)	.0516	.29	0.2908
1,169,726.0	6_{51} 7_{44}	oo → ee	888.74	927.76	(0.252)	.0648	.36	(0.374)
1,187,113.0	7_{62} 8_{53}	ee → oo	1216.38	1255.98	(0.223)	.0542	.30	0.3061
1,208,996.6	8_{71} 9_{64}	oo → ee	1591.11	1631.44	(0.199)	.0445	.32	0.2381
1,213,193.5	8_{72} 9_{63}	oe → eo	1591.11	1631.58	(0.199)	.0447	.34	0.2411
1,213,193.5	4_{13} 4_{22}	oo → ee	272.23	315.70	3.6547	.09507	.72	0.5091
1,227,882.5	2_{11} 2_{20}	oo → ee	95.19	136.15	1.2594	.09792	.67	0.4658
1,227,945.1	6_{52} 7_{43}	oe → eo	888.70	931.33	(0.253)	.0688	.45	0.2682
1,294,432.8	7_{34} 8_{27}	oe → eo	842.51	885.69	(0.184)	.0819	.55	0.4577
1,309,721.3	9_{18} 8_{45}	oe → eo	1079.20	1122.89	(0.047)	(.060)	(.25)	(0.348)
1,323,211.3	5_{32} 6_{25}	oe → eo	508.80	552.94	0.3117	.08313	.571	0.4939
1,329,806.3	9_{81} 10_{74}	eo → oe	2010.19	2054.55	(0.173)	.0390	.39	0.2077
1,329,806.3	9_{82} 10_{73}	ee → oo	2010.19	2054.55	(0.173)	.0390	.39	0.2077
1,342,696.7	8_{17} 7_{44}	oo → ee	882.97	927.76	(0.036)	(.066)	(.30)	(0.375)
1,407,448.3	5_{14} 5_{23}	oe → eo	399.44	446.39	4.2239	.09470	.722	0.5123
1,423,336.4	10_{19} 9_{46}	oo → ee	1293.22	1340.70	(0.059)	(.055)	(.24)	(0.322)
1,435,927.0	6_{33} 7_{26}	oo → ee	661.54	709.44	(0.258)	.0830	.59	0.4642

Appendix A-II

The Absorption Coefficient for Oxygen

The regions of the electromagnetic spectrum in which we are chiefly concerned do not include resonances of any other important atmospheric constituent. However, the wings of the 5 mm complex of magnetic dipole resonances of oxygen are strong enough that their effect must be taken into account in the region near the lowest water vapor resonance at 1.35 cm. Near 1.64 mm the only absorption of potential consequence besides that of the water vapor resonance at 183 GHz is contributed by the high frequency wing of the single oxygen resonance near 2.5 mm. The strength of the oxygen absorption is so slight, however, when compared to the water vapor absorption that it may be safely neglected for all normal computations.

Since oxygen absorption cannot be totally neglected, it will be necessary to provide a working expression to compute its value under atmospheric conditions. The equations which are given below are taken from Meeks and Lilley[35] and this reference along with van Vleck[4] should be consulted for a detailed account of how the equations were derived.

The oxygen molecule has two electrons with unpaired spin. They contribute to a magnetic dipole moment of total strength two Bohr magnetons and spin angular momentum quantum number of $S = 1$. The dumbbell shaped oxygen molecule rotates end over end with angular momentum described by odd values of the quantum number N, even values not being permitted by the Pauli Exclusion Principle. The total

angular momentum is the vectorial sum between N and S. Therefore,
for a given rotational quantum number N, a total rotational quantum
number J may have the values N-1, N, or N+1 depending upon the orien-
tation of S with respect to N. Each of the states of total angular
momentum has slightly different energies. Selection rules allow tran-
sitions between (J = N) $\rightarrow$ (J = N+1) and (J = N) $\rightarrow$ (J = N-1), the reso-
nant frequencies of which all cluster about the region of 5 mm except-
ing only one transition whose resonant frequency occurs near 2.5 mm.

The expression for the absorption by these fine structure tran-
sitions is given by the following equation

$$\gamma_{O_2}(\nu, P, T) = C_1 P T^{-3} \nu^2 \sum_N S_N \exp\left(-E_N / kT\right) \quad \text{(A-II-1)}$$

where γ_{O_2} is the absorption coefficient for oxygen at a given fre-
quency ν , atmospheric pressure P, and atmospheric temperature T .
The summation is taken over all N states of non-negligible population,
usually up to N = 45. The definition of the other terms in (A-II-1)
are as follows:

$$S_N = F_{N+} \mu_{N+}^2 + F_{N-} \mu_{N-}^2 + F_0 \mu_{N_0}^2 \quad \text{(A-II-2)}$$

in which N+ and N- refer to the transitions $N \rightarrow N+1$ and $N \rightarrow N-1$
respectively and the F's and μ 's have the meanings

$$F_{N\pm} = \frac{\Delta\nu}{(\nu_{N\pm} - \nu)^2 + \Delta\nu^2} + \frac{\Delta\nu}{(\nu_{N\pm} + \nu)^2 + \Delta\nu^2} \quad \text{(A-II-3)}$$

$$F_o = \frac{\Delta \nu}{\nu^2 + \Delta \nu^2} \qquad \text{(A-II-4)}$$

$$\mu_{N+}^2 = \frac{N(2N+3)}{N+1} \qquad \text{(A-II-5)}$$

$$\mu_{N-}^2 = \frac{(N+1)(2N+1)}{N} \qquad \text{(A-II-6)}$$

$$\text{and} \qquad \mu_{N_0}^2 = \frac{2(N^2+N+1)(2N+1)}{N(N+1)} \qquad \text{(A-II-7)}$$

The argument of the exponential function may be written as

$$E_N/kT = 2.06844 \; N(N+1)/T \qquad \text{(A-II-8)}$$

For ν_{O_2} to be given in decibels per kilometer C_1 takes on the value

$$C_1 = 2.0058$$

when the pressure is in millibars, the temperature is in degrees Kelvin and the frequency is in gigacycles.

The line width $\Delta \nu$ is, like the case for water vapor, proportional to the pressure, but has peculiar properties due to the very strong overlap of the various individual lines at pressures found in the atmosphere below about 30 kilometers. The expression for the line width may be written as

$$\text{(A-II-8)}$$

$$\Delta \nu(P,T) = \alpha \, P \left[0.21 + 0.78 \, \beta \right] \left[\frac{300}{T} \right]^{0.85}$$

with the empirically derived values for α and β as follows:

$$\alpha = 1.44 \text{ MHz/mb}$$

$$\beta = 0.25 \text{ for } \quad z < H_1 \ (P > 356 \text{ mb})$$

$$\beta = 0.25 + 0.50 \ (h - H_1) \ / \ (H_2 - H_1)$$

$$\text{for } H_1 \leq z \leq H_2$$

$$\beta = 0.75 \text{ for } \quad z > H_2 \ (P < 25.3 \text{ mb})$$

where z refers to height above ground, P the total pressure in milli-
bars and T the temperature in degrees Kelvin.

Appendix A-III

The Emissivity of an Aqueous Solution of NaCl Simulating Sea Water.

The reflection coefficient for an electromagnetic field at the boundary between two lossy dielectrics may be found from Fresnel's equation applied to the conditions depicted in Figure A-III-a below:[46]
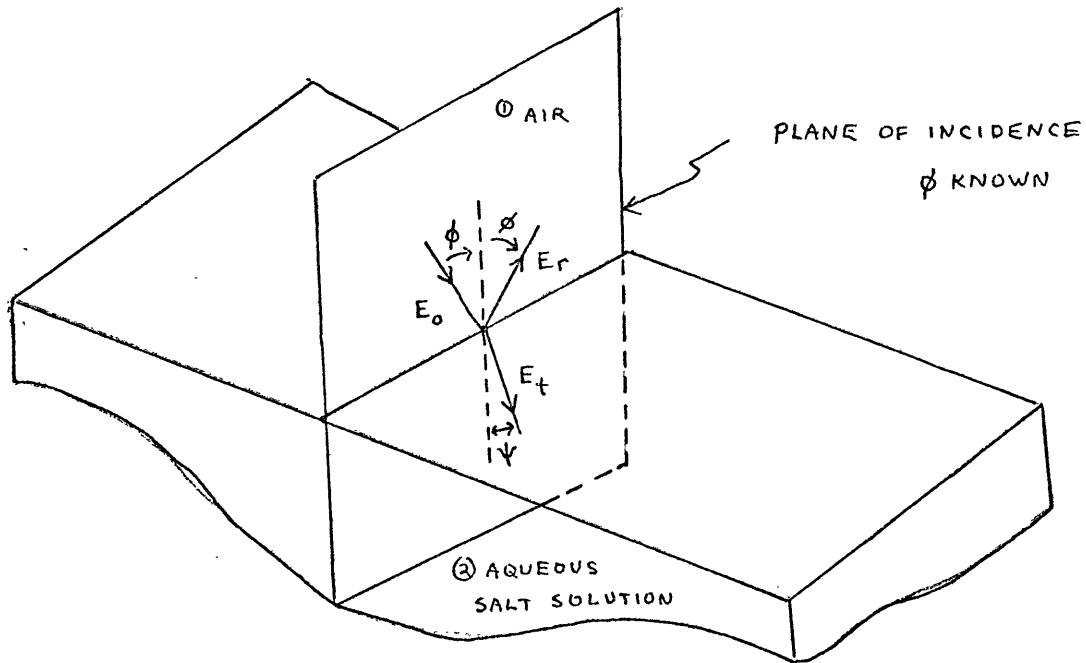
Figure A-III-a

The reflection coefficient for the component of the electric field normal to the plane of incidence is given by:

$$r_n = \frac{E_{r,n}}{E_{o,n}} = \frac{z_2 \cos \phi - z_1 \cos \psi}{z_2 \cos \phi + z_1 \cos \psi} \tag{A-III-1}$$

in which Z_1 and Z_2 are the characteristic impedances of medium 1 and 2

respectively defined as

$$z = \sqrt{\frac{\mu^*}{\epsilon^*}} \qquad \text{(A-III-2)}$$

where μ^* is the complex permeability and ϵ^* is the complex permittivity. The angles ϕ and ψ are related by Snell's Law:

$$\sin \phi = \frac{\gamma_2}{\gamma_1} \sin \psi \qquad \text{(A-III-3)}$$

in which the γ's are the complex propagation factors for each medium defined by

$$\gamma = j\omega \left(\epsilon^* \mu^* \right)^{1/2} \qquad \text{(A-III-4)}$$

where $j = \sqrt{-1}$ and ω is 2π times the frequency.

In general $\sin \psi$ is a complex number and therefore so is $\cos \psi$ in Equation A-III-1. It may written as

$$\cos \psi = \alpha e^{j\xi} \qquad \text{(A-III-5)}$$

where α and ξ are given by

$$\alpha^2 = \left\{ \left[1 - (a^2 - b^2) \sin^2 \phi \right]^2 + 4a^2 b^2 \sin^4 \phi \right\}^{1/2} \qquad \text{(A-III-6)}$$

and

$$\tan 2\xi = \left[\frac{-2ab \sin^2 \phi}{1 - (a^2 - b^2) \sin^2 \phi} \right] \qquad \text{(A-III-7)}$$

If medium 1 is air, we can approximate μ_1^* and ϵ_1^* as

$$\mu_1^* = \mu_0 \qquad\qquad \text{(A-III-8)}$$

$$\epsilon_1^* = \epsilon_0 \qquad\qquad \text{(A-III-9)}$$

the permeability and permittivity of vacuum. Further, we can approximate the permeability of sea water as

$$\mu_2^* = \mu_0 \qquad\qquad \text{(A-III-10)}$$

Under these conditions, the variable a and b in (A-III-6) and (A-III-7) can be written as

$$a = \left[\frac{K_2'^2}{(K_2'^2 + K_2''^2)^2} + \frac{K_2''^2}{(K_2'^2 + K_2''^2)^2} \right]^{1/4} \cos\theta \qquad \text{(A-III-11)}$$

$$b = \left[\frac{1}{K_2'^2 + K_2''^2} \right]^{1/4} \sin\theta \qquad\qquad \text{(A-III-12)}$$

and
$$\tan 2\theta = \frac{K_2''}{K_2'} \qquad\qquad \text{(A-III-13)}$$

where

$$\frac{\epsilon_2^*}{\epsilon_0} = K_2' - j K_2'' \qquad\qquad \text{(A-III-14)}$$

Returning to Fresnel's Equation A-III-1, it may rewritten as

$$r_n = |r_n| e^{j\delta_n} \qquad\qquad \text{(A-III-15)}$$

where

$$|r_n| = \sqrt{e^2 + f^2} \qquad \text{(A-III-16)}$$

$$\text{TAN } \delta_n = f/e \qquad \text{(A-III-17)}$$

$$e = \frac{|z_2|^2 \cos^2 \phi - |z_1|^2 \alpha^2}{|z_2|^2 \cos^2 \phi + |z_1|^2 \alpha^2 + 2|z_1||z_2| \alpha \cos \phi \cos \Omega_n} \qquad \text{(A-III-18)}$$

$$= \frac{N_n}{D_n}$$

$$f = \frac{-2|z_1||z_2| \alpha \cos \phi \sin \Omega_n}{D_n} \qquad \text{(A-III-19)}$$

$$z_1 = |z_1| e^{j \zeta_1} \qquad \text{(A-III-20)}$$

$$z_2 = |z_2| e^{j \zeta_2} \qquad \text{(A-III-21)}$$

and

$$\Omega_n = \zeta_1 - \zeta_2 + \xi \qquad \text{(A-III-22)}$$

The normal emissivity can be written as

$$e_n = 1 - R_n = 1 - |r_n|^2 = 1 - (e^2 + f^2) \qquad \text{(A-III-23)}$$

in which R_n is the power reflection coefficient for electric fields polarized normal to the plane of incidence.

For the reflection coefficient of the electric field parallel to the plane of incidence Fresnel's equation is

$$r_p = \frac{E_{R,P}}{E_{0,P}} = \frac{z_2 \cos \psi - z_1 \cos \phi}{z_2 \cos \psi + z_1 \cos \phi} \qquad \text{(A-III-24)}$$

$$= g + jh$$

where

$$g = \frac{|z_2|^2 \alpha^2 - |z_1|^2 \cos^2 \phi}{|z_2|^2 \alpha^2 + |z_1|^2 \cos^2 \phi + |z_2||z_1|\alpha \cos \phi [2 \cos \Omega_p]} \qquad \text{(A-III-25)}$$

$$= \frac{N_p}{D_p}$$

$$h = \frac{2 |z_2||z_1| \alpha \cos \phi \sin \Omega_p}{D_p} \qquad \text{(A-III-26)}$$

and the remaining symbols have already been defined.

Rewriting Equation (A-III-24) in complex notation gives

$$r_p = |r_p| e^{j\delta_p} \qquad \text{(A-III-27)}$$

where

$$|r_p| = \sqrt{g^2 + h^2} \qquad \text{(A-III-28)}$$

and

$$\text{TAN } \delta_p = h/g \qquad \text{(A-III-29)}$$

The parallel emissivity can be expressed from the above as

$$e_p = 1 - R_p = 1 - |r_p|^2 = 1 - (g^2 + h^2) \qquad \text{(A-III-30)}$$

where R_p is the power reflection coefficient for electric fields

polarized parallel to the plane of incidence.

The question which now presents itself is how do we characterize

ϵ_2^* or k_2^* the complex permittivity or dielectric constant for sea

water. Hasted, et al.[47] have made an experimental study of the electrical

properties of aqueous NaCl solutions of molality close to that of sea

water (0.66 moles per liter concentration) at various frequencies and

temperatures. Their results provides us with the information we need.

The complex dielectric constant of the solution can be written

as

$$k_2^* = k_2' - j\, k_2'' \qquad (A-III-31)$$

where k_2' is the real part and k_2'' is the imaginary part arising

from electrical losses in the medium. k_2'' may be further broken down

into a part which is due to dielectric losses alone, i.e., analogous to

frictional losses as the atomic and molecular dipoles continually attempt

to align themselves with the external oscillating electric field, and

conduction losses, due to the collisions of migrating ions. Symbolic-

ally this may be represented as

$$k_2'' = k_{diel.}'' + k_{d.c.}'' \qquad (A-III-32)$$

where $k_{diel.}''$ results from the so-called Debye losses of the di-

electric and $k_{d.c.}''$ results from the ohmic losses of the solution. The

conduction losses are assumed to be unchanging over at least 10^{10} cycles

per second so that these losses can be estimated from the d.c. con-
ductivity of the solution. This assumption is apparently borne out from
some of the measurements done by Hasted, et al. However, it turns out
to be a very important matter to the behavior of the emissivity of the
solution and certainly needs more definite proof.

Hasted, et al. showed that the real part of the dielectric con-
stant and that portion of the imaginary part which explained dielectric
losses could be expressed as simple functions of the frequency governed
by one relaxation time τ under any given set of physical conditions
for the fluid. The functions were first derived by Debye[18] to explain
the behavior of a signal passing through an assemblage of polar mole-
cules. As discussed in Chapter 2, the expression for the dielectric losses
is exactly that which van Vleck and Weisskopf's important modification
to the Lorentz line shape produced in the limit of zero resonant fre-
quency. The two expressions are

$$K_2' = \frac{K_s - K_o}{1 + (\lambda_s/\lambda)^2} + k_o \qquad \text{(A-III-33)}$$

and

$$K_{diel.}'' = \frac{(K_s - K_o)(\lambda_s/\lambda)}{1 + (\lambda_s/\lambda)^2} \qquad \text{(A-III-34)}$$

where K_s is the dielectric constant for a static (non-oscillating)
field, K_o is the dielectric constant at frequencies where the polar
molecules can no longer follow the field oscillations and atomic polari-
zation is therefore the only important dielectric mechanism, and λ_s

may be written as

$$\lambda_s = 2\pi c \, \tau \qquad \text{(A-III-35)}$$

where τ is the natural relaxation time for the polar molecules.
τ is a function of the physical parameters of the molecules and
their fluid environment.

That portion of the imaginary part of the dielectric constant
due to conduction losses may be written as

$$K''_{d.c.} = \frac{2 \, \sigma_{d.c.}}{f} \qquad \text{(A-III-36)}$$

where σ is the d.c. conductivity in e.s.u (rationalized MKS units
x 9×10^9) and f is the frequency in cycles/sec.

Hasted, et al. measured the values of λ_s and K_s for various
temperatures. A condensed version of those results appears in Table 1
below.

TABLE 1

Values for λ_s and K_s for 0.66 Molal NaCl Solution

Temperature (°C)	λ_s(cm)	K_s(dimensionless)
0	2.96	79.1
10	2.17	75.5
20	1.70	72.0
30	1.35	66.6
40	1.10	63.0

Values for $\sigma_{d.c.}$ are also needed if it is desired to compute K_2^*. For these, data was extracted from the American Institute of Physics Handbook[48]. For sea water of salinity equal to 35 (parts per thousand), a representative value for many oceanic regions. The values of the conductivity so obtained as a function of temperature in rationalized MKS units (mhos/meter) together with the same data which Hasted, et al. measured for the 0.66 molal solution of NaCl is presented in Table 2 below.

TABLE 2

Conductivities of Sea Water and an Aqueous NaCl Solution

Temperature (^{o}C)	Conduct. from Hasted, et al. (mhos/m)	Conduct. from Am Ins. of Phy. H. (mhos/m)
0°	3.31	2.85
10°	4.18	3.81
20°	5.37	4.78
30°	6.52	5.76
40°	7.73	6.75

The last value of column three for sea water (6.75) is an extrapolated value. It can be seen that the sea water values are consistently below the 0.66 NaCl solution values, but the trend is very similar and unmistakable: higher conductivities occur for higher temperatures. This latter fact will be of great importance to the temperature dependence of the emissivity.

Using the formulas and data collected above, it is possible to show several important features of the emissivity of sea water-like solutions. Figure A-III-b shows the real part of the dielectric constant as computed from Equation (A-III-33) for several temperatures. Notice the peculiar reversal of temperature dependence near 3 cm.

Figure A-III-c illustrates the frequency and temperature dependence of the dielectric portion of the imaginary part of the dielectric constant. Again a temperature dependence reversal occurs, but in the vicinity of 1 cm.

Figure A-III-d plots the wavelength dependence and temperature dependence of the conduction loss part of the imaginary part of the dielectric constant (Equation (A-III-36)). A linear dependence on wavelength shows as expected with the slope increasing with temperature.

The total imaginary part of the dielectric constant for simulated sea water and for several temperature is shown in Figure A-III-e.

The dependence of the emissivity at 1 cm on the angle of incidence and temperature for both polarizations is shown in Figure A-III-f. Notice the large temperature dependence.

Finally, the brightness temperature is plotted as a function of solution temperature for several wavelengths in Figure A-III-g. Of importance to note is that at short wavelengths the brightness temperature goes through a minimum; at intermediate wavelength it increases monotonically with temperature; and at long wavelengths it decreases
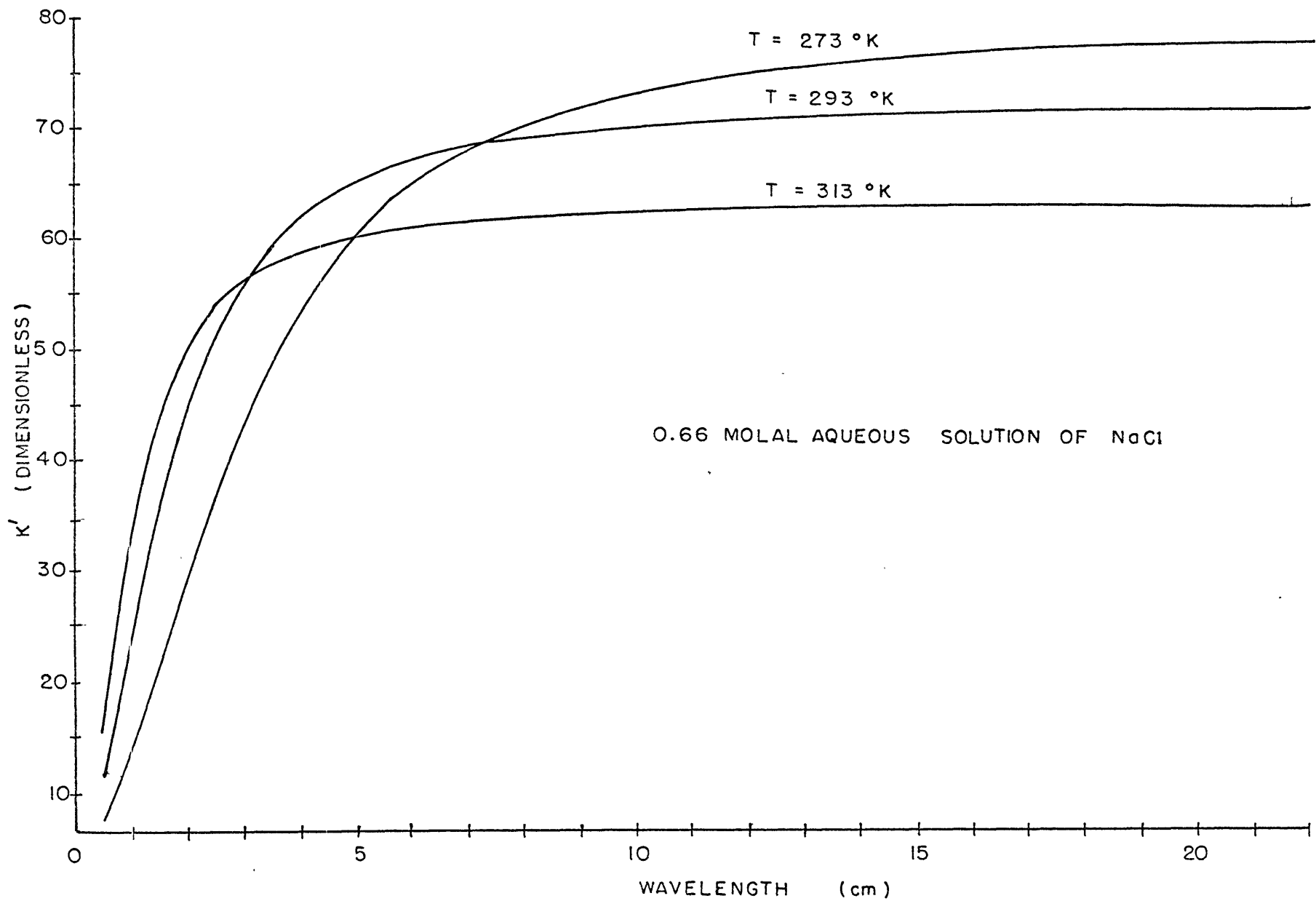
Figure A-III-b. The real part of the dielectric constant
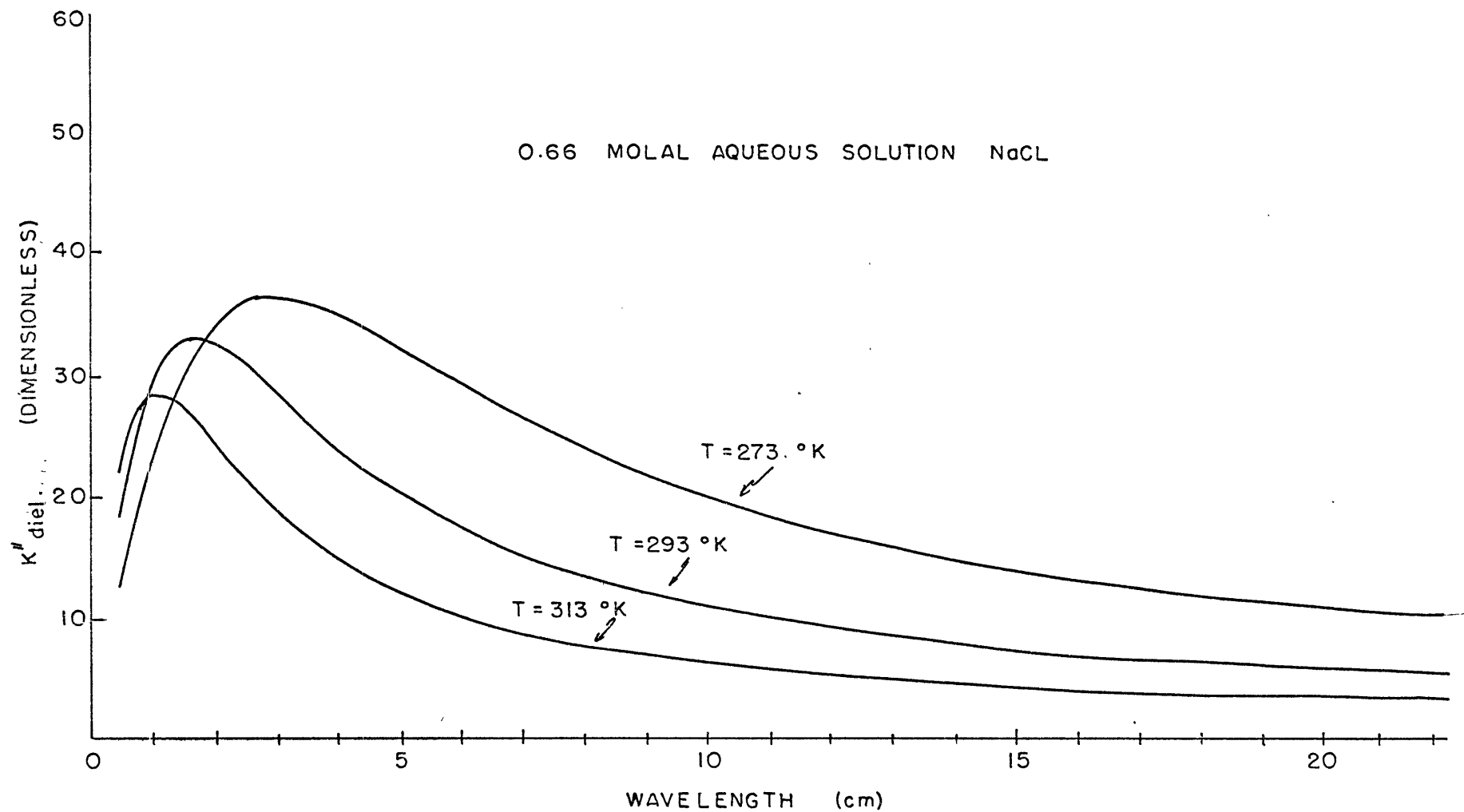for simulated sea water as a function of
wavelength.

Figure A-III-c. The dielectric portion of the imaginary part of the dielectric
constant for simulated sea water as a function of wavelength.

Figure A-III-d. The conduction loss portion of the imaginary part of
the dielectric constant for simulated sea water as
a function of wavelength.
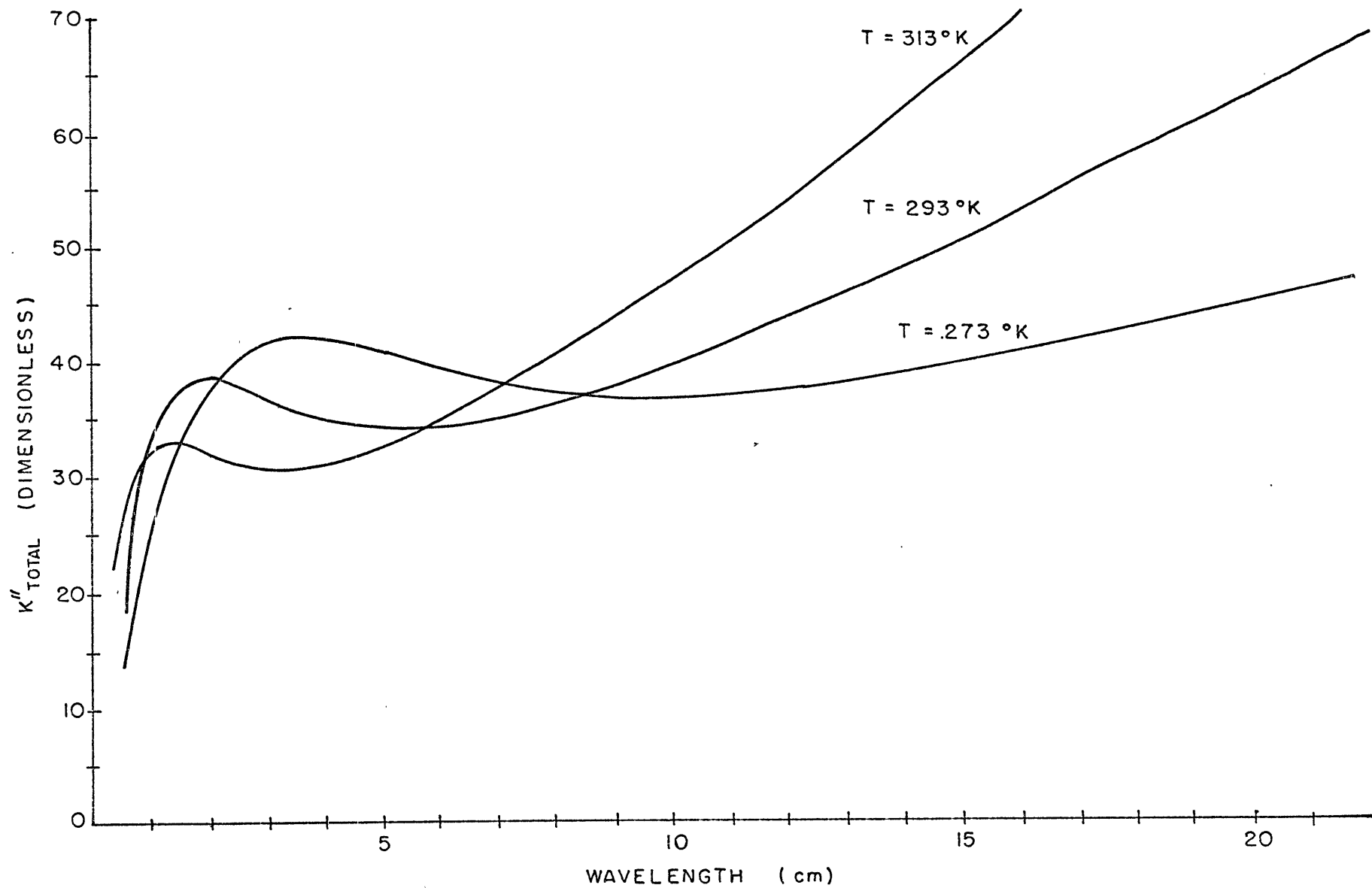
Figure A-III-e. The total imaginary part of the dielectric constant for simulated sea water as a function of wavelength and for several temperatures.
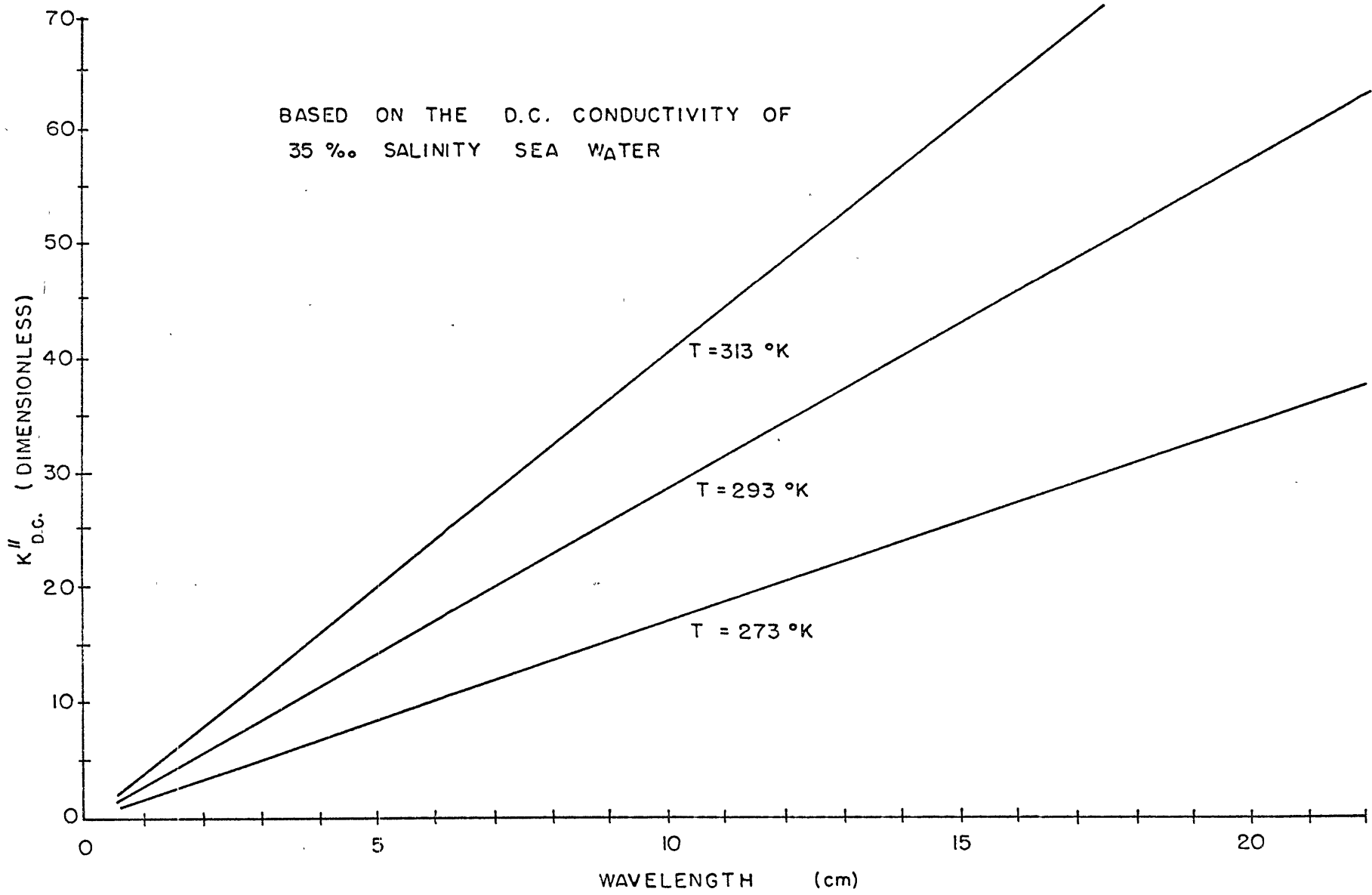
Figure A-III-f. The dependence of the emissivity at 1 cm on the angle
of incidence and temperature.

Figure A-III-g. The brightness temperature as a function of sea surface temperature for several wavelengths.

monotonically with temperature. The change in temperature dependence as a function of wavelength is a result of the changing dominance between K''_{diel} and $K''_{d.c.}$ with wavelength.

Appendix A-IV

Details of Data Reduction

A typical 10 minute sunscan, baseline, calibration sequence looks much like Figure A-III-a below.

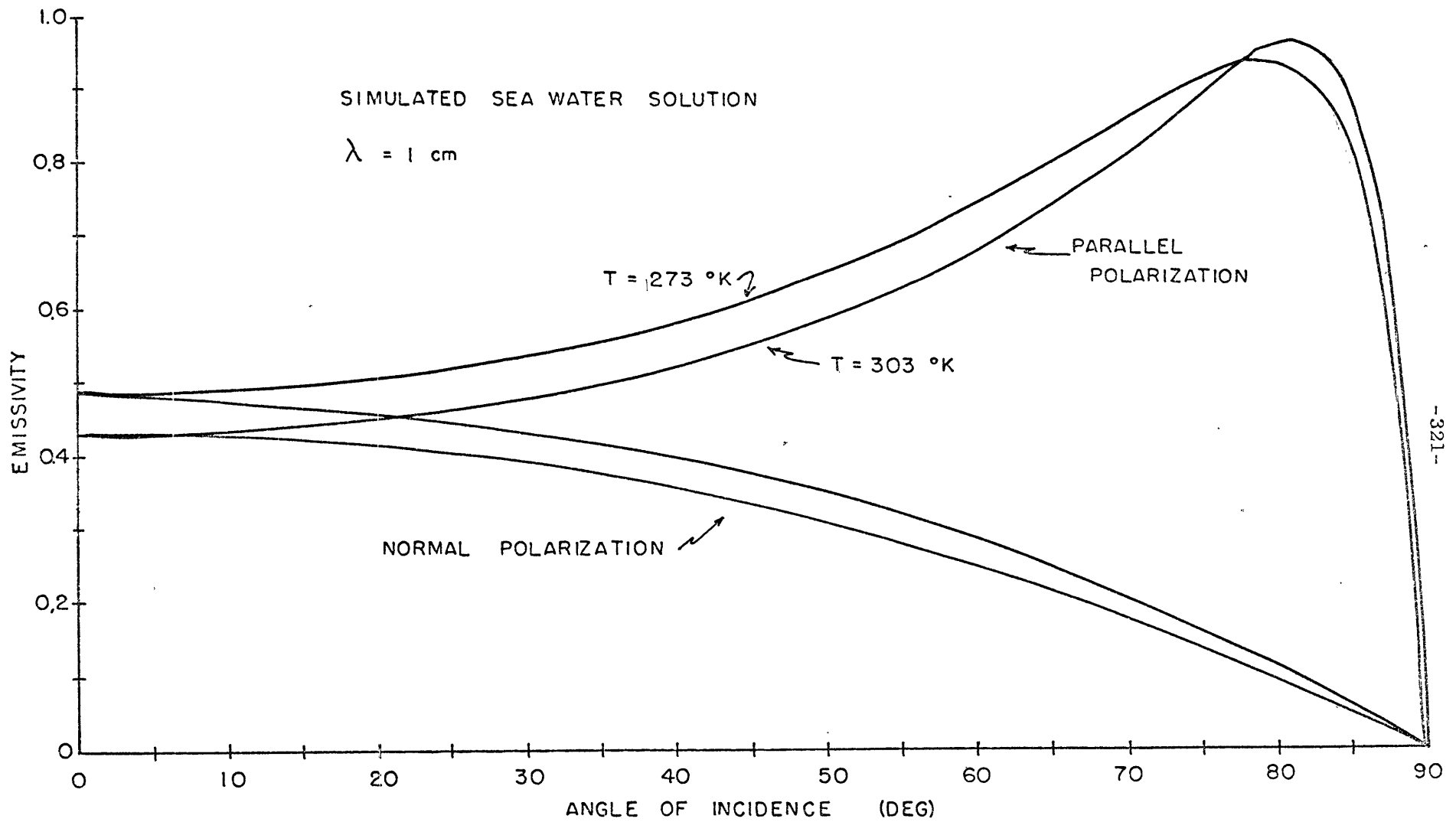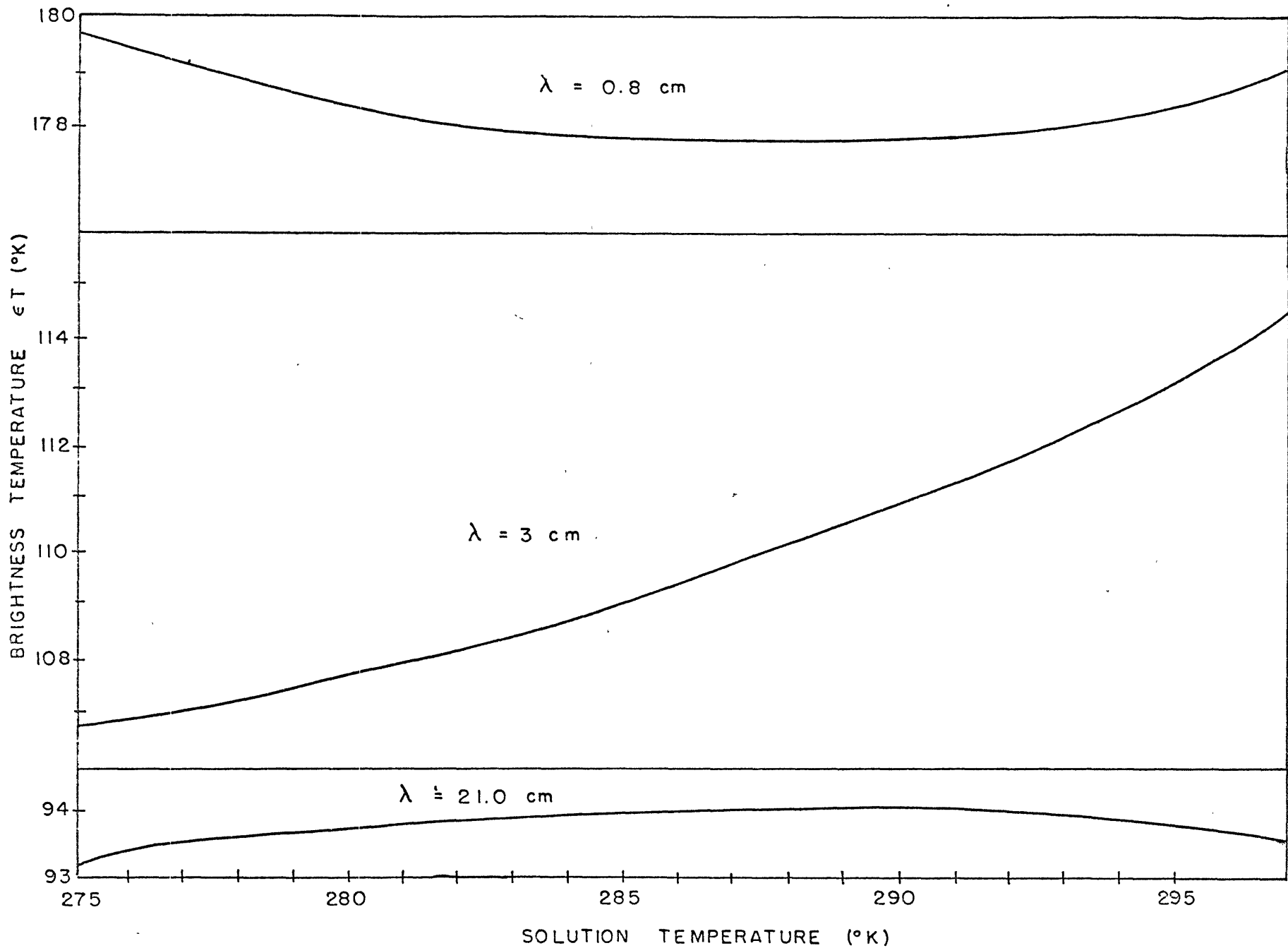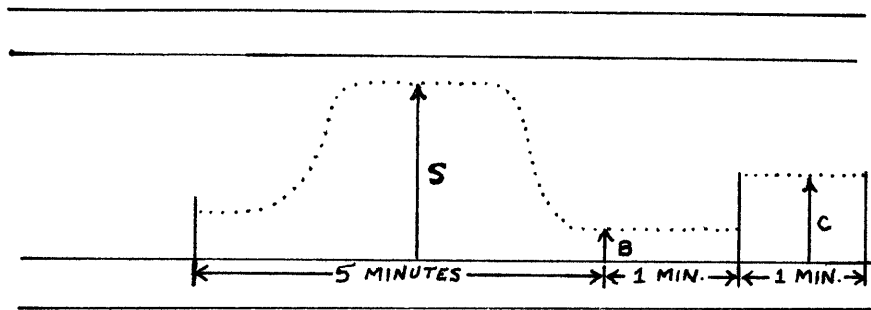Figure A-IV-a. A typical sequence of data as seen on a strip recorder chart during solar extinction measurements.

From processing on the PDP-1, one obtains $\bar{S}$, $\bar{B}$, $\bar{C}$, and $\sigma_{\bar{S}}^2$, $\sigma_{\bar{B}}^2$ and $\sigma_{\bar{C}}^2$. $\bar{S}$, $\bar{B}$, and $\bar{C}$ are the means of the individual samples, and the σ^2 are their variances.

The quotient $(\bar{S} - \bar{B})/(\bar{C} - \bar{B}) = \dfrac{N}{D} = A$ is formed.

The variances of N and D are given by

$$\sigma_N^2 = \sigma_{\bar{S}}^2 + \sigma_{\bar{B}}^2 \quad , \quad \sigma_D^2 = \sigma_{\bar{C}}^2 + \sigma_{\bar{B}}^2 \qquad \text{(A-IV-1)}$$

σ_A^2 is formed from

$$\sigma_A^2 = \left(\frac{\partial A}{\partial N}\right)^2 \sigma_N^2 + \left(\frac{\partial A}{\partial D}\right)^2 \sigma_D^2 \qquad \text{(A-IV-2)}$$

$$= \frac{1}{D^2} \sigma_N^2 + \frac{N^2}{D^4} \sigma_D^2 \qquad \text{(A-IV-3)}$$

Weighting factors for the various sunscans were taken to be

$$W_{A_i} = w_{A_i} + \frac{1}{3} \sum_i w_{A_i} \qquad \text{(A-IV-4)}$$

where

$$w_{A_1} \sigma_{A_1}^{-2} = w_{A_2} \sigma_{A_2}^{-2} = \ldots = \sigma^{-2} \qquad \text{(A-IV-5)}$$

The second term was added to the right hand side of Equation (A-II-4) to diminish the effect of the variances in the weighting functions. The variances are indicators of the internal consistency of the data and are random variables. They do not measure systematic errors, hence, they were not relied upon as the sole indicators of goodness for the data.

Figure A-IV-b presents the parameters which are input to the least squares determination of the slope and intercept of a typical day's data used to determine the opacity.
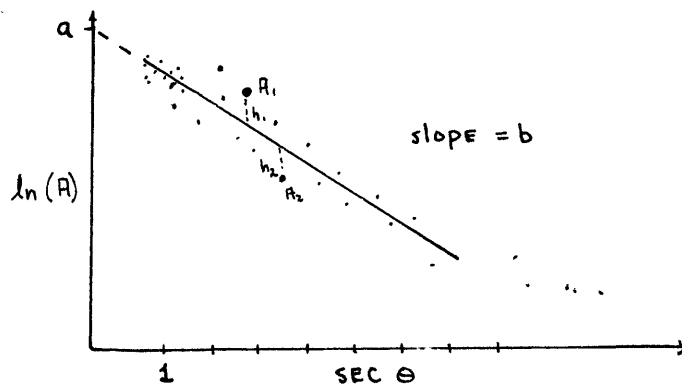

Figure A-IV-b. The details of a hypothetical plot to determine τ_{max} .

A point A_i will lie a distance h_i away from some "best" line passing through the data. Its weight will be determined by (A-IV-4). If the slope is b and the intercept is a, then we want to find a and b such that

$$\sum_i W_{A_i} h_i^2 \qquad \text{is a minimum.} \qquad \text{(A-IV-6)}$$

The solutions for a and b are the following[43]:

$$a = \frac{\left(\sum_{i=1}^{N} W_{A_i} \sec^2 \theta_i\right)\left(\sum W_{A_i} \ln A_i\right) - \left(\sum W_{A_i} \sec \theta_i\right)\left(\sum W_{A_i} \sec \theta_i \ln A_i\right)}{\left(\sum W_{A_i}\right)\left(\sum W_{A_i} \sec^2 \theta_i\right) - \left(\sum W_{A_i} \sec \theta_i\right)^2} \qquad \text{(A-IV-7)}$$

$$b = \frac{\left(\sum_{i=1}^{N} W_{A_i}\right)\left(\sum W_{A_i} \sec \theta_i \ln A_i\right) - \left(\sum W_{A_i} \sec \theta_i\right)\left(\sum W_{A_i} \ln A_i\right)}{\left(\sum W_{A_i}\right)\left(\sum W_{A_i} \sec^2 \theta_i\right) - \left(\sum W_{A_i} \sec \theta_i\right)^2} \qquad \text{(A-IV-8)}$$

The "best" straight line is then given by

$$\ln(A) = a + b \sec \theta \qquad \text{(A-IV-9)}$$

The variances of a and b may be estimated from the following formulas: if $y_i = \ln A_i$, then

$$\sigma_y^2 = \frac{\sum_{i=1}^{N} \left[y_i - (a + b \sec \theta_i)\right]^2}{N - 2} \qquad \text{(A-IV-10)}$$

and

$$\sigma_a^2 \approx \sigma_y^2 \frac{\sum W_{A_i} \sec^2 \theta_i}{F} \qquad \text{(A-IV-11)}$$

$$\sigma_b^2 = \sigma_y^2 \frac{N}{F} \qquad \text{(A-IV-12)}$$

where

$$F = \left(\sum W_{A_i} \right)\left(\sum W_{A_i} \sec^2 \theta_i \right) - \left(\sum W_{A_i} \sec \theta_i \right)^2 \qquad \text{(A-IV-13)}$$

Equation (A-IV-10) gives the variance of the data points about the "best" straight line through them. All equations assume negligible error in sec θ .

Appendix A-V

Estimation of and Correction for Atmospheric Curvature and Atmospheric Refraction.

In a horizontally stratified atmosphere, the following method may be used to determine the zenith opacity $\tilde{\tau}_{max}$:

Given that:

A = amplitude of the solar signal

C = constant of proportionality

T_s = solar brightness temperature at the observing frequency

ϵ_o = elevation angle of antenna = $\pi/2 - \theta_o$

θ_o = zenith angle of antenna

then

$$A = C\, T_s\, e^{-\tau_{max}\, \sec \theta_o} \qquad \text{(A-V-1)}$$

where the exponential term represents atmospheric attenuation. Taking logarithms of both sides gives

$$\ln A = \ln C\, T_s - \tau_{max}\, \sec \theta_o \qquad \text{(A-V-2)}$$

τ_{max} may be determined from (A-V-2) by using the expression

$$\tau_{max} = -\frac{\Delta\left(\ln \frac{A}{C T_s}\right)}{\Delta\left(\sec \theta_o\right)} \qquad \text{(A-V-3)}$$

since, for the conditions given and perfect data, the right hand side is a straight line.

Unfortunately, the real atmosphere is spherical and Equation (A-V-3) is not applicable at low elevation angles. It may be modified, however, to take into account both the sphericity of the atmosphere and the refraction which occurs at elevation angles less than 5°.

A-V-1. Reformulation of the Solution for τ_{max} in a Refracting Curved Atmosphere.

Atmospheric opacity at a fixed frequency is defined as

$$\tau_{\theta_o} = \int Y(\nu, z) \sec\theta \, dz \qquad \text{(A-V-4)}$$

where the absorption coefficient is integrated over height, and the secant of the local zenith angle provides the proper increased path length for a non-vertical propagation path. In a planar, non refracting atmosphere, $\theta = \theta_o$ everywhere where θ_o is the zenith angle of the antenna. τ_{θ_o} can therefore be expressed as

$$\tau_{\theta_o} = \sec\theta_o \int_o^\infty Y(\nu, z) \, dz \qquad \text{(A-V-5)}$$

$$= \tau_{max} \sec\theta_o$$

The use of Equation (A-V-3) is then warranted.

For the more general case τ_{θ_o} may be expressed as

$$\tau_{\theta_o} = \tau_{max} W'_{\theta_o} \qquad \text{(A-V-6)}$$

where W'_{θ_o} is the factor which when multiplied by τ_{max} gives the

true opacity of an antenna whose elevation angle is $\pi/2 - \theta_o$. W_{θ_o}' is evidently

$$W_{\theta_o}' = \frac{\int_0^\infty \gamma(\nu, z)\, \sec\theta\, dz}{\mathcal{T}_{max}} \qquad \text{(A-V-7)}$$

Because of the usefulness of Equation (A-V-3) it is convenient to define a new correction factor W_{θ_o} such that

$$W_{\theta_o} = W_{\theta_o}' \Big/ \sec\theta_o \qquad \text{(A-V-8)}$$

and therefore

$$\mathcal{T}_{\theta_o} = \mathcal{T}_{max}\, \sec\theta_o\, W_{\theta_o} \qquad \text{(A-V-9)}$$

Equation (A-V-3) may be reformulated using Equation (A-V-9) as

$$\mathcal{T}_{max} = -\frac{\Delta\left(\ln\frac{A}{CT_s}\right)}{\Delta\left(\sec\theta_o\, W_{\theta_o}\right)} \qquad \text{(A-V-10)}$$

retaining the linearity of the plot with all of the concomitant advantages for graphical or numerical evaluation.

A-V-2. **The Correction Factor** W_{θ_o} **for a Curved Refracting**

        Atmosphere.

The local zenith angle of source ray detected at a surface based antenna will change along its atmospheric path length. Its exact dependence upon its environment may be easily shown as follows[34] if reference is made to Figure A-V-a.
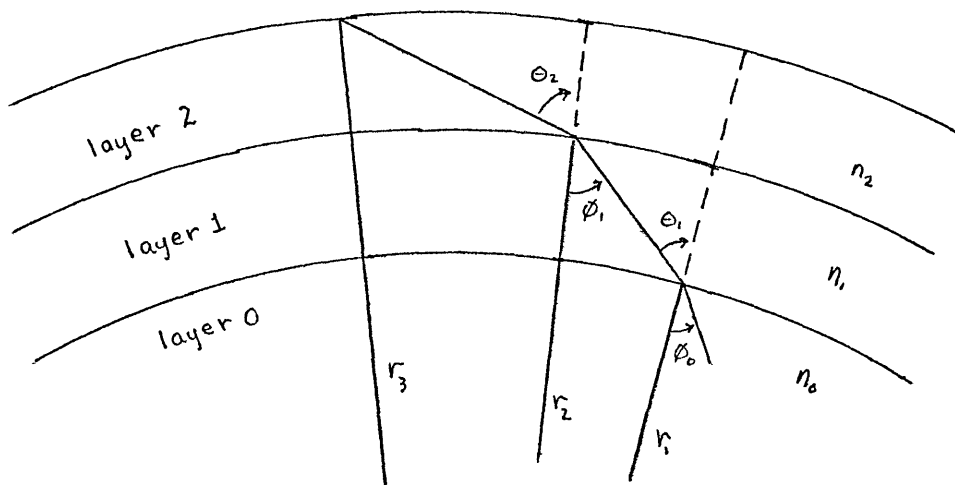
Figure A-V-a.   The geometry of a spherical, refracting
               atmosphere.

By crossing the boundary between the layers having differing

indices of refraction n, a ray propagating other than vertically will

be refracted, altering its absolute direction.   Also, because of the

sphericity of the atmosphere, the angle which a ray makes with respect

to a local radius will change as it progresses even if no refraction

takes place.

At the boundary between two layers of differing indices of

refraction, say layers 0 and 1, a ray will change direction with

respect to the radius passing through the point of penetration so

that Snell's Law will be satisfied, i.e.

$$n_0 \sin \phi_0 = n_1 \sin \phi_1 \qquad\qquad (A-V-11)$$

θ_1 is related to ϕ_1 by the Law of Sines,

$$\frac{\sin \phi_1}{r_1} = \frac{\sin(\pi - \theta_1)}{r_2}$$ (A-V-12)

allowing (A-V-11) to be rewritten as

$$n_0 \sin \theta_0 = \frac{r_2 \, n_1}{r_1} \sin \phi_1$$ (A-V-13)

Invoking Snell's Law again, (A-V-13) can be expressed as

$$n_1 r_1 \sin \theta_1 = n_2 r_2 \sin \theta_2$$ (A-V-14)

a result which does not depend upon which two atmospheric layers were chosen nor upon their thickness or refractive qualities. Any two consecutive layers would be equal, leading to the conclusion that each side must equal a constant, i.e.

$$n r \sin \theta = s = n_0 r_0 \sin \theta_0$$ (A-V-15)

The correction factor W_{θ_0} may now be specified in more detail. The integrand of Equation (A-V-7) requires knowledge of $\sec \theta$ as a function of $z(r)$. Equation (A-V-15) gives it to us as

$$\sec \theta = \frac{1}{\sqrt{1 - (s/nr)^2}}$$ (A-V-16)

and, therefore, W_{θ_0} may be expressed as

$$W_{\theta_0} = \frac{\displaystyle\int_0^R \frac{\gamma(z', z)}{\sqrt{1 - (s/nr)^2}} \, dz}{\tau_{max} \, \sec \theta_0}$$ (A-V-17)

In (A-V-17), R is some convenient height outside the atmosphere,

$\mathcal{T}_{max}$ is the zenith opacity, θ_0 is the zenith angle of the antenna,

$r = r_0 + z$ where r_0 is the radius of the earth, s is given by

Equation (A-V-15) and n is the index of refraction at the height z .

The next section will discuss n in more detail.

The quantities of Equation (A-V-18) can be divided into those

which are known or easily measured: s , θ_0 , r ; and those which

depend upon a knowledge of the vertical structure of the atmosphere:

$\gamma(\nu, z)$, $n(z)$, and $\mathcal{T}_{max}$. Radiosonde measurements of

the atmosphere's vertical structure give a reasonably good idea of

$n(z)$; $\mathcal{T}_{max}$ can be adequately inferred from the radiometer measure-

ments above antenna elevation angles where W_{θ_0} becomes significant.

However, $\gamma(\nu, z)$ has been shown to be on the average poorly repre-

sented by radiosonde measurements for a number of reasons. The repre-

sentation of $\gamma(\nu, z)$ no doubt can be improved by using $\mathcal{T}_{max}$

measured from the secant θ_0 plots as a guide to increasing the water

vapor density at all levels by some factor to bring $\int_0^R \gamma(\nu, z)\, dz$ into

approximate agreement with $\mathcal{T}_{max}$, and using the new water vapor pro-

file to calculate $\gamma(\nu, z)$ and $n(z)$.

A-V-3. The Index of Refraction n in the Radio Range of Frequencies.

In the atmosphere, two effects work to change n independently:

(1) changes in density of the air; and (2), changes in moisture con-

tent. Their effects are almost independent of frequency over the

radio range of frequencies. In terms of temperature T in degrees Kelvin, pressure P in millibars, and the partial pressure of water vapor e in millibars, the expression for the index of refraction in terms of N the refractivity is given by the following equation[33]:

$$N = (n-1) \times 10^{-6} = 79 \frac{P}{T} + \frac{3.8 \times 10^5}{T^2} e \qquad \text{(A-V-18)}$$

The overall shape of N(z) is dominated by the first term of Equation (A-V-18), the total atmospheric pressure term. It causes N, in the mean, to decrease with height exponentially. In the lowest two kilometers, however, water vapor variations will normally play the most important role in controlling the shape of the N(z) curve. And since it is in the lowest two kilometers that the bulk of atmospheric absorption occurs, the knowledge of the water vapor distribution becomes quite important.

The entire discussion above points out the pitfalls and the tasks necessary to produce even approximate correction terms W_{θ_0}. They require, for a precise evaluation, a great deal of information and even results from the radiometer experiment itself. And, although W_{θ_0} was computed in a number of cases, it was determined that unless the departure of the data points from a straight line were being used to study the distribution of water vapor in height (as it can be), it would be more efficient for the purposes of this thesis to ignore points where significant corrections were needed. This was finally done.

Appendix A-VI

Equations Used in Atmospheric Computations

Radiosondes report temperature, pressure and relative humidity

at distinct levels in the atmosphere. To convert this data to other

parameters of interest, the following equations were used:

1. The lapse rate between two temperature reports was assumed

to be linear. Therefore the mean temperature in the layer is

$$T = (T_2 + T_1)/2. \qquad \text{(A-VI-1)}$$

2. The rate of change of water vapor density between two

levels was assumed to be constant. Therefore the mean water vapor

density is

$$\bar{\rho} = \left(\rho_1 + \rho_2 \right)/2 \ . \qquad \text{(A-VI-2)}$$

This approximation is not good when layers are separated by large

distances. A more useful average in this case was determined to be

the average of an exponential decrease, so that

$$\bar{\rho} = - \frac{H\rho}{z_2 - z_1} \left(\rho_2 - \rho_1 \right) \qquad \text{(A-VI-3)}$$

where H is the scale height given by

$$H_\rho = - \left(z_2 - z_1 \right) / \ln \left(\frac{\rho_2}{\rho_1} \right) \qquad \text{(A-VI-4)}$$

3. The virtual temperature was approximated by

$$T^* = T(1 + 0.608 \ W) \qquad \text{(A-VI-5)}$$

where T is in $^\circ$C or $^\circ$K and W is the mixing ratio in grams of water

vapor per gram of dry air.

4. The mixing ratio W can be computed from

$$W = \epsilon \frac{e}{p-e} \qquad \text{(A-VI-6)}$$

where $\epsilon = 0.622$.

5. The height of a constant pressure surface P_2 above another, P_1, which is at level z_1 is given by

$$z_2 = z_1 - \left(R_{AIR} \, T^* / 9.8 \right) \ln \left(\frac{P_2}{P_1} \right) \qquad \text{(A-VI-7)}$$

where T* is the mean virtual temperature in $^{\circ}$K, R_{AIR} is the gas constant for dry air equal numerically to approximately 287 for z_1 and z_2 in meters.

6. When the partial pressure of water vapor is known in millibars, the density of water vapor in g/m^3 is given by

$$\rho = \frac{e}{R_{wv} T} = 561 \frac{e}{T} \qquad \text{(A-VI-8)}$$

where R_{wv} is the gas constant for water vapor and T is in $^{\circ}$K.

7. The mean pressure in a layer of an exponential atmosphere is given by

$$\overline{P} = -\frac{H_P}{(z_2 - z_1)} \left(P_2 - P_1 \right) \qquad \text{(A-VI-9)}$$

where

$$H_P = -\left(z_2 - z_1 \right) / \ln \left(\frac{P_2}{P_1} \right) \qquad \text{(A-VI-10)}$$

8. If the thickness of a layer is known, i.e., z_2 and z_1, then the pressure of the upper surface is

$$P_2 = P_1 \, e^{-(z_2 - z_1)/H_P} \qquad \text{(A-VI-11)}$$

where H_p is defined in (A-IV-10).

9. If the dew point or frost point temperature is known, then the logarithm of the partial pressure of water vapor   given in millibars is

$$\log_{10} e_w = -7.90298\left(373.16/T - 1\right) + 5.02808 \log_{10}\left(373.16/T\right)$$
$$- 1.3816 \times 10^{-7}\left(10^{11.344\left(1-T/373.16\right)} - 1\right)$$
$$+ 8.1328 \times 10^{-3}\left(10^{-3.49149\left(373.16/T - 1\right)} - 1\right) + \log_{10}\left(1013.25\right)$$

(A-VI-12)

$$\log_{10} e_i = -9.09718\left(273.16/T - 1\right) - 3.56654 \log_{10}\left(273.16/T\right)$$
$$+ 0.876793\left(1 - T/273.16\right) + \log_{10} 6.1071$$

where e_w is the saturation vapor pressure over water and e_i is the saturation vapor pressure over ice. Equation (A-VI-12) is the Goff-Gratch formula[78] for saturation vapor pressure at the temperature T.

10. If the temperature and relative humidity q are known, then the partial pressure of water vapor is given by

$$e = q \, e_s$$

(A-VI-13)

where e_s is computed from Equation (A-VI-12) using the temperature.

Miscellaneous data:

1 atmosphere = 1013.25 millibars = 760 mm of Hg

1 millibar = 1000 dynes/cm^2

BIOGRAPHY

The author was born in the mining town of Gilman, Colorado, September 20, 1937. His parents were Marvin Joseph and Margaret Carl Gaut. From age four until his military service began in 1959, he resided in southern California near Los Angeles. He graduated valedictorian of his Hawthorne High School class in 1955. In 1959 he graduated with honors in Physics from the University of California at Los Angeles and was elected to Phi Beta Kappa. Three years of military duty beginning in 1959 consisted of one year of graduate work in meteorology at the University of California at Los Angeles, followed by two years of weather forecasting at Harmon Air Force Base, Newfoundland, Canada. He came to M.I.T. in 1962 and earned an S.M. in meteorology in February 1964. From September 1962 to June 1963 he worked part time as a teaching assistant; from June 1963 to June 1967 support was supplied through a N.A.S.A. Traineeship. The author was married to the former Madeleine Suzanne Dupuy of Paris, France in August 1964. They have two boys, Christopher Carl born in 1966 and Eric Kerwin born in 1967.